PHOTOCATALYTIC NANOCOMPOSITES FOR DEGRADATION OF ORGANIC POLLUTANTS IN WATER UNDER VISIBLE LIGHT

by

MOPE EDWIN MALEFANE

submitted in accordance with the requirements for
the degree of

MAGISTER TECHNOLOGIAE

in the subject

ENGINEERING: CHEMICAL

at the

UNIVERSITY OF SOUTH AFRICA

SUPERVISOR: Dr A. T. KUVAREGA

CO-SUPERVISOR: Dr U. FELENI

NOVEMBER 2019

DECLARATION

Name: MOPE_EDWIN_MALEFANE

Student number: 62231855

Degree: MAGISTER TECHNOLOGIAE in Chemical Engineering

Exact wording of the title of the dissertation as appearing on the electronic copy submitted for examination:

PHOTOCATALYTIC NANOCOMPOSITES FOR DEGRADATION OF ORGANIC POLLUTANTS IN WATER UNDER VISIBLE LIGHT

I declare that the above dissertation is my own work and that all the sources that I have used or quoted have been indicated and acknowledged by means of complete references.

I further declare that I submitted the dissertation to originality checking software and that it falls within the accepted requirements for originality.

I further declare that I have not previously submitted this work, or part of it, for examination at Unisa for another qualification or at any other higher education institution.

(The dissertation will not be examined unless this statement has been submitted.)

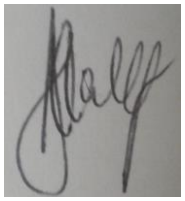

SIGNATURE

NOVEMBER 2019
DATE

SUMMARY

Heterojunctions were generated between tungsten trioxide and tetraphenyl porphyrin with reduced graphene oxide or exfoliated graphite support for mineralisation of acid blue 25 dye under visible light radiation. Moreover, degradation of pharmaceuticals was conducted using p-n heterojunctions between WO_3 and Co_3O_4 and a direct Z-scheme heterojunction between BiOI and Co_3O_4 prepared using in-situ method and solvothermal self-assembly method respectively. The synthesized materials were characterised using Raman, FTIR, SEM/EDS, TEM, XRD, TGA, BET, UV-Vis and PL techniques. UV-Vis, TOC and HPLC-QTOF-MS were used to study the degradation efficiency and pathway. Scavenger trapping experiments were conducted to propose the charge transfer mechanisms. The highest degradation efficiency (99 %) was achieved for the dye and the pharmaceuticals using visible light. The mineralisation ability of the fabricated nanomaterials was pH dependent with acidic conditions favouring the removal of the dye (pH 5) while alkaline conditions favoured the mineralisation of pharmaceuticals (pH 10 – 11).

KEY TERMS:

Heterojunctions; Metal oxide semiconductors; Synergy; Proposed charge transfer; Total organic carbon; Visible light irradiation; Photocatalysis; Dyes; Pharmaceuticals; Batch reactor set-up

DEDICATION

I dedicate this dissertation to the following people;

1. My beloved parents Moleko Raphael Malefane and Makemelo Cecilia Malefane; you raised me to become a gentleman that I am by ensuring that I get the opportunity to go to school.
2. My precious and caring siblings Mamoliehi A. Letuka and Mamoipusi E. Malefane for their patience, love, encouragement and support during hard times.

ACKNOWLEDGEMENTS

I would like to thank the following people and institutions for their contributions towards the success of this project

- Jehovah for keeping me alive, giving me the strength and perseverance do endure through the hard times. YOU alone are GOD.
- My supervisors, Dr. A.T Kuvarega and Dr U. Feleni for their guidance, understanding and support. You allowed me to grow not only as a student through your professional advices but also by allowing me to take the lead in this research.
- Dr. Bulelwa Ntsendwana for giving me an opportunity to become a student at UNISA. I really appreciate everything she has done for me.
- Many thanks to Dr N. Mabuba for hosting me at University of Johannesburg DFC campus. I got to appreciate how other institutions are and I must admit that being there taught me a lot of things. The experience was immeasurable.
- Dr. S.J. Mkhize for allowing me to conduct some of my experiments in the organic chemistry lab at UNISA and providing some chemicals to perform experiments, you will remain the best.
- I would like to thank the Physics Department staff at UNISA for their dedication in helping me to analyse my samples with FE-SEM, XRD and PL. Special thanks to Dr P. Mbule, Dr L. Matebula, Mr M. Fokotsa and Mr T. Mlotshwa.
- I would also like to pass my gratitude to UWC for helping me with TEM analysis.
- My heartfelt appreciation goes to my parents who raised me up with love and suffered for me to get this far. Special mention to my mother for all the things she went through just to make sure I get proper education.
- My heartfelt gratitude to my sisters Mamoliehi A. Letuka and Mamoipusi E. Malefane. You provided shoulders for me to cry on. Thanks for your prayers, encouragement and never giving up on me.
- Mr. Kagiso for always ensuring that there is enough room for everyone to approach him and for training on some laboratory equipment.
- I would like to sincerely pass my gratitude to Chemical Engineering Department for their help with analysis of some of the samples. Special thanks to Mrs. P. Moroenyane and Mr. T. Ntelane for their assistance.
- Mr. P.J Mafa who really helped me a lot with equipment training, the numerous discussions and encouraging words.

- The photo/electrochemistry group, thank you for the contributions that you made to make me a better person. The discussions and fun moments that we shared together will always be in my heart.
- I would like to direct my special thanks to CATSA for partially funding my grant to attend the EAAOP-6 conference held in Slovenia in June 2019. The attendance helped me to learn from many renowned professionals in the field of Advanced Oxidation Technologies.
- UNISA for providing the research facilities, training and staff that is understanding and always willing to help. I appreciate.
- Nanotechnology and Water Sustainability Research Unit at UNISA, I am honoured for the financial support and the opportunity to pursue my studies.

PRESENTATIONS AND PUBLICATIONS

Conference Presentations:

- M. E Malefane and A. T. Kuvarega, Tetraphenylporphyrin/tungsten (vi) oxide/exfoliated graphite nanocomposite for photocatalytic degradation of acid blue 25 dye under visible light irradiation. **Oral presentation.** 6th European conference on Environmental Applications of Advanced Oxidation Processes. Portoroz-Portorose, Ljubljana, Slovenia. 26 – 30 June 2019.
- M. E. Malefane, P. J. Mafa, U. Feleni, A. T. Kuvarega, Facile synthesis of self-assembled BiOI decorated cobalt oxide microspheres and its applications for mineralisation of pharmaceuticals. **Oral presentation.** US-Africa Forum on Nanotechnology Convergence for Sustainable Energy, Water and Environment. Glenburn Lodge & Spa, Johannesburg, South Africa. 11 - 15 August 2019.

Publications:

- M. E. Malefane, B. Ntsendwana, P. J. Mafa, N. Mabuba, U. Feleni, A. T. Kuvarega, In-Situ Synthesis of Tetraphenylporphyrin/Tungsten (VI) Oxide/Reduced Graphene Oxide (TPP/WO3/RGO) Nanocomposite for Visible Light Photocatalytic Degradation of Acid Blue 25. Published in *ChemistrySelect*. DOI: 10.1002/slct.201901589.
- M. E. Malefane, U. Feleni, A. T. Kuvarega, A tetraphenylporphyrin/WO_3/exfoliated graphite nanocomposite for the photocatalytic degradation of an acid dye under visible light irradiation. Published in *New Journal of Chemistry*. DOI: 10.1039/c9nj02747e.
- M. E. Malefane, U. Feleni, A. T. Kuvarega, Visible light driven Cobalt (II/III) oxide and tungsten (VI) oxide p-n heterojunction photocatalyst for degradation of diclofenac sodium. Submitted to *Journal of Environmental Chemical Engineering*. Status: Accepted. DOI: 10.1016/j.jece.2019.103560.
- M. E. Malefane, U. Feleni, J. P. Mafa, A. T. Kuvarega, Fabrication of direct Z-scheme Co_3O_4/BiOI for ibuprofen and trimethoprim degradation under visible light irradiation. Submitted to *Applied surface science.* Status: Under review.

ABSTRACT

Water resources are under constant threat due to pollution from numerous organic pollutants that are used on daily basis such as dyes and pharmaceutical products that have been detected in the aquatic environment. This research investigated the degradation of organic pollutants using visible light activated semiconductors tungsten trioxide (WO_3) and bismuth oxyiodide (BiOI). WO_3 was used to form composites with tetraphenyl porphyrin and exfoliated graphite or reduced graphene oxide for degradation of acid blue 25 (AB25) under visible light irradiation. Moreover, it was also used in fabricating a heterostructure with cobalt (II/III) oxide (Co_3O_4) for mineralization of diclofenac sodium salt (DFC). A Z-scheme heterojunction was synthesized by Co_3O_4 combining with BiOI for degradation of a mixture of ibuprofen (IBU) and trimethoprim (TMP). The synthesized materials were characterized with physico-chemical techniques such as BET, EDS, FTIR, PL, Raman, SEM, TEM, TGA, UV-Vis and XRD. All the nanocomposites absorbed in the visible range due to small bandgaps below 2.8 eV. The bandgap of BiOI or WO_3 was shifted more towards the visible range by formation of heterojunctions of Co_3O_4 and WO_3 or BiOI and the formation of nanocomposites using TPP, WO_3 and EG or RGO. The incorporation of TPP and EG changed the heterogeneous morphology of WO_3 nanoparticles and was determined to depend on the amount of TPP used. High photocatalytic activities were obtained when there was less agglomeration of the nanoparticles for all synthesized composites. The materials exhibited reduced electron-hole recombination compared to the pristine semiconductors. Presence of oxygen vacancies as confirmed by elemental analysis and lattice defects confirmed by XRD resulted in enhanced photocatalytic activity. The photodegradation activities were followed by UV-Vis, TOC and HPLC-QTOF-MS and the highest efficiency reached was 99.9 % in 180 minutes using TPP/WO_3/EG nanocomposite and 99.98 % in 60 minutes using Co_3O_4/BiOI nanocomposite for degradation of AB25 and IBU respectively. The degradation of a mixture of IBU and TMP occurred after 100 minutes of irradiation with efficiency of 97.02 % and TOC removal percentage of 87 % using Co_3O_4/BiOI nanocomposite. The highest TOC removal achieved was 99 % and 89.95 % for degradation of AB25 and IBU respectively. Mineralization of DFC was achieved in 180 minutes with efficiency of 98.7 % at pH 10.7 when using the Co_3O_4/WO_3 nanocomposite and the HPLC-QTOF-MS results confirmed that it was mineralized into water, carbon dioxide and nitrate or aliphatic compounds. Reactive species were probed to hypothesize the mechanistic charge transfer processes and predict the reactive species involved in the degradation of the selected pollutants. TPP, WO_3 and EG or RGO and the Co_3O_4/BiOI

nanocomposites generated the superoxide and hydroxyl radicals to initiate photodegradation processes while Co_3O_4/WO_3 composite generated mainly the nonselective hydroxyl radicals. The catalysts were re-used, and their stability was evaluated using XRD. Moreover, FTIR and TGA were used for evaluation of coke layer formation in degradation of DFC and proved that coking occurred on the catalyst surface with little effects on reduction of photocatalytic activity. Interestingly, the fabricated composites demonstrated stability and went through different reusability cycles without any effect on the crystallinity and this was attributed to the strong interactions between the individual materials in the composite matrix. The nanocomposites gave high photodegradation activities for mineralization of organic pollutants in water under visible light and can be considered for large scale applications.

TABLE OF CONTENTS

Section ***Page***

Declaration....i
Summary....ii
Dedication....iii
Acknowledgements....iv
List of presentations and publications....vi
Abstract....vii
Table of contents....ix
List of figures....xiii
List of tables....xvi
List of abbreviations....xvii

CHAPTER 1 INTRODUCTION....1
1.1 Problem statement....1
1.2 Justification....3
1.3 Aim of the study....5
1.4 Objectives of the study....5
1.5 Thesis outline....6
CHAPTER 2 LITERATURE REVIEW....8
2.1 Organic pollutants....8
2.1.1 Dyes....9
2.1.1.1 Acid blue 25....10
2.1.2 Pharmaceuticals....11
2.1.2.1 Diclofenac Sodium....13
2.1.2.2 Ibuprofen....14
2.2 Current treatment menthods and their drawbacks....15
2.3 Advanced oxidation processes....17
2.3.1 Homogeneous photocatalysis....17
2.3.2 Heterogeneous photocatalysis....17
2.4 Semiconductor photocatalysis....18
2.5 Selected materials....23
2.5.1 Exfoliated graphite....23
2.5.2 Reduced graphene oxide....26
2.5.3 Tetraphenylporphyrin....27
2.5.4 Tungsten (VI) oxide....31
2.5.5 Cobalt (II, III) oxide....35

2.5.6 Bismuth oxyiodide 38
2.6 Summary 43
CHAPTER 3 METHODOLOGY 45
3.1 Introduction 45
3.2 General procedures 45
3.2.1 Materials and chemicals 45
3.2.2 Synthesis of exfoliated graphite 45
3.2.3 Synthesis of tungsten (VI) oxide 46
3.2.4 Synthesis of reduced graphene oxide 46
3.2.5 Synthesis of cobalt (II,III) oxide 47
3.2.6 Synthesis of bismuth oxyiodide 47
3.2.7 Synthesis of TPP/WO_3/EG 47
3.2.8 Synthesis of TPP/WO_3/RGO 48
3.2.9 Synthesis of Co_3O_4/BiOI 50
3.2.10 Synthesis of Co_3O_4/WO_3 50
3.3 Photocatalytic experiments 51
3.4 Instrumentation 51
3.4.1 Scanning Electron Microscopy (SEM) 52
3.4.2 Transmission electron microscopy (TEM) 53
3.4.3 Energy Dispersive X-Ray Spectroscopy (EDS/EDX) 53
3.4.4 X-ray diffraction spectroscopy (XRD) 54
3.4.5 Fourier Transform Infra-Red spectroscopy (FTIR) 54
3.4.6 Raman spectroscopy 55
3.4.7 Brunauer-Emmett-Teller (BET) analysis 56
3.4.8 Thermogravimetric analysis (TGA) 57
3.4.9 Photoluminiscence (PL) spectroscopy 57
3.4.10 Ultraviolet visible light spectroscopy (UV-Vis) 58
3.5 TOC 60
3.6 HPLC-QTOF-MS 60
3.7 Degradation kinetics 61
3.7.1 Half life 62
CHAPTER 4 IN-SITU TPP/WO_3/RGO NANOCOMPOSITE FOR PHOTODEGRADATION OF AB25 64
4.1 Introduction 64
4.2 Results and Discussion 65
4.2.1 SEM and EDS 65
4.2.2 Raman 68

4.2.3 FTIR 69
4.2.4 TGA 70
4.2.5 XRD 71
4.2.6 BET 73
4.2.7 Photoluminiscence 74
4.2.8 UV-Vis 75
4.3 Degradation of acid blue (AB25) 77
4.3.1 Effect of calcination temperature 79
4.3.2 Effect of catalyst concentration 79
4.3.3 Effect of dye concentration 79
4.3.4 Effect of composition of TPP in the composite 79
4.3.5 Effect of pH of pollutant solution 80
4.4 Reaction kinetics and catalyst stability 80
4.5 Photocatalytic reaction mechanism and charge transfer 82
CHAPTER 5 DEGRADATION OF AB25 WITH A NANOCOMPOSITE OF TPP/WO_3/EG UNDER SIMULATED SUNLIGHT LIGHT IRRADIATION 85
5.1 Introduction 85
5.2 Results and Discussion 86
5.2.1 SEM/EDS 86
5.2.2 TGA and BET 89
5.2.3 Raman analysis 90
5.2.4 FTIR 92
5.2.5 XRD 93
5.3 Optical properties 95
5.3.1 Photoluminescence (PL) 95
5.3.2 UV-Vis 96
5.4 Degradation of AB25 dye 98
5.4.1 Optimisation of catalyst concentration 99
5.4.2 Optimisation of dye concentration 100
5.4.3 Polutant pH optimisation 100
5.4.4 Optimisation of TPP composition 101
5.4.5 Reaction kinetics 101
5.4.6 Catalyst photostability and reusability 103
5.4.7 Reactive species 104
5.5 Proposed mechanism 105
CHAPTER 6 CO_3O_4/WO_3 P-N HETEROJUNCTION PHOTOCATALYST FOR DEGRADATION OF DICLOFENAC SODIUM 108

6.1 Introduction 108
6.2 Results and Discussion 109
6.2.1 FTIR 109
6.2.2 XRD 110
6.2.3 BET 112
6.2.4 SEM/EDS 113
6.2.5 TEM/HR-TEM/SAED 115
6.2.6 TGA 117
6.2.7 UV-Vis 117
6.2.8 PL 119
6.3 Degradation of diclofenac sodium 120
6.4 Photocatalyst recycling and stability 127
6.5 Probing reactive oxygen species 129
6.6 Charge separation and proposed photocatalyst activity 130
CHAPTER 7 DIRECT Z-SCHEME Co_3O_4/BiOI FOR IBUPROFEN AND TRIMETHOPRIM DEGRADATION 134
7.1 Introduction 134
7.2 Results and Discussion 135
7.2.1 SEM/EDX 135
7.2.2 TEM/HR-TEM/SAED 138
7.2.3 XRD and FTIR 140
7.2.4 BET 142
7.2.5 TGA 143
7.2.6 Optical properties analysis 144
7.3 Degradation of ibuprofen 146
7.4 Catalyst stability, recycling and scavenging 151
7.5 Charge transfer and proposed mechanism 153
CHAPTER 8 CONCLUSIONS AND RECOMMENDATIONS 157
8.1 Conclusions 157
8.2 Recommendations 158
REREFENCES 159

LIST OF FIGURES

Figure	***Description***	***Page***
Fig. 2.1:	Structure of acid blue 25.	10
Fig. 2.2:	Sources of pharmaceuticals water pollution and human exposure	12
Fig. 2.3:	Structure of DFC.	13
Fig. 2.4:	Structure of ibuprofen.	15
Fig. 2.5:	Mechanism of semiconductor photocatalysis.	18
Fig. 2.6:	Classification of band positions of some visible light driven semiconductors.	22
Fig. 2.7:	Structure of Tetraphenylporphyrin	29
Fig. 2.8:	Crystal structure of (a) monoclinic, (b) cubic and (c) hexagonal WO_3	32
Fig. 2.9:	Crystal structure of (a) cobaltosic and (b) cobaltous oxides	36
Fig. 2.10:	Temperature transformation of BiOI	39
Fig. 2.11:	Crystal structure of BiOI reported by Han et al	41
Fig. 3.1:	The schematic presentation of the composites synthesis by wet impregnation (Chapter 5).	48
Fig. 3.2:	Synthesis of RGO from EG and summary of In-situ fabrication of composites (Chapter 4)	49
Fig. 3.3:	General synthesis of nanomaterials in Z-scheme heterostructure (Chapter 7)	50
Fig. 4.1:	SEM images of (a) TWR3 (350), (b) TWR3 (400), (c) TWR3 (550), (d) RGO, (e) TWR1 (350), (f) TWR2 (350), (g) TWR4 (350) and EDS spectra of (h) WO_3, (i) RGO and (j) TWR3 (350)	67
Fig. 4.2:	Raman spectra of (a) WO_3, TWR1, TWR2 and TWR4 calcined at 350 °C and (b) RGO, TWR3 calcined at different temperatures.	69
Fig. 4.3:	FTIR spectra of (a) TPP, RGO, WO_3, TWR3 (400) and TWR3 (550) and (b) TWR1, TWR2, TWR3 and TWR4 calcined at 350 °C.	70
Fig. 4.4:	TGA graphs of RGO, TPP, WO_3 and TWR3 calcined at 350	71
Fig. 4.5:	XRD spectra of (a) pristine materials and (b) different composites.	71
Fig. 4.6:	N_2 Adsorption desorption isotherms of RGO and catalyst	74
Fig. 4.7:	PL spectra of WO_3 and different composites	74
Fig. 4.8:	UV/Vis spectra of solids (a) TPP and WO_3 and (b) Composites	75
Fig. 4.9:	Tauc plot of (a) WO_3 calcined at 700 °C and (b) TWR composite calcined at 350 °C	76
Fig. 4.10:	Degradation of AB25 (a) with 25 mg of TWR3 (350) degrading 20 ppm dye, (b) Effect of catalyst amount, (c) effect of dye concentration, (d) Effect of composition at pH 7, (e) effect of pH and (f) TOC results at pH 4	78

Fig. 4.11: Rate constants for (a) Photolysis, (b) WO_3, (c) TWR4 (350), (d)TWR5 (350), (e) TWR1 (350), (f) TWR3 (550), (g) TWR3 (400), (h) TWR2 (350) and (i) TWR3 (350) 81

Fig. 4.12: Efficiency of catalyst during recycling and (b) XRD spectra of catalyst before and after recycling 81

Fig. 4.13: Schematic diagram of charge transfer and AB25 degradation over TPP/WO_3/RGO nanocomposite 82

Fig. 5.1: SEM image of (a) WO_3, (b) EG, (c) TWE0, (d) TWE1, (e) TWE5 and (f) TWE10 composites 87

Fig. 5.2: FE-SEM images of (a) WO_3, (b) EG, (c) TWE 5 and TWE 10. 88

Fig. 5.3: EDS Spectra of (a) EG, (b) WO_3 and (c) TWE5 89

Fig. 5.4: (a) TGA of WO_3, EG, TPP and TWE5 and (b) N_2 adsorption desorption of EG, WO_3 and TWE5 90

Fig. 5.5: Raman results for WO_3, EG, TWE0, TWE1, TWE5 and TWE10 91

Fig. 5.6: FTIR spectra of (a) pristine materials and (b) composites 92

Fig. 5.7: XRD spectra of (a) pristine materials and (b) different composites. 94

Fig. 5.8: PL spectra of WO_3, TWE0, TWE1, TWE5 and TWE10 composites 95

Fig. 5.9: UV-Vis absorption for solids (a) WO_3 and TPP, and (b) TWE0, TWE1, TWE5 and TWE 10 96

Fig. 5.10: Tauc plot of WO_3, TWE0, TWE1, TWE5 and TWE10 97

Fig. 5.11: Degradation of 20 ppm dye solution 50 ml with 25 mg TWE5 at pH 5 ..98

Fig. 5.12: Variation of (a) catalyst concentration, (b) dye concentration, (c) pH of solution and (d) TPP amount on the degradation of AB-25 at pH 7 99

Fig. 5.13: Rate constants for (a) Photolysis, (b) WO_3, (c) TWE0, (d) TWE10, (e) TWE1 and (f) TWE5 102

Fig. 5.14: Stability of TWE5 at pH 5 for 20 ppm dye 103

Fig. 5.15: Comparison of effect of different scavengers on degradation of AB-25 104

Fig. 5.16: Proposed charge transfer and degradation mechanism 105

Fig. 6.1: FTIR results of as synthesised materials 109

Fig. 6.2: XRD pattern of (a) Co_3O_4 and (b) WO_3 and the composites 110

Fig. 6.3: N_2 Adsorption-desorption of Co_3O_4, WO_3 and CW2 113

Fig. 6.4: SEM images of (a,b) WO_3, (c,d) Co_3O_4 and (e,f) CW2 114

Fig. 6.5: EDX images of (a) WO_3, (b) Co_3O_4 and (c) CW2 115

Fig. 6.6: TEM, HR-TEM and SAED images of (a, b, c) Co_3O_4, (d, e, f) WO_3 and (g, h, i) CW2 116

Fig. 6.7: TGA micrographs of Co_3O_4, WO_3 and CW2 117

Fig. 6.8: (a) UV-Vis absorption spectra (b) Kubelka-Munk function and (c) Tauc-plots of WO_3, Co_3O_4 and CW2 118

Fig. 6.9: Photoluminescence spectra of WO_3, CW1, CW2, CW3 and CW2A 119

Fig. 6.10: Degradation of DFC (a) UV-Vis curve, Optimisation of (b) catalyst amount, (c) DFC concentration, (d) Catalysts composition and (e) pH of DFC, and (f) reaction kinetics at pH 6.8 121

Fig. 6.11: Concentration of released Chloride ions as a function of degradation time 124

Fig. 6.12: Mass spectra of UHPLC-TOF-MS during degradation of DFC at (a) 0 minutes, (b) 60 minutes, (c) 120 minutes and (d) 180 minutes..... 125

Fig. 6.13: Hypothesised pathway for mineralisation of DFC by CW2 at pH 10.7. 126

Fig. 6.14: Photocatalyst (a) re-usability, (b) stability and (c, d) coking formation evaluation..... 128

Fig. 6.15: Used scavengers to determine ROSs in CW2 degradation of DFC 130

Fig. 6.16: (a) Interaction and (b) charge transfer mechanism in CW2 composite 131

Fig. 6.17: Proposed degradation mechanism in Co_3O_4/WO_3 p-n heterojunction . 132

Fig. 7.1: SEM images of (a) Co_3O_4, (b) BiOI, (c) CoBi2 and (d) CoBi3..... 135

Fig. 7.2: EDX spectra of (a) Co3O4, (b) BiOI, (c) CoBi2 and EDS mapping of CoBi2 138

Fig. 7.3: TEM, HR-TEM and SAED images of (a, b, c) Co_3O_4, (d, e, f) BiOI and (g, h, i) CoBi2 140

Fig. 7.4: (a) XRD and (b) FTIR spectra of as synthesised nanocomposites..... 142

Fig. 7.5: N_2 adsorption desorption isotherms and (b) Pore diameter distribution of Co_3O_4, BiOI and CoBi2 143

Fig. 7.6: (a) TGA of Co_3O_4, BiOI and CoBi2 and (b) corresponding phase transformation in BiOI 144

Fig. 7.7: UV-Vis spectra of different composites and (b) Tauc plots of CO_3O_4, BiOI and CoBi2 145

Fig. 7.8: Photoluminescence spectra of BiOI, COBi2 and CoBi3 146

Fig. 7.9: UV-Vis spectra for degradation of (a) IBU and (b) IBU and TMP 146

Fig. 7.10: Optimisation of (a) Catalyst amount, (b) IBU concentration, (c) pH of solution and (d) Catalyst composition (e) effect of TMP and (f) TOC results 148

Fig. 7.11: Changes to Lewis base of IBU and corresponding pKa 149

Fig. 7.12: (a) Adsorption isotherms and (b) Pseudo second order rate constants for IBU and IBU + 2 mg TMP 150

Fig. 7.13: Rate constants and linear regression constants for (a) Photolysis, (b) BiOI, (c) Co_3O_4, (d) CoBi1, (e) CoBi3 and (f) CoBi2 151

Fig. 7.14: (a) Catalyst reusability and (b) Stability at pH 11.3..... 152

Fig. 7.15: Scavenger results for (a) IBU and (b) IBU and TMP degradation..... 153

Fig. 7.16: Charge transfer and proposed degradation mechanism..... 155

LIST OF TABLES

Table	***Description***	***Page***
Table 3.1:	Summary of rate laws and half-life	63
Table 4.1:	Bandgap energy mean crystallite diameter, surface area, pore size, pore volume, and number of reduced graphene layers of TPP, WO_3 and TPP/WO_3/RGO composites with different calcination temperature and amount of TPP.	73
Table 5.1:	XRD Data obtained from the different samples	94

LIST OF ABBREVIATIONS

AB25	Acid blue 25
AOPs	Advanced oxidation Processes
API	Active Pharmaceutical Ingredient
BET	Brunauer-Emmett-Teller
BiOX	Bismuth oxyhalides
CB	Conduction Band
BQ	Benzoquinone
CoBi1	Cobalt (II, III) oxide and Bismuth oxyiodide composite (weight ratio of 1:1)
CoBi2	Cobalt (II, III) oxide and Bismuth oxyiodide composite (weight ratio of 1:2)
CoBi3	Cobalt (II, III) oxide and Bismuth oxyiodide composite (weight ratio of 1:3)
CW1	Co_3O_4/WO_3 composite (prepared in 0.01M cobalt acetate)
CW2	Co_3O_4/WO_3 composite (prepared in 0.02M cobalt acetate)
CW2A	Co_3O_4/WO_3 composite (prepared in 0.02M cobalt acetate and calcined)
CW3	Co_3O_4/WO_3 composite (prepared in 0.03M cobalt acetate)
DFC	Diclofenac sodium
DWF	Dry Weather Flow
E_{CB}	Energy of conduction band
ECs	Emerging contaminants
EDCs	Endocrine disrupting contaminants
EDS/EDX	Energy Dispersive X-ray Spectroscopy
EDTA	Ethylenediaminetetraacetic acid
E_f	Fermi-Level Energy
EG	Exfoliated graphite
E_g	Bandgap energy
EGO	Exfoliated graphite oxide
EHPs	Electron Hole Pairs
E_{VB}	Energy of Valence Band
FE-SEM	Field Emission Scanning Electron Microscopy
FT-IR	Fourier Transform Infra-Red Spectroscopy
FWHM	Full Width at Half-Maximum
GICs	Graphite intercalated compounds
HPLC-TOF-MS	High Performance Liquid Chromatography Time of Flight Mass spectroscopy
HRTEM	High Resolution Transmission Electron Microscopy

IBU	Ibuprofen
IUPAC	International Union of Pure and Applied Chemistry
K_{OW}	Octanol-Water partition coefficient
NHE	Normal Hydrogen Electrode
NGF	Natural graphite flakes
NPs	Nanoparticles
NSAIDs	Non-steroidal anti-inflammatory drugs
PAHs	Polycyclic Aromatic Hydrocarbons
PhACs	Pharmaceutical active agents
PL	Photoluminescence
POPs	Persistent Organic Pollutants
RGO	Reduced graphene oxide
SEM	Scanning Electron Microscopy
TEM	Transmission Electron Microscopy
TGA	Thermogravimetric Analysis
TiO_2	Titanium (IV) oxide
TMP	Trimethoprim
TOC	Total Organic Carbon
TPP	Tetraphenylporphyrin
TW	A composite made from tetraphenyl porphyrin and WO_3
TWE	A composite made from tetraphenyl porphyrin, WO_3 and exfoliated graphite
TWR	A composite of tetraphenyl porphyrin, WO_3 and reduced graphene oxide
UV	Ultra-Violet
UV-Vis	Ultraviolet-Visible
VB	Valence Band
WASH	Water, sanitation and hygiene
WHO	World Health Organization
WO_3	Tungsten (VI) oxide
WWTPs	Wastewater treatment plants
XRD	X-Ray Diffractometer
ZnO	Zinc (II) oxide

CHAPTER 1
INTRODUCTION

1.1. Problem statement

Water scarcity is one of the key challenges facing the world in the 21st century with numerous studies underpinning this mayhem to global warming, population increase and industrial development. Currently, over 1.2 billion and 1.6 billion people live in physical water scarcity and water shortage respectively.[1] The situation is projected to worsen by 2025, due to approximately 13 % increase in water consumption, with 800 million people expected to be living under absolute water scarcity, 2 billion people living without access to safe water and over 2.8 billion people in 48 countries living under water stress or scarcity conditions.[2,3] By 2050, 7 billion people in 60 countries could be facing water scarcity.[4] Therefore, water availability is attracting global political agenda with recommendations for the right to water legal implementation and enforcement through the rule of international law.[2] Globally, the water footprint like the carbon footprint will become a serious factor for consideration in future energy systems, resource and technology approach for better, reliable and sustainable development.[2] Some countries are already applying extraordinary and drastic measures to solve acute water shortages.

Water is an essential resource for life, ecosystems, economic development and food production. However, potable water is scarce, costly to distribute or abstract and can be obtained from wastewater after costly treatment processes. Only 2.5 % of the planet's estimated 1.4 billion cubic kilometers of water is available for drinking, agriculture and economic development (industry) of which 69 % is not readily accessible under current or foreseeable technology as it is locked up in polar ice caps, mountain glaciers and deep underground aquifers.[5] The patterns of water use are regionally based on population size, climate and economic development. The total amount of fresh water sources are 45, 28, 16 and 9 % in America, Asia, Europe and Africa respectively.[5] Current water usage projections in South Africa depicted a 17 % water deficit by 2030. A recent wake-up call was the 2018 drought experienced in Western Cape Province that resulted in declaration of day zero in the city of Capetown. Therefore, there is an urgent need to address these challenges with immediate effect considering the UN sustainable development goals that include access of clean water for all by 2030 (goal number 6).[6]

Pollutant loads should be reduced to preserve the little fresh water sources that are available to enable water re-use. Organic pollutants are some of the most common and

problematic sources of water pollution. Textile industries discharges huge quantities of raw coloured effluents to aquatic systems (rivers and streams) which provide breeding media for viruses and bacteria, affecting marine life and negatively influencing the ecosystem of the receiving water bodies.[7] Besides dyes, pharmaceuticals also enter the environment through diverse processes such as incorrect disposal of waste or expired medication, excretion after consumption for an intended purpose, etc. Pharmaceuticals are endocrine disrupters with various adverse health effects such as behavioural impairment reported in marine life.[8] The accumulation of organic dyes and pharmaceuticals in the environment is a concern due to the high daily discharges even to human health.

Access to clean water is considered a human right and different technologies used towards achieving this goal are utilising large-scale water re-use processes that are generally summarized as conventional water decontamination methods. Moreover, just recently, membrane filtration technologies have been applied in some parts of the world towards treatment of contaminated water reuse for human consumption. This has resulted in improvements in quality and supply of clean water. Operational cost for membrane filtration processes has limited their application to a few developed countries and major challenges still exist for development in third world countries where the issue of water scarcity is a major concern. Therefore, there is an urgent need for research and development in cost-effective methods of water treatment for sustainable provision of clean water to disadvantaged communities worldwide.

Nanotechnology through advanced oxidation processes that include semiconductor photocatalysis provides a promising alternative method of addressing the current issues related to water pollution. Photocatalysis using the abundantly available visible range of the solar spectrum is believed to offer sustainable and cheap solutions for accessibility to clean water in developing countries. Numerous studies have been conducted in different parts of the world with numerous novel discoveries and there is a consensus that advanced oxidation processes are a promising solution towards a clean and healthy environment.[9,10] Despite all these innovative attempts reported in literature, efficient and commercially viable photocatalysts for effective degradation of various pollutants at low cost are yet to be realized. This has prompted further research to be directed towards the development of cheap synthesis methods for use of visible light active materials in heterogeneous photocatalysis.

1.2 Justification

Water pollution has been a global issue attracting attention from governments and scientists because of the continued scarcity and depletion of water resources. Diarrhoeal diseases that encompass those of epidemic or cyclic nature (cholera) and those of endemic persistent nature (gastroenteritis) are being reported in various parts of the world.[11,12] The incompetency of current treatment technologies to eliminate emerging pollutants is a concern. This has resulted in more campaigns for access to clean water by different stakeholders. Therefore, the demand for freshwater due to accelerated pace of industrialization by extensive urbanization, agricultural practices, industrialization, and population expansion is increasing daily.

In the past few years, advanced oxidation processes have been proved as promising alternative methods towards complete mineralisation of traditionally difficult to degrade organic pollutants. Irrespective of the reagent system used (heterogeneous or homogeneous), the mechanism of advanced oxidation processes towards removal of organic pollutants involves radical chain reactions which are initiated by in-situ formation of strong oxidising hydroxyl radicals.[13] Moreover, the hydroxyl radicals are non-selective towards complete mineralisation of resilient pollutants into less toxic by-products. The advantages of these methods are high oxidation power of the generated radicals, low operation costs and robustness.

Photocatalysis is a form of advanced oxidation processes that involves the use of semiconductor oxides to degrade pollutants. Traditional metal oxide semiconductors such as TiO_2 and ZnO have been shown to absorb in the UV region of the spectrum to initiate the photocatalytic reactions. Limitations such as activation by high energy and rapid recombination of photogenerated charge carriers have been the major stumbling block for their large scale applications. Research attention is now focused on improving the visible light photocatalytic applicability of TiO_2 in environmental pollution management. Towards this effect, different strategies have been reported in literature such as metal or/and non-metal doping, use of carbon materials and formation of heterojunctions with other semiconductors to reduce its bandgap.[14] Despite the numerous efforts of enhancing TiO_2 photocatalysis, there is still limited industrial application for water pollution due to the large bandgap and need for using UV light for activation.

The successful use of photocatalytic techniques therefore necessitates the design, engineering and fabrication of appropriate semiconductors. The selection of semiconductors, methodology design and optimisation of different operational parameters

is important for efficient and effective photocatalytic performance. Recent trends are being tailored towards visible light absorbing semiconductors and improvement thereof to minimize costs and improve efficiency through integration into already existing wastewater treatment processes or designing entirely different heterogeneous systems for efficient and effective wastewater treatment for domestic use. Heterogeneous photocatalysis using visible light driven semiconductors has recently attracted attention as one of the most promising advanced oxidation processes because of the possibility to use inexhaustible solar energy.

Visible light active photocatalysts such as Co_3O_4, BiOI and WO_3 are promising alternatives to the widely studied TiO_2. Cobalt oxides and tungsten oxide are earth-abundant photocatalytically active materials with relatively narrow bandgap energies (about 1.2–2.1 eV) and (2.5-2.7 eV), respectively.[15] The increasing interest garnered by bismuth oxyhalides (BiOX, X = F, Cl, Br, I) can be attributed to their high photocatalytic activity, high stability and appropriate energy gaps with more work done on bismuth oxyiodide (BiOI) as it is easy to synthesise.[16,17] BiOI is anticipated to form a direct z scheme heterojunction with Co_3O_4 according to their respective band edge positions and induced internal electric field. Tungsten oxide has strong oxidative catalytic properties but like TiO_2, the use of pristine WO_3, BiOI and Co_3O_4 results in rapid electron-hole recombination. The use of cobalt oxides can result in leaching of potentially toxic cobalt ions into the solution. Different strategies have been used to control this including optimisation of the operation pH and green synthesis of Co_3O_4. WO_3 on the other hand has limitations such as inappropriate conduction band for water splitting (i.e. unsuitable for reduction of ambient oxygen to superoxide anion radical).

To enhance visible light photocatalytic activity of semiconductors, porphyrins are used as photosensitizers and tetraphenyl porphyrin (TPP) is the simplest and cheapest porphyrin.[18] TPP can shift the absorption edge, reduce electron hole recombination and align the mismatched band edge potential of WO_3 for water splitting. The incorporation of exfoliated graphite and reduced graphene oxide to photocatalysts will minimize electron-hole recombination due to their ability to act as electron trapping and transporting materials even at room temperature.[19] Moreover, the formation of a p-n heterojunction between Co_3O_4 and WO_3 can have positive effect on visible light harvesting, reduction of the recombination of photoexcited electron-hole pairs and reducing the possibility of cobalt leaching when small quantities of Co_3O_4 are used with the chemically inert WO_3.

The photocatalytic systems designed using Co_3O_4. BiOI, TPP, WO_3, EG and RGO are cheap materials as these are readily available materials that are easy to synthesise. The composites fabricated from these materials are stable and can be re-used or recycled and will be sustainable as they can be used under visible light irradiation. Moreover, scanty literature is available on the use of these materials. There is very little understanding of the charge transfer mechanisms and the sequence of the photocatalytic reactions involved which is important towards realising their large scale applications. Moreover, there are misconceptions on the degradation pathways of the pharmaceuticals which are suspected to result in more toxic by-products from the parent molecule. Therefore, efficient removal of pharmaceuticals and their metabolites is very important and would add to the literature acumen required towards removal of organic pollutants in water to improve access to portable clean water.

The search for inexpensive abundant and sustainable light harvesters provides a strong impetus to the development of more affordable, active, selective and stable photocatalysts to convert solar radiation into useful chemical energy for driving oxidative pollutant degradation reactions in aqueous medium. An understanding of charge transfer mechanisms and kinetics between different semiconductors is imperative towards the design and fabrication of efficient photocatalytic systems towards organic pollutants remediation in aqueous media.

1.3 Aim of the study

The aim of this study was to develop visible active semiconductor photocatalysts for degradation of various organic pollutants. The photocatalysts were supported on carbon materials (EG and RGO) to enhance their photocatalytic activity with specific focus on dyes and pharmaceuticals.

1.4 Objectives of the study

The specific objectives of this study based on the aim are the following:

1. To synthesise tungsten oxide, cobalt oxide and bismuth oxyiodide semiconductors that absorb in the visible range of the solar spectrum.
2. To incorporate tetraphenyl porphyrin on WO_3/EG and WO_3/RGO nanocomposites using wet-impregnation and in-situ method respectively.
3. To synthesise WO_3/Co_3O_4 and Co_3O_4/BiOI heterojunctions using in-situ and self-assembly method respectively.

4. To characterise the synthesised materials using various physico-chemical techniques such as UV-Vis, PL, XRD, BET, TGA, FTIR, SEM/EDS, TEM/HRTEM and Raman.
5. To evaluate the photocatalytic activity of the synthesised photocatalyst nanocomposites towards degradation of acid blue 25 dye (AB25), trimethoprim, ibuprofen and diclofenac sodium salt using a batch photocatalytic setup under visible light irradiation.
6. To study the degradation mechanisms, kinetics and pathways of the dyes and pharmaceuticals using UV-Vis, TOC and HPLC-QTOF-MS.

1.5 Thesis outline

This thesis is organised into 8 chapters

Chapter 2 is the literature review. This chapter provides a brief description of different pollutants; dyes and pharmaceutical and the need for their degradation, the literature review of conversional wastewater treatment methods and their disadvantages in treatment of organic pollution, and advanced oxidation processes are discussed in detail with detailed literature review on all selected semiconductors and support materials in this project.

Chapter 3 is the experimental methodology. In this chapter, the materials and equipment specifications are given together with the general methodology used for synthesis of photocatalysts and their application for degradation of dyes and pharmaceuticals. Moreover, the different characterisation techniques are briefly discussed.

Chapter 4 discusses the degradation of AB25 using in-situ synthesised TPP/WO_3/RGO composite under visible light radiation. Effects of calcination temperature were investigated on the different properties and applications of the catalysts.

Chapter 5 details the degradation of AB25 using wet-impregnation synthesised TPP/WO_3/EG composite under visible light radiation. Effect of TPP was studied on the performance of the nanomaterials that were evenly distributed on the surface of the EG.

Chapter 6 highlights visible light driven Cobalt (II/III) oxide and tungsten (VI) oxide p-n heterojunction photocatalyst for degradation of diclofenac sodium. Detailed degradation pathway was proposed on DFC degradation based on HPLC and the effect of Co_3O_4 amount was investigated. Moreover, synergy and facet engineering were explored to enhance performance of the materials.

Chapter 7 provides details on the degradation of Ibuprofen using direct Z-scheme Co_3O_4/BiOI nanocomposite and the effect of trimethoprim under visible light radiation.

Adsorption was studied to ensure its effect on the overall degradation efficiency of the nanocomposite with spherical platelets of Co_3O_4 engulfed by cauliflower BiOI.

Chapter 8 provides the general conclusions and recommendations.

CHAPTER 2
LITERATURE REVIEW

2.1 Organic pollutants

Pollutants from point sources and nonpoint sources can taint water quality. Irrespective of the source, water pollutants are classified into three categories: biological (bacteria, fungi, viruses, etc.), chemical (organic and inorganic compounds) and physical (colour, odour, sediment and heat).[20] The development, design and engineering of water pollution prevention or treatment systems vary depending on the source and the type of the targeted pollutant.

Majority of organic pollutants are due to human activity and mostly found in sewages, runoffs, and industrial discharges. The various types of organic pollutants can be placed into three general classes: (i) hydrocarbons, (ii) oxygen, nitrogen and phosphorus compounds or (iii) organometallic compounds.[21–23] The conventional water treatment technologies cannot effectively and efficiently remove these contaminants from water. The hydrocarbons group containing compounds like pesticides, dyes, the dioxins, the polycyclic aromatic hydrocarbons (PAHs) and pharmaceuticals is of major scientific interest due to their abundance in the environment and data scarcity with regards to their monitoring and treatment. Persistent organic pollutants (POPs) are chemicals of global concern due to their potential for global transboundary transport, environmental persistence, knack to bio-magnify and bio-accumulate in ecosystems, and their substantial adverse effects on human health and the environment.[24] They have low polarity ensuing their high solubility in fats (i.e. lipophilic). The lipophilicity of compounds is determined by the measure of their octanol-water partition coefficient (K_{OW}). The higher the K_{OW} value the higher the lipophilicity. Consequently, they are adsorbed by sediments and bio-accumulate in organisms (in fatty tissues) and have low concentrations in water and the atmosphere.[25]

The number of potential organic chemicals (those that may possibly be synthesized and those that are unidentified despite their existence) is incredibly massive resulting in emission of so-called “emerging” or “new” unregulated contaminants being an environmental global problem. There is a consensus that this kind of contamination may require legislative intervention.[26] Though dyes and pharmaceuticals have been identified in the drinking water supply chain, mainly in source waters,[27,28] they are currently not

included in routine drinking water monitoring programs. Currently, there are over 100 health-related chemicals or group of chemicals for which guideline values have been set by the World Health Organization (WHO).[29] This list does not include all emerging organic contaminants. This necessitates further research to model emerging organic contaminants treatment methods or like other individual groups, select pollutants of interest for efficient removal to increase the technical know-how and acumen in environmental pollution control and monitoring systems with focus on rapidly deteriorating water quality.

2.1.1 Dyes

Dyes are described as substances that provide colour by permanent or temporary variation of the crystal structure of a coloured constituent.[30] Dyes are mainly synthetic in nature and the first dye “Mauveine,” was synthesized by William Henry Perkin and since then new groundwork and publicised research on the use of these xenobiotics have emerged.[31] Like most environmentally persistent organic pollutants, most dyes are highly coloured (visible even at low concentration), they possess high stability under sunlight and are resistant to microbial attack, and are stable to light, water, detergents, chemicals, soap and other chemicals such as bleach.[30]

The number of reports on different industries such as clothing textiles, pharmaceuticals, quality assurance laboratories, production industries, furniture manufacturing and numerous others polluting the environment is of global concern. Effluents from these industries are toxic, recalcitrant and not easily degradable causing serious ecological problems as small amounts of the pollutants can result in significant colouring of the receiving waters.[32] Dyes deserve attention due to high industrial quantities involved (more than 800,000 tons is produced annually worldwide).[33]

Unfortunately, 1–20% of the total world production of dyes ends up in the environment as effluent discharge because they get lost during the dyeing process. Most industries do not adhere to the pre-treatment process and thus only 12% of dyes are correctly discharged.[34] Generally, dyes are highly toxic, carcinogenic and mutagenic in nature, and can also result in bioaccumulation in the food chain.[33] They result in significant health concerns even at low concentrations (0.001 mg/L) and cause diseases such as dermatitis, mucous membrane, severe irritation of respiratory tract and perforation of nasal septum.[35] Therefore, the complete removal of dyes from wastewater is a necessity.

A dye molecule consists of two components (chromophore and auxochrome). The chromophores are the functional groups that gives the dye its colour while the auxochrome give additional support to the chromophores for colour, stability and other properties.[36] Dyes can be classified by their high structural diversity (chemical structure) or their usage that is triggered by their properties.[24] The different classes of dyes include azo, anthraquinone, benzodifuranone, quinophthalones, etc They can also be classified as acid, basic, direct, disperse, mordant, sulphur, reactive, solvent and vat dyes.

2.1.1.1 Acid blue 25

Acid Blue 25 ($C_{20}H_{13}N_2NaO_5S$) is a poorly water-soluble anionic acid dye that belongs to the anthraquinone group. (Figure 2.1).[37]

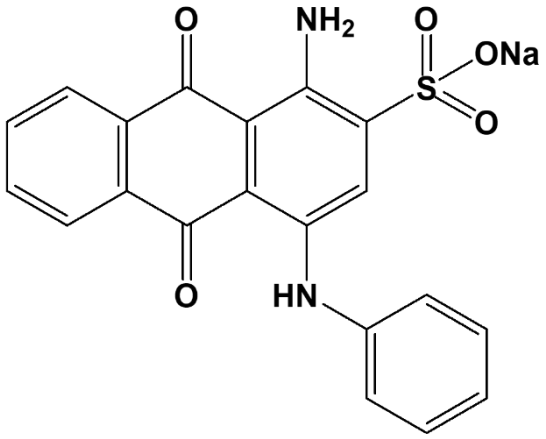

Figure 2.1: Structure of Acid Blue 25

The chromophore of acid blue 25 is the anthraquinone with the sulfonic anion attached as its auxochrome.[37,38] It absorbs visible light at a maximum absorption wavelength between 600 – 650 nm which together with the structure of its auxochrome and the presence of the chromophore gives it an intense blue colour even at low concentrations. Acid Blue 25 is used for dyeing wool, silk and mixed fabric and printing them in a direct method. The dye is also extensively utilized to color leather, polyamide, paper, cellulose, model compound for removal of anthraquinone dyes from aqueous media, PC blends during the manufacturing process and for adsorption research. Equation 2.1 shows the use of acid blue 25 to colour nylon.[38]

$$\textbf{Dye-SO}_3^- \textbf{ Na}^+ \textbf{ + Nylon-NH}_3^+\textbf{Cl}^- \rightarrow \textbf{Dye-SO}_3^- \,{}^+\textbf{H}_3\textbf{N-Nylon + NaCl} \qquad \textbf{(2.1)}$$

The dyeing process does not remove or alter the chromophore and the auxochrome of any dye molecule and the excess dye enters the environment causing pollution. It causes skin and eye irritation, and may also create respiratory problems hence the

decontamination, removal and complete mineralisation of this dye is a major concern to the environmental toxicologists.[39] The literature involving the use of different methods for removal of acid blue 25 is very scarce, but methods such as adsorption and advanced oxidation processes, electrocoagulation and non-thermal plasma advanced oxidation processes have been reported.[39,40]

2.1.2 Pharmaceuticals

Pharmaceutical formulations form part of the thousands of important prescriptions purchased over the counter and veterinary therapeutic drugs used daily for prevention or treatment of human and animal diseases. Non-steroidal anti-inflammatory drugs (NSAIDs) used to treat pain, inflammation and arthritic conditions[41] are amid extensively used human pharmaceuticals with more than 30 million prescriptions made daily. Diclofenac, ibuprofen and naproxen are collectively responsible for 45 % of global NSAIDs sales.[42] The quantity of pharmaceuticals manufacturing and consumption is gradually swelling inter alia with their discharge, detection or release of their metabolites.[43,44]

Human health can be exposed to pharmaceuticals through food and drinking water. Food exposure through seafood and animal produce is a universal concern due to global trading.[45] The main sources of pharmaceutical water pollution are intensive farming, aquaculture, or hospital, urban, industrial and domestic wastewater or effluents from sewage treatment plants.[46] Pharmaceutical active agents (PhACs) sources in drinking water (Figure 2.2) are mainly due to human activities.

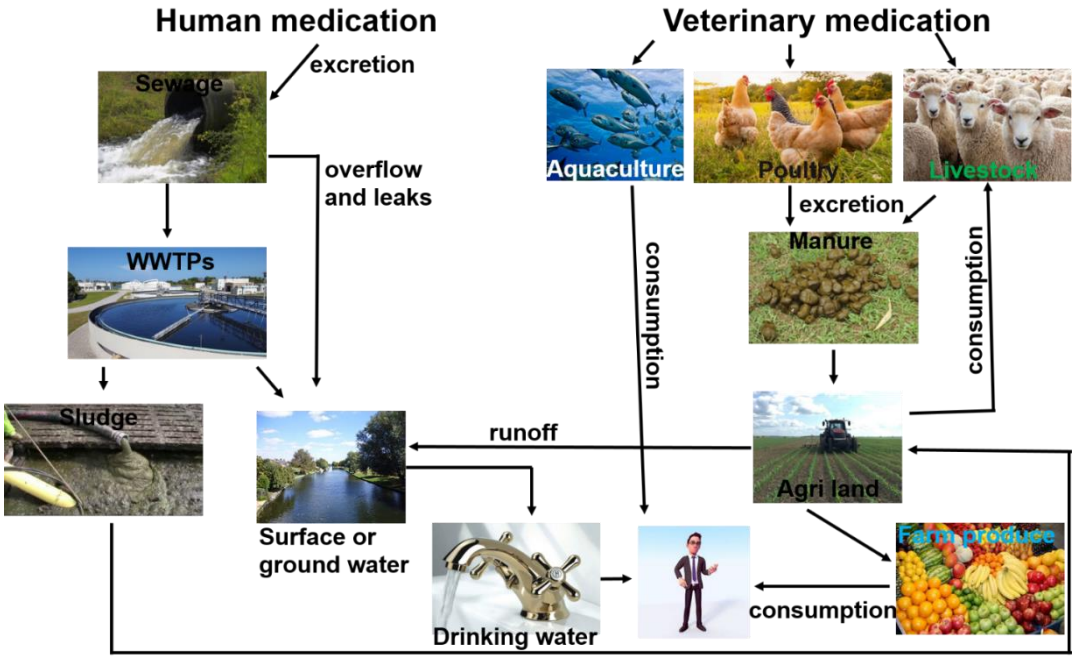

Figure 2.2: Sources of pharmaceuticals water pollution and human exposure

Human activities termed as 'involuntary' or 'purposeful' are the main causes of environmental pollution by pharmaceuticals.[47] Furthermore, pharmaceutical production sites have been identified as sources for PhACs contamination. Boxall et al. used inverse modelling to guesstimate removal efficiency of PhACs in small scale sewage treatment works using a hydrological model as well as prescription and monitoring data within a few representative sites for a small region.[48] The overall removal rates were used to model exposure across England and Wales for 12 studied compounds resulting in a sewage treatment process inflow concentration (C_i) estimation from the projected/actual per capita mass of chemical used/excreted (M, µg/cap/day) and the sewage treatment process's dry weather flow (DWF, L/day (Equation 2.2).

$$\mathbf{Ci} = \frac{\mathbf{M.P}}{\mathbf{DWF}} \qquad \textbf{(2.2)}$$

where P is the population served by the sewage treatment works across the studied area per sewage treatment process. The discharges of an active pharmaceutical ingredient (API) through a sewage treatment process are consequential of prescription data of the API and characteristics of the sewage treatment process. Since little can be done to reduce prescription of pharmaceuticals, the best approach is to design sewage treatment processes such that the concentration of APIs in drinking water is within acceptable limits. Two of the most frequently determined PhACs (diclofenac and Ibuprofen) in surface waters are discussed in detail below.

2.1.2.1 Diclofenac Sodium

Diclofenac is a weakly soluble acid (its solubility depends on the pH of the solvent used) that is mostly used as its sodium salt in medical care.[49] The NH and carboxylic groups are responsible for the Lewis acid-base characteristics of the drug.[50] Figure 2.3 shows the structure of diclofenac sodium.

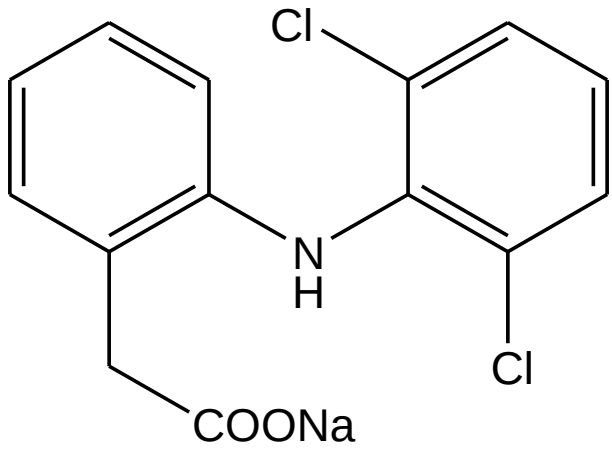

Figure 2.3: Structure of DFC

Diclofenac sodium salt, also known as phenylacetic acid 2-[(2,6-dichlorophenyl)amino] benzene acetic acid sodium salt (IUPAC name), has a chemical formula $C_{14}H_{1o}Cl_2NO_2Na$[51] and will be referred to as DFC sodium hereinafter. There are reports in literature of its photodegradation under natural sunlight which involves four main steps: (i) formation of an inter-ring carbon–carbon bond after loss of a chlorine atom, (ii) subsequent loss of the second chlorine atom on further irradiation, (iii) formation of photo-substituted hydroxyl carbazole after the second photochlorination, and (iv) decarboxylation after the second dechlorination.[49,50] The release of hydrochloric acid in the dechlorination process increases the acidity which may have negative effects if produced in prominent quantities and since all these mechanisms are activated by light in the UV region as reported by Musa et al.,[50] the use of UV radiation is rendered unsuitable for large scale treatment of DFC.[51]

Since the early 2000s, Diclofenac (DCF) became a persistent pollutant of concern identified as a future emerging priority candidate as it is toxic and tends to bioaccumulate.[12] Subsequent studies of its toxicity encompassed the near extinction of different vulture species in Asia (Gyps bengalensis, G. indicus and G. tenuirostris),[52] and the African vultures (G. coprotheres).[52] Studies conducted on over two days resulted in cardiac, liver, pulmonary and renal lesions.[53,54] Diclofenac also affects organ histology and gene expression in fish at concentrations as low as 1 $\mu g \cdot L^{-1}$.[47,55] High quantities of

diclofenac assimilation could lead to health effects such as liver and kidney damage, and stroke in humans.[56] There is intensified prospect of synergistic effects with other pharmaceuticals or chemicals in the aquatic environment accompanying DFC pollution despite its truncated concentrations in wastewaters. For example, a 10 to 200 fold additive effect due to Prozac, Ibuprofen and Ciprofloxacin in aquatic plants and fish was reported.[57]

The global annual consumption of diclofenac is estimated above 940 tons[58] excluding over the counter medication and 15% of it is excreted unchanged after human consumption.[58] Diclofenac is prevalently used among human and veterinary medical care, making it the most detected persistent pollutant in the environment.[59,60] It was detected in groundwater and surface water at concentrations of up to 50 µg/L.[51] Madikizela et al. conducted a study of Kingsburgh and Umbilo Wastewater treatment plants (WWTPs) in eThekwini, South Africa and detected DFC presence in both the influent and effluent.[61] The effluents contained 1.4–2.0 µg/L of DFC for both WWTPs with a maximum of 13 % removal efficiency. Moreover, there are other reports on NSAIDs in some other WWTPs in South Africa.[60,62] Therefore, permissible limits are set in some countries with the highest permissible limit of DFC in European rivers set at 100 ng/L in 2011.[63]

2.1.2.2 Ibuprofen

Ibuprofen (IBU) or 2-(4-isobutylphenyl) propionic acid, is a non-steroidal anti-inflammatory drug (NSAID) widely used in the treatment of pain and fever and it has been found in various waters.[64] It is available in several formulations with the generic names like Brufen, Advil, Nurofen and Alivium which are intended for core applications use as humans and veterinary medicinal products.[65]. Since it is one of the core medicines listed in Essential Drugs List of World Health Organization, it is produced in kilotons per annum globally and it is designed to be biologically active like many pharmaceuticals.

More than 70% of ibuprofen is metabolized and excreted in urine and its dominant metabolic forms are hydroxylated and carboxylated compounds.[66,67] In aquatic environment, hydroxyl-IBU and carboxy-IBU revealed comparable toxicological significance.[68,69] The pKa of ibuprofen is 4.593 and it dissociates as it becomes more basic and exceeds the pKa value.[66] Ibuprofen interferes with the enzyme cyclooxygenase needed for catalysis of arachidonic acid to synthesise prostaglandin that causes inflammation.[68,70] Figure 2.4 shows the chemical structure of ibuprofen.

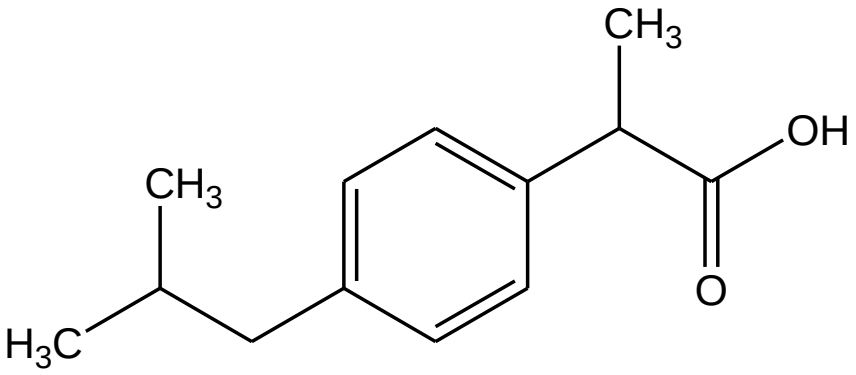

Figure 2.4: Structure of Ibuprofen

Ibuprofen is extensively used and its occurrence in surface waters such as rivers and wastewater treatment plant effluents has been reported using different technologies by several researchers.[61,71,72] The major contributors portrayed as sources of IBU are hospitals and WWTPs, with concentrations that could reach some hundreds of micrograms per liter.[61] Spain has reported one of the highest contamination levels followed by Brazil and then Portugal which had more than 2 million prescriptions of IBU per annum in 2009.[64,69,73] Moreover, trace amounts of IBU have been detected in other European countries such as Germany and in USA which resulted in its inclusion in a shortlist of 19 possible new priority substances considered to set their limits in aquatic environments.[73,74] Despite little research being done on the detection of ibuprofen in South Africa, it has been reported in influents and effluents of wastewater treatment plants that are trusted with delivery of clean water for human consumption.[61] Moreover, it has been reported to have synergistic effects with other pharmaceuticals making its removal a priority.

The high quantities of dyes and pharmaceuticals consumption ensure that they are widely available in the environment with a great potential for human exposure that includes additive effects, hence these compounds merit their investigations.

2.2 Current treatment methods and their drawbacks

In drinking water quality monitoring programs, the emphasis is on the detection and management of contaminants to help protect the environment and human health. Pollutants alter either appearance (in terms of taste, odour and colour) or quality of drinking water and therefore should regularly be monitored. The occurrence, exposure or health effects of water contaminants is essential to determine and prioritize their removal and produce water of quality that is reflective of the requirements and features of the drinking water industry.[29,75] The scientific consensus is that current treatment

methodologies do not adequately address the challenges of persistent organic pollutants presence that threaten supply of clean drinking water and pose health risks to the end user especially in developing countries.

Conventional water treatment methods employed in most wastewater treatment plants such as adsorption, filtration, chlorination, coagulation, sedimentation, membrane technology and biological treatment technologies often have drawbacks such as incomplete degradation of organic pollutants, transfer of this pollutants from one medium to another, sludge formation and high energy consumption.[21] Coagulation introduces coagulants that may result in formation of by products and generate sludge. Sludge is the residue generated during physical, chemical and biological treatment of wastewater and its disposal is a major challenge. Other processes that may result in formation of sludge include, membrane technology, filtration processes, sedimentation and biodegradation. The other developed methods of wastewater treatment like nanofiltration, UV radiation combined with oxidizing agents such as ozone are effective to remove these pollutants, but they are not always feasible for wastewater treatment plants due to their high operational cost requirements.[21] Chlorination as a tertiary treatment process results in formation of more toxic chlorinated organic compounds that are more carcinogenic than the corresponding parent organic molecules. Though anaerobic wastewater treatment seemed like a promising alternative, complete replacement of aerobic with anaerobic technology is not yet possible.

Wastewater treatment processes have mostly been developed in temperate, Northern climates limiting their applications to these regions. Application of some of these treatment systems in developing countries is met with challenges such as high energy requirements, lack of technical skills, high operation and maintenance requirements, production of large volumes of sludge (solid waste material) and unreliability in pathogen reduction.[76] Moreover, public acceptance of water reuse is a core factor in successful implementation of wastewater reuse projects. For sustainable provision of clean water to communities, the treatment technologies require low level of maintenance, must be controlled using local expertise for operation, maintenance and development, and should result in minimal pollution footprint. Simple solutions that are easily replicable, that allow further upscaling with subsequent development, and that can be operated and maintained by the local community expertise, are often considered the most appropriate and cost-effective. Advanced oxidation processes (AOPs) are promising alternatives in this regard.

2.3 Advanced oxidation processes

Advanced oxidation processes (AOPs) involve the in-situ generation of hydroxyl radicals ($OH^{\bullet}$) that oxidize degradable organic compounds and offer possibility of complete destruction/mineralization to carbon dioxide, water and inorganic salts.[7,77,78] The mechanism of $OH^{\bullet}$ production highly depends on the kind of AOP technique employed. Hence, ozonation or UV/H_2O_2 and photocatalytic oxidation rely on different mechanisms of OH radicals generation with different limitations.[79] Among the AOPs developed, three that are mostly studied are ozonation, UV/H_2O_2, and photocatalysis utilizing either ultraviolet (UV) or solar irradiation.

2.3.1 Homogeneous photocatalysis

In homogeneous photocatalysis, the reactants and the catalyst have similar states (mostly liquid) and the reactions are pioneered by light with a wavelength up to 600 nm.[80] The effectiveness of homogeneous photocatalysis depend on dosage of oxidizing chemical additives such as hydrogen peroxide (H_2O_2) or ferrous salts. Presence of carbonate ions in pH ranges of 8 – 9 acts as scavengers for UV/H_2O_2 processes while excess addition of H_2O_2 reduces the rate of oxidation by reducing generation of hydroxyl radicals.[80,81] The efficiency of UV-based methods is retarded by high turbidity and intensive colour of wastewaters and the expensive artificial UV lamps while photo-Fenton processes result in production of sludge, high concentration of chloride or sulphate anions depending on the ferrous salt used and high acid consumption for pH reduction. In general, homogeneous processes incur huge operation costs due to use of chemical oxidants or requirement for sludge disposal.[80,81]

2.3.2 Heterogeneous photocatalysis

Heterogeneous photocatalysis is the use of photons by semiconductors to enhance reactions without themselves being consumed during the cause of the reaction and the reactants (normally liquids and gases) and the photocatalyst (solid or liquid) are in different states. The chief advantage of heterogeneous photocatalytic processes over homogeneous processes is that the catalyst recovery and recycling is relatively cheaper as the reagents and the semiconductor are in different phases and their operation cost is also cheaper as ambient oxygen is the oxidant as opposed to expensive oxidizing chemicals such as hydrogen peroxide.[82] Moreover, semiconductors are mostly recycled and reused easily, can harness the use of profuse visible radiation that promises to provide sustainable energy solutions and they are also self-regenerated.[83]

2.4 Semiconductor photocatalysis

Semiconductor photocatalysis is one of the heterogeneous Advanced Oxidation Processes (AOPs) in which a photoreaction occurs on the surface of a catalyst.[84] Photocatalysis entails a wide variety of applications that include fuel regeneration (through water splitting and carbon dioxide reduction), degradation of organics and dyes and antibacterial action, etc. Semiconductors are materials with special configuration of electrons and electronic properties that are intermediate between those of insulators like silicon dioxide (electronic excitation of above 4 eV) and metals or semi-metals such as titanium (electronic excitation of 0 eV).[85] Semiconductor photocatalysis exponentially advanced since the discovery made by Fujishima and Honda on photocatalytic water splitting ability of titanium (IV) oxide (TiO_2) nanoparticles photocatalyst.[79] There are numerous publications on different aspects of synthesis, characterization and application of TiO_2 as a semiconductor and it is the most widely studied.

Photoinduced reactions occur when a semiconductor/catalyst such as TiO_2 is irradiated with photons that carry energy equal to or greater than its bandgap energy (E_g = 3.2 eV for TiO_2) (Figure 2.5).

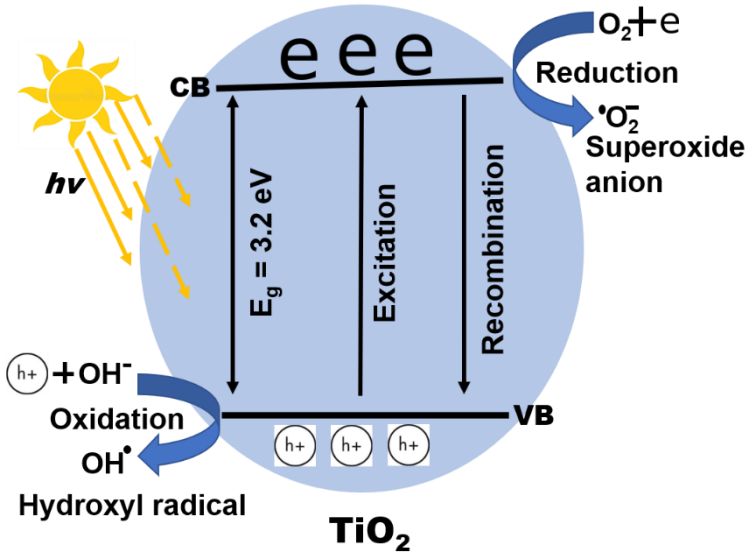

Figure 2.5: Mechanism of semiconductor photocatalysis

The absorption of photons results in excitation of electrons from the VB to the CB of the semiconductor, leaving behind holes in the VB. The holes themselves are highly oxidizing and they migrate to the surface where they scavenge water molecules to form highly reactive hydroxyl radicals.[79] The radicals can oxidize organic compounds to CO_2, H_2O and inorganic acids. The electrons on the other hand react with ambient oxygen to form superoxide radicals through a series of reducing reactions. The formed superoxide

radicals can either convert water into hydroxyl radicals or directly initiate degradation of organic pollutants to aliphatic compounds, H_2O and CO_2. Photoexcited electrons and holes can recombine and dissipate the input energy as heat or trapped in metastable surface states resulting in less redox capability of the semiconductor. The photoexcited electrons or holes can also be trapped by suitable reductants (electron donor) or oxidants (electron acceptors) inhibiting the rate of recombination of excited state electrons and holes for subsequent occurrence of efficient photocatalytic reactions on the semiconductor surface. The fabrication of semiconductors is therefore designed with the purpose of hindering electrons and holes recombination.

Generally, the mechanism of degradation of pollutants involves radical chain reactions with the highly oxidative and non-selective hydroxyl radicals the major role players and they can be summarized by Equation 2.3 – Equation 2.6 for TiO_2 Photocatalysis.[86,87] The summary of photocatalytic oxidation steps with TiO_2 involves formation of photoexcited electrons ((e^-) and hole (h^+) generation due to irradiation (Equation 2.3), water adsorption onto Ti (IV) surface (Equation 2.4), the formation of highly reactive hydroxyl radicals (Equation 2.5), and the destruction of adsorbed pollutants (Equation 2.6).

$$\mathbf{TiO_2 + UV \rightarrow e^- + h^+} \qquad \mathbf{(2.3)}$$

$$\mathbf{Ti\ (IV) + H_2O \rightleftharpoons Ti(IV)\text{-}H_2O} \qquad \mathbf{(2.4)}$$

$$\mathbf{Ti(IV)\text{-}H_2O + h^+ \rightleftharpoons Ti(IV)\text{-}{\cdot}OH^{\bullet} + H^+} \qquad \mathbf{(2.5)}$$

$$\mathbf{Pollutant + OH^{\bullet} / {}^{\bullet}O_2^- \rightarrow CO_2 + H_2O} \qquad \mathbf{(2.6)}$$

TiO_2 semiconductor photocatalysis may by performed in a fixed bed reactor like set-up where the nanomaterials are on the surface of a stationary support with the main limitation being inefficient mass transfer that reduces photoactivity and leaching of the nanoparticles.[88] Alternatively, TiO_2 photocatalysis might be performed in a slurry with the major drawback of this system being requirement of complementary separation technique to recover the catalyst. The advantages of TiO_2 is that it is has appropriate band edge potentials for overall water splitting, low operational costs compared to homogeneous photocatalysts, capability to non-selectively and completely mineralize organic contaminants from water, availability and low production of toxic by-products that can further be degraded due to its non-selective nature.[14,88,89]

There are numerous disadvantages associated with the use of TiO_2 semiconductor for effective water splitting such as requirement of high energy bandgap that can only be

activated by light in the UV region of the solar spectrum.[90,91] The high recombination of electrons and holes associated which can retard the redox kinetics that are necessary for efficient photocatalytic processes.[14] The hazards related to use of artificial UV light sources and the cost of designing such lamps as only around 5 % of the solar radiation is composed of UV light which could limit efficient photoexcitation reactions that are necessary for photocatalytic reactions. Therefore, studies were conducted to try and solve the problems associated with TiO_2 photocatalysis and to this effect, a lot of novel advances were made.

The most common method used to address the high bandgap of TiO_2 was metal or non-metal doping and co-doping with both metals, both non-metals and a combination of metals and non-metals was evaluated for different applications. Torres-Luna et al. evaluated the effect of iron (III) doped TiO_2 directly from ilmenite and obtained a reduced bandgap from 3.13 eV to 2.30 eV with little sulfur content.[92] The co-doped TiO_2 enhanced visible light absorption which was attributed to the presence of mainly rutile crystal phase of TiO_2 and reduction in new energy states (valence band and conduction band) compared to pure TiO_2 as a result of sulfur filled molecular orbitals and antibonding iron (III) orbitals. Moreover, Kuvarega et al. evaluated nitrogen and iridium co-doped TiO_2 for degradation of eosin yellow where the N doped TiO_2 showed more efficiency than the co-doped N, Ir- TiO_2.[90] Their results vividly displayed that N, Ir- co doping was effective in improving visible light absorption properties of TiO_2 but more photocatalytic activity was mainly achieved while only N was used as a dopant under simulated sunlight. Doping and co-doping of semiconductors therefore is effective towards improved visible light adsorption properties of TiO_2 as complemented by other researchers.[14,93,94]

Support of carbon-based materials have been investigated on TiO_2 with the most common one being exfoliated graphite due to its electrical, physical and mechanical properties as well as its low cost when compared to carbon nanotubes and graphene. Baldissarelli et al. synthesized an exfoliated graphite oxide (EGO) using both ozone and thermal treatment to make composites of TiO_2-EGO by thermal assisted hydrothermal method with improved photodegradation activity than TiO_2 P25 for degradation of methylene blue under UV radiation.[95] However, other researchers have used carbon nanotubes and graphene oxide as a support material for different applications with efficacious results.[14,96]

Photosensitizers are other materials used to successfully enhance photocatalytic activity of TiO_2 for different applications. The selected method and photosensitizer are very

important towards successful application of this materials. Zhao et al. studied Copper (II) porphyrin sensitizer on TiO_2 for degradation of 4-nitrophenol under UV-Vis radiation.[97] The high photocatalytic activity and stability was due to the presence of anatase TiO_2 and the strong interaction it formed with copper (II) porphyrin. Moreover, photosensitizers can also improve the photocatalytic activity of TiO_2 in the visible light range. For example, composites of TiO_2 and novel tin (IV) porphyrins with proposed axial OH interactions of porphyrin with TiO_2 were investigated under UV-Vis radiation by Duan et al. for degradation of 4 nitrophenol.[98] They obtained more efficiencies of the composites compared to bare TiO_2 even under only visible light radiation which depended on the space tropisms of peripheral substituents in meso positions of the porphyrin ring.

Generation of heterojunctions or use of supports has been another useful and cheap strategy to enhance visible TiO_2 photocatalytic efficiency. Different heterostructures that have been constructed with TiO_2 include core shells,[99] p-n heterojunctions[100] and Z-scheme[101] heterojunctions for different applications under visible light irradiation. Ferraz et al. studied the removal of methylene blue on hexagonal niobium (V) oxide (Nb_2O_5) and anatase TiO_2 mixtures under UV light, visible light and visible light plus H_2O_2. The highest performance was achieved under visible light and visible light plus H_2O_2 and was correlated to the presence of anatase TiO_2 that as 60 % weight of Nb_2O_5 was proposed to inhibit the formation of less photocatalytic rutile TiO_2. Drmosh et al. fabricated a double Z-scheme heterojunction of ternary $Bi_2S_3/MoS_2/TiO_2$ with microwave assisted hydrothermal method for photodegradation of methylene blue under sunlight radiation and photocatalytic hydrogen generation under visible light.[101] The improved performance was attributed to the double Z-scheme heterostructure and a large surface area that enhanced available catalytic active sites and redox potential.

The efficiency of a photocatalyst is determined by the number of reactions initiated by captivation of a photon.[102] Meanwhile, photon absorption depends on properties related to photo excited EHPs like their regeneration rate, energy levels and rate of migration.[86,103–105] Irradiation conditions (photon energy and flux) and optical absorption properties of the photocatalyst (bandgap, size and surface area) affect EHPs regeneration rate and the fate of the EHPs control the catalytic reactions on its surface or within the photocatalyst.[106,107] The EHP recombination occurs if the carrier diffusion time to the surface is longer than the electron/hole recombination time.[108–110]

Band positions indicate the thermodynamic limitations for the photoreactions that can be induced by charge carriers when creating and analyzing photocatalysts.[111,112] In summary, the valence band edge of the semiconductor must have high negative redox potential with respect to a standard electrode than the intended analyte to be oxidized to avoid forming the positive cation radical of the analyte. Figure 2.6 shows classification of visible light semiconductors classified based on their band positions as suitable for water oxidation, reduction and water splitting. Iron (III) oxide is classified as suitable for water oxidation and nitrogen-based semiconductors such as graphitic carbon nitride are appropriate for overall water splitting.[82]

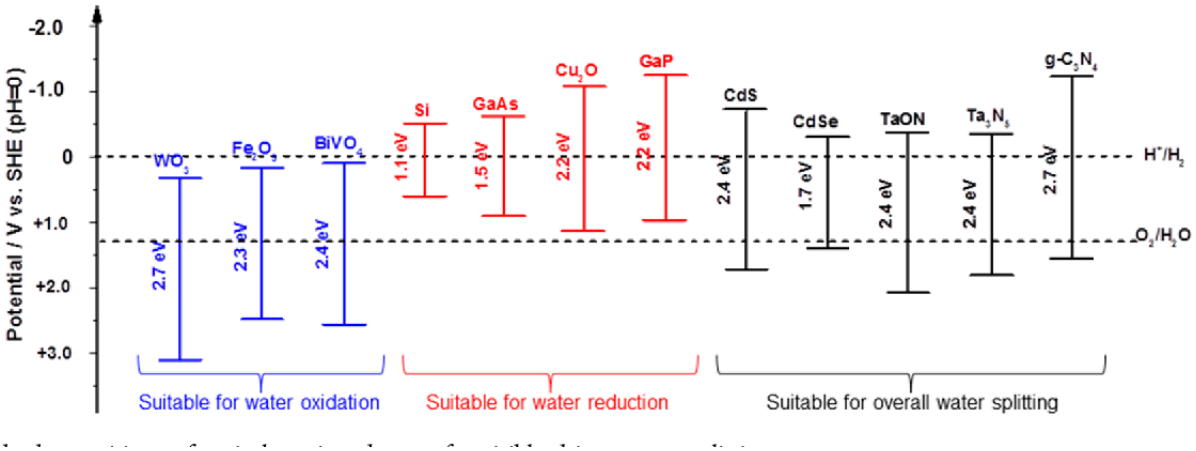

Figure 2.6: Classification of band positions of some visible light driven semiconductors

On the other hand, if the reduction of a molecule is required, then the conduction band edge of the semiconductor must be positioned favorably relative to the reduction potential of the molecule.[113] In this category falls gallium phosphate and other related semiconductor materials. The energy levels of the valence (E_v) and conduction bands (E_c) for many photocatalysts is determined experimentally (usually through flat band potential measurements in contact with aqueous solutions of known pH). Some can be estimated, like virgin semiconductor materials, through the relationship between its bandgap (E_g, units of eV) and the absolute electro negativity ($-\chi$, units of eV) [114] as shown by Equation 2.7 and 2.8.

$$\mathbf{E_c = - X + 0.5\ E_g} \qquad \mathbf{(2.7)}$$

$$\mathbf{E_v = - X - 0.5\ E_g} \qquad \mathbf{(2.8)}$$

Recently, research is focused on a photocatalyst that can be activated by visible light hence smaller bandgaps than TiO_2.[115] In general, a good heterogeneous photocatalyst

should absorb light efficiently (ideally in the visible range), have high photocatalytic activity, and can be stable against photo corrosion. Moreover, it should be cheap, non-toxic, have long-term stability, recyclable and easy to separate. On this note, WO_3, Co_3O_4, TPP and BiOI are important visible light driven semiconductors as they are easy to synthesize and can be fabricated to harness visible light absorption and enhance photodegradation of pollutants. This can be achieved via different strategies to form heterojunctions and if cheaper synthesis methods are chosen, the large-scale application of the resulting nanocomposites can be achieved. Moreover, formation of heterojunctions was considered a very easy method towards reduction of photoexcited electrons and holes successfully. The use of carbon nanomaterials has recently gained attention towards easy separation of photocatalytic semiconductors with enhanced properties.

2.5 Selected Materials

The selected materials used to fabricate semiconductors, the general synthetic methods already reported, their properties and their structures are discussed in detail together with some literature reviews of work already done by several authors related to remediation of organic pollutants form aqueous media to further cement their selection in this project. Their crystal structures where possible are also discussed as crystallinity is an important property of photocatalytic materials.

2.5.1 Exfoliated graphite

Exfoliated graphite (EG) is a light-weight carbon material with all the graphite properties complemented with a developed pore structure and the ability to be compacted without a binder. It is characterised by the presence of micro-, meso- and macro-pores that are responsible for some of its applications.[116,117] Exfoliated graphite bargains a unique set of properties including compactibility, flexibility, high electrical and thermal conductivity, and corrosion resistance and is characterised by low bulk density (3–10 kgm^3).[118]

Exfoliated graphite (EG) can be fabricated through thermal, chemical or mechanical methods that are generally referred to as exfoliation which follows the intercalation of the graphite lattice or structure. Graphite intercalation was first reported in 1841 but the intensive studies of these compounds gained momentum in the early 1930s with detail investigation of factors that affect the structural, electronic and lattice properties of GICs.[118,119] Intercalation is the non-destructive addition of foreign materials (ions, atoms, or molecules) to the interplanar layers of a lamellar structure leaving the layered network intact. Strangely, the insertion of different chemical reagents between the graphite grids

simply increases the distance between the layers and leave the structure of the graphite intact.[119]

The expansion that happens during exfoliation is pioneered by the shear of carbon layers that slide in relation to one another to enable its walls to stretch and expand into a balloon. The balloon walls are broken during exfoliation and ensures that the exfoliation process is irreversible upon cooling to room temperature and this breakage requires a substantial increase in volume upon conversion of the intermediate GICs into vapour or smaller molecules. The decomposition of the intercalate results in a huge increase in volume compared to vaporization and the amount of gas evolved during exfoliation depends on the type of intercalate species.[117,120] When the intercalate is sulfuric acid, the cell wall typically consists of about 60 carbon layers, so that the cell wall thickness is about 20 nm. Moreover, the volume of the EG (not just the surface) can be improved by fluorination.
Exfoliated graphite has been widely used in gasket, electromagnetic interference shielding, electrochemical applications, stress sensing and thermal insulator due to its lightweight, soft, porosity, high-surface area, high-surface activity, fire-resistant composites, resin composites and is an easily disposable and environmentally friendly material with low density and high porosity.[121–123] The exfoliated graphite can be compacted into foils due to the presence of macropores and the combination of micro- and meso-pores makes it suitable for use as a hydrocarbons adsorbent and a gas storage container.[124] Exfoliated graphite has received attention as filler in composites in recent times due to prominent properties it imparts to the host polymeric matrices. These special attributes make the resulting composites suitable in certain areas of application. Exfoliated graphite/polymer composites are finding applications in varied areas such as charge storage devices, electronics packaging, electromagnetic interference shielding and antistatic coatings, and conducting packaging due to the conducting nature of graphite.[125–127] EG can be used as a filler in composites for electrical and thermal conduction applications that are enhanced by the EG microstructure.

The use of carbon nanostructure composites is another evolving area that gives photocatalysts consisting of tailored properties (EG providing a unique opportunity for catalysts with multifunctional features) due to a combination of superior mechanical, multifunctional and physical properties including its ability to capture and shuttle electrons.[128] This triggered research interest focusing on its applications for photocatalytic treatment of waste with several reports on TiO_2/EG composites dominating for use in visible or UV light for photodegradation of pollutants.[129] Moreover, the pore structure, light

density and high specific surface area coupled with its compacting ability makes EG a good candidate as a catalyst support.[130] From the mid 1990 after first success of fabricating EG/TiO_2 composites, it has been extensively studied (unique combination of the photocatalytic activity of TiO_2 and the buoyancy of EG) with limitations on its industrial use being due to lack of simple and inexpensive methods of synthesis.[116]

A new method for synthesis of EG, amorphous carbon and TiO_2 was developed and the composite demonstrated immense potential towards removal of organic pollutants from water by photocatalysis.[129] Ndlovu et al synthesised an EG/TiO_2 nanocomposite with enhanced photocatalyst activity ascribed to the ability of graphitic layers to accept and transport electrons to improve electron-hole recombination.[128] Therefore, the cheap and abundant carbon is good for attracting and channelling electrons during photocatalysis to improve efficiency of active species. The EG/TiO_2 nanocomposite was prepared in situ by Li et al. for decomposition of dichlorvos under different conditions. The nanocomposite showed good photocatalytic activity and could be reproduced by baking at 700 ^{0}C.[131]

EG has been used with other semiconductors besides TiO_2. Umkuro et al. produced a nanocomposite of palladium, zinc oxide and exfoliated graphite (Pd-ZnO-EG) with enhanced efficiency of 87 % compared to 3 and 25 % of ZnO and Pd-ZnO using acid orange 7 dye as a model pollutant under visible light irradiation.[132] Gou et al. made a silver/silver chloride/exfoliated graphite (Ag/AgCl/EG) nano-photocatalyst by precipitation and photoreduction processes which exhibited high visible light photocatalytic activity for degradation of RhB (99.5%) and phenol (89.1%) solution and reusability stability exceeding 6 cycles.[108] Zhao et al. synthesised different(1, 4, 7, 10 and 15 wt %) copper oxide/exfoliated graphite (Cu_2O/EG) composites by precipitation for decolorization of methyl orange (MO).[109] The decolorization of MO under optimum conditions reached 96.7% in 60 min with the Cu_2O/EG (10 %) enduring 5 repeated photocatalytic cycles.

The choice of the method and the semiconductor to be incorporated in EG depends on different factors. The optimisation of the amounts of semiconductors to EG, the method of synthesis, the conditions of degradation (type, concentration, amount of pollutant, the concentration of catalyst as well as the pH of pollutants, the type of pollutant, the use of inhibitors and the choice of irradiation type) are paramount to achieve the noticeable efficiencies.

2.5.2 Reduced graphene oxide

Graphene, reduced graphene oxide and exfoliated graphene oxide are used interchangeably to refer to a single flat layer of carbon atoms compactly packed into a two dimensional honey comb lattice of a benzene ring structure.[133,134] It is widely used to define properties of other carbon-based materials such as carbon nanotubes, large fullerenes, exfoliated graphite etc. such that carbon nanotubes are described as nanometer sized cylinders of trundled graphene sheets.[135,136] It is the world's thinnest sheet often referred to as the "miracle material" of the 21st Century with sp2 hybridised carbon lattice and remarkable physical, chemical and mechanical properties such as high aspect ratio, outstanding electrical conductivity, large surface area, low coefficient of thermal expansion, astonishing mechanical properties and zero bandgap.[136–138] Moreover, there is a ballistic electron transmission in reduced graphene oxide layers at ambient temperature and it contains a range of highly reactive functional groups decorating the edges or chemically reactive epoxy groups on their basal planes.[133,134,138]

The pioneering research on two dimensional materials was achieved in 2004 by isolation of monolayer graphene sheets from three dimensional graphite through micromechanical cleavage.[139] Since then, various methods such as chemical vapour deposition, bottom-up organic synthesis, epitaxial growth, thermal expansion, mechanical exfoliation, and chemical and electrochemical reduction of graphite oxide have been developed to improve different properties and make it suitable for various applications in materials science, condensed matter physics and other related scientific fields.[139–142] Fascination with reduced graphene oxide (rGO) stems from its remarkable properties that render it useful for numerous applications.[137] The large surface-to-volume ratio and highly conductive nature of reduced graphene oxide make it suitable for revocable lithium storage in lithium-ion batteries.[143] Moreover, it is attractive for use in storage materials, biosensors, drug delivery, nanomotors, molecular imaging, nanomedicine and stem cell based tissue engineering, and catalysis or photocatalysis applications.[133,138,139,144–149].

Catalytic and photocatalytic applications of RGO are popular for qualitative destruction of undesirable air and water pollutants and solar energy conversion with semiconductors,[150] TiO_2 being the most common.[142,151–153] Zhang et al. studied the photocatalytic degradation of rhodamine B (RhB) using graphene-based hollow TiO_2 composites (TiO_2/RGO) prepared by the solvothermal method with expressively improved photocatalytic activity under both UV or visible light irradiation.[153] Moreover other researchers have reported that

RGO enhances visible light performance of semiconductor metals by improving charge transfer and reducing electron hole recombination.[154]

2.5.3 Tetraphenyl porphyrin

The word porphyrin is derived from the Greek word ‘porphura’ meaning purple and befits their intense colour.[155] The study of porphyrins started with discovery of natural porphyrins some centuries back. Küster suggested the general accepted structure of porphyrins as four pyrrole derivative rings connected by methane bridges, and termed it the porphyrin macrocycle.[156] In summary, numerous advances in porphyrin synthesis have been realised through different synthetic approaches such as MacDonald dipyrromethane synthesis[157] but symmetrical porphyrins (tetraphenylporphyrin, etc.) synthesis is efficiently accomplished by one-pot monopyrrole tetramerization method (Adler-Longo method).

Porphyrins offer an interesting alternative use as ordered organic semiconductors. They have semi-conductivity and the ability to convert one form of energy (photoconductivity) to another (electrical and chemical). Porphyrins with aromatic rings fused to the *β*-positions of the pyrrole residues are referred to as *π*-extended porphyrins, and they have been a subject of interest recently. The improved conjugation due to the fused rings to the porphyrin macrocycle improves both light absorption and emission near-infrared (near-IR) region of the spectrum. The photophysical properties of some *π*-extended porphyrins have been reported,[158] although there is still a gap in the literature of this interesting class of molecular chromophores. Moreover, porphyrins make an excellent film growth and are chemically and thermally stable.[158] However, the chemical structures of porphyrins and the sizes and morphologies of their self-assembly aggregates distract their photocatalytic activity,[159,160] due to photo-induced electron-hole recombination and their poor photo-stability. The phenomenon of aggregation is associated with changes in spectral properties observed when increasing the concentration of the porphyrin in solution. Dougherty et al. were the first to report aggregation (polymerisation) of porphyrins in solution.[161] Their findings which were echoed by several researchers proved that polymerisation altered hydrophobicity, absorption and fluorescence properties, and transport and localisation of the porphyrins in solutions. The observed property changes in solution are linked to dimerization based on a "face-to-face" or "sandwich" model of two units. Therefore, solvent composition, concentration of porphyrin and its structure can affect its catalytic activity by affecting properties that improve catalytic efficiency such as absorption, hydrophilicity, aggregation, etc.

The porphyrin macrocycle contains 22 conjugated π electrons, but only 18 of these are delocalised.[162] Consequently, porphyrins do not lose their aromaticity during addition and substitution reactions, redox reactions, and cross couplings to improve their structures to either a variety of functionalised macrocycles or linear tetrapyrroles for applications in materials science, biology and medicine.[163] The understanding of the spectra of synthetic porphyrins, their ability to mimic biological processes and their unique planar geometry resulted in porphyrins being used in different applications such as solar energy conversion, optical devices, photoelectronic, sensors and most recently for photocatalysis.[159,163–165] The photosensitization of wide band-gap semiconductors is common after the successful development of nanocrystalline TiO_2 films with high conversion efficiency.[166] Porphyrins gained momentum for use as photosensitisers due to the nature of their absorption spectrum (intense Soret bands and Q bands). The several reports made on Zinc-5,10,15,20-tetrakis(4-carboxyphenyl)-porphyrin (ZnTCPP) use as an efficient sensitizer for TiO_2 proves the effectiveness of metallated porphyrins use in this regard.[167–170] Cherian et al. investigated the use of 5,10,15,20-tetrakis(4-carboxyphenyl)-porphyrin (TCPP) as a sensitizer.[166] TCPP was found to strongly adsorb on TiO_2 and to efficiently act as a photosensitizer for solar energy conversion by TCPP-TiO_2 electrodes. The conversion was 55 % at the Soret peak and 25-45 % at the Q-band peaks with an overall energy conversion efficiency of 3 %.

The solar spectrum consists of 8 % UV and 45 % visible light energy and this inevitably encourages researchers to focus on fabricating hybrid materials that exploit the abundant visible light for photocatalytic applications. Recently, porphyrin sensitized photocatalysts are common and the porphyrin-TiO_2 systems have also been considered as an alternative material for visible-light photocatalysis.[98] Porphyrins are considered better photosensitizers of TiO_2 than other dye sensitizers such as erythrosine and rose Bengal.[171–173] This is because of their small singlet-triplet splitting, the long triplet excited state lifetimes,[174] high quantum yield for intersystem crossing and good chemical stability. Their photophysical properties are positively affected by inserting a metal ion in the centre which is coordinated by the porphyrin resulting in a stronger and broader visible light photo response.

The efficiency of the porphyrin-metal oxide semiconductor system is based on generating electron-hole pairs and radicals' which in turn affects the recombination dynamics of photo-induced electron and holes.[172–175] The ultrafast charge transfer from the excited state porphyrin to the conduction band of metal oxide semiconductors (MOSs) increases

photocurrent response.[172,174] Ahmed et al. incorporated tetra (4-carboxyphenyl) porphyrin (TCPP) photosensitizer on the surface of TiO_2 for photocatalytic degradation of Rhodamine B (Rh B) dye.[175] The photocatalytic activity of 0.1 % TCPP-TiO_2 was 1.5 times greater than that of pure TiO_2 and the lifetime of photo-generated electron-hole pairs doubled under UV-Vis irradiation. TCPP was found to be chemisorbed on TiO_2 surface through the O=C-O-Ti bonds. The presence of this bonds facilitated fast electron transfer from excited state TCPP to TiO_2 conduction band increasing charge separation.

In recent years, the focus shifted from only synthesising visible light driven photocatalysts to creating cheap, affordable and efficient photocatalytic hybrid systems for wastewater treatment. To this effect the simplest meso-substituted porphyrin, tetraphenylporphyrin (TPP) (Figure 2.7), promises to be a good candidate, although not much has been done on its photocatalytic applications.

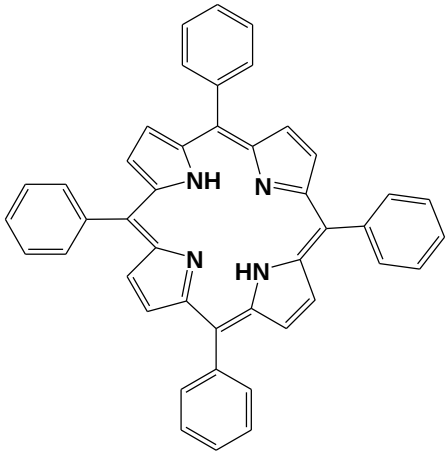

Figure 2.7: Structure of tetraphenylporphyrin

TTP has polymorphic crystal structures like triclinic, tetragonal and monoclinic forms.[158,176] The TPP is centrosymmetric with two independent pyrrole and phenyl groups. The electronic absorption spectra of tetraphenylporphyrin consist of a strong absorption band around 400 nm (Soret band) and a weak absorption band around 550 nm (Q-band) [162]. These electronic transitions are assigned to Π - Π* transitions. The Gouterman four orbital model which involves two nearly degenerate Π orbitals and two degenerate lowest unoccupied Π* orbitals describe these transitions.[155] The intensity and peak positions of the bands depends on both the solvent and the concentration of the absorbing species. More importantly, there is a correlation between the type of the porphyrin substituents and the positions and the relative intensities of the absorption bands. This results in four general types of spectra which are exhibited by different porphyrins referred to as the etio-type, rhodo-type, oxorhodo-type and phyllo-type.[177]

Makhlouf et al. studied the structural and optical characteristics of tetraphenylporphyrin which clearly indicated that it is a good candidate for visible light photocatalysis due to its high absorption coefficient within the solar spectrum[158] and its low bandgap (1.6-1.8 eV).[158] Their results showed that film thickness does not influence the optical properties of the TPP films which were reported to be affected slightly by annealing temperature. The generation of radicals is a necessity for photocatalytic degradation of organic pollutants, but the produced radicals may degrade the porphyrin molecule.[166,178] The oxidative attack of the porphyrin molecule by radical species is accountable for the light-induced porphyrin degradation process. Despite metalation of the porphyrin system, supporting the porphyrin in either its free base or in metallated form helps to achieve good results. Careful selection of a support material can lead to improved photocatalytic performance of the TPP-semiconductor system.

Gokakakar et al. studied photocatalytic degradation of methyl orange using tetraphenyl porphyrin and its metal derivatives (Cu, Ag and Sn as metals).[178] The free base TPP and $SnTPPCl_2$ showed more efficiency compared to the AgTPP and CuTPP and sodium lauryl sulphate (SLS) acted as a good photocatalyst promoter at pH 7 and 10. Their results at different pH values (6, 7 and 10) showed that although free base tetraphenyl porphyrin is a good photocatalyst, its efficiency was just above 50 % for dye degradation during a four-hour degradation interval. At pH 6, the photocatalytic activity was found to be at its peak. Additionally, their work is important towards understanding the photocatalysis of porphyrins as from the selected metals used, not all of them improved the photocatalytic efficiency for dye degradation as only $SnTPPCl_2$ was comparatively the only photocatalyst that performed better than free base TPP. At pH 7 and 10, sodium lauryl sulphate (SLS) was used to promote the catalytic performance of the photocatalysts but still gave low comparative efficiencies to pH 6.

The generation of heterojunctions and sensitizers in photocatalysis has been a topic of great interest for researchers globally. The main aim is to develop catalysts that absorb more in the visible region of the solar spectrum to exploit its abundance and reduce cost, enhanced organic pollutants removal and to some extent the ability to be able to degrade different pollutants to below permissible standard values. Some work was reported using either free base TPP or its metal derivatives with TiO_2, ZnO and reduced graphitic carbon nitride (g-C_3N_4) by different researchers.[179] The material selection process is determined by the individual components, their composition and properties, the synthesis method and the intended application.

2.5.4 Tungsten (VI) oxide

Tungsten trioxide (WO_3), which is a d^o-transition metal oxide, has many interesting optical, electrical, structural, and defect properties.[180] Nano WO_3 has been used as a sensor to detect different oxidizing and reducing gases, in windows for solar cells, colour memory devices, electronic information displays and photocatalysis.[181] Optimal performance of the tungsten oxide on the mentioned technologies depends on its surface adsorption,[182] which to some extent is controlled by the method of synthesis and the type, shape and size of the prepared nanoparticles.[183] A better understanding of surface adsorption of WO_3 nanoparticles is key to unlocking the understanding of improving its efficiency especially in applications such as gas-sensing and photocatalysis.[106,184] For example, the higher the surface area of WO_3 nanoparticles, the greater the opportunity for adsorption and light harvesting that are known to improve photocatalytic activity as more pollutant is adsorbed on the surface of the catalyst, and more visible light absorption will produce more electron-hole pairs.[182] Generally, the optical and electrical properties of WO_3 depend on the size and shape, and a large surface-to-volume ratio is favourable for all the above applications.

Among transition metal oxides, WO_3 is the second most studied material due to its properties.[185] In the nanoscale, WO_3 is an n-type narrow bandgap (2.5-2.7 eV) semiconductor metal oxide that is activated by irradiation with visible light of approximately 500 nm.[183,186] Several factors have been reported to influence the photocatalytic activity of various MOSs, for example, the intensity and spectrum of the irradiating lamp, the solution pH and concentration, the concentration of the catalyst, the composition of the solution, and the particle size and crystal structure of the catalyst as well as the presence of oxidizing agents, surfactants or inorganic ions.[186–188]

The band edge position of WO_3 conduction band is slightly positive with respect to the normal hydrogen electrode (NHE) and excludes its ability of photocatalytic water reduction.[15] However, its valence band edge position is greater by more than 1 eV and can easily oxidise water without a need of a co-catalyst. This limits its use for important reactions such as, reduction of CO_2 to CH_4 hence selection of a strategy to improve its photocatalytic activity is inevitable and is governed by the intended application. Crystal facet engineering may bring a possibility towards elevating conduction band edge positions of metal oxide semiconductors as anion doping is a challenging route to solve this problem. However, despite all these shortcomings, reports exist in literature for

application of WO_3 in photocatalysis synthesised using different methods for degradation of different pollutants.[189]

WO_3 nanostructures can be synthesised by different methods like thermal evaporation, sputtering, chemical vapor deposition, electro deposition and sol-gel deposition.[190,191] Controlling the size of WO_3 nanoparticles improves its photocatalytic performance for indoor applications in the absence of UV irradiation.[192] Therefore, most preferable synthesis methods of WO_3 nanoparticles are those in which size and crystallinity can be controlled. WO_3 has three different crystalline arrangements (the monoclinic/triclinic/ orthorhombic/tetragonal, the hexagonal (h-WO_3), and the cubic).[193] The distortion of the polyhedrons inside the crystal structures affect the W-O bond length and results in significant changes in electronic properties of WO_3 despite all the WO_3 crystal structures having WO_6 units on their vertices or edges.[15] The triclinic, monoclinic (m-WO_3), orthorhombic, and tetragonal WO_3 phases have similar chessboard-like patterns of WO_6 octahedra; thus, they can transform reversibly into each other (Figure 2.8 a).[194]

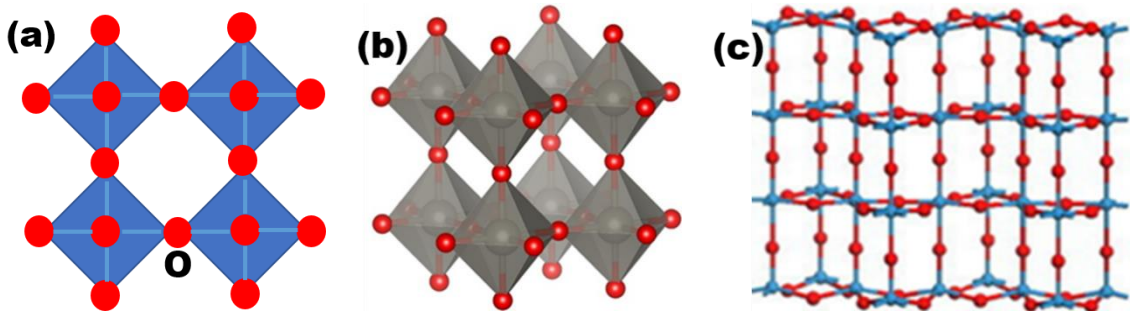

Figure 2.8: Crystal structure of (a) monoclinic, (b) cubic and (c) hexagonal WO_3

The difference emerges from the extent of the displacement of the W atoms from the centre of the WO_6 octahedra.[190,194] The WO_6 octahedra in m-WO_3 is arranged at corner sharing octahedra emulating a distorted ReO_3 structure[195] that should be of simple cubic symmetry. Nevertheless, the structure is unsymmetrical and different from ReO_3 due to distortions of the WO_6 octahedra.[196]. m-WO_3 is considered a promising visible light photocatalyst for oxygen evolution with the help of an electron acceptor due to its low valence band edge maximum and low bandgap of 2.7 eV.[197] At room temperature m-WO_3 and triclinic (WO_3) are stable (or metastable) and the phase transitions are not the recombination of tungsten and oxygen atoms, but the distortion of tungsten atoms in the original ideal crystal structure.[198] The m-WO_3 has been studied in detail by different groups.[199]

Zhang et al. described successful synthesis of γ-monoclinic WO_3 nano-multilayers with highly reactive (002) facets exposed through a facile solvothermal method using ethylene

glycol as the solvent.[200] High-resolution transmission electron microscopy (HRTEM) image of WO_3 nano-multilayers showed a fringe spacing of 0.3835 nm and 0.3729 nm, which is consistent with the (002) and (020) lattice planes of γ-monoclinic WO_3.[200] On the contrary, the structure of tetragonal WO_3 was first explained with power X-ray diffraction at 1223 K and the space group was reported as P4/*nmm*, with the tungsten position at (Z_W = 0.06) and the oxygen position at ($Z_O = Z_W + \frac{1}{2}$).[201] Several authors reported aberrations on the tetragonal phase a-axis thermal and strong expansion between 1140 K and 1170 K[201–203] and the suspicion was that phase transformation takes place.[203] Moreover, Locherer et al. proved the presence of tetragonal WO_3 at 1100 K.[204]

Ramana et al. investigated major phase changes with respect to annealing temperature. Annealing of the sample at lower temperatures to around 400 °C changed the monoclinic phase, which is stable at annealing temperatures up to ~300 ^{0}C.[205] The corresponding phase identified as orthorhombic WO_3 was obtained at a temperature of about 350 °C and is completely different when compared to those obtained at lower annealing temperatures. At 500 °C, the pattern clearly showed that the distance between the diffraction maxima in the vertical and horizontal directions changed significantly, indicating the transformation to the new phase which matched with the hexagonal phase. In the semiconducting oxide WO_3 the oxygen sublattice is distorted and the metal ion lies off-centre in its coordination octahedron.[206] The solid display different temperature-induced phase transitions, changing from monoclinic to triclinic, monoclinic, orthorhombic, and tetragonal upon heating.[206] WO_3 goes through different structure transitions in the temperature range of −180 to 900 °C and the dominance of each crystal structure is temperature dependant. The crystal structures of cubic WO_3 is shown by Figure 2.8 b.

The ideal cubic WO_3 primitive cell is a kind of octahedral structure; W and O occupy the central and six corners of the octahedron, respectively. Simple cubic crystal structure of WO_3 has not been observed at high temperatures, however, it is used mostly as a reference structure on many reports on theoretical and experimental studies of WO_3.[198] However, it is difficult to synthesise cubic WO_3 nanostructures through aqueous synthesis at room temperatures.[207] Among tungsten oxides, h-WO_3, is currently of particular interest because it is a promising material for negative electrodes of rechargeable lithium batteries.[208] It has an open-tunnel structure and intercalation chemistry.[209] In h-WO_3, the WO_6 octahedra shares corner oxygen atoms along the (001) plane and its arrangement is a six-membered ring which make inflexible tunnels laterally to the c-axis throughout the whole unit cell (Figure 2.8 c).[195] h-WO_3 is chemically alike with m-WO_3 with the only

difference being a periodic ultra-microporous structure. The role of intra-crystalline tunnels in reactivity can be understood through a direct comparison.[195] It has been synthesised by acidification and hydrothermal treatment of alkali tungstates, spray pyrolysis using WCl_6, thermal or wet chemical oxidation of hexagonal ammonium tungsten bronzes, by thermal evaporation and oxidation of tungsten metal and by thermal oxidation of ammonium polytungstates.[209] Moreover, the increased interest in studying h-WO_3 has resulted in different morphologies (nanofilms, nanotubes, nanosheets, nanoparticles and nanowires). The composition (W/O ratio) of all WO_3 nanosystems are important in some fields, e.g. photocatalysis.[209]

Gu et al. synthesised wire-like h-nanocrystals in grams quantities using the hydrothermal method without a catalyst or templates and assessed them as Li-ion batteries anodes.[208] The nanocrystals performed exceptionally well and were suggested for use as nanosensors, catalysts, microelectronic devices, etc.[208] Szilagyi et al. synthesised h-WO_3 by annealing hexagonal ammonium tungsten bronze and the sample contained 50-100 nm particles, had average surface area of 8.3 M^2/g and thermal stability up to 450 ^0C. The h-WO_3 was sensitive to (10-50 ppm) NH_3 with the shortest response and recovery times of 1.3 and 3.8 minutes, respectively.[196]

The phase transformation in the WO_3 thin films with grains of ~60 nm in size and a root-mean-square (rms) surface roughness of 10 nm were investigated by annealing in the TEM column at 30-500 °C by Xiang et al., and were found to occur in a sequence (monoclinic, orthorhombic and hexagonal) as temperature was increased.[210] Distortions and tilting of the WO_6 octahedra occur during the phase transitions and expressively disturb the electronic properties and, hence, the electrochemical device applications of WO_3. WO_3 samples with triclinic/ monoclinic /orthorhombic/ tetragonal phases have been reported as photocatalysts due to their stability at room temperature.[190,191,194] Hexagonal WO_3 was just recently confirmed photocatalytic.[189]

In gas sensing, the crystal structure (monoclinic or hexagonal) and the composition (oxidized or partially reduced) of WO_3 infer observable differences in their performance,[211] and the same trend is expected in photocatalysis.[194] However, unlike in TiO_2 where crystalline structure (rutile and anatase) play a major role in photocatalysis, with WO_3, the composition is the influential factor.[191,212] The crystal structure of WO_3 is not completely out of the picture though as it influences the WO_3 samples composition since different compositions belong to different structures [211] as confirmed by studying the composition

(partially oxidised or partially reduced) effects on photocatalysis.[189] The most prominent parameter that influences the photocatalytic properties of WO_3 was found to be its composition regardless of the crystal structure.[191] For example, oxidized m-WO_3 always have better photocatalytic performance than oxidized h-WO_3 which contains trace amounts of NH_4^+ (or alkaline) ions, which are necessary to stabilize its structure.[191]

The selection of WO_3 synthesis method will depend on the required composition and the intended application.[213] The other important aspect to consider are the other components that will be incorporated on the WO_3 to enhance its photoactivity; whether an organic or inorganic support or even another photocatalytic material. Optimisation is required to achieve the best possible interaction of the materials to give the best synergistic effect in photocatalysis. Moreover, the target pollutant and the intended use (industrial waste or drinking water or air pollution control) play a major factor.

2.5.5 Cobalt oxides

Cobalt oxide occurs in different forms that are characterised by the oxidation state of the cobalt cation. The various oxides reported include cobalt (IV) (CoO_2), cobalt (III) oxide (Co_2O_3), cobalt oxyhydroxide (CoO(OH)), tricobalt tetraoxide (Co_3O_4) and Cobalt (II) oxide (CoO) with Co_3O_4 (oxidation state +8/3) and CoO (oxidation state +2) being the stable and imperative forms based on their distinguishing structural features and properties.[214–216] Cobalt (II) oxide (CoO) is referred to as cobalt monoxide or cobaltous oxide, cobalt (III) oxide (Co_2O_3) is simultaneously called cobaltic oxide while cobalt (II, III) oxide (Co_3O_4) is called cobaltosic oxide and it is an antiferromagnetic material.[217,218] Recent research has evidenced that cobalt oxide polymorphs (i.e. CoO and Co_3O_4) are promising materials for photocatalytic applications because of the relatively low cost, simple and scalable synthesis, and less health or environmental related hazards (harmful only by excessive inhalation).[219] These oxides possess narrow to wide bandgap energies determined by their dimensions or morphologies.[220]

Cobalt oxide crystals have been successfully synthesised in different morphologies such as nanospheres, nanorods, nanocrystalline, nanocubes, hollow spheres, nanorods bunches and arch-like nanocrystals.[221,222] Cobalt oxyhydroxide prefer hexagonal coordination with the divalent cobalt cation occupying the octahedral site coordinated by six hydroxyl oxygens.[214] Cobalt tetraoxide has a cubic spinel crystal structure (space group Fd3m) in which the Co^{2+} ions and the Co^{3+} ions occupy the tetrahedral and

octahedral sites respectively (Figure 2.9 a) and show good conductivity due to the presence of Co^{3+} ions.[223,224]

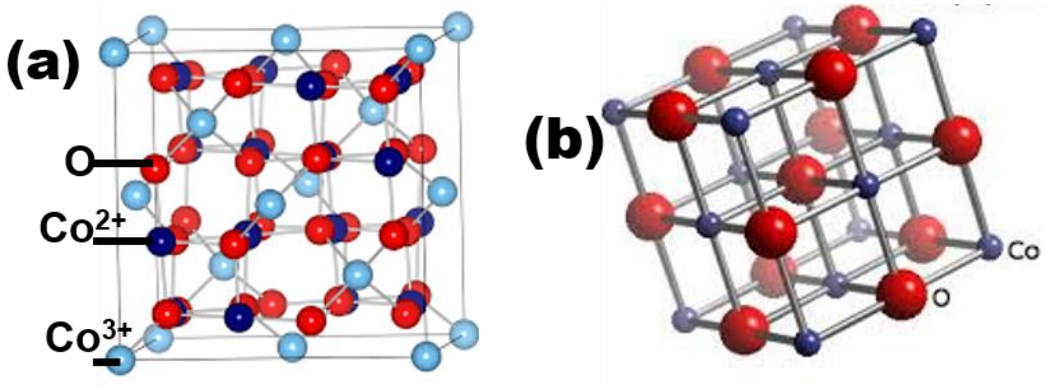

Figure 2.9: Crystal structure of (a) cobaltosic and (b) cobaltous oxides

The Co^{3+} ions at the octahedral sites are diamagnetic and the Co^{2+} ions at the tetrahedral sites form an antiferromagnetic sublattice with a diamond structure.[225] It forms a close-packed face-centered cubic (fcc) lattice with the oxygen ions. In contrast, due to the large number of oxygens coordinated on the Co^{3+}, there are more electrons due to the Co-O bonds than on the Co^{2+} tetrahedral coordination.[226] Cobalt (II) oxides have cubic, fcc or hcp with cubic fcc-Co often synthesized by the decomposition of organometallic precursors in non-aqueous solvents (Figure 2.9 b) while the product of ecumenic chemical reduction is hcp-Co or a mixture of fcc-Co and hcp-Co.[222] The cobaltous oxide or cobalt monoxide (CoO) crystallizes in the periclase (rock salt) crystal structure or NaCl structure consisting of two interpenetrating face centered cubic (fcc) sublattices of Co^{2+} and O^{2-} with space group Fm3m.[217,227] These two sublattices are shifted along the body diagonal by half its length such that each ion has six of the other ions as its nearest neighbours and each cubic unit cell (not the primitive unit cell) has four Co^{2+} and four O^{2-} ions.[228]

The call for economical catalysts with suitable energy and electronic structures stemmed various synthesis methods of cobalt oxides for diverse applications. Cobalt oxides nanoparticles were effectively synthesized by sol-gel, thermal decomposition, precipitation, chemical spray pyrolysis and sono-chemical, vapour deposition, solvothermal, hydrothermal, microemulsion, hard templating and mechanochemical methods.[229–231] The simplest and cost effective technique is solid state thermal decomposition with unique advantages and merits over others such as short reaction time, easy work up and the possibility to achieve unique particle sizes, specific shapes and narrow size distribution and improved morphology.[232] Co_3O_4 and CoO(OH) can be synthesised by thermal decomposition of cobalt organic salts under oxidizing environment while simple decomposition leads to cobalt (II) oxide.[214]

Cobalt oxides have different applications that depend on their particle size. Cobalt oxides are important transition metal oxides used for research and industrial applications as magnetic materials, pigments, anode materials for rechargeable Li- batteries, gas sensors, electrochemical systems, catalysts, electrochromic devices, high-temperature solar selective absorbers and electronic devices.[233] The variance in oxygen holes, oxygen defect and oxygen adsorbed in different states of cobalt are thought to be the reason for high activity and selectivity of these metal oxide catalysts.[234,235] Moreover, cobalt oxide is a p-type semiconductor with interesting properties such as high thermal and chemical stability, low solubility, interesting electronic, optical, magnetic and catalytic properties[236] and a narrow bandgap (about 1.2–2.1 eV) and also oxidation catalysis properties.[233,237] Bandgaps of cobalt oxides changes with their configuration, oxidation state, size and morphology.[238] Cobalt oxyhydroxide applications include carbon monoxide detection at low temperatures, rechargeable alkaline batteries, fuel cells and capacitators.[214] However, there are no reports of their catalytic properties.

The magnetic properties of cobalt oxides can be tuned by chemical composition, morphology, crystal structure, degree of its defectiveness and interaction with neighbouring particles in the matrix.[239] Magnetic nanoparticles (NPs) were proposed for biomedical applications, such as cancer diagnosis, radioactive vectors in cancer therapy, and as drug delivery systems.[240] CoO and Co_3O_4 are used as contrast agents in magnetic resonance and for drug delivery, and as adjuvants for use in human vaccination when both lymphocytes Th1 and Th2 responses are desirable to remove pathogens.[241] Another study demonstrated toxicity due to magnetic Co_3O_4NPs which can penetrate through dented skin and is cytotoxic for HaCat cells after long term exposure.[215]

Energy conservation and environmental pollution concerns triggered advances in visible light driven photocatalysis and the development of visible light photocatalysts is indispensable in order to exploit the use of abundant solar radiation. Cobalt oxides are emerging as potential photocatalysts owing to their visible light harvesting ability and electron mediating properties.[242] The use of cobalt ions in homogeneous[58] and heterogeneous[243,244] catalysis systems has been reported with the former further contributing to environmental pollution while the latter provides a promise for validation provided it entails proper photocatalyst recovery.[230,245] Moreover, cobalt oxide has oxidation catalysis properties.[233]

To enhance photocatalytic activity of cobalt oxides, reducing the particle size is another method that achieved positive results. This is due to generation of more active sites and promotion of charge transfer. Aggregation also plays an important role and can be reduced by use of support materials such as conjugated polymers,[246] silica and aluminium oxide.[247] Formation of metal oxides heterounions does not only promote photogenerated charge separation[245] but also reduces aggregation.[237] The heterojunctions can be with other p type semiconductor metal oxides , organic semiconductors or n type semiconductors.[237] The heterojunction $Co_3O_4/BiVO_4$, was reported to exhibit an improved photocatalytic activity for phenol degradation under visible light irradiation which was attributed to the p-n heterojunction and the diminution in recombination of photoexcited electron and hole pairs.[248]

Co_3O_4 can be applied as co-catalyst with bismuth oxyhalides for visible-light-driven photocatalytic reactions. Co_3O_4/BiOCl photocatalyst was reported by Tan et al for degradation of Rhodamine B and Methyl orange.[249] However, bandgap engineering of such oxides is a challenge and mainly depends on the morphology, size, and configuration of the nanocomposite.[238] Rao et al. successfully synthesised heterogeneous C_3O_4/Oxone for the degradation of diclofenac in slightly alkaline media and reported an increase in solubility of cobalt oxide in acid conditions for 10 minutes.[58]

2.5.6 Bismuth oxyiodide

Bismuth oxyiodides ($Bi_xO_yI_z$) are currently in the limelight as they are considered as promising visible light photocatalysts. The known bismuth oxyiodides are BiOI, $Bi_4O_5I_2$, $Bi_7O_9I_3$ and Bi_5O_7I.[250] BiOI and Bi_5O_7I are photocatalytic semiconductors for degradation of organic pollutants owing to their special electronic structures according to literature reports. Their conduction band bottom comprises of 6p orbitals of Bi and their valence band maxima is due to Bi 6s, O 2p and I 5p orbitals resulting in a dispersed hybridised valence band which favours the migration of photogenerated holes and the oxidation reaction.[250] Moreover, the different bismuth oxyiodides formation depends on annealing temperature. Periasamy et al. showed the transformation from BiOI at room temperature to Bi_5O_7I which eventually becomes Bi_2O_3 with further increase in temperature (Figure 2.10).[251]

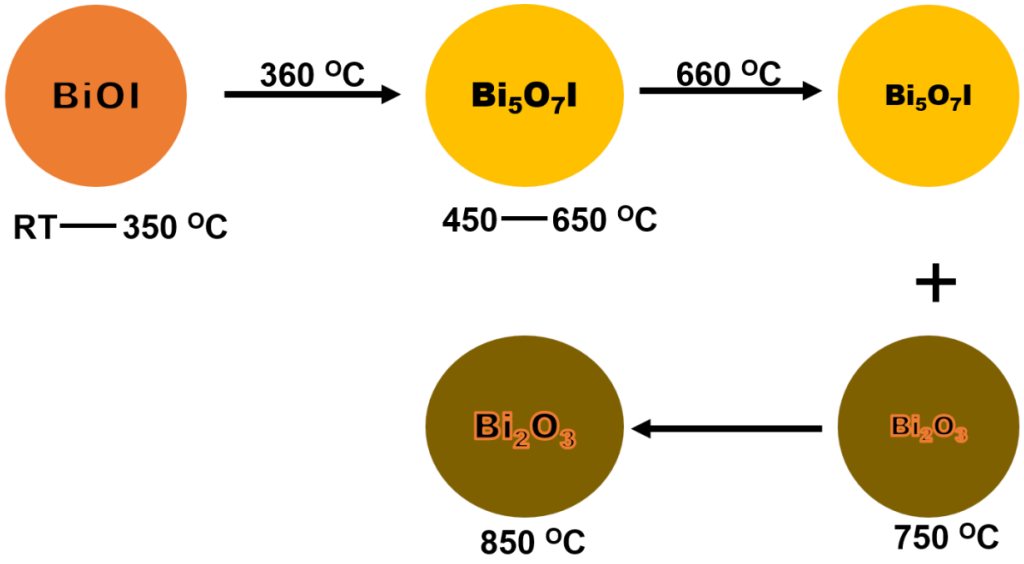

Figure 2.10: Temperature transformation of BiOI

These transformations were matched with the equations (Equation 2.9 and 2.10) corresponding to different weight losses as determined by thermogravimetric analysis.

$$5BiOI + O_2 \rightarrow Bi_5O_7I + 2I_2 \quad (2.9)$$

$$2Bi_5O_7I + 1/2O_2 \dashrightarrow 5Bi_2O_3 + I_2 \quad (2.10)$$

The different methods reported for successful synthesis of BiOI are room temperature precipitation or coprecipitation, solvothermal, microwave-assisted solvothermal, facile microwave irradiation, and hydrothermal methods.[252–256] A combination of different methods have been reported for synthesis of 3D hierarchical architectures and nano-phases.[257] The methods resulted in different structural changes, morphologies and sizes which were related to efficiencies for different applications. Mostly, BiOI is used for visible light driven photocatalytic removal of organic pollutants in water[256,258] though there is scarce reports on degradation of pharmaceuticals. Moreover, there are only a few reports on photocatalytic water splitting for hydrogen generation[259], microbial activity[253], control of air pollution[260], electrochemical[261] and photovoltaics applications.[259]

Hierarchical photocatalysts like BiOI possess organised and readily accessible porous networks that increases their specific surface areas, improve their light harvesting capability and enhance adsorption/desorption mechanisms of reactants. Therefore, synergetic effects of their dimensions and porosity can profoundly enhance their photocatalytic efficiency.[257] BiOI has been extensively studied for photocatalysis due to its simplest atomic stoichiometric ratio and small band energy requirement (1.7–1.9 eV)[257]

with rare reports on its enzyme mimicking properties. Its excellent visible light absorption ability makes it a promising photocatalyst for organic pollution degradation. The fast recombination of photogenerated electrons and holes warrants that it is indispensable to enhance its photocatalytic activity.[262]

Numerous techniques involved in promoting the photocatalytic efficiency of BiOI are reported in literature. They can be generally classified into structural and optical property changes. Structural strategies involve promoting the photocatalytic activity by tuning its size, specific surface area and morphology or by controlling the exposed facet for degradation.[261,263,264] Generally, hierarchical structures effect the mass transfer and light harvesting ability of photocatalysts while high specific surface area improve the surface accessibility of the photocatalyst to enhance the utilization of photo-generated electrons and holes.[265] Li et al. studied the effects of pH on composition and photocatalytic activity of the bismuth oxyiodides and reported a relationship between structure and improvement on BiOI photocatalytic efficiency.[250]

The crystal structure of BiOI has been studied as early as 1900 by different researchers but further knowledge and understanding of its properties advanced after 2000.[266,267] The crystal structure of BiOI is composed of three facets (001, 102 and 110) and the manipulation of facets exposure is important because different facets composes diverse internal electronic properties. BiOI crystal structure is a tetragonal PbFCl (matlockite) with $[Bi_2O_2]$ slabs interweaved between double layers of iodine ions (Figure 2.11).[268] This configuration has induced internal electric field and was determined to be pH dependent during hydrothermal synthesis by Han et al.[268] The electrons in the 5s orbital of the iodine ions are easily excited and thus it can utilize a large proportion of the visible light spectrum for activation.

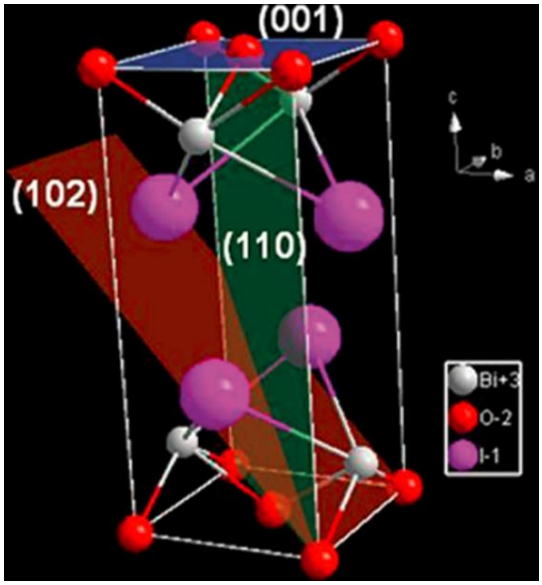

Figure 2.11: Crystal structure of BiOI reported by Han et al

Pan et al. proposed that exposure of different BiOI facets for enhanced photocatalytic activity by the (110) facet which produces more superoxide and hydroxyl radicals than the (001) facet can be tuned by reaction time during hydrothermal synthesis.[269] Ye et al. demonstrated improved photoinduced charge separation resulting in high photoactivity by a single exposed BiOI (001) facet than irregular crystals.[270] Moreover, Luo et al. accomplished high photocurrent density and high degradation efficiency with a TiO_2/BiOI heterostructure with highly exposed BiOI (110) facet prepared via hydrothermal method for degradation of nitrophenol and methylene blue.[271]

Appropriate exposure of active facets for photocatalysis can increase the active sites on the particle surface and reduction in particle size increases electron and holes diffusion compared to their bulk counterparts. The two parameters are valuable tools for increasing the photocatalytic activity of photocatalysts.[257] Promoting the photocatalytic efficiency of BiOI by designing nanostructures with high specific surface area has been well demonstrated[252] and facet controlling was determined as a good structure-tuning property to improve photocatalytic activity.[272] He et al. reported improved photocatalytic activity on the heterojunction between 001 and 110 facet of BiOI for phenol degradation[265] due to efficient charge separation. The property changes are normally accompanied by changing different synthesis methods.

Optical property changes are mostly brought by alteration in composition of BiOI. The composites containing more than one halogen (BiOBrI) have been reported to have improved photocatalytic activity than the pristine BiOI. The improved photocatalytic

performance was due to their narrowed bandgap, enhanced light absorption and improved charge separation.[253,265] However, their photocatalytic activity still need to be improved.[252] Another strategy involves forming a heterojunction among BiOX semiconductors with other bismuth based photocatalysts.[273,274] Chen et al. reported enhanced visible light driven photocatalytic activity of BiOF/BiOI composite with 1.2 and 100 times efficiency compared to BiOI and BiOF respectively.[263]

Reports demonstrated that metals or carbon nanoparticles hybridized with BiOI materials exhibit excellent photocatalytic activity.[253,259] Mabuti et al. studied BiOI-graphene hybridised nanocomposite and attributed its increase in photocatalytic efficiency to the enhanced carrier separation due to graphene as an electron acceptor, anti-reflecting and light trapping properties. Hsu et al. reported gold doped BiOI with 4-fold high oxidative activity.[253] Moreover, the Au/BiOI nanocomposites showed enormous potential to treat bacterial induced infections and bacterial inactivation. However, other than photocatalysis using visible light, BiOI studies for other applications such as photovoltaic cells rarely exist.[259] This could be due to unmatched band positions and narrow bandgap which results in insufficient redox ability and high recombination of electrons and holes during migration.[275]

A simple strategy for enhancing the performance of BiOI entails coupling of semiconductors (SCs) to form heterojunctions. BiOI has been coupled with organic semiconductors, metal oxide semiconductors and other bismuth-based semiconductors for heterostructure incorporation. This strategy exhibits considerable aptitude for tuning photocatalyst electronic properties to the desired levels and promoting photoinduced electron–hole pair separation efficiency.[274] The choice of the semiconductor and the preparation method are the most important factors towards construction of heterojunctions that possess excellent photocatalytic activities to ensure that the lattice and energy level match between the two semiconductors is satisfied.[254] The p–n heterojunction forms an internal electric field that enhance separation of photogenerated electrons and holes to improve the photocatalytic activity of BiOI.[17,276]

Xiang et al. reported a novel visible-light-sensitive BiOI/$BiVO_4$ photocatalyst for photocatalysis and antimicrobial activity under visible light.[17] The p–n heterojunction structure had high activities for inactivation of *Pseudomonas aeruginosa* (*P. aeruginosa*) and photocatalytic degradation of methylene blue. Wang et al. investigated a novel Ag_3PO_4/BiOI p-n heterostructure for degradation of dyes under visible light.[277] Their

results affirm an improvement in degradation for rhodamine B, methylene blue and methyl orange for the p-n heterojunction than pristine BiOI.

2.6 Summary

Cobalt oxides and WO_3 are earth-abundant catalytically active materials with relatively narrow bandgap energies (compared to TiO_2). These oxides present advantages such as extended photosensitivity in the visible region, long-term physical/chemical stability, and/or ease of preparation. WO_3, BiOI and Co_3O_4 were selected for their narrow bandgap (2.5 – 2.7, 2.1 – 2.5 and 1.6 – 2.1 eV respectively) that can be easily excited using visible light irradiation to enhance the optical properties of the fabricated composites. As supports, RGO and EG provides the easy recovery of the catalyst and enhanced interaction was achieved by functionalising the materials to minimize leaching of the metal oxide semiconductors and improve photocatalytic stability of the nanocomposites. Traditional methods of visible light enhancement in semiconductors include doping with metals or nonmetals, use of electron conducting or high surface area support materials, heterojunction formation and use of photosensitizers. Heterostructures were generated between TPP, WO_3 and EG or RGO to enhance separation of electrons and holes and improve photodegradation. The use of p-n heterostructures between Co_3O_4 and WO_3 was pioneered by the impressive ability of this heterojunctions to effectively retard photoexcited electrons and holes recombination resulting in enhanced formation of non-selective hydroxyl radicals for complete mineralisation of organic pollutants and their intermediates. Lastly, the internal intrinsic properties of BiOI in fabrication of Z-scheme heterostructure was investigated. Co_3O_4 was selected as it can easily form photoexcited electrons and holes due to its small bandgap and has multiple unoccupied energy levels due to its empty d and p orbitals (referred to as false energy levels). Moreover, crystal phase engineering of BiOI and CO_3O_4 can be achieved for enhanced photoactivity. The EG or RGO supported heterostructures were used for degradation of acid blue 25 dye that has a possibility to exist in abundance in South Africa textile industries and it is normally used as a model pollutant for degradation of anthraquinone dyes. The pharmaceuticals that were selected (DFC, IBU and TMP (trimethoprim)) have been reported to be the most detected active agents. Moreover, they are manufactured with the highest global consumption rate that is anticipated to intensify and they normally occur concomitantly in the environment hence the degradation of both TMP and IBU was studied. Therefore, different stakeholders are concerned about their accumulation and negative effects to humans and the environment. The use of heterostructures to enhance visible light

photocatalytic activity of either WO_3 or BiOI is discussed in subsequent chapters of this thesis.

CHAPTER 3
METHODOLOGY

3.0 Methodology

3.1 Introduction

This chapter presents a detailed information executed towards the synthesis of various materials and nanocomposites. Moreover, the main analytical procedures or techniques used are briefly discussed with specific information and outcomes expected from each technique. Where possible, chapters related to the use of a technique or synthesis procedure are specified.

3.2 General procedures

3.2.1 Materials and chemicals

Acid blue 25 (AB25, 45 %), ammonium hydroxide (NH_4OH, ≥ 30 %), benzoquinone (BQ, ≥ 98 %), bismuth nitrate hexahydrate ($Bi(NO_3)_2$, 99 %), cobalt (II) acetate dihydrate ($Co(AOC)_2.2H_2O$, 99 %), diclofenac sodium (DFC, 100 %), ethylene glycol (EG, 98 %), glacial acetic acid ($CH_3CH_2CH_2OH$, 98.9 %), ibuprofen (IBU, 100 %), meso-tetraphenyl porphyrin (TPP, ≥ 99 %), methanol (CH_3CH_2OH, 99 %), natural graphite flakes (NGF), nitrobenzene (NB, ≥99 %), potassium iodide (KI, 98 %), potassium permanganate ($KMNO_4$, ≥ 99 %), silver nitrate ($AgNO_3$, 99 %), sodium chloride (NaCl, 99 %), sodium hydroxide pellets (NaOH, ≥ 98 %), sodium tungstate dihydrate ($Na_2WO_4.2H_20$, 98 %), tert-butanol (t-BuOH, 99.9 %) and trimethoprim (TMP, 99.7 %) were purchased from Sigma Aldrich, (South Africa). Hexane, nitric acid (HNO_3, 55 %) and sulphuric acid (H_2SO_4, 98%) were purchased from Merck (Germany). Citric acid was purchased from pal chemicals and ethylene diamine tetra-acetic acid sodium salt (EDTA, 98.5 %) was purchased from SAARCHEM (South Africa). All reagents in this study were of analytical grade and they were used without any further purification. In addition, all aqueous solutions were prepared with deionized water (18.2 MΩ cm resistivity at 20 °C) that was obtained with a Millipore Mili-Q water purification system (Merk Millipore, Burliton, MA, USA).

3.2.2 Synthesis of exfoliated graphite

Exfoliated graphite was prepared using the method reported in literature.[128] Natural graphite flakes (above 200 µm) were treated with a mixture of concentrated sulphuric acid and concentrated nitric acid (3:1 v/v) for 48 hours before washing with distilled deionized

water until pH 7 was reached. The resulting graphite intercalated compound was air dried for 24 hours and exfoliated through heating in a furnace at 800 °C for 60 seconds to give a worm-like exfoliated graphite material with cellular structure.

3.2.3 Synthesis of tungsten (VI) oxide

Tungsten (VI) oxide (WO_3) nanoparticles were synthesised through the citric acid assisted precipitation method reported in literature.[278] In a typical procedure, almost 30 % or 40 % v/v , nitric acid solution (50 ml) was heated to 70 °C while stirring to dissolve 6.9076 g or 9.724 g of sodium tungstate dihydrate. When the salt was dissolved, 0.501 or 0.531 g of citric acid was added (as pH 1-3 buffer) to the reaction mixture keeping temperature and stirring speed constant until a yellow precipitate was formed. The reaction continued for about 2 hours to reach completion after which the solution was dried in the oven at 80 °C or 90 °C. The powder was subjected to thermal treatment at different temperature times in the furnace for {(350 °C, 4 hours), (400 °C, 3 and 4 hours) and (700 °C, 2 hours)}, respectively. The resulting cake obtained at 700 °C was ground with a pestle and mortar to a fine powder of white WO_3 nanoparticles while yellow nanoparticles were obtained at low temperatures (350 °C and 400 °C). The anticipated activation energy (∆G) mandatory to form a critical nucleus of solid radius (r) can be related to the reactant concentration by equation 3.1.[279]

$$\Delta G = \frac{16\pi\sigma^2 M^2}{3(\text{þ}RTlinS)^2} \qquad \textbf{(3.1)}$$

where σ is the interfacial tension between the precipitate and its surroundings, þ is the precipitate density, M is the molecular weight of the precipitate, and S is the supersaturation. The rate of precipitation can be explained based on the activation energy such that a positive value of (∆G) is necessary, the magnitude of which determines the rate of formation of WO_3 derived from the equation ($Na_2WO_4 + HNO_3 + H_2O \rightarrow WO_3 + 2Na^+ + NO_3^-$). Therefore, the rate of formation of WO_3 depends on both the concentration of nitric acid and the concentration of the tungstate precursor salt used.

3.2.4 Synthesis of reduced graphene oxide

Reduced graphene oxide method was developed from synthesis of tungsten (VI) oxide (**Section 3.2.3**) and literature.[280] 100 ml 0f 30 % (v/v) concentrated nitric acid was placed in a beaker and heated to 70 °C. 0.6 g of prepared exfoliated graphite was added under constant temperature and magnetic agitation and 1 g citric acid was added as a buffer (pH

1-3). The reaction continued for 3 hours or until the liquid was little and dried in an oven at 80 °C before heating at 350 °C for 4 hours in furnace. The thin layer reduced graphene oxide is formed collected and stored for further characterisation.

3.2.5 Synthesis of cobalt (II,III) oxide

Cobalt (II,III) oxide was synthesised by simple thermal decomposition of cobalt acetate tetrahydride in air at 500 °C for 3 hours.[281] The obtained dark solid was washed two times with ethanol, then deionized water to remove unreacted acetate and cobalt ions under centrifugation. Subsequently, the product was then dried in an oven at 90 °C for 12 hours. Another method employed for cobalt oxide spinel (Co_3O_4) was the pH assisted quick precipitation method. In this method, a 100 ml purple solutions of cobalt acetate tetrahydrate (0.01 M, 0.02 M and 0.03M) was prepared by mixing it vigorously with water (100 ml) and 1 ml glacial acetic acid in a closed conical flask at 120 °C. When the mixture exhibited a blue colour, 30 % NH_4OH was added dropwise until a black precipitate was formed (75 minutes). After cooling, the black precipitate was collected by centrifugation, washed with water then ethanol and dried in oven at 90 °C for 8 hours.

3.2.6 Synthesis of bismuth oxyiodide

Bismuth oxyiodide was synthesised through the microwave assisted precipitation method.[282] In a typical synthesis method, bismuth nitrate hexahydrate (8 mmol) was dissolved in ethylene glycol (40 ml) with magnetic stirring at room temperature to form a clear solution, named solution A. Solution B was achieved by dissolving potassium iodide (8 mmol) in ethylene glycol (40 ml). Then solution B was added dropwise into solution A at room temperature and under magnetic agitation. The resulting solution was stirred vigorously for 24 hours before being subjected to hydrothermal synthesis in a microwave chemical reactor (SynthWAVE single Reaction Chamber Microwave Synthesis System with Magnetic stirrer and water-cooled condenser) at a temperature of 160 °C, power of 1000 W and pressure of 170 bar for 20 minutes. After cooling the autoclave to room-temperature, the solution was centrifuged to obtain a yellowish precipitate. The obtained solid was washed three times with deionized water followed by absolute ethanol. Thereafter, the solid material was dried at 70 °C for 24 hours in an oven.

3.2.7 Synthesis of TTP/WO_3/EG

The preparation of the composite material (wet-impregnation)[283] involved the combination of between tetraphenyl porphyrin, tungsten (VI) oxide and exfoliated graphite 50 ml of 70 % methanol was mixed with 0.2 g of exfoliated graphite. Then, 5 ml of concentrated nitric

acid was added under mild heating (70 °C) and vigorous stirring whereby the colour of the mixture changes to red. After 15 minutes, 0.2 g of WO_3 nanoparticles and different percentages of TPP (0, 0.1, 0.5 and 1 % mol/mol of WO_3) were added. The reaction endured for 2 hours under similar conditions. The colour changed to brownish grey when the reaction is complete. The mixture was transferred into an oven and allowed to dry at 90 °C for 48 hours and then calcined at 400 °C for 3 hours in a furnace to give a flowery, buoyant and shiny composite. The method is summarized in Figure 3.1

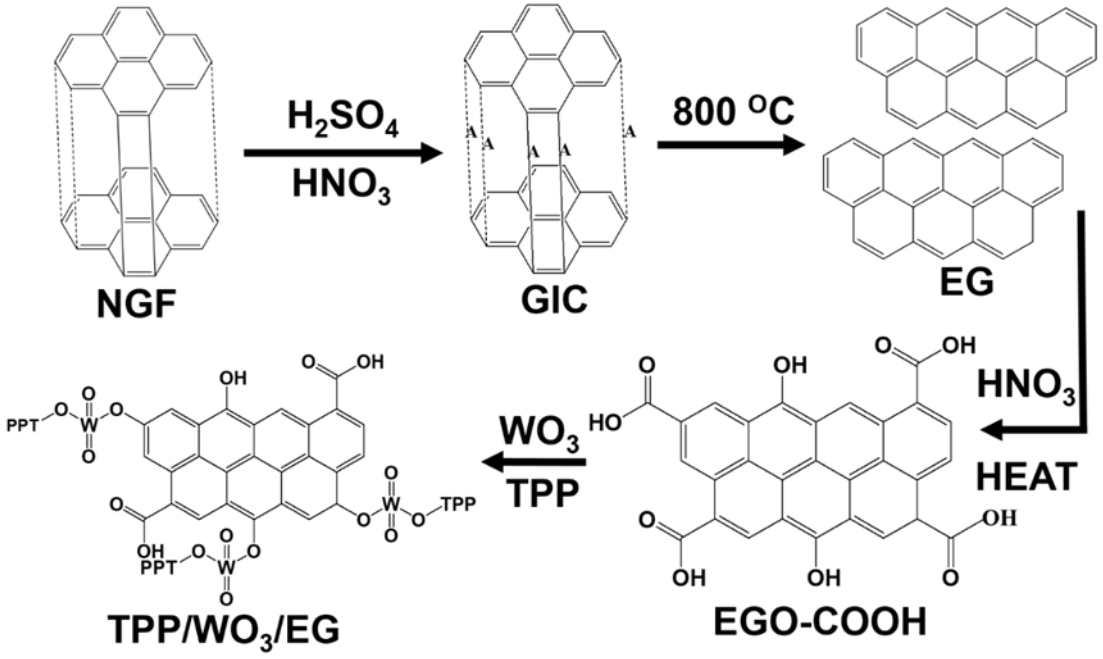

Figure 3.1: The Schematic presentation of the composites by wet impregnation (Chapter 5)

In Figure 3.1, A represents the intercalating species (HSO_4^-). Addition of nitric acid to EG will result in functionalised EG oxide with some carboxylic acid groups attached on its edges and basal planes. The degree of interaction between EG and TPP/WO_3 depends on the amount of TPP and/or WO_3 and occurs through bond formation between the OH groups on the edges and basal planes of EG and the W–O–H of functionalised WO_3, the OH and the NH groups of TPP, resulting in the formation of CONH groups on the composite.

3.2.8 Synthesis of TPP/WO_3/RGO

The in-situ synthesis of the tetraphenyl porphyrin, tungsten (VI) oxide and reduced graphene oxide (TPP/WO_3/RGO) composite was derived from the synthesis of WO_3 nanoparticles. In a typical synthesis, 3.0 g of sodium tungstate dihydrate was dissolved in 30 % v/v, nitric acid solution (50 ml) at 90 °C while stirring to give a pale-yellow solution.

After complete dissolution, 0.3 g of EG and 20 mg of TPP were added and stirred for about 30 minutes. Then 0.5 g of citric acid was added to the reaction mixture. The temperature was maintained while the solution was being stirred for at least 2 hours to monitor the colour changes from dark brown to yellow. The solution was dried in an oven at 80 °C overnight and then heated in a furnace at 350 °C for 4 hours, then at 400 °C and 550 °C for 3 hours to check the effect of calcination temperature on the composite. Moreover, different porphyrin amounts (0, 10, 20, 30 mg) were added to monitor its effect on the efficiency of the synthesised composites. Figure 3.2 displayed the steps involved including synthesis of EG.

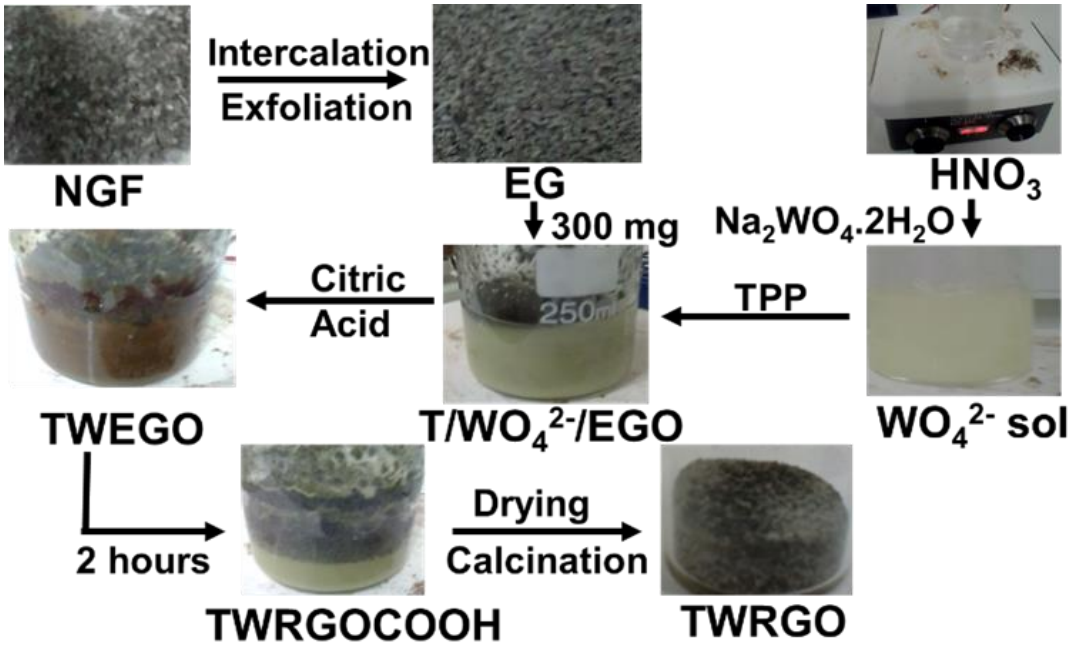

Figure 3.2: Synthesis of RGO from EG and summary of In-situ fabrication of composites (Chapter 4)

As illustrated in Figure 3.2, the functionalisation of EG and TPP materials was achieved by adding concentrated nitric acid. TPP/WO_3 formed inside the craters of EG which was first converted to exfoliated graphene oxide and then reduced to RGO layers. The reaction temperature plays an important role in enhancing the dissolution of sodium tungstate and to also catalyse the reduction of graphene oxide to reduced graphene as supported by literature. The layers are not only reduced, thus the addition of carboxylic acid groups and the OH groups for hydrogen bonding and covalent bonds caused an interaction increase between nanoparticles and the RGO. Furthermore, annealing the resulting cake removes the excess unbonded COOH groups to give an ash-like composite that does not float in aqueous media during degradation.

3.2.9 Synthesis of Co_3O_4/BiOI

In the case of Co_3O_4/BiOI, the composite material was synthesised by dispersing 0,308 g of WO_3 in 100 ml of cobalt acetate solution at pH 7 and heated at 90 °C under magnetic agitation. The pH of the solution was adjusted using 30 % ammonium hydroxide solution and a series of Co_3O_4/WO_3 were prepared by adjusting the concentration of cobalt acetate to 0.01, 0.02 and 0.03 M. Notably, the reaction was allowed to continue for 75 minutes. The subsequent solution was cooled to room temperature and the solid collected by centrifugation. The grey solid was dried in oven at 90 °C for 8 hours and labelled as CW1, CW2 and CW3 for 0.01 M, 0.02 M and 0.03 M cobalt acetate respectively. Co_3O_4 was synthesised following the same route except for the addition of WO_3 nanoparticles. Moreover, CW2 was annealed at 300 °C for 2 hours and labelled CW2A to check the effect of annealing temperature on the working nanocomposite.

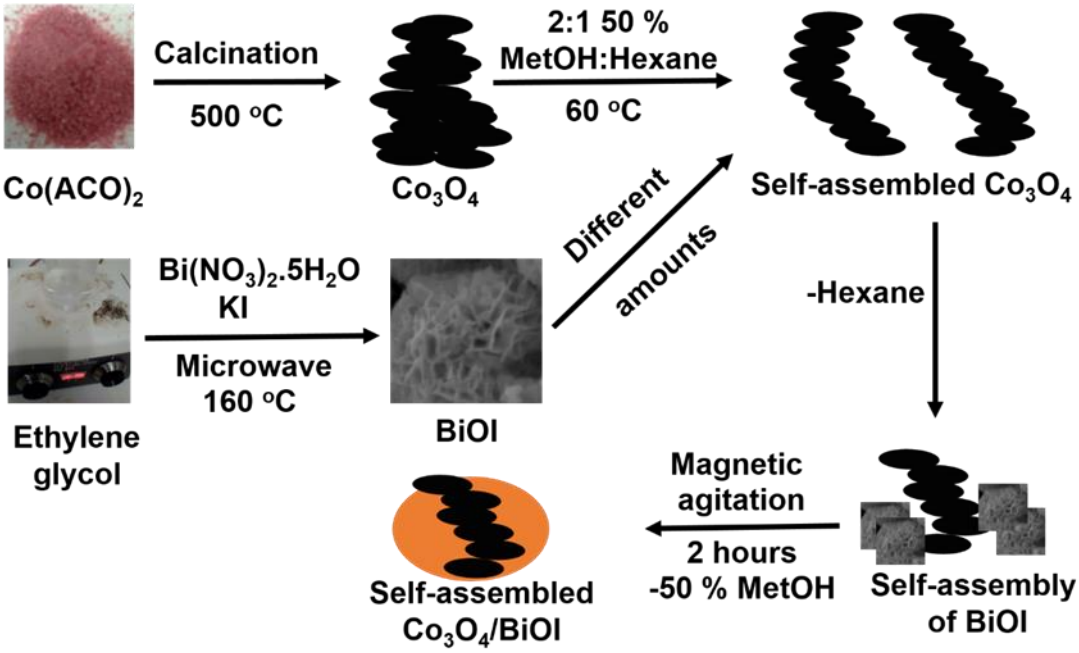

Figure 3.3: General synthesis of nanomaterials in Z-scheme heterostructure (Chapter 7)

The supernatant was discarded after centrifugation and the resulting grey solid dried in an oven at 60 °C to give pale green nanocomposites labelled as CoBi1, CoBi2 and CoBi3 for 1:1, 1:2 and 1:3 weight ratios of Co_3O_4:Bi, respectively.

3.2.10 Synthesis of Co_3O_4/WO_3

The Co_3O_4/WO_3 the composite material was synthesised by dispersing 0,308 g of WO_3 in 100 ml of cobalt acetate solution at pH 7 and heated at 90 °C under magnetic agitation. The pH of the solution was adjusted using 30 % ammonium hydroxide solution and a

series of Co_3O_4/WO_3 were prepared by adjusting the concentration of cobalt acetate to 0.01, 0.02 and 0.03 M. Notably, the reaction was allowed to continue for 75 minutes. The subsequent solution was cooled to room temperature and the solid collected by centrifugation. The grey solid was dried in oven at 90 °C for 8 hours and labelled as CW1, CW2 and CW3 for 0.01 M, 0.02 M and 0.03 M cobalt acetate respectively. Moreover, CW2 was annealed at 300 °C for 2 hours and labelled CW2A to check the effect of annealing temperature on the working nanocomposite.

3.3 Photocatalytic experiments

The photocatalytic evaluations of the synthesised nanomaterials were conducted using a solar simulator (Chapter 4 and 5) and a batch like reactor setup using a Philips 60 W LED lamp with a cut-off wavelength of 420 nm (Chapter 6 and 7). The solar simulator used was HAL-320 with compact xenon lamp light source purchased from Japan. In a typical experiment, a box was used to cover the solar simulator lamp and generate a small dark room to shield external light such that the only source of light comes from the solar simulator lamp or LED lamp appearing from the top of the box. 50 ml of a pollutant (5 – 50 ppm) was measured and placed in 100 ml beaker and placed inside the solar simulator generated light shield on a magnetic stirrer and an insulator cloth was placed between the beaker and the stirrer to minimize heat transfer. A known amount (10 – 50 ppm) of the photocatalyst was weighed and mixed with the pollutant through magnetic agitation in the dark so as the pollutants and the photocatalyst could reach adsorption-desorption equilibrium. After specific time intervals (20 and 30 min), the sample is taken and denoted as the initial concentration before degradation and light is illuminated on the sample, the distance between the lamp to the solution is adjusted to a known value, the mixture of catalyst and pollutant is illuminated with radiation from the lamp and sampling is done at specific time intervals. The aliquots were filtered using Millex-LH syringe filters (0.45 µm) or PALL (0.45 µm) GPH ACR DISC 13 syringe filters and then analysed using UV/Vis spectrometer from 350 nm to 750 nm (Chapter 4 and 5) and between 200 nm – 350 nm (Chapter 6 and 7) after standards were prepared to determine the wavelength of maximum absorption (602 nm) of the selected pollutants (acid blue 25, diclofenac sodium, trimethoprim and ibuprofen). TOC was used to monitor their differences with respect to radiation time and HPLC was used to determine reaction intermediates.

3.4 Instrumentation

The equipment used for FTIR measurements was a PerkinElmer FTIR with a detector and KBr was mixed with the solid samples using mortar and pestle. PerkinElmer UV/Vis/NIR

spectrometer Lambda 1050 (South Africa) and PerkinElmer UV/Vis spectrometer Lambda 650 (South Africa) was employed to analyse the absorption properties of the solid nanomaterials (in the range of 200 - 800 nm) to determine their bandgaps using $BaSO_4$ as reference. The TEM machine employed in this research study was FEI Tecnai G220 (Netherlands). Raman results for all the synthesised nanoparticles and the composite were obtained using Raman low power TS-150 (South Africa) with a laser power of 532 nm wavelength. The results of PL results were obtained from HORIBA Flourolog 3 FL-1057 (South Africa) equipped with an S1-PMT detector using 450 W xenon lamp as the excitation source at 325 nm and in the range of 350 - 600 nm. TGA curves and derivatives data was done using Thermogravimetric analyser Pyris 1 TGA (USA). The SEM/EDS experiments were performed using JEOL JSM-IT300 and JSM-7800F (China). XRD analysis were performed on Rigaku SmartLab X-Ray Diffractometer (South Africa) equipped with Cu K_α x- ray wavelength radiation of 0.15418 nm with a voltage and current of 45 kV and 200 mA, respectively. Diffraction patterns were recorded from 2θ of 5 to 90°. Surface area analysis (BET) was achieved using micromeritics Trista II Surface Area and Porosity analyser (USA) after degassing the samples at 180 °C for 12 hours using micromeritics VacPrep 061 sample degas system (USA). PerkinElmer UV/Vis spectrometer Lambda 650 (South Africa) was used to monitor degradation efficiency of pollutants (acid blue 25, diclofenac sodium, trimethoprim and ibuprofen) at different time intervals. TOC measurements were obtained from TOC-V_{WP} Total Organic Carbon Analyzer (Japan). Reaction intermediates and degradation pathway of DFC was studied with HPLC-QTOF-MS using Dionex ultimate 3000 ultrahigh performance liquid chromatography (USA) coupled to impact II Quadrupole time of flight tandem mass spectrometer (Germany).

3.4.1 Scanning electron microscopy (SEM)

SEM is an instrument used for observing and analysing the surface microstructure (size and morphology of nanoparticles) of a bulk sample using a finely focused beam of energetic electrons.[284] An electron-optical system is used to form the electron probe which is scanned across the surface of the sample. There are various signals generated through the interaction of this beam with the sample. These signals are collected by appropriate detectors. The signal amplitude obtained at each position in the raster pattern is assembled to form an image.[284] The electrons interacting with the solid are affected by elastic scattering, due to the electrostatic interaction with the atomic nuclei, and inelastic scattering due to the interaction with the atomic electrons.[284,285] Elastic scattering is an interactive process which results in the fact that the direction of the basic electrons

changes without any obvious energy loss. Since the electron beam leaves the sample (the process called "backscattering"), the elastic scattering can give important information for the SEM image about the topology and morphology of the nanoparticles.[286] In this study, SEM was used to give an image of the synthesized materials in the micro-scale. The images were used to illustrate the surface microstructure that is used to predict the arrangement of the particles. Moreover, it gave information about the morphology and aggregation of the particles of the synthesized material.

3.4.2 Transmission electron microscopy (TEM)

High-resolution transmission electron microscopy (HRTEM) is an imaging mode of the transmission electron microscope (TEM) that allows for direct imaging of the atomic structure of the sample.[287,288] This is better understood by considering a very thin slice of crystal that has been tilted so that a low-index direction is exactly perpendicular to the electron beam. All lattice planes parallel to the electron beam will be close enough to the Bragg position and will diffract the primary beam. The diffraction pattern is the Fourier transform of the periodic potential for the electrons in two dimensions. In the objective lens all diffracted beams and the primary beam are brought together again; their interference provides a back-transformation and leads to an enlarged picture of the periodic potential. This picture is magnified by the electro-optical system and is finally seen on the screen at atomic magnifications.[287] HRTEM is a powerful tool to study properties of materials on the atomic scale, such as semiconductors, metals, nanoparticles and sp2-bonded carbon (e.g., graphene, C nanotubes).[288] However, many materials require extensive sample preparation to produce a sample thin enough to be electron transparent, which makes TEM analysis a relatively time consuming process with a low throughput of samples[289,290] and the structure of the sample may also be changed during the preparation process.[290] The field of view is relatively small, raising the possibility that the region analysed may not be characteristic of the whole sample, and there is a potential of sample damage by the electron beam, particularly in the case of biological materials. Hence in this study, TEM was used to determine the crystal structure, particle sizes and shapes, as well as the morphology and agglomeration of the synthesized nanomaterials.

3.4.3 Energy dispersive spectroscopy (EDS)

EDS is an analytical technique used for the elemental chemical characterization of a sample and relies on an interaction of some source of x-ray excitation on a sample. Its characterization capabilities are due to the fundamental principle that each element has a unique atomic structure allowing a unique set of peaks on its electromagnetic emission

spectrum.[291] The sample to be studied is focused with a high-energy beam of charged particles such as protons or electrons, or a beam of x-rays to stimulate the emission of characteristic x-rays from a specimen. The incident beam may excite an electron in an inner shell, ejecting it from the shell while creating a hole where the electron was. An electron from an outer, higher-energy shell then fills the hole, and the difference in energy between the higher-energy shell and the lower energy shell may be released in the form of an x-ray.[287] The number and energy of the x-rays emitted from a specimen can be measured by an energy-dispersive spectrometer[291,292] even though it has numerous limitations. Hence, EDS experiments were performed to confirm the presence of various elements involved in all the as-prepared nanomaterials.

3.4.4 X-ray diffraction spectroscopy (XRD)

X-ray diffraction is the most important technique for crystal structure analysis and is mostly used for determining the internal structure and provides details about electron distributions in the molecule, bond length, bond angle, etc.[287,293] The X-ray diffraction process is non-destructive, and it is conveniently used for routine analysis. XRD analysis is based on constructive interference of monochromatic X-rays and a crystalline sample: The X-rays are generated by a cathode ray tube, filtered to produce monochromatic radiation directed toward the sample. When X-rays interact with a solid material, the scattered beams reinforce each other in few directions due to the regular arrangements of atoms in the crystal structure.[294] This constructive interference results in diffraction patterns when conditions satisfy Bragg's Law ($n\lambda=2d \sin \theta$).[287,295] This law relates the wavelength (λ) of electromagnetic radiation to the diffraction angle (θ) and the lattice spacing (d) in a crystalline sample. The randomly oriented crystals in nanocrystalline materials cause broadening of diffraction peaks. As a primary characterization tool for obtaining critical features such as crystal structure, crystallite size, and strain, x-ray diffraction patterns have been widely used in nanoparticle research.[289] XRD was used in this study as the id of the crystallinity of the synthesised material and determination of phases of the material or the crystalline form. Moreover, the average size of the particles will be determined from the XRD spectra.

3.4.5 Fourier-transform infrared (FTIR) spectroscopy

Infrared spectroscopy is a technique used to probe molecular vibrations or identification of certain functional groups in a molecule. Infrared spectroscopy analysis is possible since atomic bonds in molecules have specific frequencies of internal vibrations that can be used as finger prints of different functional groups present and the vibrations occur in the

infrared region of the electromagnetic spectrum (4000 cm^{-1} to 200 cm^{-1}).[296] A sample that is exposed to a beam of infrared radiation will absorb radiation at frequencies corresponding to present vibrations between atoms in the molecule and transmit all other frequencies such that the absorbed radiation frequencies are measured or detected by the infrared spectrometer to give a plot of absorbed energy vs the frequency known as the infrared spectrum of the material.[296,297] The absorption of infrared (IR) energy to higher excited energy state result in different vibrations of bonds between atoms such as bending, rocking, out-of-plane deformation, wagging and stretching that occur at specific frequencies or wavenumbers in the IR region of the light spectrum.[297] The substance identification is possible as the infrared spectra of different materials is a characteristic of the different vibrations occurring and the magnitude of the absorption is related to the species concentration.

When a molecule has a centre of symmetry, all symmetrical vibrations are infrared inactive while asymmetric vibrations of all molecules are IR active and it lacks selectivity such that all IR active chemical groups in a sample will be detected and polar bonds or groups with permanent dipole moment have strong IR absorptions.[298] In a nutshell, not only the type of chemical bonds but also the present atoms give rise to vibrational frequencies in specific regions with different intensities. Infrared (IR) or FTIR spectroscopy has massive applications ranging from the analysis of small molecules or molecular complexes to the study of cells or tissues. FTIR spectroscopic studies were successfully conducted in medical applications for monitoring drug release and to differentiate between healthy and cancerous cells.[299–301] In addition, FTIR has been successfully employed to investigate growth of cell walls in plants, confirm identity of pure molecules or identify contaminants, predict physical properties of polymers and investigate the efficiency of modifications of their surfaces.[302,303] FTIR was used to validate molecular fingerprint of the synthesised nanomaterials.

3.4.6 Raman spectroscopy

Raman spectroscopy is a spectroscopic technique used to observe vibrational, rotational, and other low frequency modes in a system. It is the shift in wavelength of the inelastically scattered radiation that provides the chemical and structural information, and provides the fingerprint by which molecules can be identified.[304–306] It relies on inelastic scattering, or Raman scattering, of monochromatic light, usually from a laser in the visible, near infrared or near ultra-violet range [287]. The laser light interacts with molecular vibrations, phonons or other excitations in the system, resulting in the energy of the laser photons being shifted

up or down.[304] The shift in energy gives information about the vibrational modes in the system and is classified as structural fingerprints of the molecules that are present.[307] The vibrational frequency and position of Raman band is very sensitive to the orientation of the bands and weight of the atoms present at either end of the bond.[304,306] Raman shifted photons can be of either higher or lower energy, depending upon the vibrational state of the molecule under study. Since the shifts in Raman spectra are structural fingerprints, Raman spectroscopy was used in this research to determine the crystal structure and the chemical bonds of all the synthesized nanomaterials.

3.4.7 Brunauer-Emmet-Teller (BET) analysis

BET theory explains the physical adsorption of gas molecules on a solid surface and serves as the basis for the measurement of the specific surface area of materials. The BET theory applies to systems of multi-layer adsorption because the true surface area, including surface irregularities and pore interiors, cannot be calculated from particle size information, but is rather determined by the adsorption of an inert or unreactive gas.[308] Nitrogen is the most commonly employed gaseous adsorbate used for surface probing by BET methods hence the analysis is often conducted slightly above the boiling temperature of N_2 (77 K).[308,309] The amount of gas adsorbed is a function not only of the total amount of the exposed surface, but also (i) temperature, (ii) gas pressure and (iii) the strength of interaction between gas and solid.[308–310] Increase in gas pressure increases amount of gas adsorbed on the surface (in a non-linear way) and adsorption of a cold gas continues even after it has covered the surface in a complete layer one molecule thick.[310] Multilayers are formed as the relative pressure of the gas increase until it reaches equilibrium where no gas adsorption occurs.[311] Because the interaction between gaseous and solid phases is usually weak, the surface is cooled using liquid N_2 to obtain detectable amounts of adsorption. Prior to determining the specific surface area of the sample, it is necessary to remove gases and vapours that may have become physically adsorbed onto the surface after synthesis and during treatment, handling and storage.[312,313] Outgassing of many substances is often achieved by applying a vacuum, or by purging the sample in a flowing stream of a non-reactive, dry gas, or by applying a desorption-adsorption cycling method, sometimes at elevated temperature to increase the rate at which the contaminants leave the surface of the sample.[312] Data is obtained by passing (for adsorption) or removing (for desorption) a known amount of adsorbing gas from known amount of the material to be characterised in a sample cell maintained at constant temperature (slightly higher than 77 K).[313] BET analysis was used in this research to obtain the specific surface area of

synthesized nanomaterials, pore volume and pore size distribution. The data showed the BET adsorption isotherm type the material represents.

3.4.8 Thermogravimetric analysis (TGA)

Thermogravimetric analysis uses heat to induce chemical and physical changes in materials and performs a corresponding measurement of mass change as a function of temperature or time.[313] A thermo balance is used to measure the mass change of a sample as a function of temperature or time, under a defined and controlled environment with respect to heating rate, gas atmosphere/pressure, flow rate, crucible type, etc.[314,315] Thermal stability is widely dependent on the type of material being investigated, and major decomposition mechanisms for different materials can occur over wide temperature ranges.[315] This is advantageous in composition analysis of multicomponent materials as each component can be individually decomposed in a stepwise fashion to quantitatively determine the amount of each component in the material. In this report, TGA was used to obtain information about the type of material under investigation, the thermal stability of materials was obtained and their decomposition temperatures.

3.4.9 Photoluminescence (PL) spectroscopy

Photoluminescence is a contactless, non-destructive method of probing the electronic structure of materials widely used for characterization of the optical and electronic properties of semiconductors and molecules.[316] In chemistry, it is more often referred to as fluorescence spectroscopy, but the instrumentation is the same. The relaxation processes can be studied using Time-resolved fluorescence spectroscopy to find the decay lifetime of the photoluminescence.[316–318] These techniques can be combined with microscopy, to map the intensity (Confocal microscopy) or the lifetime (Fluorescence-lifetime imaging microscopy) of the photoluminescence across a sample. Light is directed onto a sample, where it is absorbed and imparts excess energy into the material in a process called photo-excitation.[319] One way this excess energy can be dissipated by the sample is through the emission of light, or luminescence. In the case of photo-excitation, this luminescence is called photoluminescence.[316] Photo-excitation causes electrons within a material to move into permissible excited states. When these electrons return to their equilibrium states, the excess energy is released and may include the emission of light (a radiative process) or may not (a nonradiative process). The energy of the emitted light (photoluminescence) relates to the deference in energy levels between the two electron states involved in the transition between the excited state and the equilibrium state.[316,319] The quantity of the emitted light is related to the relative contribution of the radiative

process. In this research, PL was used to survey the separation efficiency of the photogenerated charge carriers in the semiconductors. The higher the PL intensity the bigger the probability of charge carrier recombination.

3.4.10 Ultraviolet-Visible light spectroscopy (UV-Vis)

UV-Vis use light in UV and visible part of the electromagnetic spectrum to effect the excitation of electrons in the atomic or molecular ground state to higher energy levels, giving rise to an absorbance at wavelengths specific to each molecule or material.[320–322] Molecules or semiconductors containing π-electrons or non-bonding electrons can absorb the energy in the form of ultraviolet or visible light to excite these electrons to higher anti-bonding molecular orbitals.[92,111] Molecules with easily excited electrons (i.e. lower energy gap between the highest occupied molecular orbital (HOMO) and the lowest unoccupied molecular orbital (LUMO)), absorb longer light wavelength in the UV-Vis range on the electromagnetic spectrum.[111] UV-Vis is a common and well established analytical technique because compared to other techniques, it is simple, versatile, quick, accurate and cost-effective.

In a UV-VIS spectrophotometer a light source emits light at all wavelengths of the UV and visible spectrum. The light is collimated and focused on an entrance slit, and then falls on a monochromator, that separates the white light in its constituent wavelengths.[322] From the monochromator the light is sent through the sample, and finally reaches a photocell that measures the intensity of the light at each specific wavelength. The intensity of the light reaching it is measured and recorded as the absorbance A or the Transmission T (or %T). UV-Vis is both a qualitative and quantitative technique. The wavelengths of absorption peaks can be correlated with the types of bonds in a given molecule and give qualitative information valuable in determining the functional groups within a molecule/sample.[111] Quantitatively, Beer-Lambert law states that the absorbance (A) of a solution is directly proportional to the concentration (c) of the absorbing species in the solution and the path length (L).[320]

$$A = \varepsilon cL \qquad (3.2)$$

Where ε is the absorption coefficient and A is calculated as ($A = \log10 (I_0/I)$, where I_0 is the intensity of light before it enters sample, and I is the intensity of light after it passed through the sample. Thus, for a fixed path length, UV/Vis spectroscopy can be used to determine the concentration of the analyte in a solution.[175]

The qualitative analysis of semiconductor materials using UV-Vis is achieved by using the UV-Vis diffuse reflectance spectrum to find the reflectance (R) of the material and the data can be can be transformed to the Kubelka-Munk function F (%R) from the % R or the UV-Vis equipment may allow obtaining the values of Kubelka-Munk function.[92] The electronic structure of semiconductor crystallites shows a three dimensional size effect in nanoscale which can be measured by UV-Vis absorption spectroscopy. The determination of the optical bandgap using Tauc relationship is expressed by Equation 3.3.[322]

$$\alpha h\nu = A\,(h\nu - E_g)^n \qquad (3.3)$$

Where α is absorption coefficient, h is planks constant, v is photon frequency, A is a constant and E_g is the optical bandgap. In crystalline semiconductors, where crystal momentum is conserved and electron transitions obey well-defined selection rules, n is 1/2, 3/2, 2, and 3 when the transitions are direct-allowed, direct-forbidden, indirect-allowed, and indirect-forbidden, respectively.[111,320] On the Tauc plot of $(\alpha h\nu)^n$ as y axis versus photon energy (hv) on the x axis in its linear region, at Y = 0, extrapolating to the X-axis will give the bandgap of the material.

UV-VIS will be used to determine whether the synthesized nanomaterials absorb energy in the visible spectrum as the wavelength at which the materials absorb will generally show if it absorbs visible light which is between 390 nm and 700 nm. The wavelength of maximum absorption will be determined, and the absorption edge will be used to calculate the bandgap of the nanocomposites for qualitative analysis. The UV-VIS will also be used to determine the rate constant of degradation experiments and find the rate constant even though it cannot be trusted with highly intense materials if the absorption is nearly 100 % or mixed matrix absorbing pollutants which is normally the case in surface waters. It will be used for quantitative analysis of the degradation experiments to determine the amount of pollutant still available at given time. From the UV-Vis spectra, a concentration of the material can be calculated from the sample. In this research study, PerkinElmer UV/Vis spectrometer Lambda 650 was used for monitoring degradation experiments of synthetic samples and some materials characterisation (Chapter 6 and 7) while PerkinElmer UV/Vis/NIR spectrometer Lambda 1050 was used to analyse the absorption of the solid nanomaterials to determine their bandgaps using barium sulphate, $BaSO_4$, standard (Chapter 4 and 5).

3.5 TOC

The possible organic carbon compounds are diverse and the quantitative determination of individual organic components of natural and anthropogenic origin is not always possible making it obligatory to bank on the measurement of total quantities where total organic carbon (TOC) is one of them. TOC is the amount of carbon found in an organic compound and is often used as a non-specific indicator of water quality and it may also refer to the amount of organic carbon in soil, or in a geological information, particularly the source rock for a petroleum clay.[323–325] In general, carbon is present in two forms: inorganic (IC) and organic carbon (OC).[323] TOC is independent of the oxidation state of the organic matter and does not measure other organically bound elements, such as nitrogen and hydrogen, and inorganics that can contribute to the oxygen demand.[323] The TOC applications include indication of water contamination by synthetic organic compounds, chemical characterization and degree of humification of wastes, estimation of carbon content of soil, carbon cycling of soil; and carbon fluxes in aquatic systems.[324] A typical analysis for TOC measures both the total carbon present and the so-called "inorganic carbon" (IC), the latter representing the content of dissolved carbon dioxide and carbonic acid salts. Subtracting the inorganic carbon from the total carbon yields TOC.[323,326] In this research study, TOC was used to confirm that degradation occurred and not only decolourisation to some coloured pollutants and that the catalyst achieved degradation of the pollutants to less hazardous organic pollutants during the degradation experiment at a given sampling time. This is achieved since as the material gets degraded into soluble organic compounds, water and carbon dioxide, the total organic carbon content is reduced and will be detected by the TOC analyser.

3.6 HPLC - QTOF - MS

High performance Liquid Chromatography is an analytical separation technique that involves the high-pressure flow of a liquid (mobile phase) through a column that contains the stationary phase (Liquid or solid) and a mixture of compounds that are injected at one end separates as they pass through the column.[327] The separated compounds are detected electronically as they elute at the other end of the column by different techniques and Quadrupole time of flight mass spectroscopy was used for detection of analytes in this report. Quadruple time-of-flight (Q-TOF) mass spectrometers have been suggested as suitable analytical tools for the identification of metabolites.[327,328] High-pressure liquid chromatography (HPLC) was developed in the 1970s for quantitative separation and identification of a complex mixture of analytes. HPLC greatly expands the range of possible analytes with analysis of compounds range of molecular weights to less than one

million Daltons. Chromatographic resolution is influenced mostly by selectivity term which depends on the appropriate choice of the mobile and stationary phase systems. Moreover, dispersion that is influenced by separation efficiency of the column and retention also contribute to chromatograph resolution. Chromatographic peaks should possess Gaussian profiles in the optimal case and are characterised by retention time, peak parameters (symmetry, height, width) and standard deviation. High performance liquid chromatography−quadrupole time of flight-mass spectrometry (HPLC−QTOF-MS) is a converted profiling technique for metabolites due to high sensitivity and selectivity coupled with structural elucidation for quantitative and qualitative analysis of infinitely small levels of analytes.[328–330] This feature prompted the selection of this technique for qualitative determination of degradation intermediates during degradation of diclofenac sodium (Chapter 6).

3.7 Degradation kinetics

The emphatic understanding of reaction kinetics is of paramount importance in photocatalysis that govern the design and engineering of photocatalytic applications in large scale for optimum performance. Chemical reaction rates are governed by the temperature of the reaction, state of the reactants (gas, liquid or solid), catalyst use and the available surface area of the reactants[163,331] and they are modelled by the law of mass which mathematically express the relationship between the proportional dependence of the reaction rate with concentration into a rate law and the constant of proportionality is termed rate constant.[332] The rate law for elemental reactions can be easily deduced from the balanced reaction equation while the rate law of a multi-step reaction is unswerving consequence of sequential elementary steps that establish the reaction mechanism and provides the best tool for determining an unknown reaction mechanism.[333] For multi-step reactions, the rate law, the rate constant, and the reaction order are determined experimentally by monitoring the change in concentration of a reactant with time during the reaction, and the orders are not generally the same as the stoichiometric coefficients in the reaction equation.

The overall rate laws for a reaction may contain reactant, product and catalyst concentrations and the rate of degrading organics is determined by the change in concentration of the reactant with respect to time and different kinetics models have been used to describe it such as the Eley–Rideal model, Alberty-Hammes-Eigen's model, the Langmuir-Hinshelwood model, the Deal–Grove model, Laminar finite rate model, Eddy dissipation and dissipation concept models and the Chou's model, etc. The Langmuir-Hinshelwood (L-H) model is the commonly used model for degradation of organics as it

effectively and efficiently articulates rate constants for most degradation experiments.[332,334] It relates the rate of degradation (r) and concentration of reactant (C) at a given time (t) (Equation 3.4) with different rates involved throughout the degradation process.[331]

$$r = -\frac{dC}{dt} = -\frac{KrKadC}{1+KadC} \quad \textbf{(3.4)}$$

Where K_r is the rate constant and K_{ad} is the adsorption equilibrium constant. According to L-H model, at infinitely small initial concentrations often experienced in photocatalytic experiments[333], $K_{ad}C$ <<1 and the reaction follows the pseudo-first order equation (Equation 3.5)

$$\textbf{In } (C_0/C_t) = K_rK_{ad}t = K_{app}t \quad \textbf{(3.5)}$$

Where K_{app} is the apparent rate constant, C_0 is the initial concentration (mM) and C_t is concentration at given time during degradation. A plot of ln (C_0/C_t) versus time represents a straight line, the slope of which upon linear regression equals the pseudo-first order observed rate constant (K_{obs}). They are prefixed with pseudo- because one of the reactants is unchanged and acts as a catalyst and its concentration during reaction is constant such that the reaction is observed as pseudo–first or pseudo–second order instead of second and third order respectively.[331–333] The pseudo-second order and the zero order rate laws are summarised in table 3.1.

3.7.1 Half-life

The half-life, $t_{1/2}$, of a rate determining material in a reaction is defined as the time required for its concentration to be half the initial concentration of the material during a chemical reaction.[331] Half-life is defined with respect to a substance that is not present in excess at the start of the reaction and in photocatalysis, the half-life of the photocatalyst is important to determine its stability and efficiency for use in large scale degradation applications. Catalysts are not used up during a chemical reaction, hence the higher the half-life, the more suitable it is for photocatalytic applications as it can endure multiple photocatalytic circles since it is stable. The material that will entice must have half-life of days or several hours in photocatalytic applications. The half-life of a pseudo-first order reaction (Equation 3.6) is deduced from its rate law equation (3.4) as at half-life, $t = t_{1/2}$ and $C_t = C_0/2$. The first order equation for half-life becomes:

$$t_{1/2} = \frac{Ln\,2}{Kapp} \qquad (3.6)$$

The half-lives for reactions of various orders are obtained by substituting the values $t = t_{1/2}$ and $C_t = C_0/2$ into their rate laws as shown in table 3.1 where $k = K_{app}$.

Table 3.1: Summary of rate laws and half-life

Order	**Rate law**	**Half-life ($t_{1/2}$)**
0	$C_t = C_0 - kt$	$t_{1/2} = C_0/2k$
1	$\ln(C_0/C_t) = kt$	$t_{1/2} = \ln 2/k$
2	$1/C_t = 1/C_0 + kt$	$t_{1/2} = 1/C_0k$

The half-life of a pseudo-zero order and pseudo-second order reactions are determined by the initial concentration of the material under investigation contrary to the half-life of pseudo-first order reaction which is not affected by initial reactant concentration of the rate determining material. The half-life of the synthesised photocatalysts was determined from the equations in table 3.1 depending on the order of the reaction which was determined to be pseudo-first order.

CHAPTER 4
IN-SITU TPP/WO_3/RGO NANOCOMPOSITE FOR PHOTODEGRADATION OF AB25

4.1 Introduction

This chapter discusses the results stemming from the application of an in-situ-synthesized nanocomposite between tetraphenylporphyrin, tungsten (VI) oxide and reduced graphene oxide for degradation of acid blue 25. The detailed information on how the materials were synthesized appear on **Section 3.2.4 and 3.2.8** of the methodology. As elaborated in literature review, AB25 is a common dye in the textile industries and its presence in South African surface waters is possible. Despite the lack of work done on determination of this dye in South Africa, the processes that are used in textile industries may use it or other anthraquinone dyes making their removal from wastewaters imperative. Since AB25 has been used as a model pollutant towards elimination of this type of dyes which are difficult to degrade, it was selected for evaluation of the photocatalytic performance of the synthesized nanocomposites. Several factors reported to influence the photocatalytic activity of various MOSs,[335] include light source, properties of the solution (pH, concentration, etc.) and the properties of the catalysts.[336] The catalyst generated both the superoxide anion and hydroxyl radicals to pioneer the reactions. The TPP and RGO reduced were used to reduce the recombination of photoexcited charge carriers and correct mismatching band potentials of WO_3 for water splitting.

In this report, WO_3 nanoparticles were formed within the matrix of the reduced graphene oxide and porphyrin thin films were used to shift the absorption edge of the nanocomposite to the visible region. Moreover, the WO_3 and tetraphenylporphyrin nanoparticles formed a strong interaction with the exfoliated graphite as it was reduced to thin layers of reduced graphene oxide under mild heat catalysis in the presence of nitric acid. The method can be easily reproducible and can be considered for industrial applications.

4.2 Results and Discussion

Discussion of the results obtained with different equipment to characterise the synthesised nanomaterials and their interpretation is outlined. The application of the obtained composites was also carried out and the results are presented for degradation of AB25. The composites were named TWR and the calcination temperature of the final composite was changed from 350, 400 and 550 °C. This study was important as it gave a clear indication on the calcination temperature dependence of WO_3 nanoparticles with monoclinic favoured by low temperatures. Moreover, the calcination time was varied and provided an idea on the ideal calcination time for WO_3 nanoparticles synthesis. TOC and UV-Vis were used to determine the degradation efficiency of the composites after different time intervals.

4.2.1 SEM and EDS

The SEM morphological properties for RGO and the composites are shown in Figure 4.1. The in-situ synthesised photocatalysts calcined at different temperatures are illustrated in Figure 4.1 (a-c). As can be seen in Figure 4.1a, the morphology of the nanocomposite calcined at 350 ^oC exhibited homogeneous spherical particles and the distribution of the nanoparticles inside the matrix of RGO obtained less aggregation as the WO_3 and TPP nanoparticles form within the RGO and their distribution was nearly uniform.

PART OF THIS WORK IS PUBLISHED IN CHEMISTRYSELECT 4 (2019) 8379-8389

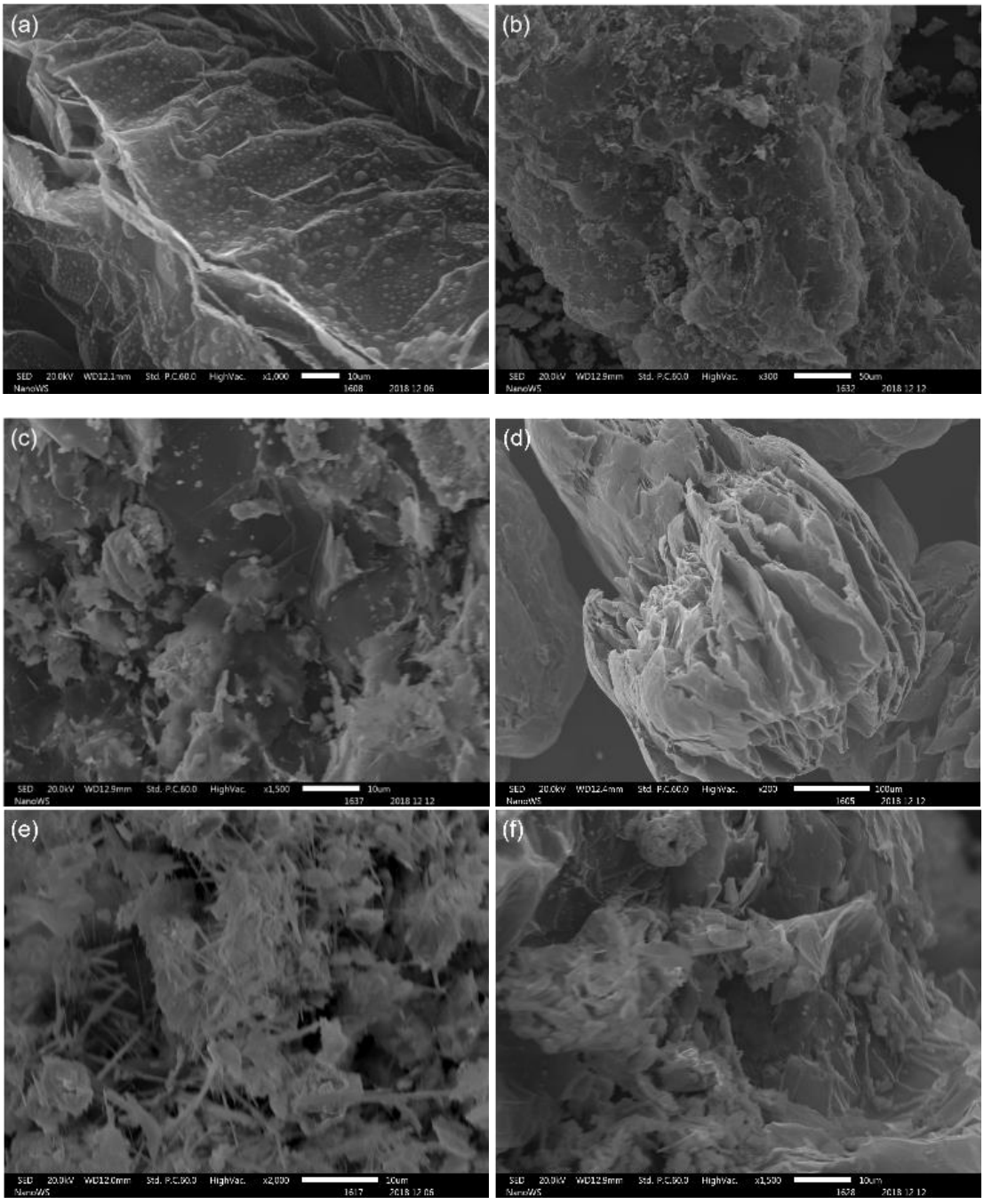

PART OF THIS WORK IS PUBLISHED IN CHEMISTRYSELECT 4 (2019) 8379-8389

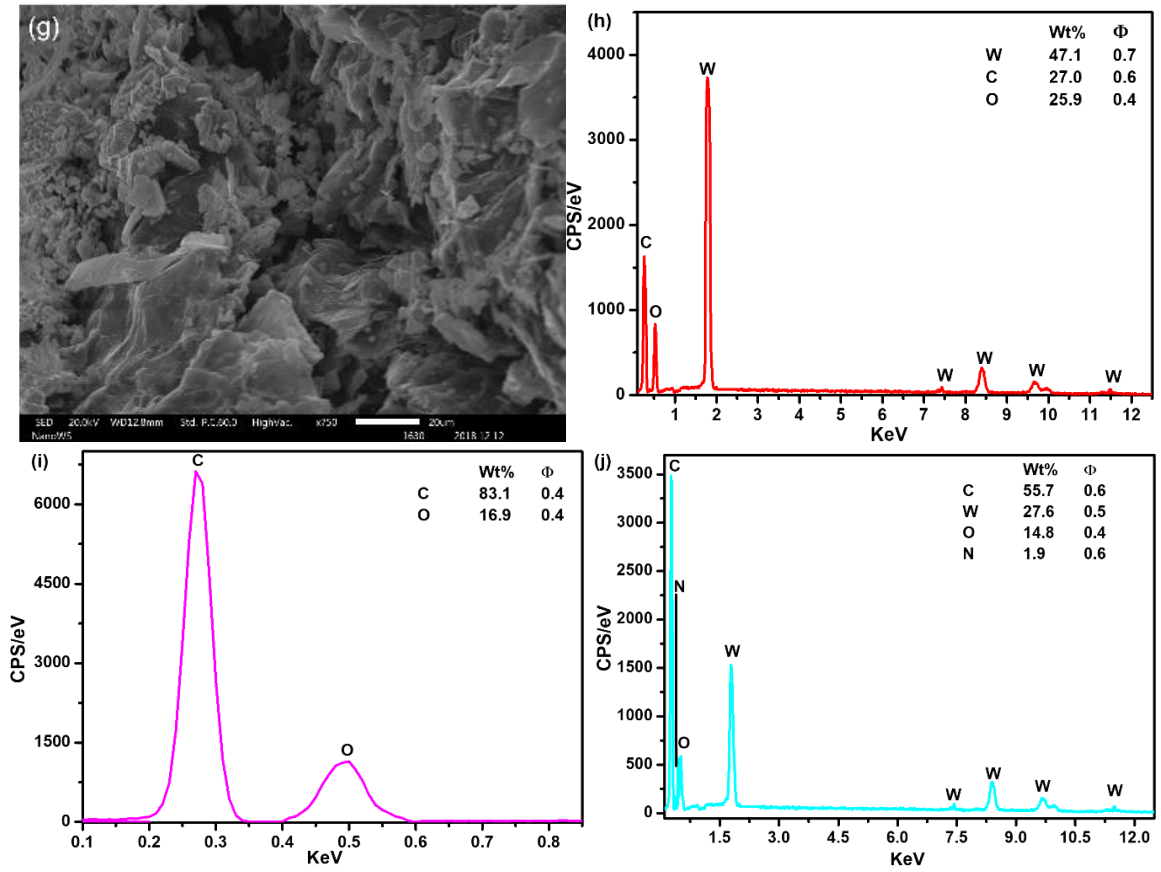

Figure 4.1: SEM images of (a) TWR3 (350), (b) TWR3 (400), (c) TWR3 (550), (d) RGO, (e) TWR1 (350), (f) TWR2 (350), (g) TWR4 (350) and EDS spectra of (h) WO_3, (i) RGO and (j) TWR3 (350)

The SEM results for the catalyst calcined at 400 °C is shown by Figure 4.1 (b) and has uneven distribution of the nanoparticles. It can be observed that increased catalyst calcination time improves the shape and distribution of the nanoparticles. Figure 4.1 (c) shows SEM results for the catalyst calcined at 550 °C. The particles were formed in different sizes and shapes unlike the improved morphology observed at lower calcination temperatures. The nanoparticles were more aggregated and showed rod-like morphologies when the catalyst was calcined at 550 °C compared to the catalyst calcined at 400 °C showing that TPP presence also influenced their morphology. The distinctive puffed-up structure of RGO (Figure 4.1 (d)) shows that it can be a host for small nanoparticles which can be accommodated in the numerous openings of the material. Thin layers of the RGO are seen from the image as supported by literature.[337] The RGO material consists of randomly aggregated, thin, crumpled sheets closely associated with each other and forming a disordered solid. SEM imaging suggested, that these RGO sheets are electrically conductive as they were analysed without coating and did not show any charging. Anchoring WO_3 on the RGO (Figure 4.1 (e)) resulted in aggregated rods

and 2D sheets of WO_3 with different sizes. However, addition of TPP (Figure 4.1 (f)) reduced particle aggregation and introduced spherical nanoparticles with increased homogeneity. Furthermore, increasing the TPP precursor amount to 20 mg resulted in a much improved nanocomposite morphology and reduced particle aggregation (Figure 4.1 (a)). However, with further increases in TPP precursor amount the particle distribution starts to deteriorate (Figure 4.1 (g)). Generally, optimum amount of TPP (20 mg) improves the morphology and reduces aggregation of nanoparticles on the surface and inside the craters of RGO. EDS gives information about the different elements present in a sample and their quantity. The EDS spectra of WO_3 confirms its formation, with W, O and C (from carbon tape) peaks (Figure 4.1 (h)). RGO spectra (Figure 4.1 (i) has only C and O peaks confirming that it is sulfur free and TWR3 (350) has the presence of N peak which proves the TPP presence (Figure 4.1 (j)) and shows the C, O, and W peaks. The amount (weight %) of W peak in the composites was affected by calcination temperature and TPP composition.

4.2.2 Raman

Raman spectroscopy was used as a fingerprint of bonding between different functional groups that are present in a molecule or composite. The Raman spectrum of WO_3 (Figure 4.2 (a)) confirms the formation of crystalline WO_3 monoclinic and hexagonal phases as supported by literature.[186] The W–W bond is identified near 187 cm^{-1} wavenumbers; however, the intensity varies because of the crystallinity of WO_3 nanoparticles which is influenced by porphyrin presence. Raman peaks observed at low wavenumbers of 268 and 327 cm^{-1} relates to the bending vibration of W–O–W bond. The higher wavenumber peak at 716 cm^{-1} is due to the O–W–O vibration and the one at 808 cm^{-1} corresponds to the crystalline WO_3 stretching vibration of the bridging oxygen of W–O–W.[338]

PART OF THIS WORK IS PUBLISHED IN CHEMISTRYSELECT 4 (2019) 8379-8389

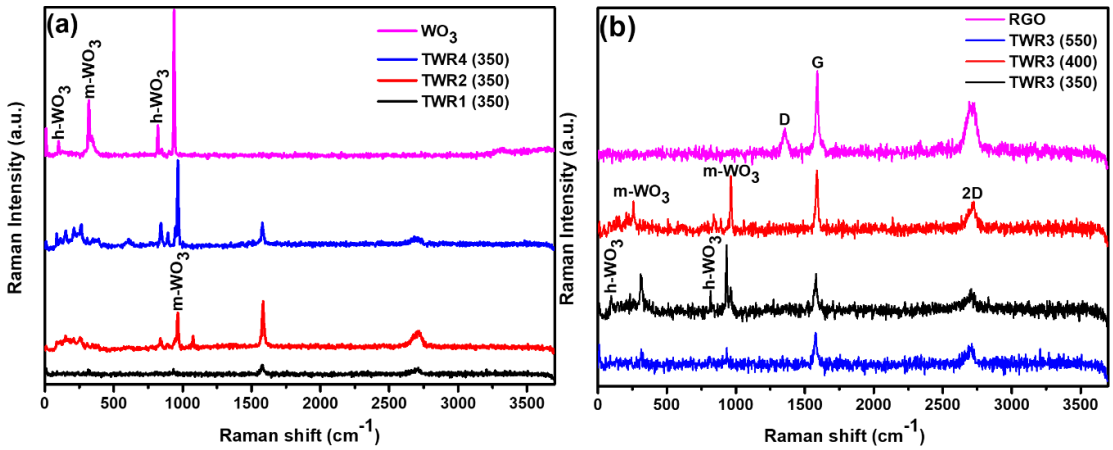

Figure 4.2: Raman spectra of (a) WO_3, TWR1, TWR2 and TWR4 calcined at 350 °C and (b) RGO, TWR3 calcined at different temperatures

The D, G and 2D peaks of RGO are located at around 1468, 1620 and 2650 cm^{-1} respectively (Figure 4.2 (b)). There was no shift in peak positions for these peaks in the composites except the disappearance of the D peak which proves the reduction in disorder of the carbon material. In contrast, TWR3 (350) and TWR3 (400) had mostly m-WO_3 due to TPP being present. Notably, TWR2 (350) and TWR4 (350) showed similar compositions of more m WO_3 than h WO_3 phases. In the absence of TPP, (TWR1 (350) and TWR3 (550)) spectra obtained similar features with almost similar peaks for both m WO_3 and h WO_3 as shown in Figure 4.2 (b). Therefore it can be deduced that the presence of TPP enhanced the formation of m WO_3 confirming the composition dependence of WO_3 phases as supported by literature.[15]

4.2.3 FTIR studies

FTIR analysis was employed to validate the functional groups and composition of the organic part of the samples as well as different available tungsten bonds in crystalline structures of the samples (Figure 4.3). WO_3 exhibit a strong peak located at 445 − 1204 cm^{-1} which is assigned to the stretching vibration of a bridging oxygen atom between two tungsten atoms *v* (W−O− W), tungsten peroxo ($W(O)_2$) and peroxo (O−O) groups are typical vibration bands of peroxotungstic acid and the stretching mode of the terminal W=O double bond.[339] This confirms mixed phases of WO_3 and peak intensity reduction in the composites proved that there was an interaction between the WO_3 and the other components in the composite. The broad vibration at 1400 cm^{-1} is attributed to NH_4^+ counter ions which are necessary to stabilize the structure of WO_3[189] (Figure 4.3 (a)) and the peak at 1684 cm^{-1} is assigned to OH and C=C or C=O from the used citric acid.

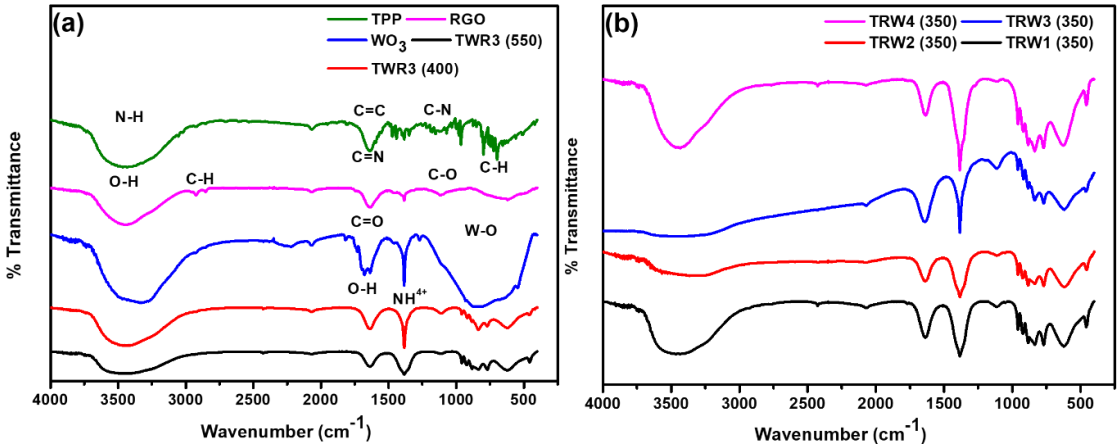

Figure 4.3: FTIR spectra of (a) TPP, RGO, WO_3, TWR3 (400) and TWR3 (550) and (b) TWR1, TWR2, TWR3 and TWR4 calcined at 350 °C.

The peak at 1638 cm^{-1} is due to the C=O stretching vibration of carbonyl functional group in RGO and overlapped with the aromatic C=C stretching of TPP. Further, peaks at 2859 and 2926 cm^{-1} were attributed to the symmetric and asymmetric stretching vibrations of CH bonds respectively.[340] The broad peak between 400 - 800 cm^{-1} was due to several vibration modes of CH like outer bending vibration, CH in plane bending, CH out of plane wagging[340] of aromatic systems. A broad peak at 3465 cm^{-1} presented by RGO could be attributed to the OH bond stretching vibrations belonging to COH and/or adsorbed moisture. For TWR2 (350) and TWR3 (350) (Figure 4.3 (b)), the peak intensity is broad and small showing a strong interaction of TPP and WO_3. The peak at 1114 cm^{-1} could be related to the stretching of CO bond in RGO and the composites.[341] The intensity of this peak is higher for TWR3 350 (Figure 4.3 (b)) and TWR3 (400) (Figure 4.3 (a)). The disappearance of the ester peak around 1000 cm^{-1} confirmed that the graphene oxide was reduced by heating EG in the presence of concentrated sulphuric acid as reported in literature.[139] The results indicate that the prepared reduced graphene oxide sheets were exfoliated and there were few oxides and other functional groups linkage formation on graphene oxide structure as confirmed by the EDS spectra hence minimal defects sites on basal plane of graphene can be inferred.[134] The peaks overlap making it difficult to ascertain presence of either, TPP, RGO or WO_3 in the composites.

4.2.4 TGA studies

As expected, the synthesised WO_3 is stable to heat in the temperature range selected (Figure 4.4). For TTP, the first decomposition stage (30 %) from 432 to 550 °C is attributed to the loss of the phenyl groups attached to the porphyrin aromatic ring and its aromatic ring decomposes afterwards as is the most stable.[158] The RGO ashed (20 %) between 700 and 800 °C and the second decomposition occurred at 850 °C.

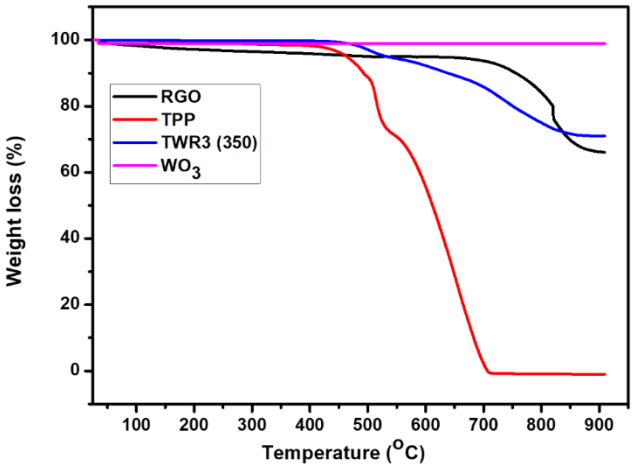

Figure 4.4: TGA graphs of RGO, TPP, WO_3 and TWR3 calcined at 350

The TGA of TWR3 composite calcined at 350 °C affirms the presence of TPP and RGO with matching decompositions.

4.2.5 XRD

The XRD diffraction pattern of WO_3 shows that it has a multiphase composition,[205] containing both monoclinic (JCPDS File no. 43-1035) and hexagonal crystalline phases (Figure 4.5 (a)). The diffraction peaks at 2θ values of 17.1°, 32.8° and 27. 2° were used to calculate the crystallite sizes of the orthorhombic, monoclinic and hexagonal phases using the Scherrer equation (Equation 4.1).

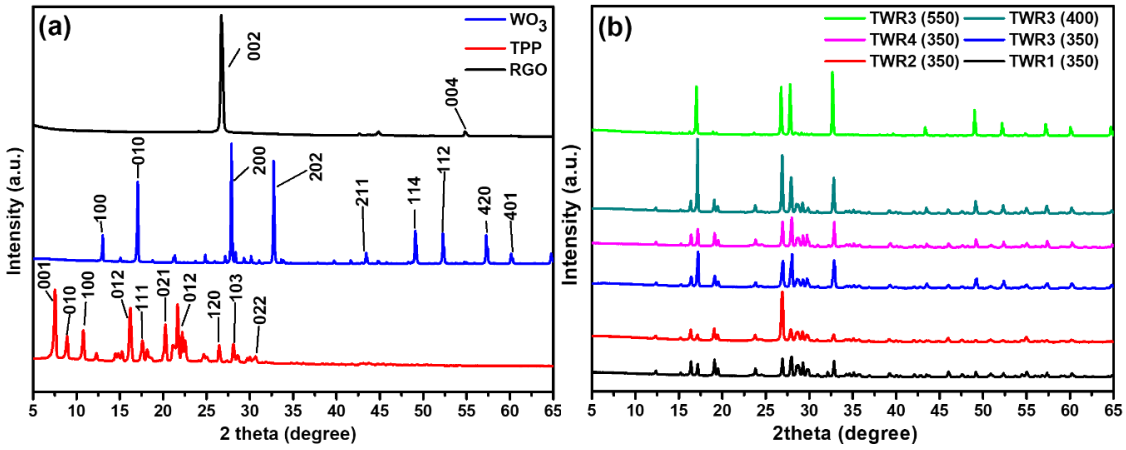

Figure 4.5: XRD spectra of (a) pristine materials and (b) different composites

All the discernible peaks in the XRD of WO_3 (Figure 4.5 (a)) were representative of the monoclinic phase (2θ = 21.4, 32.8 and 57.4), orthorhombic phase (2θ = 17.1, 39.8 and 49.4) and the hexagonal phase (2θ = 12.9, 25, 27.2, 28.0, 37.8, 41.6, 43.4, 49.1, 52.2 and 60.4). The XRD pattern of TPP in the powder form (Figure 4.5 (a)) shows multiple peaks with different intensities which indicates that the material is polycrystalline.[158] The (002) reflections (2θ = 26.9) corresponding to RGO is present with the intensity of the peak

around 2θ = 11 being absent which indicates that the prepared reduced graphene oxide (RGO) has little amount of various oxygen containing functionalities and intercalated molecules present as confirmed by the EDS and the FTIR results. Thus, it can be inferred that the RGO maintained the crystal structure of natural graphite.[342] The decrease in the interlayer spacing between the thermally reduced graphene oxide sheets is attributed to the removal of considerable oxygen functionalities from the RGO sheet during the reduction process. The interlayer spacing $d_{002,}$ was 0.2739 nm. The general decrease in the interlayer spacing of the composites annealed at 350 and 400 °C also attested to the successful incorporation of nanoparticles (Table 4.1). The increase in the peak intensity at 2θ = 55 in all composites compared to RGO suggested a lower aspect ratio than the composites.[139] The grain size or the mean crystallite diameter (nm) (C) of different phases in the samples were determined from the full width at half maximum (FWHM) of the peaks using the Debye-Scherrer equation.[343]

$$\mathbf{C = 0.9\lambda/\beta\cos\theta} \qquad \mathbf{4.1}$$

Where β is the line width at half height in radians and θ is the diffraction angle in radians. λ = 0.15418 nm as per the XRD machine used. The number of graphene layers was calculated by dividing the crystal size (C) by the interlayer distance (nm) added to the thickness of one graphene sheet (0.1 nm),[344] and the highest number of graphene sheets was determined at the annealing temperature of 550 °C. Therefore, the synthesis method produced few layer reduced graphene as reported in literature.[139]

Table 4.2: Bandgap energy mean crystallite diameter, surface area, pore size, pore volume, and number of reduced graphene layers of TPP, WO_3 and TPP/WO_3/RGO composites with different calcination temperature and amount of TPP.

Sample	Bandgap (eV)	d (nm)	C (nm)	surface area (m^2/g)	Pore volume (cm^3/g)	Pore diameter (nm)	RGO Layers
TPP	0.70	0.9611	33.6549	-	-	-	-
WO_3	3.12	0.2633	32.7222	-	-	-	-
RGO	-	0.2739	33.5757	432.1	0.4012	3.7	10
TWR1 (350)	2.39	0.2642	33.6476	-	-	-	10
TWR2 (350)	1.74	0.2729	33.5827	-	-	-	10
TWR3 (350)	2.14	0.4235	33.0276	470.1	0.3657	5.4	6
TWR4 (350)	2.31	0.2615	33.6697	-	-	-	10
TWR3 (400)	2.09	0.4235	33.0276	-	-	-	6
TWR3 (550)	2.52	0.2256	34.0423	-	-	-	11
TWR5 (350)	2.27	-	-	-	-	-	-

From XRD analysis, the interlayer spacing (d) of the materials is proportional to the degree of oxidation. All the composites annealed at 350 °C (Figure 4.5 (b)) showed presence of both the hexagonal and monoclinic peaks indicating that this annealing temperature favoured the formation of monoclinic WO_3. Formation of hexagonal WO_3 occurs with increase in calcination temperature. Therefore, at 550 °C, only hexagonal WO_3 was present in the nanocomposite. The peak at $2\theta = 26.4$ observed in the spectrum of the nanocomposite materials, corresponds to the (002) crystal plane of reduced graphene oxide and decreased in intensity with the increase in the amount of TPP. The peak intensity increased with increasing annealing temperature confirming the successful formation of the graphene based nanocomposites. From the XRD patterns it can be concluded that the crystal structure of composite materials changed compared to the pristine WO_3, indicating that the anchoring process and the annealing temperature influenced the characteristic crystal structure of WO_3.

4.2.6 BET

The BET surface area was used to determine the specific surface area of the different materials and the results are summarised in table 4.1. The specific surface area of RGO is high (432.1 m^2g^{-1}) but is low when compared to theoretical value of RGO.[345] Moreover,

nanoparticles loading significantly decreased the pore volume but increased the average pore diameter and the surface area of TWR3 350 (470.1 m^2g^{-1}). The N_2 adsorption desorption data of both samples are similar, showing a type II isotherm (Figure 4.6), indicating minimal microporosity, some mesoporosity and mainly macroporosity.[345]

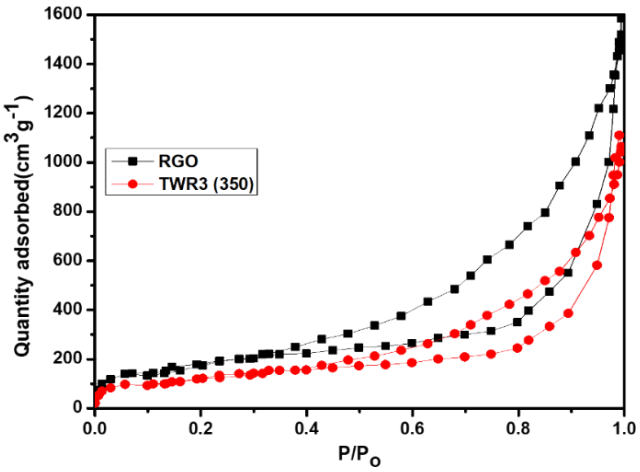

Figure 4.6: N_2 Adsorption desorption isotherms of RGO and catalyst

A hysteresis loop in the nitrogen adsorption/desorption isotherms of RGO and TWR3 (350) are also observed, which designates that they are porous. The hysteresis loop resembles type H3 IUPAC (International Union of Pure and Applied Chemistry) classification, resulting from slit shaped pores between parallel layers.[345]

4.2.7 Photoluminescence

Electron hole recombination influences photocatalytic degradation of organic pollutants by semiconductors. Photoluminescence (PL) spectra are used to show this phenomenon with decrease in the intensity of the PL peaks associated with decrease in photoexcited electron hole recombination rate. Figure 4.7 shows the results for WO_3 and catalysts with different TPP composition calcined at different temperatures.

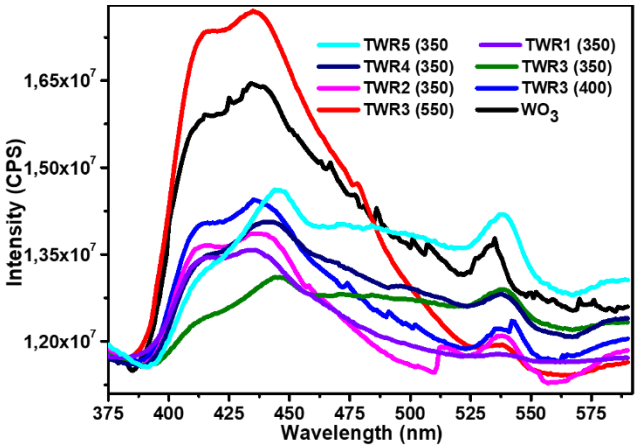

Figure 4.7: PL spectra of WO_3 and different composites

When TPP was reduced or increased from 20 mg, it resulted in increase in intensity of the PL spectra and hence high recombination. The catalyst calcined at 350 °C showed the lowest PL intensity followed by those calcined at 400 °C and 550 °C. Thus, the electron hole recombination increases with increasing the calcination temperature. The increase in electron-hole recombination resulted in decrease in degradation efficiency in the same order and this can be attributed to not only the presence of TPP but also the morphology of the composite. This is further supported by the TGA analysis results of TPP as it decomposed at 432 °C and therefore was absent in the composite calcined at 550 °C resulting in high electron hole recombination.

4.2.8 UV/VIS studies

The absorption spectra of porphyrin thin films (Figure 4.8 (a)) show a distinct separation of absorption due to Soret band and multiple Q bands at low energy. WO_3 nanoparticles absorbed in the visible region with a small peak around 400 nm and an intense UV absorption maximum around 250 nm (Figure 4.7 (a)). The spectra of composites (Figure 4.8 (b)) shows constant absorption in the visible region from around 550 throughout and the increase in intensity is high for all composites compared to pure WO_3 nanoparticles. The absorption edge of pristine WO_3 was shifted from around 300 nm to between 500 and 550 nm by the presence of either porphyrin (TWR5 (350)) or RGO (TWR1 (350)), and when both TPP and RGO were present (TWR2 (350), TWR3 (350)), TWR3 (400), TWR3 (550) and TWR4 (350).

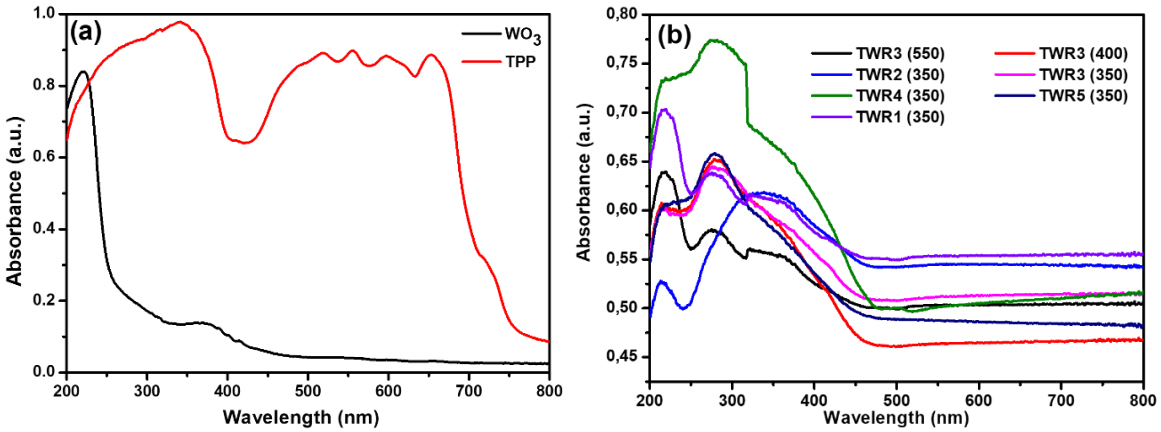

Figure 4.8: UV/Vis spectra of solids (a) TPP and WO_3 and (b) Composites

The bandgap of materials is an important parameter in photocatalysis and gives the amount of energy required to generate photoexcited electrons and holes pairs. The difference in absorbances of the different catalysts confirms that they have different bandgaps and their bandgaps were estimated from absorption spectra using the relationship of energy (hv) and wavelength (hv (eV) = 1239.8/λ). A comprehensive

bandgap investigation encompasses plotting and fitting (to direct or indirect) the absorption data and normalising the absorbance, A to the path length, *l* of light through the material (sample thickness for solid samples) to get the absorption coefficient, α = (Ln (10) x A)/l. When molecules are involved, molecular crystal proposes the valence band to be a combination of highest occupied molecular orbitals (HOMO) and the conduction band to be made of lowest unoccupied molecular orbitals (LUMO). According to the relationship that was provided by Davis and Mott for values of α (cm^{-1}) above 104 cm^{-1}, data follows a power-law behaviour ($\alpha h\nu = A(h\nu - E_g^{opt})^r$) which is known as the Tauc plot relationship. Where A is a parameter that depends on the transition probability, α is the absorption coefficient, E_g^{opt} is the optical bandgap and r is a number which characterize the transition process and can take values of 2, 2/3, ½ or 1/3 for direct (allowed), direct forbidden, indirect (allowed) and indirect forbidden transitions respectively. Tauc plots of $(\alpha h\nu)^r$ vs. $h\nu$ estimate the bandgap when extrapolated with the best possible fit to the baseline at y = 0. The best possible fit of the peak around 400 nm for WO_3 was for the direct allowed transition (Figure 4.9). This peak was used as it is in the visible region and due to degradation results, WO_3 absorbed in the visible region as its efficiency improved compared to only photolysis.

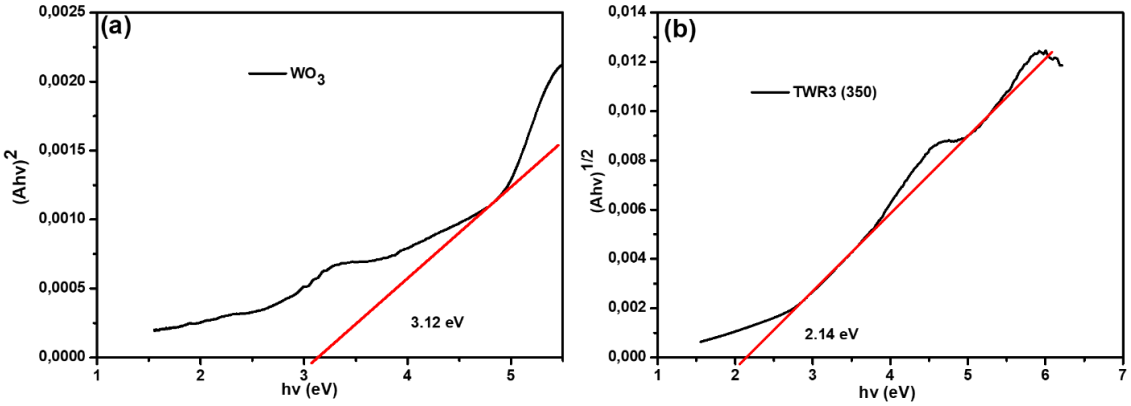

Figure 4.9: Tauc plot of (a) WO_3 calcined at 700 °C and (b) TWR composite calcined at 350 °C

The bandgap of 3.12 eV was observed for pristine WO_3 (Figure 4.9 a). The bandgaps are summarized by table 4.1. All the synthesised nanocomposites and TPP best fit the indirect allowed transitions and the example of how their bandgaps were estimated is illustrated in Figure 4.9 (b) using TWR3 (350) which gave the highest degradation efficiency. The bandgaps values are 0.70 eV, 2.39 eV, 1.74 eV, 2.14 eV, 2.31 eV, 2.09 eV, 2.52 eV and 2.27 eV for TPP, TWR1 (350), TWR2 (350), TWR3 (350), TWR4 (350), TWR3 (400) TWR3 (550) and TWR5 (350) respectively. The bandgap values of the synthesised materials proved that they absorb energy in the visible range and were all less than the bandgap of pristine WO_3. The enhancement or the reduction in the value of the bandgap

suggest that the materials therefore required less energy to have photo excited electrons and holes than pristine WO_3. Therefore, TPP and RGO managed to shift the absorbance of WO_3 more to the visible region even when only RGO was used (TWR1 (350)) or only when TPP was used (TWR5 (350)). However, optimisation of the necessary amount of each material is very important and does not only affect the bandgap but also recombination of photogenerated electrons and holes and the morphology.

4.3 Degradation of Acid Blue 25 (AB25)

Degradation of AB-25 was performed using pristine WO_3, photolysis, TWR1 (350), TWR2 (350), TWR3 (350), TWR3 (400), TWR3 (550) and TWR4 (350) at pH 7. The results are shown on Figure 4.10 (a-d) and pH was optimised using TWR3 (350) composite (Figure 4.10 (e)).

PART OF THIS WORK IS PUBLISHED IN CHEMISTRYSELECT 4 (2019) 8379-8389

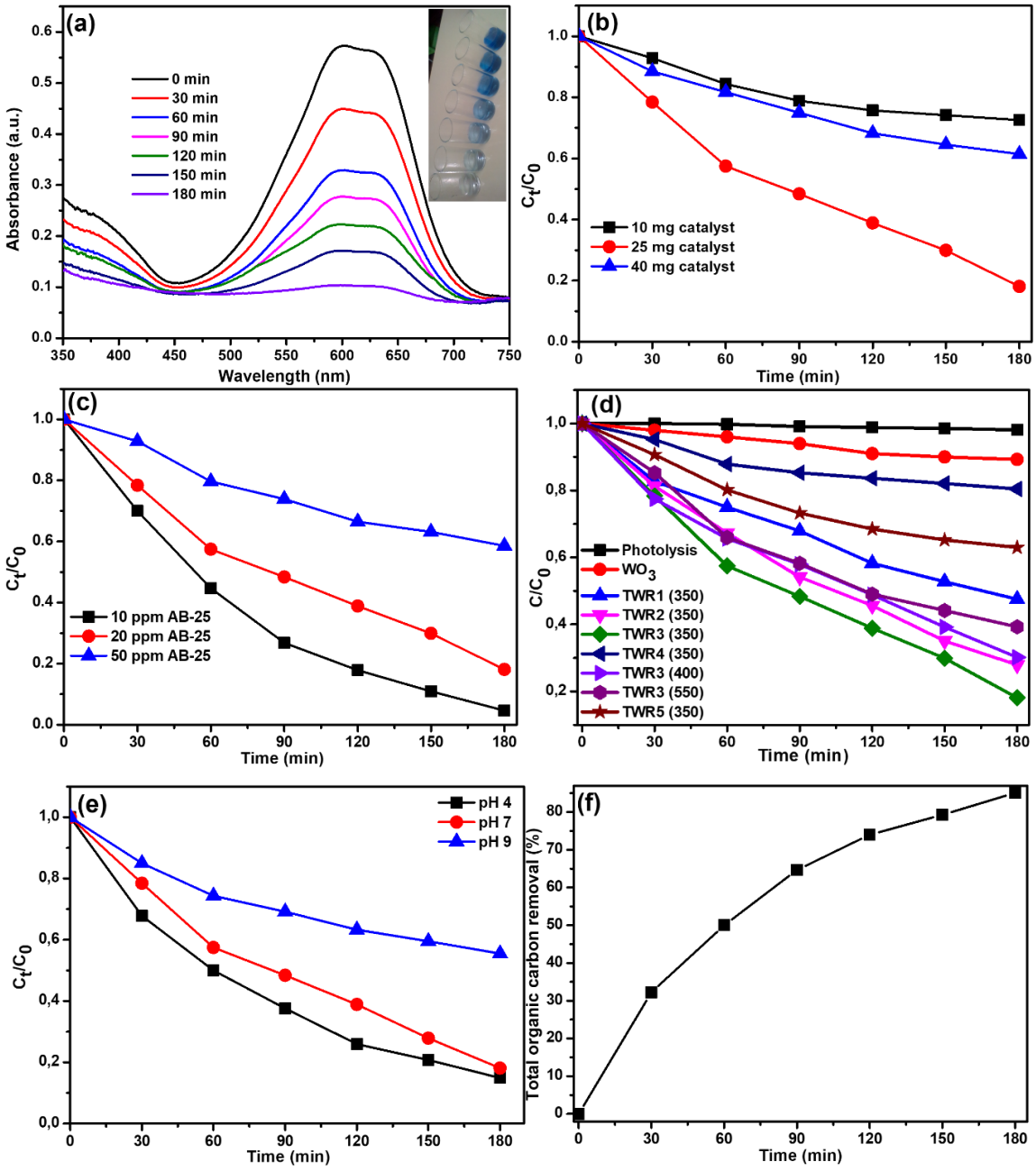

Figure 4.10: Degradation of AB25 (a) with 25 mg of TWR3 (350) degrading 20 ppm dye, (b) Effect of catalyst amount, (c) effect of dye concentration, (d) Effect of composition at pH 7, (e) effect of pH and (f) TOC results at pH 4

The chromophore of AB25 dye was successfully degraded as absorbances decreased with increasing time (Figure 4.10 (a)). The best performing photocatalyst calcined at 350 °C was used for catalyst concentration (Figure 4.10 (b)) and dye concentration (Figure 4.10 (c)) optimisation. The TOC results (Figure 4.10 (f)) confirmed the degradation of the auxochrome and chromophore of the anthraquinone AB25 dye with an efficiency of 85 % at pH 4.

4.3.1 Effect of Catalyst calcination temperature

The photocatalytic degradation profiles of the in-situ synthesised photocatalyst calcined at different temperatures (350, 400 and 550 °C) over a period of 180 minutes are shown in Figure 4.10 (d). The dye concentration decreased with increasing irradiation time. The degradation efficiency of 54, 70 and 82 % at the maximum wavelength of absorption for catalyst calcined at 550, 400 and 350 °C respectively (Figure 4.10 (a)). The high efficiency of TWR3 (350) (Figure 4.10 (d)) is due to the increased calcination time that favoured a different phase of the WO_3 (monoclinic as shown by XRD) and the presence of porphyrin to further enhance light absorption for the degradation of the AB25 as supported by TGA results (TPP decomposes at 432 °C). The spherical and less aggregated catalyst gives the high efficiency due to high surface area for adsorption of dye and desorption of by-products, and the highest charge separation as it has the lowest PL intensity (Figure 4.7).

4.3.2 Effect of catalyst concentration

The effect of the initial photocatalyst dosage was evaluated by varying the amount of the photocatalyst using the sample calcined at 350 °C as it showed the highest efficiency (Figure 4.10 (b)). The efficiency at 10 mg catalyst loading was 26 % because small amount of catalyst was used, and less hydroxyl radicals were generated. At 40 mg of catalyst the degradation efficiency increased to 67 %. The 25 mg catalyst amount (500 ppm) was the optimum catalyst dosage for in situ catalyst of TPP/WO_3/RGO calcined at 350 °C.

4.3.3 Effect of dye concentration

Based on literature of effluent discharges from different industries (textiles, etc) and the toxicology studies, dye effluents are commonly within the range of 10 to 50 mgL^{-1} and pose a health risk to the environment and human life.[28,346] The effect of initial dye concentration on the degradation efficiency was also evaluated at pH 7 (Figure 4.10 (c)). The efficiency when 10 ppm dye concentration was used was 95 %, 82 % when 20 ppm was used and reduced to 41 % when 50 ppm dye concentration was used.

4.3.4 Effect of composition of TPP in the composite

Photolysis experiments and pristine tungsten trioxide were evaluated, and the results compared with those of the synthesised composites (Figure 4.10 (d)). There was little dye degradation using a blank and pristine WO_3 as expected. The degradation efficiency of WO_3 was calculated to be 17 %. These observations concur with UV/Vis studies of WO_3 which showed a small absorption peak in the visible region. Moreover, the composition of

the WO_3 showed more of the hexagonal phase of WO_3 which is known to be less photocatalytic than the monoclinic phase.[347,348] The catalyst without RGO (TWR5 (350)) was also synthesised using 20 mg TPP and its efficiency was determined to be 37 %. The effect of porphyrin loading on the photocatalytic activity of the nanocomposites was also evaluated (Figure 4.10 (d)). The catalyst without any TPP showed a degradation efficiency of 52 % and it improved to 70 % when 10 mg TPP was used. When TPP amount was increased to 20 mg the efficiency of the catalyst was calculated to be 82 %. This can be attributed to improved charge separation by this catalyst as confirmed by PL analysis. Further increase of TPP to 30 % resulted in the lowest efficiency of 20 % which is attributed to high electron recombination as per PL analysis (Figure 4.7) and formation of hexagonal thin films of WO_3 confirmed by SEM (Figure 4.1 (d)) and XRD (Figure 4.5 (b)).

4.3.5 Effect of pH of pollutant solution

The performance of TWR3 350 at different pH values (pH 9, pH 7 and pH 4) was evaluated (Figure 4.10 (e)). The values were selected as they are reported to be the most common pH values in effluent discharges of acid blue 25 dye.[349] The efficiency of the catalyst at pH 7 was, improved to 85 % when pH was reduced to 4 and reduced to 54 % at pH 9. When the hydroxyl anions are added (basic pH), there is competition of adsorption on the catalyst active surface for adsorption and a small interaction between dye and catalyst which in turn reduces the efficiency. The high degradation rate in acidic solutions (addition of HCl) can be associated with the effect of protonation of negatively charged sulfonic anion ($–SO_3^-$) group which increases dye to catalyst interaction and improve the degradation efficiency. However, there is a possibility of the hydroxyl radical scavenging effect of chloride ion ($Cl^- + {}^{\bullet}OH \rightarrow HClO^{\bullet-}$) and ($HClO^{\bullet-} + H^+ \rightarrow Cl^{\bullet} + H_2O$) leading to inorganic radical. These inorganic radical anions show a much lower reactivity than $^{\bullet}OH$ and do not take part in the dye degradation. Moreover, there is also a drastic competition between the dye and the anions with respect to $^{\bullet}OH$ as generated hydroxyl radicals also react with chloride ions.[40]

4.4 Reaction kinetics and catalyst stability

The rate of reaction is also prominent in photocatalysis and is normally presented as rate constant. According to the Langmuir-Hinshelwood mechanism, the pseudo rate constant k for the photocatalytic degradation reaction of the dyes can be calculated by ($Ln(C_0/C_t) = kt$), where C_0 and C_t are the concentrations of the dyes before and after irradiation, respectively and t is the time of irradiation. The plot of ln (C_0/C_t) vs t is a straight line, the

slope of which gives the rate constant. The different rate constants are shown in Figure 4.11 for the different composites at pH 7.

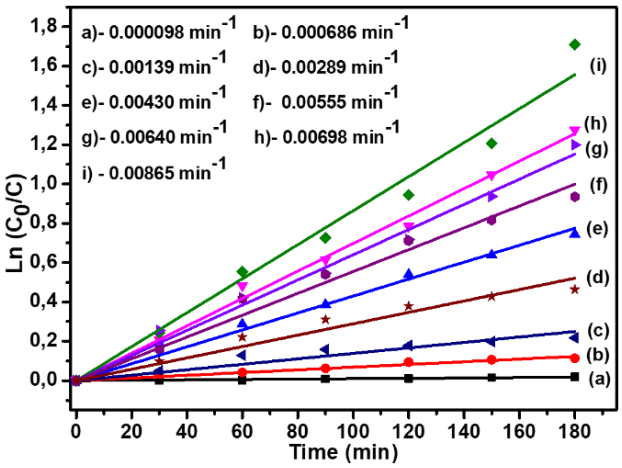

Figure 4.11: Rate constants for (a) Photolysis, (b) WO_3, (c) TWR4 (350), (d)TWR5 (350), (e) TWR1 (350), (f) TWR3 (550), (g) TWR3 (400), (h) TWR2 (350) and (i) TWR3 (350)

The highest rate constant of TWR3 (350) is more than ten times the rate of WO_3 and further proves that the TPP and RGO in the composite has greatly enhanced visible light absorption of WO_3. The stability of the catalyst was tested by recycling the catalyst (TWR3 (350)) at pH 4 and the results are shown by Figure 4.12 a. Trial 1 is when the catalyst is used after synthesis and subsequent recycling cycles are named trial 2, trial 3 and trial 4 respectively.

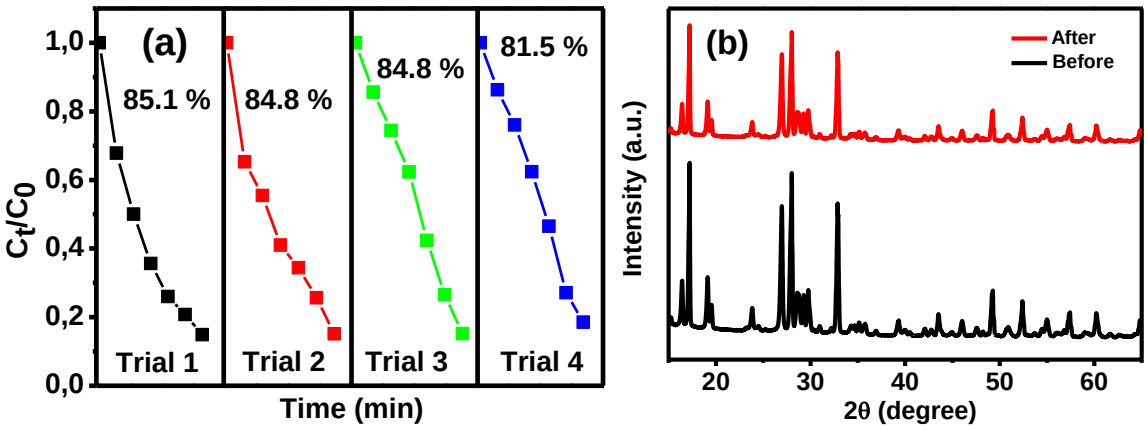

Figure 4.12: (a) Efficiency of catalyst during recycling and (b) XRD spectra of catalyst before and after recycling

The catalyst is stable for four cycles and can be recycled with efficiency of 81.5 % after four runs at pH 4. The high efficiency achieved after four cycles indicated that the catalyst could still be further re-used to accurately determine the number of cycles it will take to affect its efficiency. This implies that it can be a good candidate for large scale photocatalytic applications as it can be reused several times without prominent decrease

in its efficiency. The stability of the recycled composite was further confirmed by its XRD (Figure 4.12 b) which only showed reduction in the intensity of all the peaks observed for TWR3 (350) after four recycling tests were done.

4.5 Photocatalytic mechanism and charge transfer

Based on the above results and some literature, the mechanism and charge transfer of the TPP/WO_3/RGO ternary composite is given by Figure 4.13 and illustrates the band configuration and photogenerated charge carrier's separation.

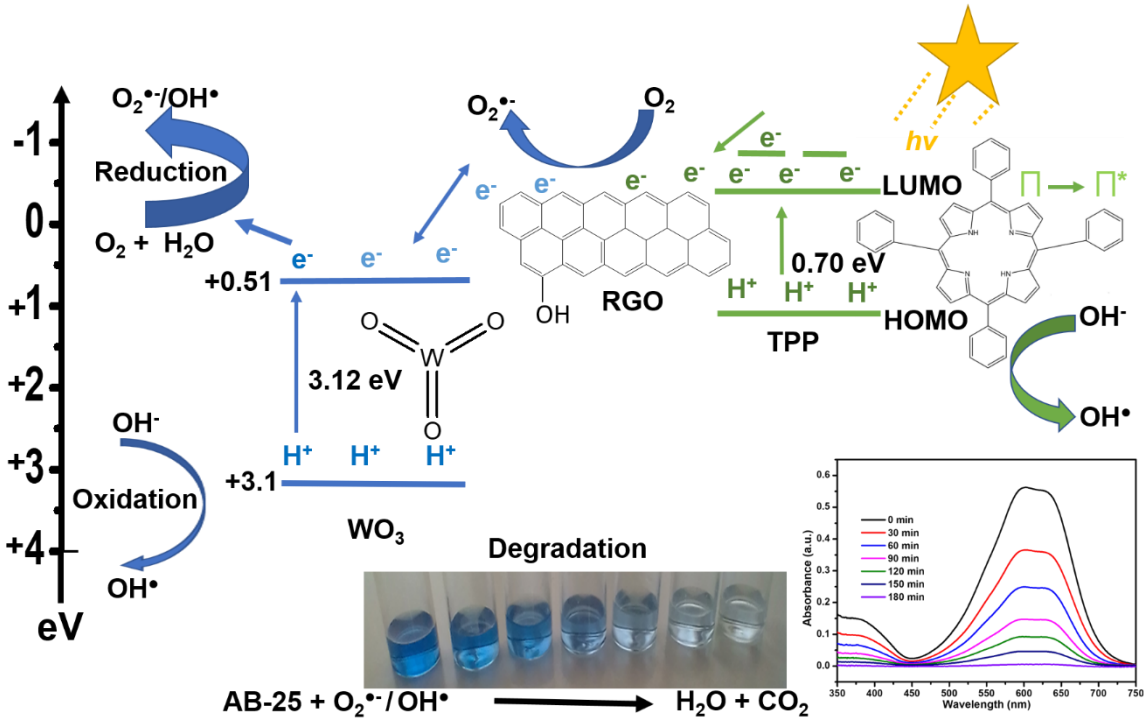

Figure 4.13: Schematic diagram of charge transfer and AB25 degradation over TPP/WO_3/RGO nanocomposite

Under UV/Vis light irradiation both TPP and WO_3 can be photoexcited to produce (e^-/h^+) pairs. TPP will form a series of transitions referred to as singlet and triplet excited states due to the nature of its UV/Vis spectra.[350] The interfacial electron-hole separation in TPP/WO_3 would be bidirectional; that is, the photo-generated electrons on the conduction band (CB) of TPP transfer to the CB of WO_3 with lower potential with the help of RGO due to its ability to shuttle electrons. These electrons could be captured by the adsorbed oxygen to produce the reactive superoxide anion radical. On the other hand, the holes on the valence band (VB) of WO_3 transfer to the VB of TPP with higher potential, the holes could be trapped by H_2O molecules to form strong oxidizing hydroxyl radical.[351] However, the holes on the valence band of WO_3 can also produce hydroxy radicals. The rate of degradation is increased by the fast formation and efficient separation of photogenerated

electron and holes. The photocatalytic degradation process of AB25 occurred via reduction with super oxide radical anions ($O_2^{\bullet-}$), and/or oxidation hydroxyl radicals ($^{\bullet}OH$).
It is well documented that improved photodegradation, a highly crystalline surface area and improved photoexcited electron hole mechanism of the material resulted in their effective migration to the photocatalytic active sites.[352] The photogenerated electron-hole pairs occurred when WO_3 was exposed to visible light as discussed in the optical properties section. The photogenerated electrons were transported through RGO to the photoactive surface of the catalyst to interact with adsorbed O_2 to form $^{\bullet}O_2^-$ while the photogenerated holes reacted with water and produced $^{\bullet}OH$ radicals.[336,353] The $^{\bullet}O_2^-$ superoxide and $^{\bullet}OH$ radicals synergistically act as strong oxidizing agents for the mineralisation of AB25 dye adsorbed. Moreover, the TWR (350) composite and the dye molecules have affinity to each other such that the larger surface area and the phenyl structure of the RGO sheets enhanced adsorption of dyes and their degradation efficiency. The FTIR results indicated that RGO contains different functional groups, such as hydroxyl, epoxy and carboxylic groups, and the π–π interaction between the aromatic rings of the TPP/WO_3/EG composite with heterocyclic dye molecules smoothed the generation of hydroxyl radical's for complete mineralisation of AB25.[354–356] The mechanism of photodegradation of the AB25 can be summarised by the following reactions as presented on Figure 4.13.[354–356]

TPP + *hv* → (TPP)*	**(singlet/triplet excitation)**	**(4.2)**
WO_3 + *hv* → WO_3 (e^- + h+)	**(photoexcitation of WO_3)**	**(4.3)**
(TPP/WO_3/RGO) + *hv* → WO_3 (h^+)+ $TPPe^-$	**(separation of photoexcited e^-/h^+ pairs)**	**(4.5)**
$TPPe^-$ + O_2→ TPP + $^{\bullet}O_2^-$	**(radical formation)**	**(4.6)**
WO_3 + OH^- → WO_3+ $^{\bullet}OH$	**(radical formation)**	**(4.7)**
AB25 + $^{\bullet}OH$ → Degraded Products	**(degradation)**	**(4.8)**
AB25 + $^{\bullet}O_2^-$ → Degraded Products	**(degradation)**	**(4.9)**

This mechanism and the final charge transfer in the nanocomposite were attained through comparison of similar studies that use RGO as the support where electron spin resonance (ESR) spectroscopy was used to confirm the involvement of the $^{\bullet}OH$ and $O_2^{\bullet-}$ radicals except the involvement of the photogenerated holes towards degradation of AB25.[357–359] Moreover, Figure 10 (d) indicated that the TWR3 (350) (0.5 % TPP/WO_3/RGO) composite resulted in a comparatively more degradation of the AB25 dye compared other materials under similar conditions.

PART OF THIS WORK IS PUBLISHED IN CHEMISTRYSELECT 4 (2019) 8379-8389

CHAPTER 5

DEGRADATION OF AB25 WITH A NANOCOMPOSITE OF TPP/WO_3/EG UNDER SIMULATED SUNLIGHT IRRADIATION

5.1 Introduction

This chapter discusses the construction of heterogeneous photocatalytic systems immobilised on an organic carrier with improved stability and enrichment of the overall efficiency of the process. The selection of a suitable carrier for immobilization of functionally active photoactive nanoparticles is an obligation to minimize leaching of the photoactive semiconductors and enhance the recovery after use.[360] The visible light active WO_3 was selected to enable easy access to the abundant sunlight radiation that promises to be a sustainable light energy source. Moreover, TPP has often been used as a strong electron donor carbon-based photosensitizer to shift absorption of semiconductors more to the visible range of the spectrum with numerous success stories achieved. Exfoliated graphite was selected because of different properties like its ability to shuttle electrons which would help as a support and in transport of photoexcited electrons and holes for efficient charge separation. Inter alia, AB25 warrants its investigation by virtue of adverse health effects it imposes on humans and the environment like other organic pollutants.

In this study, a buoyant TPP/WO_3/EG photocatalyst was prepared as outlined in **Section 3.2.7** for photocatalytic degradation of acid blue 25 dye under visible light irradiation for the first time according to our literature investigations. The interaction between the functionalised nanoparticles was discussed in detail to improve the literacy in the chemistry and chemical interactions between the TPP, WO_3 and carbon nanomaterials which can be applied for any selected metal oxide semiconductors such as ZnO, TiO_2 with porphyrins or carbon semiconductors such as graphitic carbon nitrite and supports materials like carbon nanotubes. The chemical interaction enhanced synergy and augmented the applications of the as-synthesised nanocomposite material.

5.2 Results and Discussion

The results obtained using different techniques towards characterisation of the synthesised composites are discussed and the application of the photocatalytic reactions for degradation of AB25 is included. The composites were named TWE and different amounts of TPP were used to check the effect of this photosensitizer on both properties and performance of the catalysts calcined at 400 °C. The mechanism by which the individual nanomaterials enhanced the photocatalytic performance of the fabricated heterostructure is proposed. The proposed mechanism was achieved by conducting radicals probing experiments to determine the possible generated radicals. TOC and UV-Vis were used to follow the degradation reactions.

5.2.1 SEM/EDS

The morphology of the prepared nanomaterials was observed using field emission SEM. The performance of nanostructured photocatalysts has been reported to depend on morphology i.e. shape and size.[361,362] Moreover, the orientation of visible light driven nanostructured photocatalysts requires exposure of the reactive facet for improved photocatalytic performance.[363] Figure 5.1 shows SEM images of the different nanomaterials and composites. WO_3 showed heterogeneous nanoparticles (Figure 5.1 (a)) with different sizes of rods, flat sheets and spherical particles. They appear agglomerated and the sheet like WO_3 shape was dominant. Figure 5.1 (b) shows that the synthesised EG has cellular-like structures and craters that can be useful for housing nanoparticles as reported in literature.[124] The exfoliated graphite had worm-like, accordion structures composed of stacks of graphene held together along the c-axis with distinguished nano-platelets. The addition of WO_3 (Figure 5.1 (c)) resulted in aggregation of mostly rod shaped and spherical nanoparticles on the surface and inside the craters of the support material. However, addition of TPP (0.1 %) resulted in uneven distribution (inside the craters and on the surface of EG) of spherical nanoparticles with increased aggregation (Figure 5.1 (d)). When TPP amount was increased to 0.5 %, there was formation of spherical nanoparticles with mild aggregation (Figure 5.1 (e)). Further increase in TPP to 1 % (Figure 5.1 (f)) resulted in more aggregation of rod shaped nanoparticles on the surface and inside the craters of the support material. Therefore, WO_3 shape and morphology can be tailored by changing the amount of TTP in the nanocomposites.

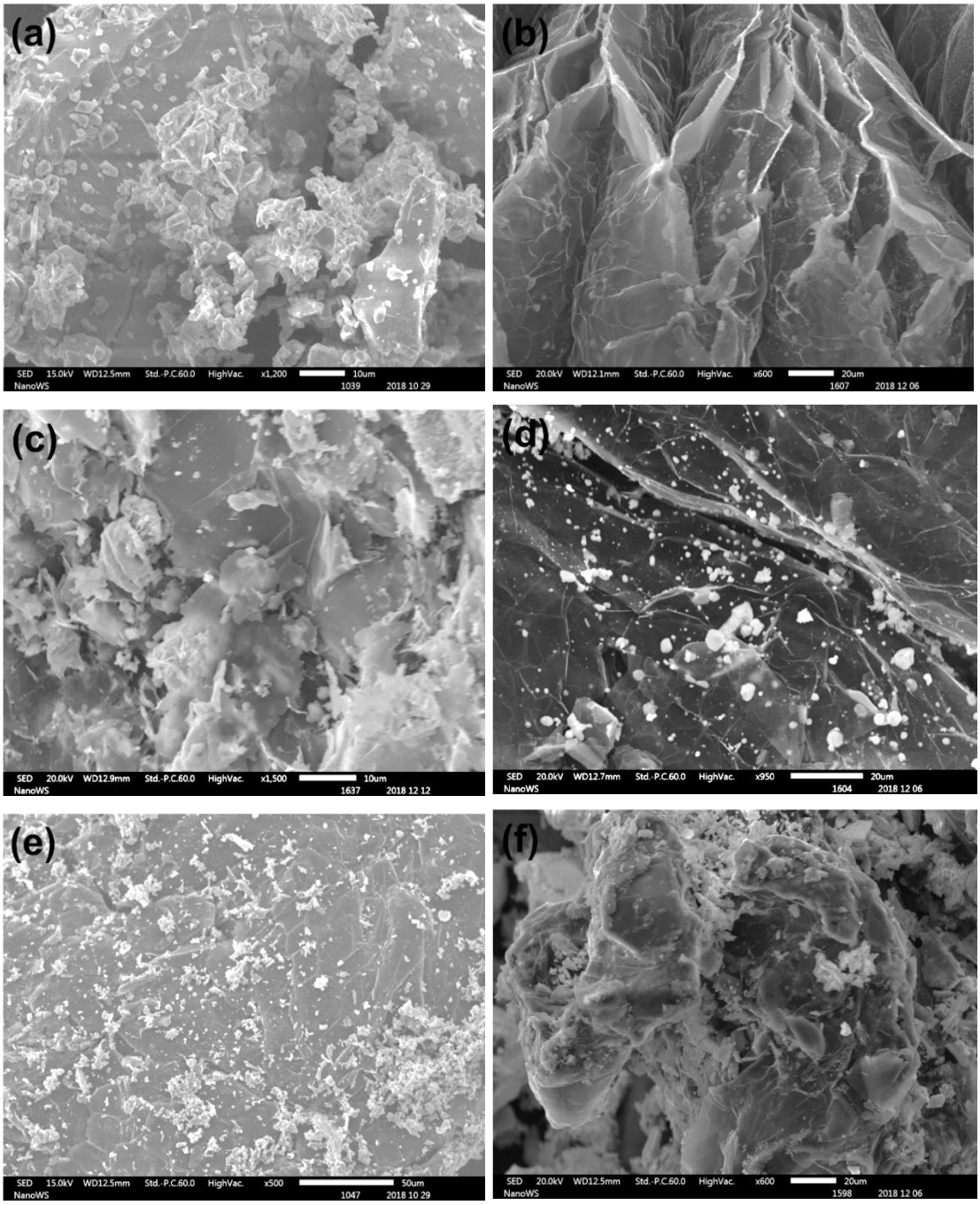

Figure 5.1: SEM image of (a) WO_3, (b) EG, (c) TWE0, (d) TWE1, (e) TWE5 and (f) TWE10

To get further insights into the morphology of the nanostructured materials, high resolution SEM images were obtained using JEOL JSM-7800F (Figure 5.2). Figure 5.2 (a) shows pristine WO_3 nanomaterials of different sizes and shapes with the large 2D platelets surrounded by smaller spherical, rod-shaped and plate-like nanoparticles that are aggregated and self-assembled into 3D spheres in different directions on the surface and around the 2D platelets.[364] From Figure 5.2 (b), the distinguished nanoplate-like 2D sheets of exfoliated graphite were seen parallel to each other with random stacking along the c-

axis that resulted in clearly defined craters. Moreover, there were impurities deposited on the surface of the sheets. After depositing WO_3 particles in EG, as shown in Figure 5.2 (d), the surface of EG was almost completely covered by rod shaped nanostructures of WO_3 composites that assembled into spongy like 3D platelets growing in different directions.[365,366] However, further addition of TPP to WO_3/EG improved the shape and distribution of WO_3 into 3D spheres of different sizes as shown on Figure 5.2 (c). This indicated that crystalline WO_3 nanoparticles grew onto the surfaces of EG to form the nanohybrid.

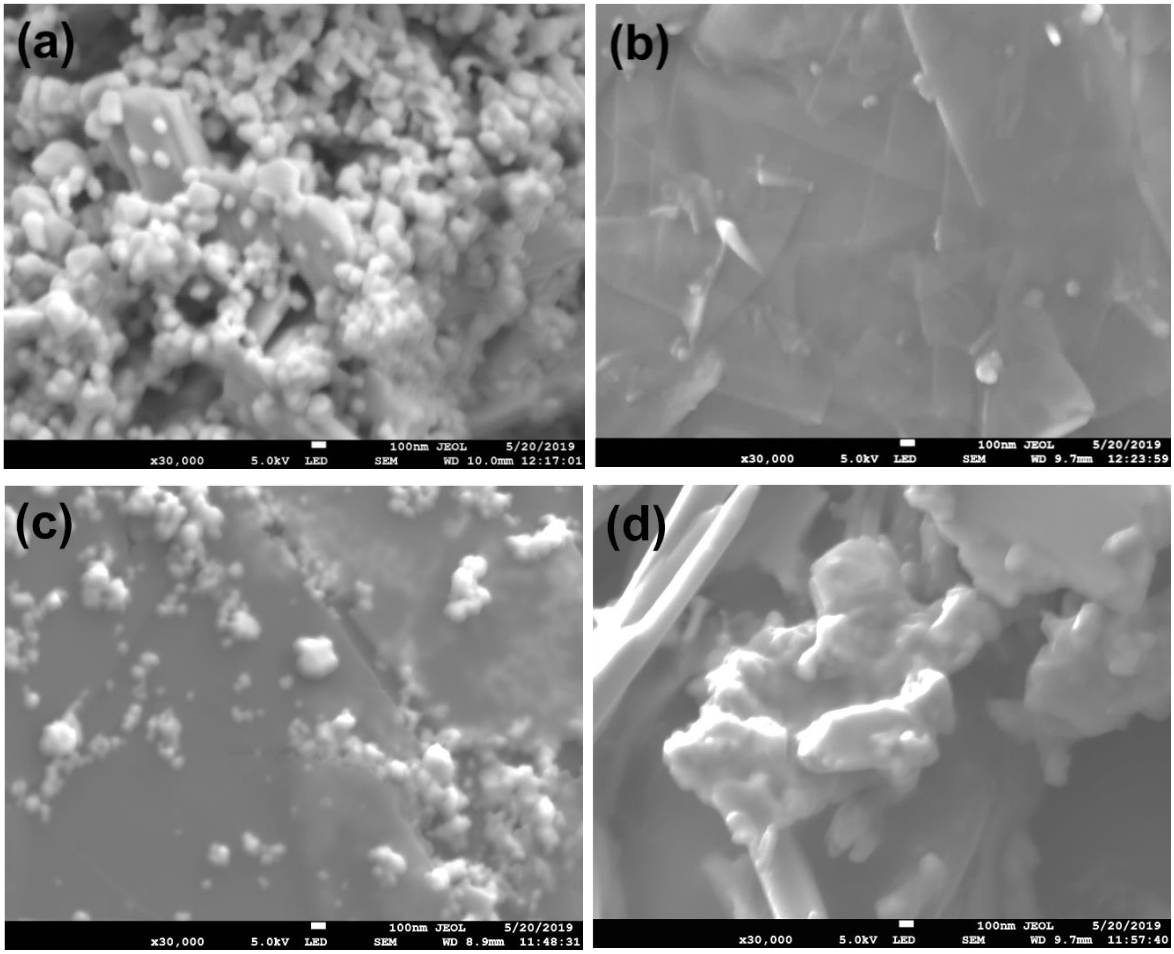

Figure 5.2: FE-SEM images of (a) WO_3, (b) EG, (c) TWE 5 and TWE 10

SEM analyses of pristine WO_3, WO_3/EG and TWE composites showed that the structural and morphological properties were entirely dependent on the amount and presence of TPP or EG.

EDS characterization was used to confirm the elemental composition and purity of the prepared samples.[361] Figure 5.3 shows the EDS of the samples. The EG spectrum (Figure 5.3 (a)) confirmed the formation of EG with small amounts of sulfur and nitrogen content left after washing. The high percentage of C (82.3 wt%) confirmed the largely carbon

nature of EG. The EDS of WO_3 showed the presence of W, C (from carbon conducting tape) and O confirming the formation of the WO_3 (Figure 5.3 (b)). The oxygen peak in the synthesised WO_3 was small confirming the oxygen vacancy of the synthesised WO_3 nanoparticles.

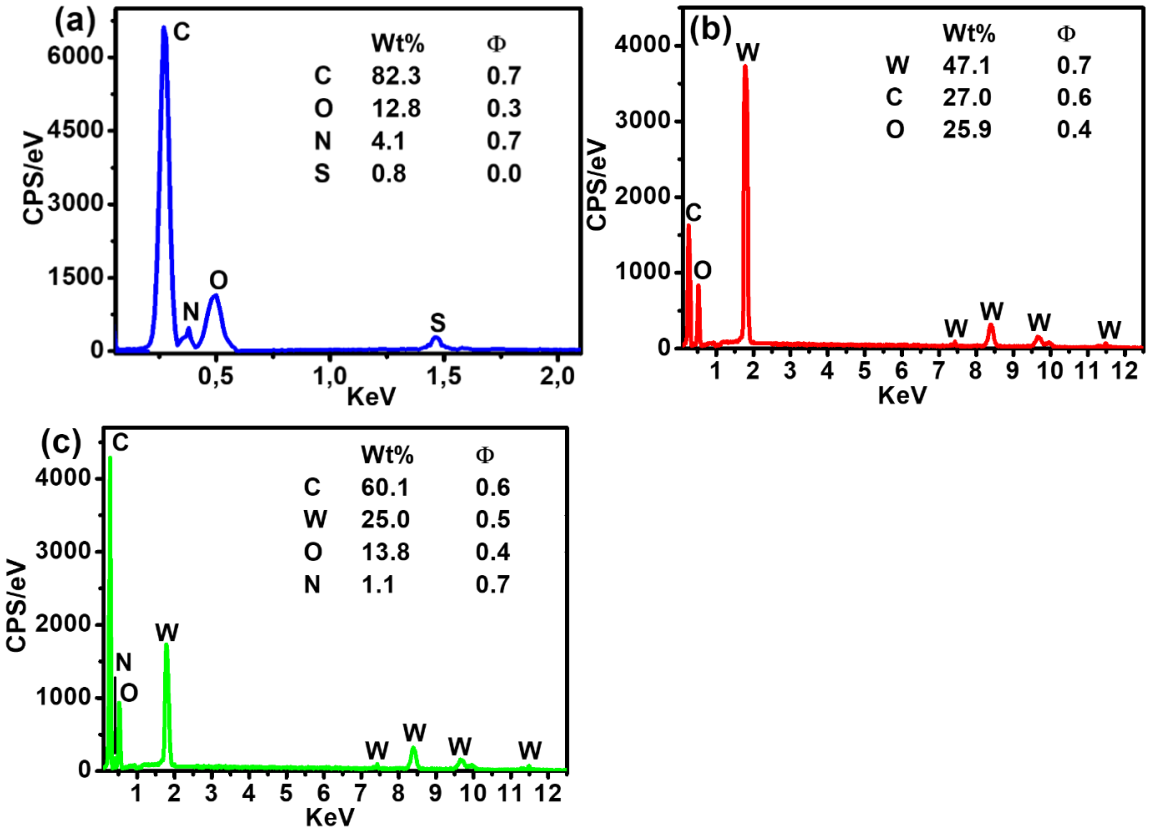

Figure 5.3: EDS Spectra of (a) EG, (b) WO_3 and (c) TWE5

The EDS peaks of the composite confirmed the formation of the TPP, EG and WO_3 composite and the presence of N (1.1 wt %) confirmed the inclusion of TPP (Figure 5.3 (c)). The oxygen deficiency or non-stoichiometric nature of the oxygen in WO_3 and TWE5 (Figure 5.3 (b) and (c)) is a property of photocatalytic materials reported by different authors.[367] This phenomenon has been reported to be a characteristic feature that will enhance photocatalytic performance of the WO_3 nanocomposites[361,368,369] due to creation of defects on the WO_3 surface. Therefore, the nanocomposite is expected to show improved photocatalytic performance in degradation of AB-25 dye due to the oxygen vacancies and formation of surface defects.

5.2.2 TGA and BET

The thermal stability of TPP, EG, WO_3 and 0.5 % TPP composite was investigated by TGA analysis (Fig. 5.4 (a)). WO_3 is thermally stable as supported by literature.[370] The TGA curve of TPP revealed two weight losses. From Figure 5.4 (a), the first decomposition (25

%) from 432 – 550 °C for TPP is attributed to the loss of the phenyl groups attached to the porphyrin microcircle as the porphin microcircle is more stable.[371] and starts decomposing from 550 to 700 °C (75 %). The EG decomposed between 600 °C - 800 °C resulting in 25 % total weight loss. These results agree with most literature values for EG , TPP and WO_3.[205] The TWE5 composite showed two major wight losses confirming the presence of TPP and EG. This further confirmed the stability of nanomaterials and the presence of TPP in the composite at the selected calcination temperature to enhance the photocatalytic performance of theTWR5 nanocomposite.

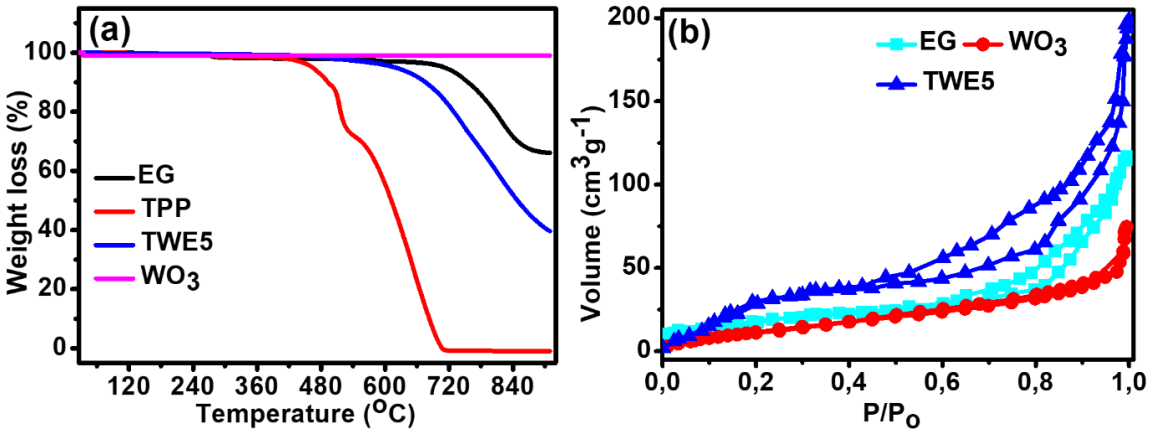

Figure 5.4: (a) TGA of WO_3, EG, TPP and TWE5 and (b) N_2 adsorption desorption of EG, WO_3 and TWE5

Bruner-Emmer-Teller (BET) method was used to obtain the surface area, pore size and pore volume of the prepared nanostructures by nitrogen adsorption/desorption mechanism. The BET plot of WO_3, EG and TWE5 (Figure 5.4 (b)) shows that the graphs are similar to type IV isotherms with different porosity. A hysteresis loop in the nitrogen adsorption/desorption isotherms of EG and TWE5 designates that they are porous while WO_3 is not. The hysteresis loop is a H3 type according to IUPAC (International Union of Pure and Applied Chemistry) classification, consequential of slit-shaped pores amongst analogous sheets.[154] This further confirmed the sheet-like morphology of the synthesised WO_3, EG and TWE5 and their surface areas were (80.2 ± 3), (21.3 ±1) and (49.5 ± 0.9) m^2g^{-1} respectively. The incorporation of WO_3 into EG increased its surface area by more than 50 % increasing the specific surface area to adsorb the pollutant for enhanced photocatalytic degradation.

5.2.3 Raman Analysis

In this study, Raman spectroscopy was employed as a fingerprint of bonding between different functional groups that are present in the synthesised nanomaterials (Figure 5.5). As illustrated, the D, G and 2D peaks in EG were located at 1400, 1600 and 2700 cm^{-1}

respectively. A slight red shift in the 2D peak position of the composites obtained an increase with increasing TPP composition which confirmed bonding between the EG, WO_3 and the porphyrin.

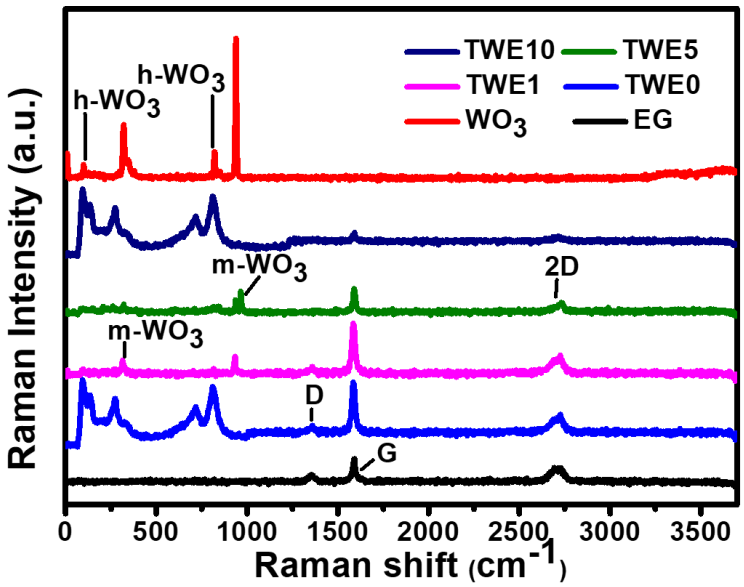

Figure 5.5: Raman results for WO_3, EG, TWE0, TWE1, TWE5 and TWE10

The Raman spectrum of WO_3 showed the W–W bond at 187 cm^{-1}; however, the intensity varied because of the crystallinity of WO_3 nanoparticles which is influenced by porphyrin presence in the composites. Raman peaks appearing at low wavenumbers of 268 and 327 cm^{-1} were assigned to the bending vibration of W–O–W bond. The peaks observed at 716 cm^{-1} and 808 cm^{-1} were assigned to O–W–O stretches and crystalline WO_3 stretching vibration of the bridging oxygen of W–O–W.[295,338] These peaks are characteristic of the monoclinic WO_3 and the abundant hexagonal phase.[186] The I_D/I_G obtained values were 0.39, 0.38, 0.34, 0.12 and 0.26 for EG, TWE0, TWE1, TWE5 and TWE10 composites respectively. The decrease in this ratio after adding 0.5 % of TPP suggest that there was improved reduction in disorder of the carbon material as confirmed by SEM (Figure 5.2 (e)) and EDS results (Figure 5.3 (c)). The presence of the hexagonal WO_3 for TWE0 and the high value of I_D/I_G confirmed that TPP enhances the reduction in the disorder of the carbon material. As can be seen in (Figure 5.5), the peaks of the composite material represented each individual component present except TPP as it is a florescent material. The peaks representing the hexagonal WO_3 increase in intensity with increasing TPP in the composite showing clearly that monoclinic WO_3 is dominant for 0.1 and 0.5 % TPP composites and hexagonal WO_3 is abundant phase at 0 % TPP and 1 % TPP. Therefore, TPP in the composite influences the crystal structure of WO_3 and increasing the amount of TPP resulted in blue shift of m-WO_3 and h-WO_3 for TWE10. The D peak of EG was no longer visible (TWE5) affirming the reduction in disorder of the carbon material by the

TPP. The I_D/I_G ratio of EG was below 0.5 showing more oxidation compared to other results[372] which can be attributed to the time period of the intercalation reaction (48 hours).

5.2.4 FTIR

The chemical environment of all samples was elucidated by Fourier Transform Infrared spectroscopy (Figure 5.6). The results agreed with the Raman results for the prepared nanomaterials. For pristine materials, the broad peak around 3500 cm^{-1} is due to O-H vibrations (Figure 5.6 (a)). The peaks observed at 2859 and 2926 cm^{-1} are attributed to the symmetric and asymmetric stretching vibrations of C-H bonds (Sp^3 hybridised carbon) in EG and TPP, the overlapping peaks of C=N, C=C, C=O, O-H were observed around 1680. Interestingly, the two peaks around this region for WO_3 are due to both O-H (adsorbed water) and C=O and/or C=C from the citric acid used. The C-H peaks (due to Sp^2 hybridised carbon) and NH_4^+ ions appeared around 1380 cm^{-1} with the latter being sharp and intense (Figure 5.6 (a)). The NH_4^+ ions were reported to stabilize the crystal structure of WO_3.[189] The C-H (aromatic) in bending and out bending vibrations appeared between 550 and 750 cm^{-1} for EG and TPP while the broad and intense peak between 500 and 1000 cm^{-1} is due to metal oxygen bond in WO_3. The shoulder around 870 cm^{-1} is attributed to W=O vibrations.

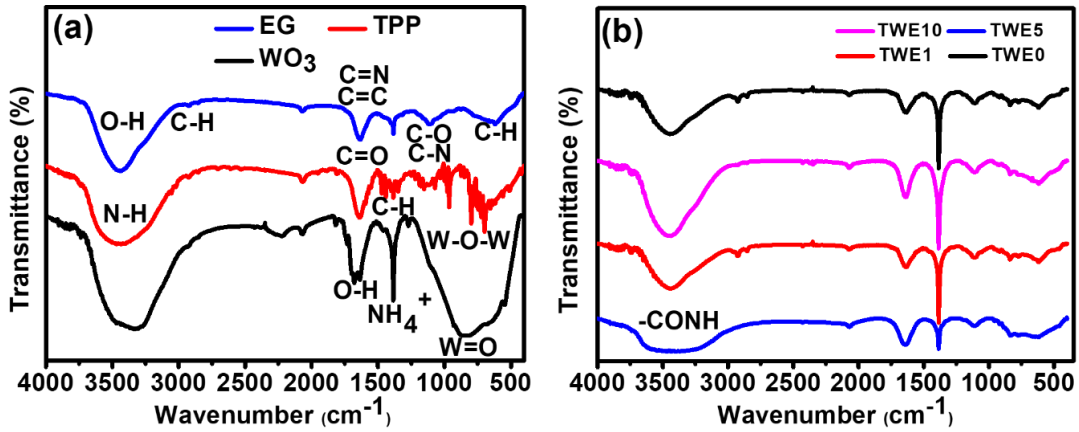

Figure 5.6: FTIR spectra of (a) pristine materials and (b) composites

The spectra of the composites (Figure 5.6 (b)) are identical due to the overlapping peaks of the different materials as discussed above (Figure 5.6 (a)). The composites exhibited a sharp peak around 3500 cm^{-1} (Figure 5.6 (b)) showing the combined effect of O-H and N-H groups. When inspected carefully, TWE5 peak showed a slight shift to 3321 cm^{-1} and became more intense and broader. This, therefore suggests a strong interaction between these groups and can also be attributed to the presence of the -CONH group caused by chemical interaction between TPP, WO_3 and EG when they are functionalised with nitric

acid. Therefore, it can be concluded that for a strong chemical interaction to occur between TPP, WO_3 and EG at the same calcination temperature, it depends on the amount of TPP present with the interaction optimum when 0.5 % TPP is used for both 300 mg of WO_3 and EG in the nanocomposite. Notably, the intensity of the peak due to NH_4^+ ions is high in all composites except the TWE5 showing that the ions strongly adsorbed on these other composites and the adsorption was weaker in the TWE5 nanocomposite. However, the reduction of the intensity of the metal to oxygen bonds seen on WO_3 in the composites and the increase in intensity of the peak at 1644 cm^{-1} in the composite confirms that WO_3 was attached to EG on the C-O bond found on the edges and the C=C of the aromatic phenyl group of TPP. As can be seen (Figure 5.6 (b)), the presence of the pristine materials (TPP, EG and WO_3) in the composites was questionable due to the overlapping peaks.

5.2.5 XRD

XRD is an important technique and has been widely used to identify the crystal structure of compounds. In photocatalysis, crystal structure is important as different crystalline forms of different materials possess different photocatalytic activity while in nanomaterial synthesis, the amorphous form of any material is not preferred except in adsorption studies where only the available surface area and functional groups are important.[373,374] Moreover, different facets and their alignment is important towards exposing the reactive facets for more visible light adsorption as reported by different authors.[375] The phase constitution of pristine materials and the composites were determined by X-ray diffractometry (Figure 5.7). Two characteristic diffraction peaks of EG (Figure 5.7 (a)) located at 2θ equals to 26.9° and 54.95° corresponded to the (002) and (004) crystal planes, respectively. Thus, it can be inferred that the EG maintained the crystal structure of natural graphite (graphite-2H phase according to the standard card of PDF number 41-1487) and belongs to the graphite crystal family.[376] All the discernible peaks in the XRD curve of WO_3 (Figure 8 (a)) were representative of the monoclinic phase (2θ = 21.4, 32.8 and 57.4), orthorhombic phase (2θ = 17.1, 39.8 and 49.4) and the hexagonal phase (2θ = 12.9, 25, 27.2, 28.0, 37.8, 41.6, 43.4, 49.1, 52.2 and 60.4) showing that the hexagonal was predominant than the others. The XRD diffraction pattern of WO_3 showed a multiphase composition,[205,377] containing orthorhombic, monoclinic (JCPDS File no. 43-1035) and hexagonal crystalline phases (Figure 5.7 (a)). The XRD pattern of TPP in the powder form, (Figure 5.7 (a)), showed various peaks with different intensities indexed to a polycrystalline material.[378]

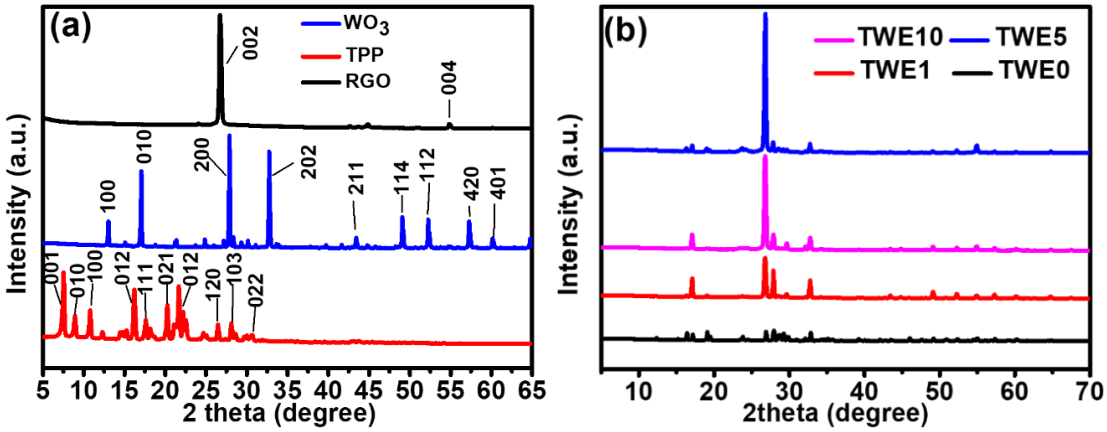

Figure 5.7: XRD spectra of (a) pristine materials and (b) different composites

XRD spectra of the composites (Figure 5.7 (b)) confirmed a mixture of both monoclinic and hexagonal crystal phases in the presence and absence of TPP. Thus, the addition of TPP favours the monoclinic phase of WO_3 only at 0.1 and 0.5 % TPP composites. The obtained results are in good agreement with Raman results (Figure 5.5) which indicated that 1 % TPP exhibited mostly hexagonal crystal phase of WO_3. The crystallite size (nm) (C) of different phases in the samples were determined from the full width at half maximum (FWHM) of the peaks using the Debye-Scherrer equation.[379]

$$\mathbf{C} = \frac{\mathbf{0.9\lambda}}{\boldsymbol{\beta}\mathbf{cos}\,\boldsymbol{\theta}} \qquad \textbf{(5.1)}$$

Where, λ is 0.15418 nm, β is the line width at half height in the radians and θ is the diffraction angle in radians. The results are summarised in table 5.1.

Table 5.1: XRD Data obtained from the different samples

Sample	2θ (º)	d (nm)	C (nm)	EG layers (n)
WO_3	28.0	0.2633	33.6549	-
TPP	7.6	0.9611	32.7222	-
EG	26.8	0.3306	29.0447	67
TWE0	28.4	0.3134	32.5141	79
TWE1	26.8	0.3294	29.0386	67
TWE5	26.8	0.5112	32.4648	75
TWE10	26.8	0.3156	28.1519	68

The full width at half maximum (FWHM) of the diffraction peaks at 2θ values of 17.1°, 32.8° and 27. 2° were used in the Scherrer equation to calculate the crystallite sizes of the orthorhombic, monoclinic and hexagonal phases respectively. The average of these measurements was used as a crystallite sizes for the three phases. The value of C and d showed an increase when 0.5 % TPP was added compared to EG and a decrease when

0, 0.1 and 1 % were used. The number of EG layers were calculated by dividing C with d after adding 0.1 nm. The number of EG layers is equal (0.1 % TPP) or more (0, 0.5 and 1 % TPP) than in pristine EG. This confirmed the successful formation of the composites with the highest value obtained in the absence of TPP. Moreover, the values of d and C for TWE5 were also high which resulted in high specific surface area in the composite (Figure 5.4 (b)) compared to EG. The results confirmed the rod shaped hexagonal WO_3 while the spherically shaped monoclinic is in agreement with the SEM results (Figure 5.1 and 5.2).

5.3 Optical properties

5.3.1 Photoluminescence (PL)

Photoluminescence (PL) emission is due to recombination of free charge carriers and its spectra are useful to survey the separation efficiency of the photogenerated charge carriers in a semiconductor.[154,380] The higher the PL intensity, the higher the probability of charge carrier recombination. The photoluminescence spectra for the different nanocomposites were compared with the one for pristine WO_3 (Figure 5.8).

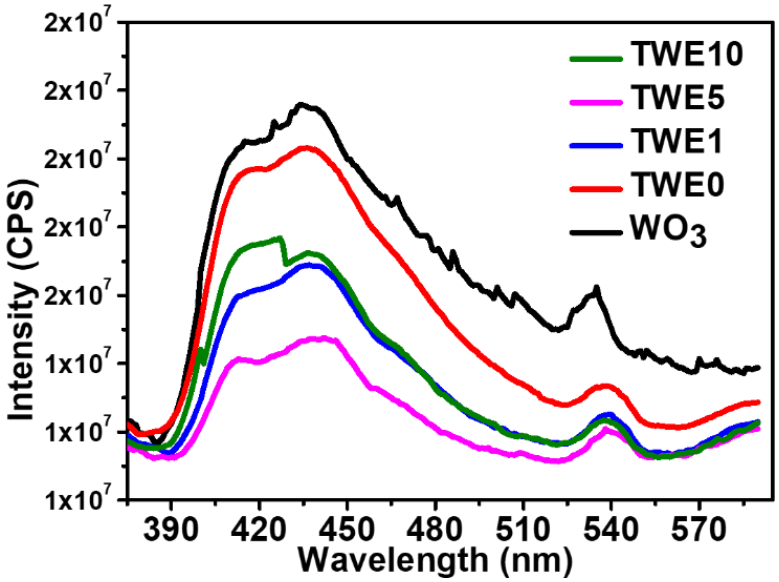

Figure 5.8: PL spectra of WO_3, TWE0, TWE1, TWE5 and TWE10 composites

As can be seen, the presence of 0.5 % of porphyrin in the nanocomposite matrix (TWE5) resulted in the lowest intensity (CPS) on the PL spectra. Decreasing or increasing the TPP composition results in high intensities suggesting high electron hole recombination. However, there was generally a reduction in the electron hole recombination compared to pristine WO_3. Addition of EG to WO_3 had little effect in the reduction of the electron hole recombination suggesting that TPP also contributes in the reduction of recombination of photoexcited electrons and holes in the nanocomposites. This could suggest that a p-n

heterojunction is formed between TPP and WO_3 that helps in reduction of photoexcited electrons and holes as reported for π conjugated semiconductors with WO_3 by other researchers.[375,381] Therefore, EG, and TPP had a combined effect towards the reduced recombination rate of photoexcited electron hole pairs in all the composites where they were both used (TWE1, TWE5 and TWE10) with the optimum observed for the TWE5 nanocomposite.

5.3.2 UV-Vis

The UV/Vis spectrophotometry was employed in this study to monitor the changes in the bandgaps of different materials. The bandgaps were calculated from the UV/Vis absorbances of the solid samples (Figure 5.9), since they are important parameters in photocatalysis that determine the amount of energy required to cause photoexcited electrons and holes pairs. The photoexcited electrons and holes pairs triggers the formation of reactive oxygen species (ROS) that are responsible for degradation of organic pollutants.[368,375] TPP and the synthesized WO_3 showed absorbance in the visible range of the solar spectrum (Figure 5.9 (a)). In contrast, TPP exhibited multiple absorption peaks in the visible range due to Soret band that had the edge around 425 nm and G bands with the absorption maxima around 540 nm, 560 nm, 620 nm and 700 nm that are matched to the $\pi \rightarrow \pi^*$, $\pi^n \rightarrow \pi^*$, and the excitation of delocalised π electrons of the aromatic macrocycle ring respectively. Moreover, the attached benzyl groups also undergo electron excitations to result in another absorption peak in the UV region. WO_3 had its absorption edge around 490 nm and confirmed that it absorbs visible light.

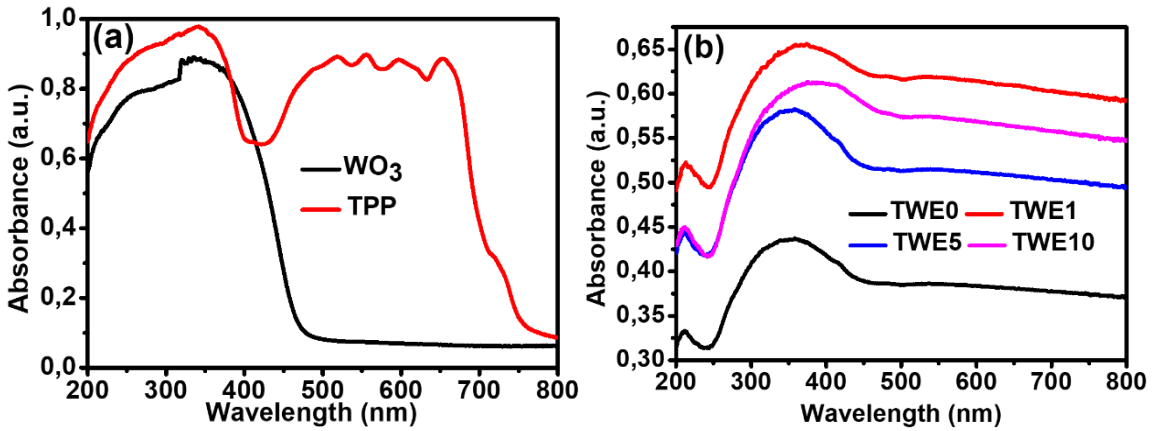

Figure 5.9: UV-Vis absorption for solids (a) WO_3 and TPP, and (b) TWE0, TWE1, TWE5 and TWE 10

When the TTP material was absent, the TWE0 composite obtained the smallest absorption intensity in the UV-Vis region and the smallest absorption edge (500 nm). Interestingly, the 0.1 % and the 1 % TPP composites showed very strong absorption edges (above 700 nm) while the 0.5 % TPP nanocomposite shifted absorption edge of

pristine WO_3 from around 490 nm to 600 nm (Figure 5.9 (b)). The greater shift of the absorption edge by 0.1 and 1 % implies that they have small bandgaps and hence they require less energy for photoexcitation . The difference in absorbances of the different catalysts confirms their different bandgaps which were estimated from absorption spectra using the relationship:

$$\mathbf{hv\ (eV)} = \frac{\mathbf{hc}}{\boldsymbol{\lambda}} = \frac{\mathbf{1239.8}}{\boldsymbol{\lambda}} \qquad \textbf{(5.2)}$$

where hv is the bandgap energy, h is planks constant, c is the speed of light. The path length (l) of light through the material (sample thickness for solid samples), absorbance (A) and absorption coefficient (α) are related by Equation 5.

$$\boldsymbol{\alpha\ (cm^{-1})} = \frac{\mathbf{lin\ (10)} * \mathbf{A}}{\mathbf{l\ (cm)}} = \mathbf{lin\ (10)\varepsilon l} \qquad \textbf{(5.3)}$$

According to Davis and Mott relationship for values of α (cm^{-1}) above 104 cm^{-1}, the data follows a power-law behaviour which is known as the Tauc relationship (Equation 6).

$$\boldsymbol{\alpha hv = A(hv - E_g^{opt})^n} \qquad \textbf{(5.4)}$$

where A is a parameter that depends on the transition probability, α is the absorption coefficient, E_g^{opt} is the optical bandgap and n is a number which characterize the transition process and can take values of 2, 2/3, ½ or 1/3 for direct (allowed), direct forbidden, indirect (allowed) and indirect forbidden transitions respectively. Tauc plots of $(\alpha hv)^n$ vs. *h*v estimate the bandgap when extrapolated with the best possible fit to the baseline at y = 0. The best possible fit for WO_3 was for the direct allowed transition (Figure 5.10) and gave a bandgap of 2.59 eV.

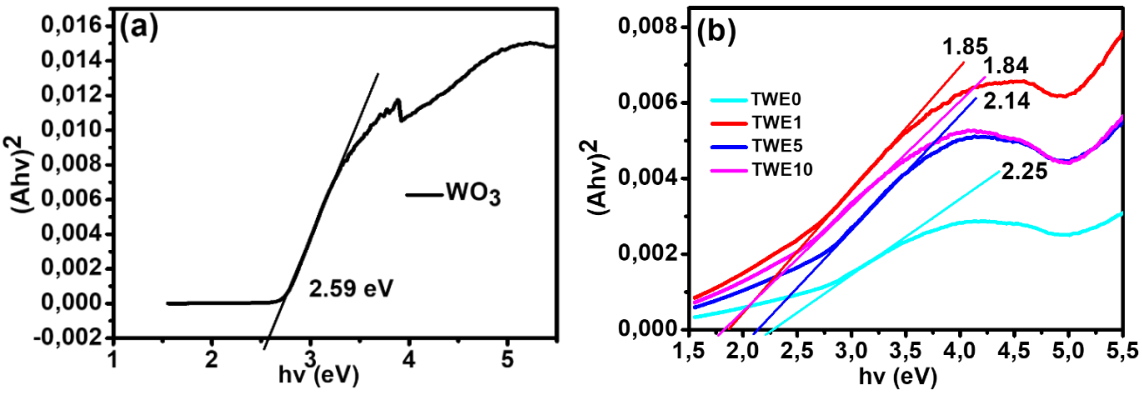

Figure 5.10: Tauc plot of WO_3, TWE0, TWE1, TWE5 and TWE10

The optical bandgap of the composites is the lowest energy required to cause photoexcited electron - hole pairs. However, the real picture is more complicated, since the energy of an unoccupied state is changed upon occupation.[364] The optical bandgaps of both the 0.1 and 1 % TPP composites were very low (1.85 and 1.84 eV respectively) as seen from the UV/Vis absorption results that they shifted the absorption of the WO_3 to above 600 nm (Figure 5.9). When 0.5 % TPP was used, the bandgap was 2.14 eV. The highest bandgap of 2.25 eV was achieved in the presence of WO_3 and EG (0 % TPP or TWE0). Therefore, EG and TPP lowered the bandgap of WO_3 from 2.59 eV. This implies that they did not only reduce the recombination of photoexcited electrons and holes as seen from the PL spectra (Figure 5.9) but also reduced the energy required to cause photoexcitation. Photoexcitation of electrons and holes is initiated by absorption of quantum amount of energy equals to the bandgap of the semiconductor and initiate formation of reactive oxidising species (ROS) such as hydroxyl radicals and superoxide anion radicals that are required for photodegradation of pollutants.

5.4 Degradation of AB-25 dye

The degradation measurements of AB-25 at pH 5 were performed in the presence of 20 ppm of dye, 500 mgL^{-1} of catalyst and 50 ml solution (Figure 5.11 (a)). The reported results showed the reduction in absorbances over a period of 180 minutes.

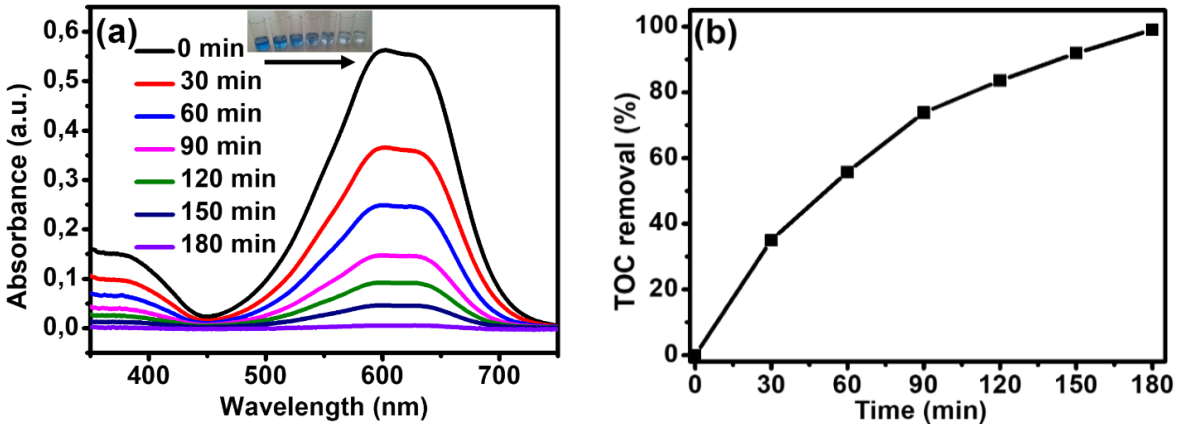

Figure 5.11: Degradation of 20 ppm dye solution 50 ml with 25 mg TWE5 at pH 5

The reduction in the absorbances of the AB-25 dye shows that the chromophore and the auxochrome of the dye was degraded and there was reduction in colour intensity (to a clear solution) as shown by the insert of sampled aliquots at different time intervals. The TOC results confirmed that the chromophore and auxochrome of AB-25 dye were indeed degraded (Figure 5.11 (b)) to 99 % efficiency. The performance of the catalysts was studied for degradation of AB-25 dye by varying different parameters (catalyst amount,

dye concentration, pH of the dye solution and different amounts of TPP) to study their effect on degradation efficiency (Figure 5.12).

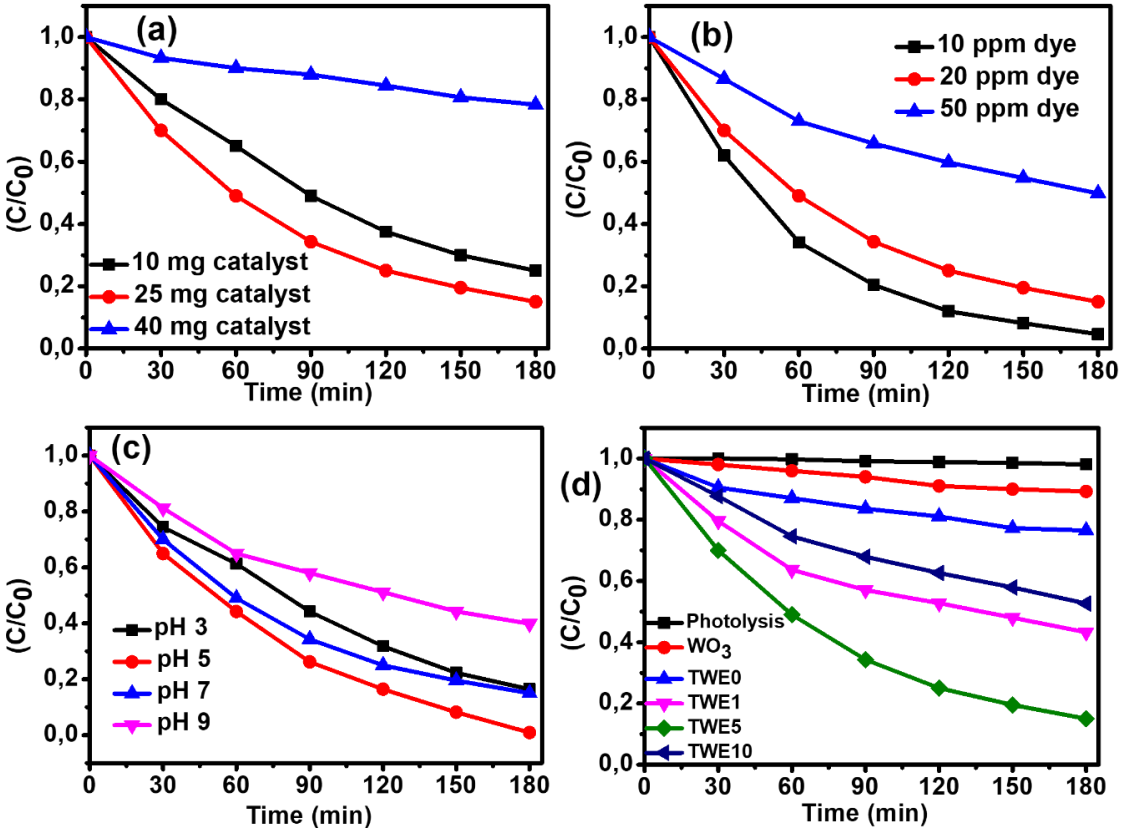

Figure 5.12: Variation of (a) catalyst concentration, (b) dye concentration, (c) pH of solution and (d) TPP amount on the degradation of AB-25 at pH 7

All the experiments were performed at pH 7 (Figure 15.12 (a), (b) and (d)) and the results were further used to study the behaviour of the catalyst under different conditions.

5.4.1 Optimisation of catalyst concentration

Different amounts of catalysts were used for degradation of dye (Figure 5.12 (a)). The obtained efficiency was 22 %, 85 % and 8 % after 180 minutes for 10, 25 and 40 mg catalyst amounts, respectively. The change in degradation efficiency can be ascribed to less adsorption and desorption at low catalyst amount of 10 mg and the obstruction of light at high catalyst amount of 40 mg. At 25 mg, there is enough photocatalytic active sites for adsorption of dye and desorption of degraded by-products, as well as illumination of light to produce photoexcited electrons and holes pairs resulting in the high degradation efficiency.[382]

5.4.2 Optimisation of dye concentration

The dye concentrations selected for optimisation were chosen on the basis that the normal range of dye concentrations found in discharged industrial effluents ranges between 10-50 ppm according to literature.[383] The selected dye concentrations were 10, 20 and 50 ppm with removal efficiencies of 98, 85 and 49 % respectively (Figure 5.12 (b)). When less dye molecules are present, adsorption and desorption occur at a faster rate for both the dye and intermediate products resulting in a high efficiency while more dye molecules reduce the rate of adsorption and desorption resulting in low efficiency. The optimum amount of catalyst concentration to degrade AB-25 dye is determined to be 500 mg/L, degrading 50 ml of 10 ppm solution. However, the same catalyst can be used to degrade dye solutions from 20 ppm with efficiency above 85 %. Therefore, 20 ppm dye concentration was used to optimise the pH and TPP composition.

5.4.3 Pollutant pH optimisation

The effect of the pH may result in different catalyst surface charges and different ionic behaviour of the pollutant. When adjusting pH, the nature of solution can either augment or impede photocatalytic degradation ability. The selected pH values were 3, 5, 7 and 9 for degradation of 20 ppm dye and efficiencies of 84, 99, 85 and 60 % were calculated respectively (Figure 5.12 (c)). In this case, the addition of sodium hydroxide resulted in decrease in efficiency as there is competition of active sites on the catalyst surface due to the presence of the hydroxide anions. At pH 7, there is little adsorption of dye which increases as the dye becomes easily protonated at low pH values (acidic). The improved efficiency at pH 5 is because the chromophore of acid blue 25 (sulfonate anion) is easily protonated leaving the dye negatively charged resulting in more interaction which eventually leads to high degradation efficiency. Further decrease in pH to 3 decreases the efficiency to 84 %. However, the hydroxyl radical scavenging effect of chloride ion from HCl (Equation 7 and 8) results in inhibition of degradation at pH 3.

$$Cl^- + {}^{\bullet}OH \rightarrow HClO^{\bullet-} \quad (5.5)$$

$$HClO^{\bullet-} + H^+ \rightarrow Cl^{\bullet} + H_2O \quad (5.6)$$

The inorganic radicals ($Cl^{\bullet}$ and $HClO^{\bullet-}$) are less reactive in photocatalytic degradation than the hydroxyl ion radical thus reducing the overall efficiency of the process.

5.4.4 Optimisation of TPP composition

The prepared nanocomposites (WO_3, TWE0, TWE1, TWE5 and TWE10) were tested for photocatalytic degradation of AB-25 in addition to photolysis (Figure 5.12 (d)). The efficiencies were calculated to be 0, 11, 24, 57, 85 and 47 % for photolysis, WO_3, TWE0, TWE1, TWE5 and TWE10 respectively. As indicated in Raman spectra results the efficiency patterns at TWE0 and TWE10 showed defects due to Sp^3 hybridised carbon and the TWE10 was mostly hexagonal WO_3. Other reasons for this decrease in efficiency can be attributed to the aggregation and rod-shaped nanoparticles as illustrated by SEM images (Figure 5.1 (c) and (f)). It is obvious that monoclinic WO_3 as shown by XRD showed high degradation as the presence of this phase in TWE1 and TWE5 composites gave high efficiency of degradation. Moreover, their SEM images showed spherical particles evenly distributed with minimum aggregation (Figure 3 (d) and (e)). The FE-SEM images of TWE5 showed that they form spherical particles that assemble into 3D plates that are deposited on the surface of EG without completely covering the surface of EG. This improves the degradation of AB-25 by ensuring that the photogenerated electrons reach the surface of EG where some of the pollutant is adsorbed. It is believed that this improves the efficiency of the nanocomposite together with the monoclinic phase of WO_3 which is present in the TWE5 nanocomposite as confirmed by XRD spectra (Figure 5.7 (b)). Comparing the results of the PL spectra (Figure 5.8), UV/Vis and estimated bandgaps with respect to the observed efficiencies for AB-25 degradation, the low optical bandgap semiconductors required less energy to get excited but were also characterised by high electron hole recombination which reduced their efficiency. The optimum catalyst (0.5 % TPP) had an optical bandgap of 2.14 eV and the lowest PL intensity peak showing efficient separation of photoexcited charge carriers.

5.4.5 Reaction Kinetics

The degradation of organic pollutants can be monitored by the change in reagent concentration with time giving rise to different models to analyse the rate at which the reaction occurs. The Langmuir-Hinshelwood (L-H) model is popular in organic pollutants degradation.[154] It works on the assumption that at trivial initial concentrations (C_0) (like most organic pollutants) the reaction follows the pseudo-first order kinetics model.

$$\mathbf{ln}\left(\frac{\mathbf{Co}}{\mathbf{C}}\right) = \mathbf{Kt} \qquad \textbf{(5.7)}$$

where C is the concentration at irradiation time of t. K is the apparent first-order rate constant that can be determined from the slope of a plot of ln (C_0/C_t) vs t. The graph for different rate constants (Figure 5.13) was derived from the optimisation of TPP amount.

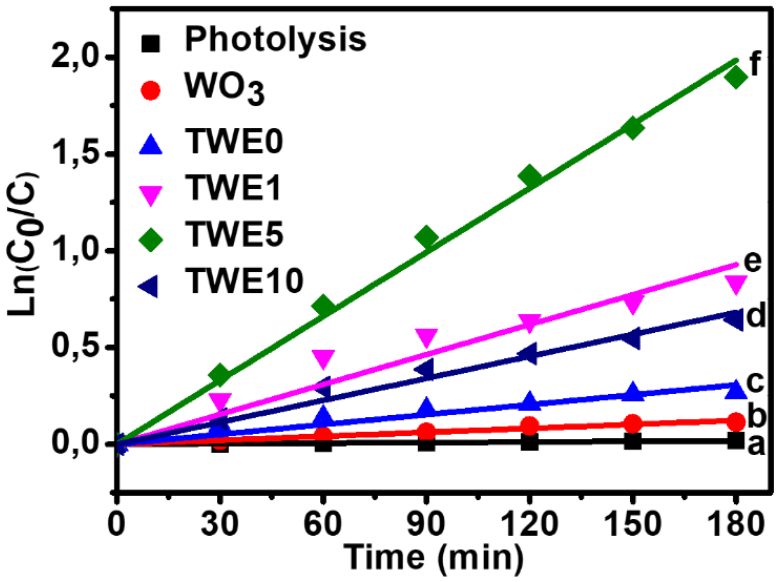

Figure 5.13: Rate constants for (a) Photolysis, (b) WO_3, (c) TWE0, (d) TWE10, (e) TWE1 and (f) TWE5

The values of linear regression for all composites were high and confirmed that this data was suitable for L-H model. From Figure 5.13, the slope is the rate of photocatalytic degradation (min^{-1}), and the higher the rate, the faster the reaction. The reaction rates were determined to be 0.000098 min^{-1}, 0.000686 min^{-1}, 0.0017 min^{-1}, 0.00515 min^{-1}, 0.01102 min^{-1} and 0.00379 min^{-1} for photolysis, WO_3, TWE0, TWE1, TWE5 and TWE 10 respectively. The rate of photolysis of (AB-25) was very slow that it can be ignored (Figure 5.13). The presence of TPP enhanced the degradation of AB-25 dye under visible light irradiation when compared such that it became 16 times the rate of pristine WO_3 and 6 times the rate when only EG is added and 2 times the rate of TWE1. However, much higher amounts of TPP (TWE10) reduced the photocatalytic rate due to high electron hole recombination. Consequently, the degradation of acid blue 25 followed the pseudo-first order L-H model with a high rate constant compared to other literature values[98] for the degradation with porphyrin composites in the visible range of the solar spectrum.

5.4.6 Catalyst photostability and reusability

The photostability and reusability of the synthesized photocatalysts were further evaluated by conducting recycling tests to an optimized TWE5 composite through photodegradation of AB-25 dye for five cycles under the same conditions. After each cycle, the recovered sample was centrifuged and dried at 60 °C for 8 hours. The obtained sample was weighed

to reaffirm that the subsequent cycles are performed with equal amount of the catalyst and losses were corrected by adding fresh catalyst. The optimum conditions were selected for all reusability studies; 20 mg catalyst degrading 50 ml of 20 ppm AB-25 at pH 5 (Figure 5.14).

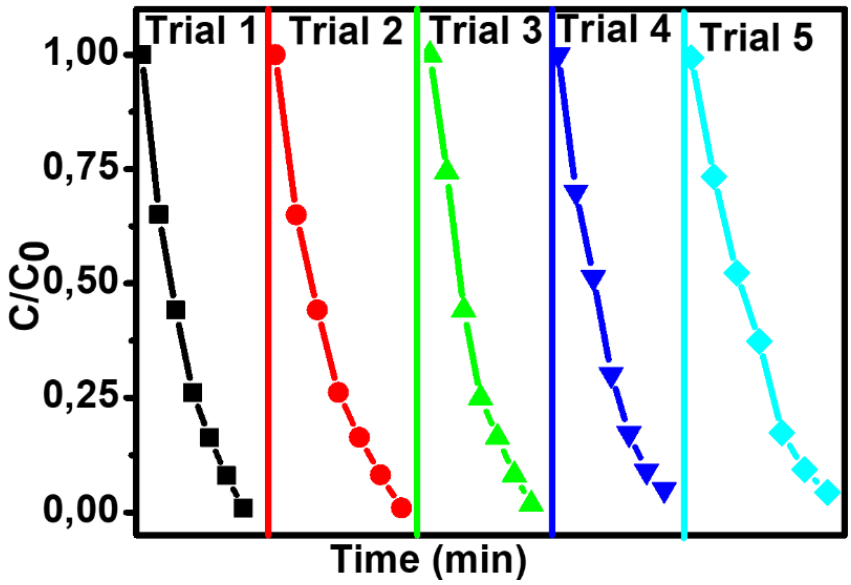

Figure 5.14: Stability of TWE5 at pH 5 for 20 ppm dye

The obtained efficiency was found to be 99.2, 99.0, 98.3, 95.1 and 94.8 % for cycles 1, 2, 3, 4 and 5 respectively. This catalyst is stable and can be reused five times without affecting its efficiency. Moreover, the small decrease in efficiency after recycling suggest that more repeatability tests can be done to determine after how many cycles the catalyst efficiency is considerably reduced. The similarity in the degradation curves also suggest that degradation of AB25 dye by recycled catalyst follows almost similar mechanism and the washing and drying had minimal effect on the overall structure, morphology and crystallinity of the TWE5 nanocomposite.

5.4.7 Reactive species

Several reports have confirmed the reactions between water and photogenerated holes ($H^+ + H_2O \rightarrow H^+ + {}^{\bullet}OH$), and oxygen with photogenerated electrons ($e^- + O_2 \rightarrow {}^{\bullet}O_2^-$) for formation of reactive oxidizing radical species (ROS) such as hydroxyl radicals (${}^{\bullet}OH$), super oxide anion radicals (${}^{\bullet}O_2^-$) and hydrogen peroxide (H_2O_2).[366,369] Except the direct decomposition of organic compounds with photogenerated holes (H^+ + organics → CO_2+H_2O), ROS partake in the degradation of aqueous organic compounds.[380,384] The mechanism responsible for visible light induced catalysis was probed with the aid of conducting scavenger experiments and comparing them with the reaction when no scavengers are added under optimum conditions (25 mg catalyst degrading 50 ml of 20

ppm pollutant at pH 5). Figure 5.15 shows the results obtained in the presence of ethylene diamine tetra-acetic acid sodium salt (EDTA, 5 mmol L^{-1}) and tert-butanol (t-Butanol, 1.5 mL) to probe the mechanism responsible for the visible light induced photocatalysis of acid blue 25 dye.

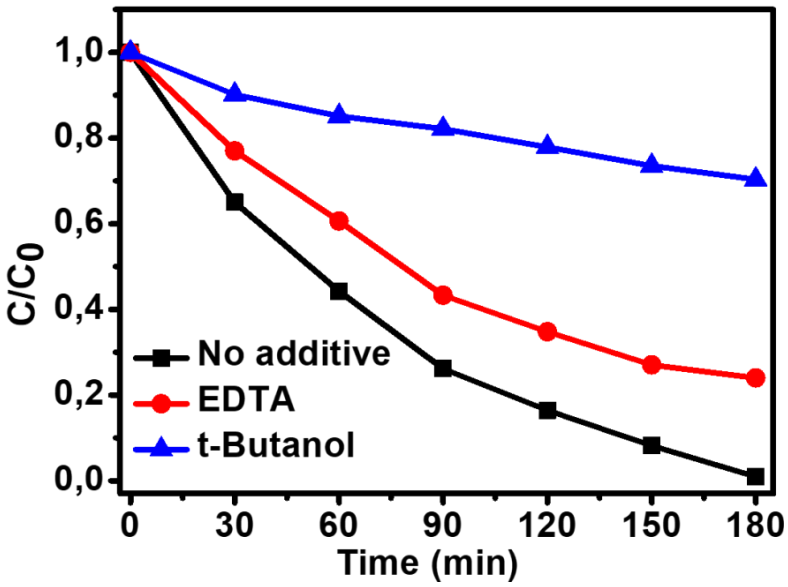

Figure 5.15: Comparison of effect of different scavengers on degradation of AB-25

Several reports have used different scavengers for quenching of different ROS towards degradation of organics.[385,386] EDTA and t-Butanol were used as holes and hydroxyl radical scavengers respectively. The addition of EDTA confirmed the activity of the photoexcited holes towards degradation of AB-25 as it decreased the reaction efficiency by 23 %. Inter alia, the addition of t-Butanol reduced the efficiency by 69.4 % and proved the hydroxyl radicals are the most reactive species involved in the degradation of AB-25. The combined effect of the two scavengers used to trap the H^+ and hydroxyl radical species suggest that there is another ROS involved in the degradation of AB-25 that is expected to be the superoxide anion radical ($^{\bullet}O_2^-$) according to literature.[360,368,387]

5.5 Proposed degradation mechanism

According to UV/Vis results, PL spectra, reactive species determination, the bandgap calculations and some literature,[361,378,381,388] the mechanism involved under visible light for degradation of acid blue 25 with TPP/WO_3/EG nanocomposite was proposed (Figure 5.16). Both WO_3 and TPP are visible light active and they will absorb radiation energy equivalent to their respective bandgaps. After absorption of the energy, photoexcited electrons and holes will be formed with respect to their respective valence band and conduction band edge potentials especially for WO_3 as delocalised electrons excitation in TPP which requires the smallest energy can easily get excited to their singlet and triplet

excited states without formation of holes. In order to clarify the separation of photogenerated electron-hole pairs and to understand the possible ROS that can be formed due to photoexcitation of the nanocomposite, the band edge potentials, versus (VS) normal hydrogen electrode (NHE), of WO_3 semiconductor are calculated. It is necessary to find out the conduction band (CB) and valence band (VB) potentials of the WO_3 and they were calculated by ($E_{CB} = \chi - E^e - 0.5E_g$) and ($E_{VB} = E_{CB} + E_g$). Where E_{VB} and E_{CB} are the VB and CB potentials, respectively. Moreover, E^e is the energy of free electrons vs. hydrogen (4.5 eV)[389] and χ is the electronegativity of semiconductor determined by ($\chi = [(A)^a\ X\ (B)^b]^{1/(a+b)}$). Here a and b are the number of atoms A and B in the compound. The values of E_g and χ for WO_3 are 2.59 and 6.3 eV, respectively. Therefore, the E_{CB} and E_{VB} of WO_3 were calculated to be +0.5 and +3.9 eV respectively VS NHE. According to the conduction band potential of WO_3, it cannot directly reduce oxygen to the superoxide anion radical ($O_2/{}^{\bullet}O_2^-$ = -0.33 VS NHE), but it can convert it to H_2O_2 (O_2/H_2O_2 = +0.693).[390]

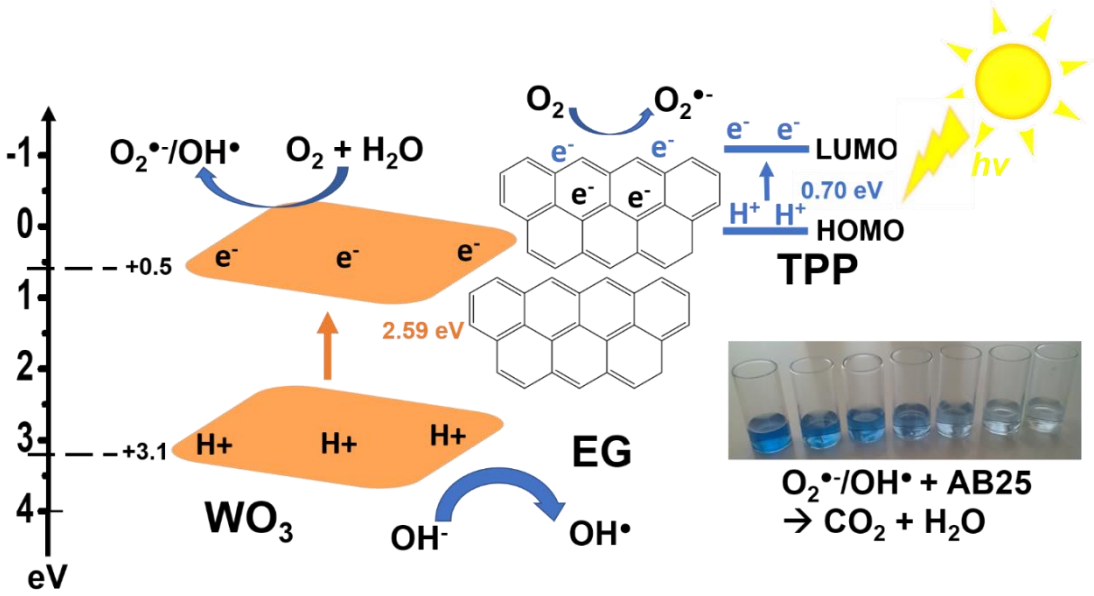

Figure 5.16: Proposed charge transfer and degradation mechanism

EG material caused a remarkable increase in the available surface area for pollutant adsorption and improved the efficiency of photocatalytic reaction by accepting and transporting the photoexcited electrons to reduce the probability of them recombining with the holes. The use of TPP as a photosensitizer is important as it has delocalised electrons that can be easily excited upon irradiation with visible light energy. The whole process in the nanocomposite is further enhanced by the presence of EG that has electron trapping and transporting properties. Therefore, the photoexcited electrons and holes recombination in the nanocomposite is reduced. The process of TPP-WO_3 photocatalytic

reaction is initiated by the excitation of the ground state of WO_3 and the sensitizer (TPP) via one photon transition (hv) to its singlet excited state $^1[TPP]^*$ while the triplet state $^3[TPP]^*$ of the sensitizer occurs due to intersystem crossing (Equation 5.8). Both excited states can produce superoxide anion radical ($^\bullet O_2^-$) with molecular oxygen under solar irradiation (Equation 5.9) which can undergo multiple radical chain reactions to form the highly reactive hydroxyl radicals $^\bullet OH$ (Equation 5.10)[391]. Moreover, the other reactions are summarised by Equations 5.11-5.14 to show how the specific ROS are produced and their activity in improving photocatalytic reactions.[381,384] The electrons adsorbed on the surface of EG can react with adsorbed oxygen to generate the superoxide anion radical while the ones on the conduction band of WO_3 react with water to form hydrogen peroxide and hydroxyl anions. Further reactions will involve the hydrogen peroxide dissociation into hydroxyl radicals under visible light irradiation. The generated radicals will then degrade AB-25 as shown by Equations 5.15 and 5.16.

$$[TPP]WO_3 + hv \rightarrow {}^1[TPP]^*WO_3 + isc \rightarrow {}^3[TPP]^*WO_3 \quad (5.8)$$

$$^1[TPP]^*WO_3/{}^3[TPP]^*WO_3 + O_2 \rightarrow [TPP]^+WO_3 + {}^\bullet O_2^- \quad (5.9)$$

$$[TPP]^+WO_3 + OH^- \rightarrow [TPP]WO_3 + {}^\bullet OH \quad (5.10)$$

$$O_2 + e^- \rightarrow O_2^- \quad (5.11)$$

$$O_2^- + e^- \rightarrow {}^\bullet O_2^- \quad (5.12)$$

$$O_2 + H_2O + e^- \rightarrow H_2O_2 + OH^- \quad (5.13)$$

$$H_2O_2 + hv \rightarrow 2OH^\bullet \quad (5.14)$$

$$AB\text{-}25 + {}^\bullet O_2^- \rightarrow H_2O + CO_2 \quad (5.15)$$

$$AB\text{-}25 + {}^\bullet OH \rightarrow H_2O + CO_2 \quad (5.16)$$

The photoexcited electrons (singlet and triplet) excited states can also be transported by the exfoliated graphite for enhanced efficiency of photocatalysis. Moreover, it has been reported after experimental findings and density functional theory calculations that in the presence of an electron mediator like exfoliated graphite, a strong metal ligand charge transfer effect causes the transfer of electrons between semiconductors in the presence of delocalised π electrons through π→π* transitions or crosslinking's between π→π transitions.[364,392] The separation is enhanced by the ability of EG to shuttle electrons. This electron transport phenomenon minimises the chance of recombination of the photoexcited electrons and holes. Moreover, the holes in the valence band of WO_3 can form hydroxyl radicals which will also be involved in the dye degradation. This is because the valence band edge potential of WO_3 is more positive (+3.1) than the energy required

to oxidise hydroxyl anion into the hydroxyl radical ($OH^-/OH^\bullet$ = +2.7 eV VS NHE). Therefore, this resulted in the synthesised nanocomposite having appropriate band edge potentials for water splitting i.e. the formation of hydroxyl radicals and superoxide anion radicals for complete mineralisation of Acid blue 25.

CHAPTER 6

CO_3O_4/WO_3 P-N HETEROJUNCTION PHOTOCATALYST FOR DEGRADATION OF DICLOFENAC SODIUM

6.1 Introduction

Diclofenac sodium (DFC) is a member of NSADs with high consumption rate and frequent detections in surface waters by numerous authors even in South Africa. There has been reports on its negative effects on aquaculture and wildlife with the most common example being the death of vultures after feeding on dead animal carcasses injected with this drug.[393] Therefore, numerous reports exist even today where different methods are evaluated for removal of DFC in water. Visible light driven photocatalytic degradation of materials was explored here by generation of a heterostructure between p-type Co_3O_4 and n-type WO_3. The generation of p-n heterostructures is a strategy that have been used to enhance the photogenerated charge separation and electronic properties of semiconductors for different applications. P- type semiconductors are normally electron donating with their fermi level energy closer to the valence band while n-type semiconductors are nucleophilic with fermi level energy closer to their conduction band. A strategy that has gained attention recently involves facets engineering and there is petite information to observe the effect of facets engineering (through solvothermal methods) in enhancing photocatalytic degradation of organic pollutants.

This work concentrated on adding to this phenomenon by analysing a Co_3O_4/WO_3 nanocomposite through a solvothermal method outlined in **Section 3.2.10** with several defects and enhanced photocatalytic performance for degradation of DFC. The strong reduction in photoexcited electrons and holes and increased crystallinity was the driving force for strong interaction with DFC. Moreover, the synergy due to each semiconductor in the working composite was evaluated. To postulate a conceivable mechanism for the enhanced photocatalytic activity of the in-situ synthesised Co_3O_4/WO_3 for the removal of organic pollutants, different parameters were evaluated in order to understand the enhanced activity of the synthesised material.

6.2 Results and discussion

Accessible techniques were used to study the structural, physical, chemical and optical properties of the synthesised nanomaterials and the Co_3O_4/WO_3 composites were labelled CW1, CW2, CW2A and CW3 for 0.01 M, 0.02 M and 0.03 M concentration of cobalt (II) acetate used as outlined in **Section 3.2.10** and A was used to differentiate the 0.02 M prepared sample before and after calcination. Moreover, studies were conducted to predict the involved reactive species to propose degradation mechanism, study the intermediates formed during the degradation with HPLC-QTOF-MS to confirm mineralization, and to study the coking effects of DFC on the reused catalyst after evaluation of its stability.

6.2.1 FTIR

The FT-IR analysis was done to evaluate the surface functional groups of the as-prepared materials (Figure 6.1). The band at 568 cm^{-1} was assigned to Co^{3+}-O stretching vibration mode and the one at 660 cm^{-1} was assigned to the vibration of Co^{2+}-O bond.[225] The bands at 3420 and 1645 cm^{-1} were assigned to the stretching and bending vibrations of absorbed water molecule on Co_3O_4, WO_3 and the synthesised nanocomposites[394] while the W-O bond appeared as a band between 1000 and 500 cm^{-1} in the pristine WO_3 but it increased to around 1200 cm^{-1} in the composites. The increase of the metal - oxygen bond vibrations in the composites could suggest an interaction between WO_3 and Co_3O_4.

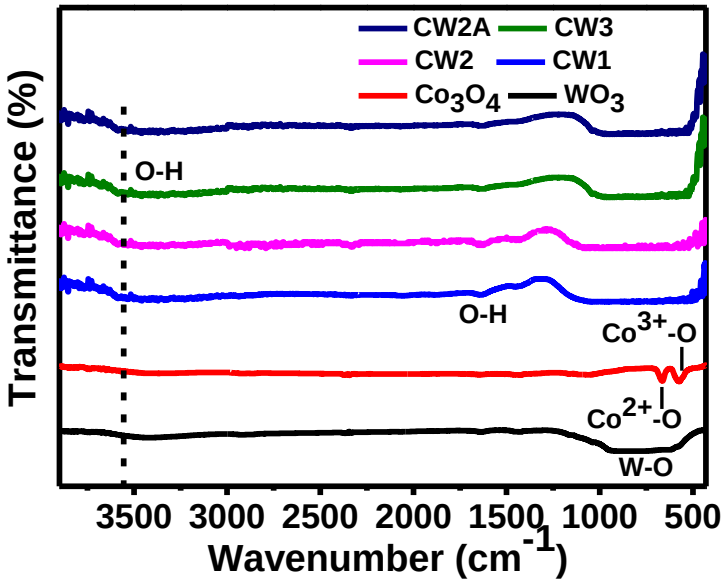

Figure 6.1: FTIR results of as synthesised materials

The interaction through the metal oxygen bonds can suggest that mixing of the p orbitals of the oxygen atoms occurred and caused an oxygen deficient nanocomposite with the weak Van der Waal forces and hydrogen bonding to improve the transfer of electrons and

holes to effectively improve the electron hole recombination and subsequently improve photocatalytic activity. Therefore, it was also observed that the interaction decreased with increase in the amount of Co_3O_4.

6.2.2 XRD

XRD analysis was performed to determine the crystalline phases of the as synthesised nanocomposites. Figure 6.2 (a) shows the representative XRD pattern of prepared Co_3O_4. All reflection peaks at 2θ of 19.1, 31.2, 36.89, 38.66, 42.42, 44.77, 55.59, 59.35 and 65.35 degree were due to 111, 200, 311, 222, 200, 400, 422, 511 and 440 planes and can be indexed to the cubic phase of Co_3O_4 (space group Fd3m) which is consistent with the value given in the standard card (ASTM no. 01-073-1701) and literature [281,395]. No other impurities were detected in the XRD pattern, indicating the high purity of the product. Moreover, monoclinic WO_3 (JCPDS No.72−0677) was synthesised as confirmed by its XRD spectra (Figure 6.2 (b)). The peaks at 2θ of 10.79, 23.05, 23.71, 24.38, 26.51, 34.10, 41.69, 49.95 and 55 94 degree can be attributed to the 020, 002, 020, 200, 120, 202, 222, 202 and 400 planes of monoclinic WO_3 [396]. Other peaks of orthorhombic WO_3 were also observed although they were very small and could be due to the differences in the distortion of W-O bond that has been confirmed to occur interchangeably by many authors.[120,397] In summary, the low temperature calcination of WO_3 synthesized from concentrated nitric acid and sodium tungstate dihydrate results in yellow crystals of monoclinic WO_3 as reported elsewhere.[279]

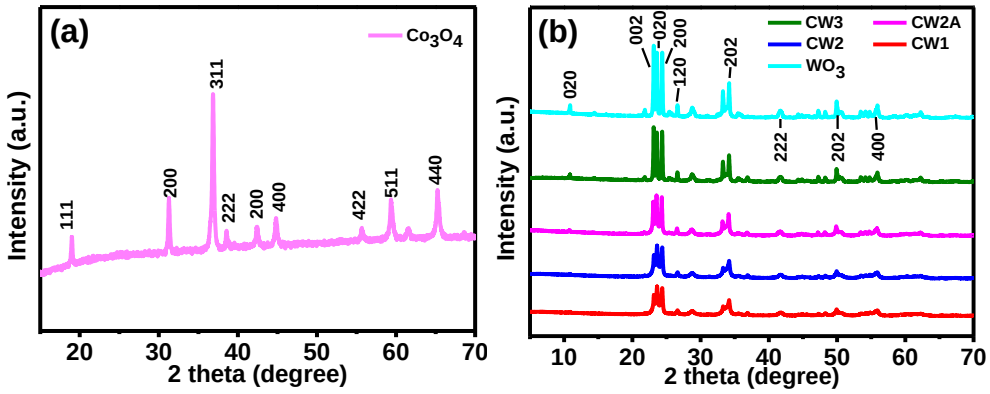

Figure 6.2: XRD pattern of (a) Co_3O_4 and (b) WO_3 and the composites

The incorporation of Co_3O_4 in the composites is evident as the 311 facet is present in all composites and increases in intensity with increase in its content. Moreover, there were changes in the 002, 020 and 200 planes intensity of the monoclinic WO_3 such that the 002 plane increased with increasing Co_3O_4 amount. However, The WO_3 maintained its monoclinic crystalline phase throughout and was not changed by adding Co_3O_4 or by

post-annealing. The crystallite sizes (D) were calculated from peak broadening using the Scherrer approximation (Equation 6.1).

$$\boldsymbol{D = \frac{0.9\lambda}{\beta \cos \theta}} \qquad \textbf{(6.1)}$$

where λ is the wavelength of the X-ray (0.15418 nm), β is the full width at half maximum (FWHM, radian) and θ is the Bragg angle (degree). The value of FWHM was obtained by performing profile fitting using the broadest peaks 002 and 020 for WO_3 and the composites. The values of D were determined to be 56.08, 18.11, 23.65, 23.65, 55.08 and 32.95 nm for WO_3, Co_3O_4, CW1, CW2, CW3 and CW2A respectively. Despite the crystalline size decreasing after incorporation of Co_3O_4 in WO_3, the reduction was only minimum when 0.03 M cobalt acetate was used in the composite such that similar D values were obtained for CW1 and CW2 while CW3 resulted in minimum reduction in crystalline size. Moreover, annealing the composite (CW2) resulted in increased crystalline size to 32.95 nm. The d spacing was calculated (Equation 6.2)

$$\textbf{d} = \boldsymbol{\frac{0.8285\lambda}{2 \sin \theta}} \qquad \textbf{(6.2)}$$

and was determined to be 0.318, 0.118, 0.311, 0.311, 0.318 and 0.312 nm for WO_3, Co_3O_4, CW1, CW2, CW3 and CW2A respectively. In photocatalysis, the micro-strain (ε) value is an important aspect to monitor changes in the crystallinity of the synthesised composites as opposed to pristine materials. The micro-strain values were estimated from Equation 6.3

$$\boldsymbol{\varepsilon} = \boldsymbol{\frac{\beta}{4 \tan \theta}} \qquad \textbf{(6.3)}$$

and were determined to be 0.00013, 0.00147, 0.000314, 0.000314, 0.000132 and 0.000225 for WO_3, Co_3O_4, CW1, CW2, CW3 and CW2A. The decrease in the micro-strain value of the annealed nanocomposite demonstrated its improved crystallinity which in turn influenced its increased photocatalytic activity when compared to the sample that was not calcined. Moreover, the positive sign of the micro-strain indicates that the stress in the photocatalysts is tensile in nature. To gain more information on the number of defects in the CW2 photocatalyst, the dislocation density (σ) is estimated using Williamson and Smallman's relationship (Equation 6.4).

$$\sigma = N/D^2 \qquad (6.4)$$

where N is a factor equals unity for the minimum dislocation density. The dislocation density is the measure of crystallographic defects or irregularities per unit volume of a crystal and its presence influences different properties (optical, physical, etc) of the material.[9] Intrinsic point lattice defects may be produced during synthesis. They were observed disseminated on horizontal planes or clustered at terrace margins and were proved to enhance photocatalytic activity by introducing defect energy levels and trapped states within the band structure of the semiconductor.[9,398] The value of minimum σ is 1.79 X 10^{-3} dislocations/nm^2 for CW2 which demonstrated good lattice structure of the CW2 photocatalytic sample compared to that of pristine WO_3 (3.18 X 10^{-4} dislocations/nm^2) as it increased. The high photocatalyst defects, will result in improved photocatalytic efficiency as it has been reported that oxygen vacancies[120] and structural defects due to dopants[362] results in improved photocatalytic efficiency of semiconductors.[398] This is expected to account for the high photocatalytic activity of the CW2 nanocomposite.

6.2.3 BET

To gain an insight into the effect of Co_3O_4 on the porous structure of the samples, BET analysis was carried out (Figure 6.3). The general shape of the curves is attributed to type IV isotherms and representative of mesoporous materials, indicating the presence of mesopores (2–50 nm) except the Co_3O_4, which is clearly a type II isotherm. Due to the small amount of the Co_3O_4 used in the composite, it resulted in little changes in the nitrogen adsorption desorption curve of WO_3. Moreover, the BET surface area, pore volume and average pore size were determined to be 2.7310 m^2/g, 0.011164 cm^3/g and 16.637 nm for Co_3O_4, 39.0427 m^2/g, 0.008830 cm^3/g and 11.46 nm for WO_3, and 21.653 m^2/g, 0.004964 cm^3/g and 8.97 nm for CW2 respectively.

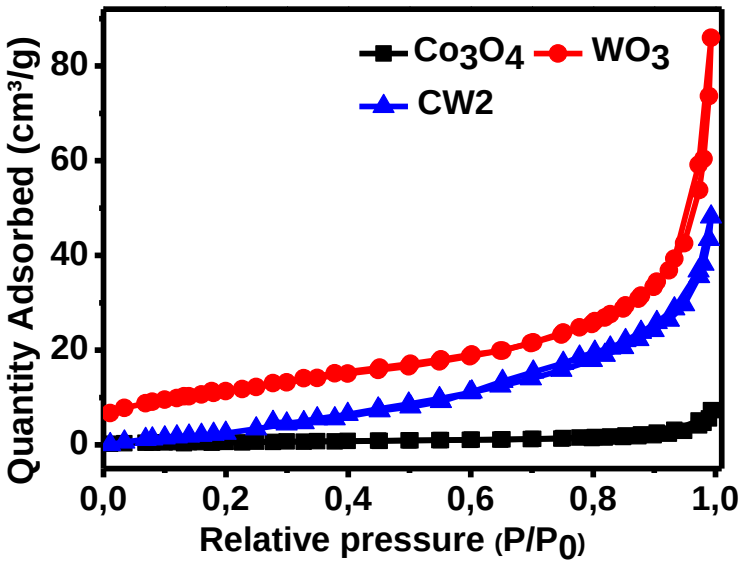

Figure 6.3: (a) N_2 Adsorption-desorption of Co_3O_4, WO_3 and CW2

The incorporation of Co_3O_4 decreased the BET surface area, pore size and pore volume of WO_3 in the CW2 prepared composite. The results vividly showed that the ability of the nanocomposite to degrade pollutants is not influenced by its surface area as there was an almost 50 % decrease in surface area and pore volume of WO_3 in the CW2 nanocomposite. The efficiency can therefore be attributed to other factors that improve photocatalytic performance of metal oxide semiconductors.

6.2.4 SEM/EDS

In order to get a clear idea about the growth mechanism and the variation of surface morphologies of the metal oxide semiconductors FE-SEM images were studied. From Figure 6.4 (a, b) WO_3 had different sizes of 2D plates that were surrounded by rod shaped and spherical particles aggregated on and around the 2D platelets. Co_3O_4 had round platelets that interconnected and formed an epitaxy of 3D spheroids stacked into worm-like rods in different directions (Figure 6.4 c, d). The spheroidal particles of Co_3O_4 which resulted in the formation of the honeycomb-like structure can be clearly seen as growing from the fractional zones. The composite (Figure 6.4 e, f) had 3D spongy platelets that were arranged in different directions. There were spherical small particles attached to each other with well-defined linkages on the surface of the 3D platelets and around them. Moreover, WO_3, Co_3O_4 and CW2 all had micro-shorts. The micro-shorts are important to strengthen the weak links between WO_3 and Co_3O_4 in the composite as they are interconnected and attached to each other for efficient photocatalytic performance. The composite SEM image at low magnification (Figure 6.4 e) shows that it consisted of porous structures with mostly spherical particles of Co_3O_4 deposited on top of WO_3

spongy-like 3D platelets that are also exposed on the surface of the well dispersed nanoparticles that leave micro-shorts that are more visible at high magnification (Figure 6.4 f).

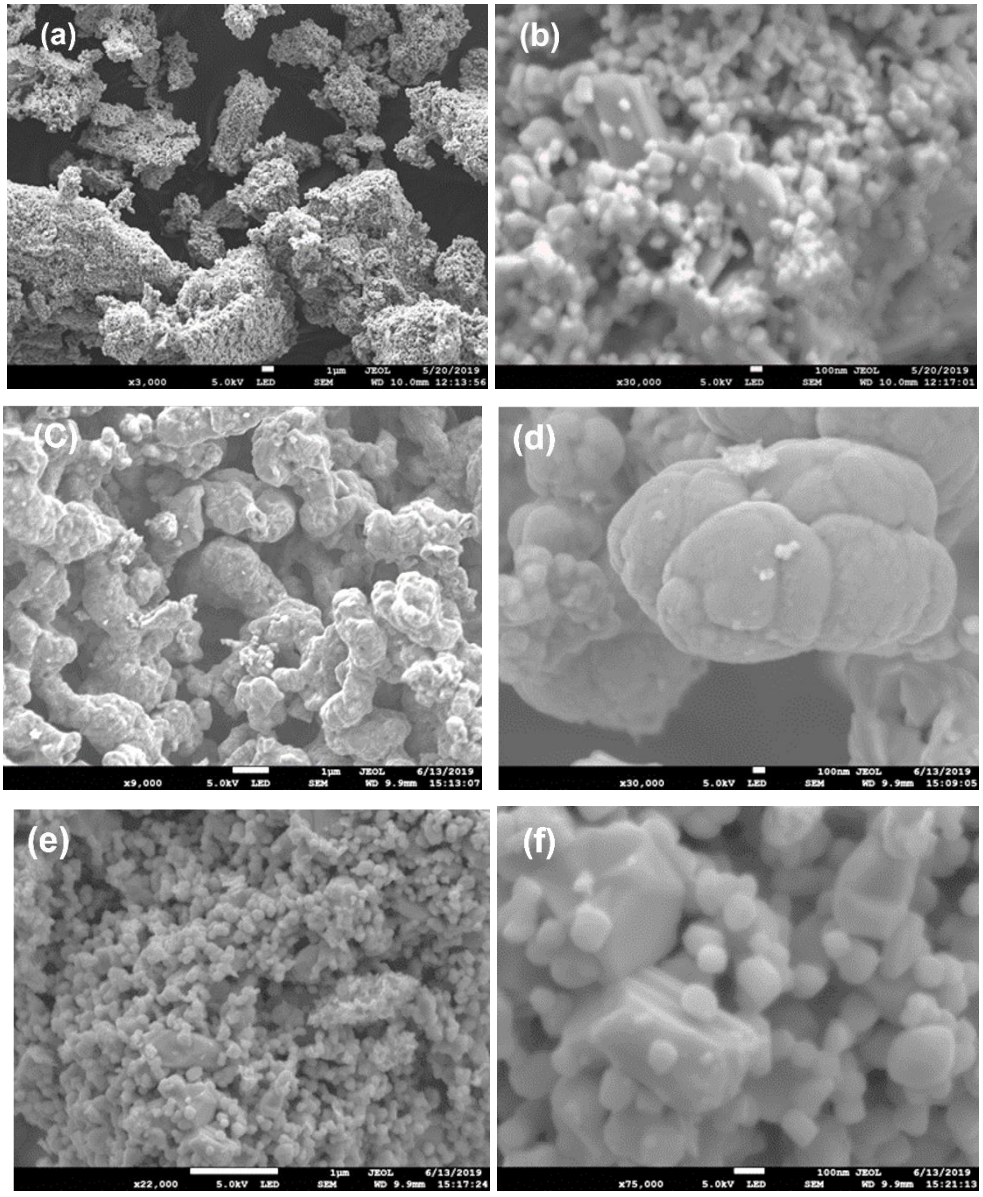

Figure 6.4: SEM images of (a,b) WO_3, (c,d) Co_3O_4 and (e,f) CW2

The nanoparticles were also evaluated using EDX to confirm the elemental composition of the as synthesised metal oxides (Figure 6.5). The EDX of all the materials had carbon from the carbon conducting tape and all had more of the metal peak than the oxygen peak meaning they had oxygen vacancies that had been reported to enhance the photocatalytic performance. The oxygen vacancies, micro-shorts and surface defects are very important parameters in semiconductor photocatalysis as they enable the effective degradation of organic pollutants and hydrogen generation by the corresponding metal oxide semiconductors.[120,397] Moreover, they help in the generation of reactive oxygen species for

efficient pollutant remediation while the micro-shorts improve the interaction of the pollutant and the photocatalyst and the oxygen vacancies enhance visible light absorption. The percentages of the different elements in the composite were 66.1 % for W, 18.8 for C and 15.1 % for O in WO_3 (Figure 6.5 a), 73.5% for Co, 19.2 % for O and 7.3 % for C in Co_3O_4 (Figure 6.5 b) while the composite had 58.5 %, 20.6 %, 14.6 % and 6.3 % of W, O, C and Co (Figure 6.5 c) respectively. These observations are consistent with the expectations in the synthesised materials.

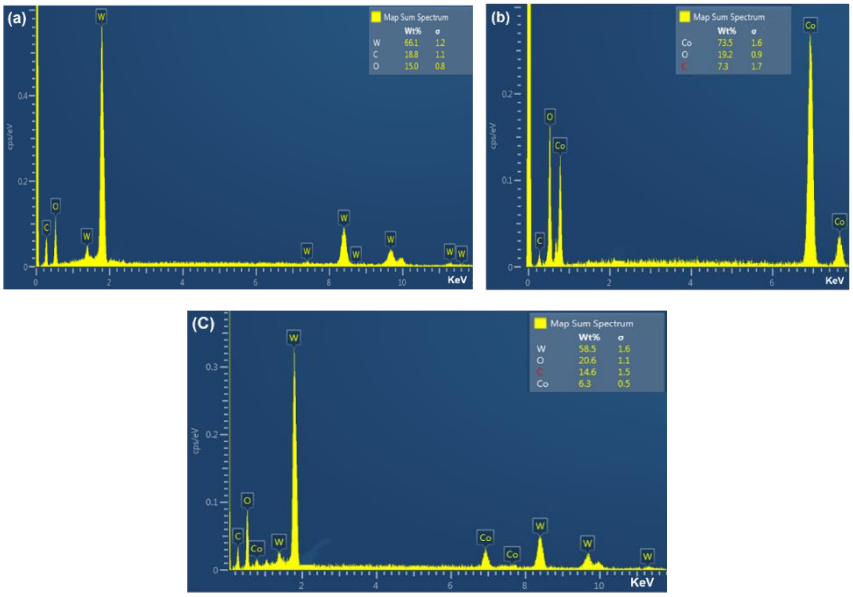

Figure 6.5: EDX images of (a) WO_3, (b) Co_3O_4 and (c) CW2

The oxygen vacancy and interconnection between the pristine materials in the CW2 composite explicitly shows that the photocatalytic performance of the composite is due to combined effect of interaction between 3D spheres of WO_3 and the spheroidal Co_3O_4, oxygen vacancies and the presence of monoclinic phase of WO_3.

6.2.5 TEM/HR-TEM/SAED

Internal morphology of the materials was investigated using TEM and HR-TEM images and selected area electron diffraction (SAED) patterns were used to match the different planes and demonstrate the crystallinity of the materials. From Figure 6.6 (a) the porous Co_3O_4 nanoparticles were observed to be irregular spherical forms, the nanoparticles were aggregated, and a porous network was created inside the sample. Figure 6.6 b which shows the HR-TEM proved that the material was indeed interconnected. The selected area electron diffraction (SAED) pattern of the sample clearly shows the highly diffused hollow concentric rings with sharp spots and the exposed facet is 111 plane (Figure 6.6 c) in agreement with XRD and some literature results.[399] The spots were formed by the diffraction of transmitted electrons through the spinel nanoparticles in

different orientations [230]. The diffraction rings were indexed to (111), (220), (311), (400), (422), (511), and (440) planes, and are well correlated to the spinel Co_3O_4. Figure 6 (d) shows a TEM image of WO_3 and the SAED pattern (Figure 6.6 f), indexed to monoclinic WO_3 demonstrating that the phase transformation to tungsten oxide occurred while preserving the nanoparticle morphology. Figure 6.6 (e) shows agglomerated spherical particles that grow into rod shaped and spherical particles. These results concur with the SEM results of WO_3. The SAED pattern shown in Figure 6.6 (f) was indexed to monoclinic P21/n WO_3, along the 020 zone axis, which was in good agreement with other results published on WO_3 x-ray diffraction card number JCPDS No. 43-1035.[400,401]

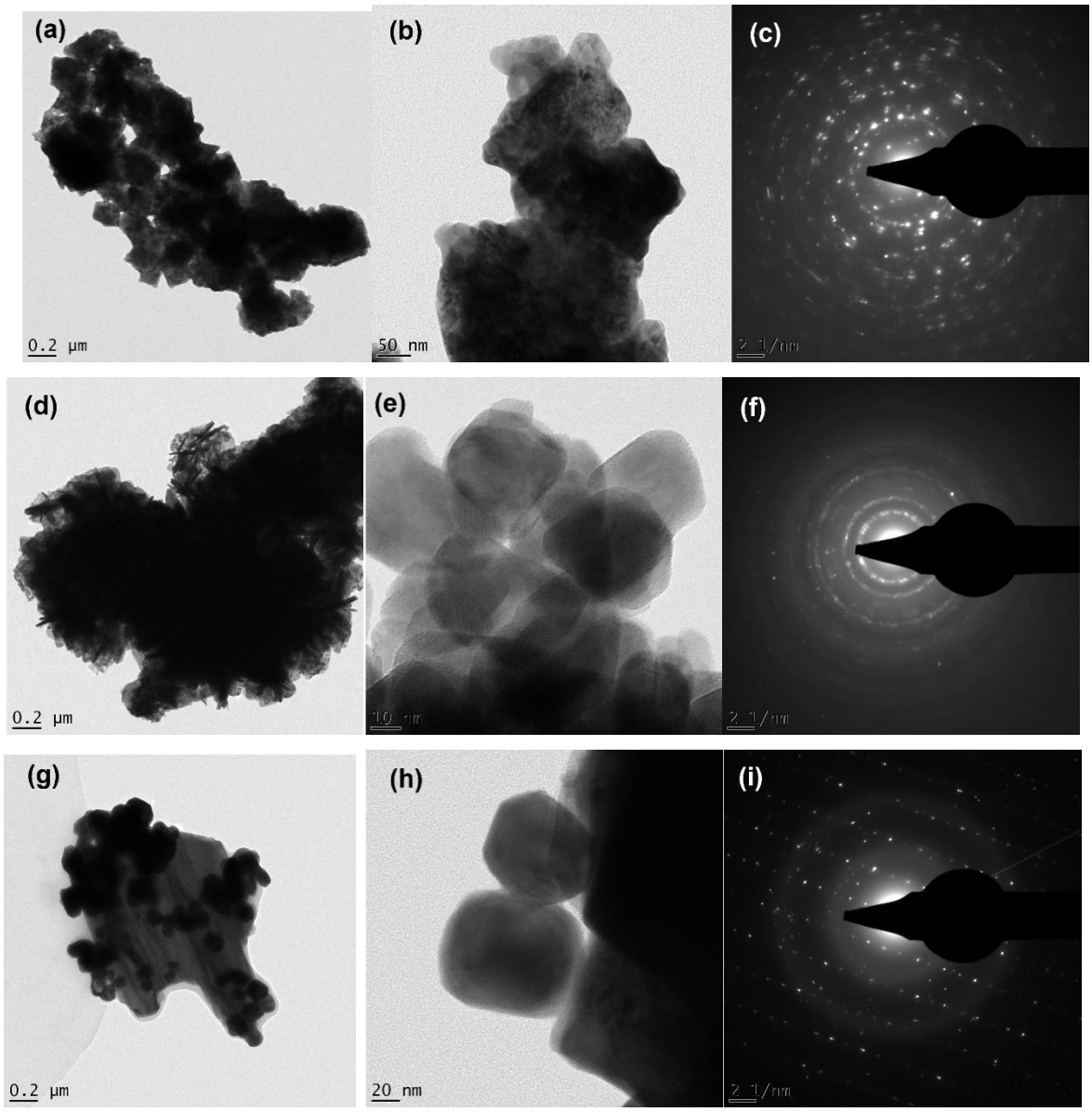

Figure 6.6: TEM, HR-TEM and SAED images of (a, b, c) Co_3O_4, (d, e, f) WO_3 and (g, h, i) CW2

From Figure 6.6 g, the Co_3O_4 spheroids were uniformly dispersed over WO_3 sheets and HR-TEM images suggested a strong interaction between WO_3 3D platelets and Co_3O_4 (Figure 6.6 h). This suggests that Co_3O_4 has a good binding affinity towards WO_3. The SAED pattern of the composite is similar mostly to WO_3 SAED suggesting that all the metal oxides maintained their parent crystal forms of monoclinic WO_3 and cubic Co_3O_4 as confirmed by XRD results. Therefore, the exposed facet in the nanocomposite can be indexed to the 020 plane of monoclinic WO_3 surrounded by 111 planes of Co_3O_4 strongly attached to it. It is reported that the 111 facets of Co_3O_4 display enhanced photocatalytic performance and hence the nanocomposite is expected to have high activity.[402]

6.2.6 TGA

The thermal stability of the synthesised nano catalysts was evaluated with thermogravimetric analysis from room temperature to 905 °C under inert atmosphere (Figure 6.7). The WO_3, Co_3O_4 and CW2 showed high thermal stability in this temperature range with overall percentage weight loss of approximately 1 %, 2.3 % and 1.5 % respectively.

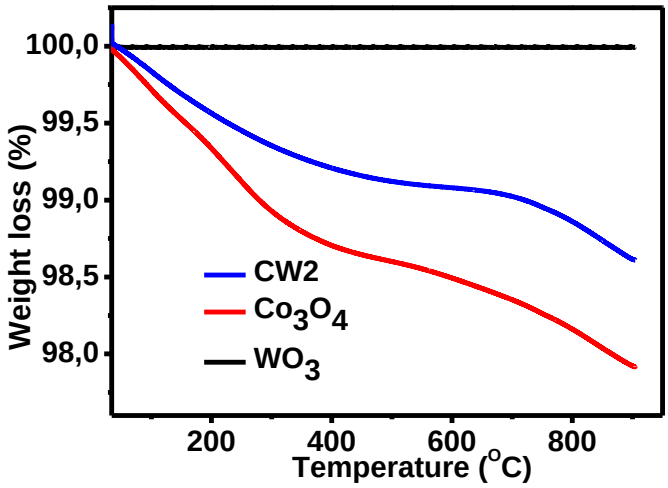

Figure 6.7: TGA micrographs of Co_3O_4, WO_3 and CW2

The TGA results are typical of metal oxides with Co_3O_4 reported to decompose to CoO at around 950 °C.[403] Moreover, the presence of Co_3O_4 in the nanocomposite was evident with matching decomposition.

6.2.7 UV-Vis

The electronic structure of semiconductors is closely related to their optical absorption performance. The optical properties of the semiconductors determine whether they absorb light in the UV region or in the visible region which is also used to determine the amount of

energy required to activate the photocatalyst to generate photo-excited electrons and holes. Therefore, optical bandgap calculations are important in photocatalysis applications to determine the suitable photoenergy required for optimum performance. Figure 6.8 (a) shows the absorption spectra of WO_3, Co_3O_4 and CW2. The absorption curve of Co_3O_4 shows two distinctive absorption peaks that can be indexed to transitions from the highest occupied molecular p orbitals of oxygen to either empty d orbitals of Co^{2+} or Co^{3+} in the spinel structure. The transition that requires the highest energy (λ_{max} of around 400 nm) has been described to be due to $O_2^- \rightarrow Co^{2+}$ while the low energy transition with λ_{max} of around 700 nm is assigned to a charge transfer $O_2^- \rightarrow Co^{3+}$.[404] Moreover, d-d forbidden transitions are also possible in the spinel Co_3O_4.

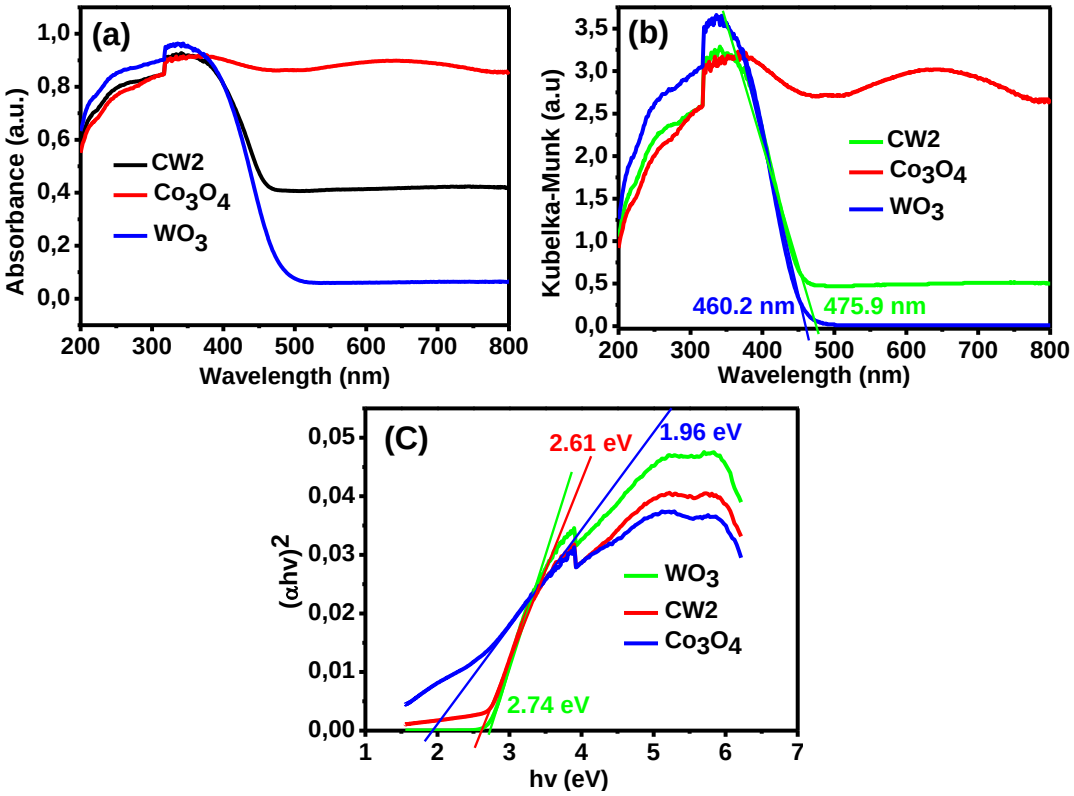

Figure 6.8: (a) UV-Vis absorption spectra (b) Kubelka-Munk function and (c) Tauc-plots of WO_3, Co_3O_4 and CW2

WO_3 had an absorption edge around 460 nm which was close to the value obtained by the Kubelka-Munk function of the same material with an edge around 460.2 nm (Figure 6.8 b). Incorporation of Co_3O_4 red-shifted the absorption edge of all the composites to low energy in the visible region to 475.9 nm for CW2. The bandgap energy of a semiconductor can be calculated using the Tauc formula:[405]

$$\alpha h\nu = A(h\nu - E_g)^{n/2} \qquad (6.5)$$

where α, h, v, E_g, and A are absorption coefficient, Planck's constant, light frequency, bandgap energy, and a constant, respectively. The inverse of absorption coefficient α^{-1} gives estimated distance a photon can travel before it is absorbed.[406] This is important towards engineering of fixed bed reactors for photocatalytic degradation under solar radiation for industrial or pilot scale applications. The value of n can be determined by the type of optical transition (n =1 or 4 for direct and indirect transitions, respectively). The value that best fitted n is 4 for WO_3, Co_3O_4 and the composites. Figure 6.8 (c) shows the plots of $(\alpha hv)^2$ versus light energy (hv) for the samples. The bandgap values for WO_3, Co_3O_4 and CW2 were approximated to 2.74, 1.96 and 2.61 eV. The bandgaps of other composites were determined to be 2.70, 2.62 and 2.61 eV for CW1, CW3 and CW2A respectively. The CW2 composite prepared in 0.02 M cobalt acetate had better photocatalytic performance compared to CW1 and CW3 due to the less energy required for activation. Interestingly, annealing did not affect the bandgap of the CW2 composite and the differences in the performance of the calcined composite cannot be discussed through their bandgap energy as they had similar bandgaps of 2.61 eV. Moreover, when using the relationship of (E_g = 1240/λ) using the value of λ obtained from the Kubelka-Munk function, the bandgaps obtained for WO_3 and the composites were almost the same.

6.2.8 PL

Photoluminescence (PL) emission spectroscopy is widely used to follow the irradiative recombination of photogenerated charge carriers, so it is useful to understand the migration, transfer and separation of charge carriers in the photocatalyst. The photoluminescence spectra of all the composites are shown (Figure 6.9).

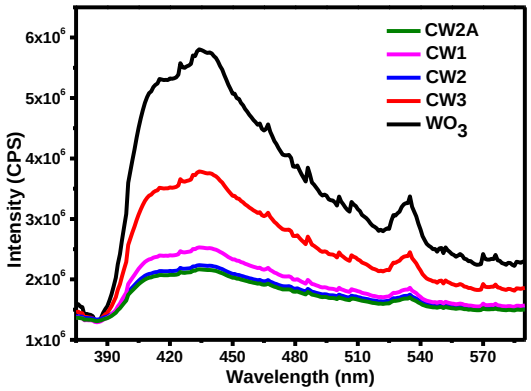

Figure 6.9: Photoluminescence spectra of WO_3, CW1, CW2, CW3 and CW2A

WO_3 had a broad luminescence peak, centred at about 460 nm and it had the strongest PL emission peak compared to all the composites. This indicated that the electrons and holes recombination rate of WO_3 was much higher than in any of the composite materials

hence confirming further that there was interaction between WO_3 and Co_3O_4 to minimize electron and holes recombination. The lowest PL intensity was observed in the case of CW2/CW2A with only a little margin separating the annealed samples PL intensity. This therefore confirmed that annealing minimally affects electron hole recombination and would be an unnecessary cost towards synthesis of the p-n heterojunctions. However, annealing reduced the recombination of photo-excited electrons and holes which can also be attributed to the high photocatalytic performance of the CW2A photocatalyst compared to the CW2 that was not calcined as they had similar band gap energies. This results are further cemented by other researches on the use of PL emission intensity to confirm suppressed recombination of photoexcited charge carriers.[407,408]

6.3 Degradation of diclofenac sodium

The photocatalytic performance of WO_3, Co_3O_4 and in-situ prepared Co_3O_4/WO_3 p-n heterostructure photocatalysts was evaluated for the photodegradation of diclofenac sodium salt (DFC) under visible light irradiation ($\lambda > 420$ nm).

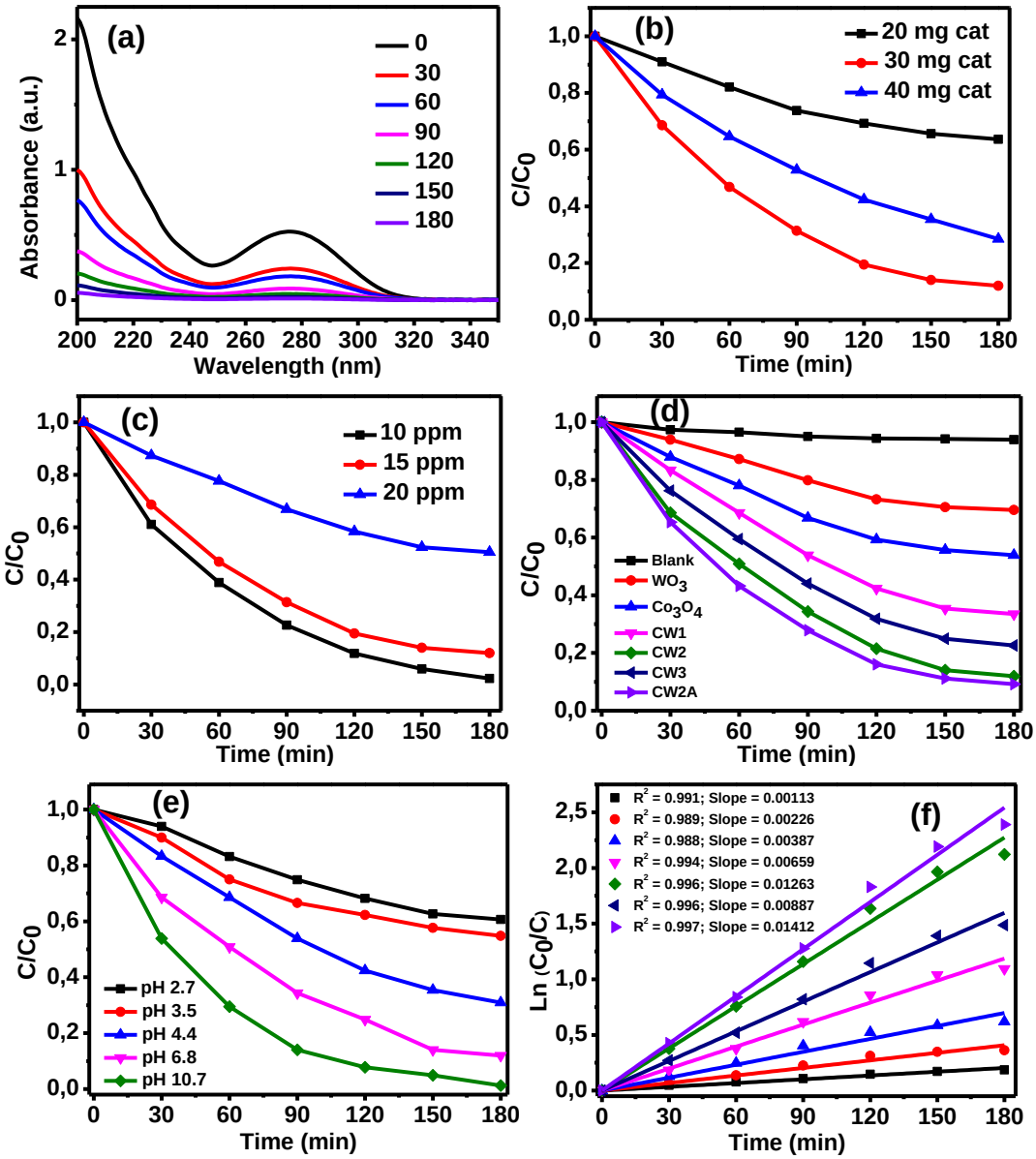

Figure 6.10: Degradation of DFC (a) UV-Vis curve, Optimisation of (b) catalyst amount, (c) DFC concentration, (d) Catalysts composition and (e) pH of DFC, and (f) reaction kinetics at pH 6.8

From Figure 6.10 (a), the absorbances decreased with increasing time interval until they become very low when 10 ppm of DFC was degraded. The decrease was rapid at first and became less rapid with increasing time. Interestingly, the reductions can also suggest that the aromatic molecules in DFC and the subsequent intermediates are converted to aliphatic compounds as observed by the decrease in the absorbance at UV_{254}. UV_{254} has been described as the indicator of aromatic substances with its reduction in value indicating that indeed the aromatic backbone of DFC and its degradation intermediates were broken down mostly to aliphatic compounds.[409,410] Westphal et al. associated an effective aggregation of organic constituents to a single absorbance rate for a

homogeneous solution (UV_{254} = 0.493(TOC) – 0.666). When using this relationship, TOC reduction of 86.15 % was achieved for 15 ppm DFC at pH 10.7. Parameter optimisations were performed and a decrease or increase in the catalyst loading resulted in reduced efficiencies due to decreased generation of reactive oxygen species (ROSs) for the former and catalyst shielding of light or competition of reactive species for the latter as described elsewhere.[411,412] The efficiencies with CW2 catalyst were 36.32 %, 71.51 % and 88.03 % for 20 mg, 40 mg and 30 mg catalyst at pH 6.8 respectively (Figure 10 b). At the same pH value, the effect of increasing concentration of DFC to 20 ppm decreased the efficiency to 49.55 %. Meanwhile, decreasing the concentration of DFC to 10 ppm increased efficiency to 97.72 % (Figure 6.10 C). Therefore, the 15 ppm was selected as the optimum concentration of DFC as it still gave good removal efficiency of 88.03 %. The study of the effect of DFC concentration changes with respect to visible light activation is important to better understand the behaviour of the pollutant under visible light irradiation and to improve efficiency on the overall process. The photolysis efficiency was determined to be 6.04 % after 180 minutes of irradiation and can be ignored in the overall degradation process as it was very low. From Figure 10 a and some literature[413], DFC absorbs light in the UV region (λ ≤ 320 nm) with its wavelength of maximum absorption of around 276 nm and has been proved to undergo photodegradation under UV light irradiation. Since the light source used had a wavelength cut-off of 420 nm, only a small portion of UV light below 420 nm could have passed through and resulted in photodegradation of DFC without the catalyst. The different synthesised metal oxide semiconductors were evaluated for degradation of 15 ppm DFC at pH 6.8 (Figure 6.10 d) and the efficiencies were 30.4 %, 46.1 %, 66.5 %, 88.03 %, 77.4 % and 90.8 % for WO_3, Co_3O_4, CW1, CW2, CW3 and CW2A respectively.

The pristine semiconductors showed efficiencies below 50 % which is due to recombination of photo excited electrons and holes and the little energy required for photo-excited electrons and holes formation could be attributed for the high degradation efficiencies observed for Co_3O_4 compared to WO_3. The increased efficiencies in the composites were due to supressed photo excited electrons and holes pairs recombination as confirmed by PL spectra of the composites. Moreover, the annealing of the CW2 composite which gave the highest degradation efficiency only had little effect on the overall performance of the composite. Annealing eradicates little adsorbed impurities, especially water, in the crystal lattice of the composite and improve charge transfer hence electron hole separation by magnetic field but the effect is small (only 2 % improvement in efficiency) meaning there was less adsorbed water molecules in the lattice of the

composite. From Figure 6.10 e, different pH values were evaluated for the degradation of DFC and the pH was adjusted using sodium hydroxide and nitric acid. The efficiencies were 39.3 %, 45.2 %, 69.1 %, 88.03 % and 98.7 % at pH 2.7, pH 3.5, pH 4.4, pH 6.8 and pH 10.7 respectively. The degradation efficiency of DFC increased with increasing pH. The pKa value of DFC is around 4.4 and when pH = pKa, the amount of neutral and negatively charged DFC molecules is at equilibrium. Below this value, the reduced degradation efficiency can be attributed to poor interaction between neutral DFC molecules and the catalyst irrespective of the surface charge of the catalyst. When DFC dissociation occurs, the presence of negatively charged DFC ions improves the interaction between the catalyst and the composite resulting in 29.8 % increase in efficiency. Further increase of pH above the pKa value of DFC resulted in more increased degradation efficiency that can be attributed to: (1) The addition of OH- which further increases the formation of the hydroxyl radicals that are the main reactive species for degradation of DFC and (2) the improved interaction between the positively charged catalyst surface and the negatively charged DFC molecule such that the optimum pH was at 10.7. The kinetics of DFC photodegradation was evaluated quantitatively by applying the pseudo-first-order model, as expressed by Equation 6.6. This model is widely used for heterogeneous photocatalysis as the initial concentration of pollutant is low.

$$-\ln\left(\frac{Ct}{C0}\right) = Kt \text{ or } \frac{dCt}{dt} = KCt \qquad (6.6)$$

where C_t and C_0 are the concentrations of DFC at time t and 0 (the time to obtain adsorption–desorption equilibrium) in aqueous solution, K is the pseudo-first-order rate constant, which can be obtained from the decrease of the peak intensity at 276 nm with time. The different rate constants were 0.00113, 0.00226, 0.00387, 0.00659, 0.01263, 0.00887 and 0.01412 min^{-1} for blank, WO_3, Co_3O_4, CW1, CW2, CW3, CW2A respectively (Figure 6.10 f). The values of the different rate constants were used to evaluate the synergy (S) caused by combining the metal oxide semiconductors in the CW2 photocatalyst from;

$$S = \frac{Kcw2 - Kwo3}{Kcw2} \text{ for } WO_3 \qquad (6.7)$$

The value of the synergy was determined to be 0.6936 and 0.8211 for Co_3O_4 and WO_3 in CW2 respectively. The positive values of the synergy confirmed the synergistic effects of the metal oxide semiconductors in the p-n heterostructure while a negative value would

have suggested an antagonist effect for degradation of DFC. Moreover, the synergy of WO_3 was higher than that of Co_3O_4 meaning WO_3 contributed more to the degradation of DFC by CW2 nanocomposite.

The optimum operation conditions were selected for the degradation of 15 ppm DFC, the used in determining the amount of chloride ions released during the degradation of DFC using Mohr's method (Figure 6.11). The theoretical concentration of DFC was 0.047 mmol/L in 15 ppm of DFC. Since there are two molecules of chlorine per DFC molecule, theoretically the composition should be 0.094 mmol/L if they were totally released. The released Cl^- determined by Mohr's method compared to the theoretical amount was 95.57 ± 0.05 % and the release rate of Cl^- ions determined in the water followed first order reaction.

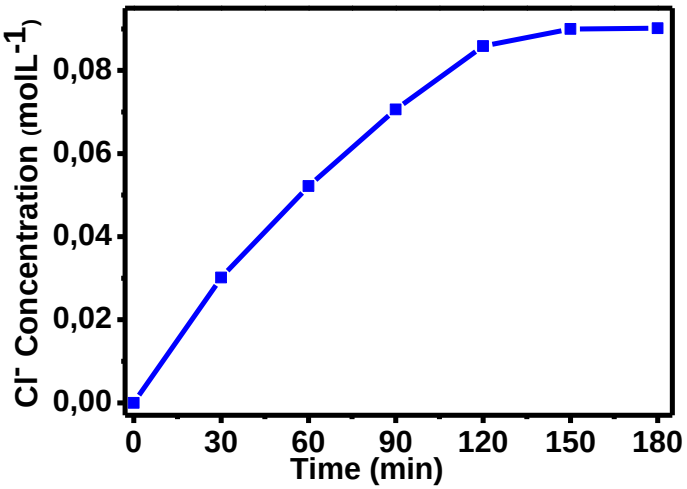

Figure 6.11: Concentration of released Chloride ions as a function of degradation time

From first order rate law ($[A]_t = [A]_o \times e^{-kt}$), the rate was determined to be 0.0213 min^{-1} which is 1.7 times faster than the rate of degradation of DFC instead of the expected 2 times rate as per molecular structure of DFC. Therefore, these results proved that not all Cl^- ions were removed and the mechanism of degradation of DFC has other routes than de-chlorination though it is the main route and agrees with the degradation results with a removal efficiency of less than 100 %. The determined rate of chloride ions released was lower than the rate determined by other authors elsewhere[414,415] and this could be attributed to the low detection limit of Mohs titration method used in this report compared to the ion chromatography method.

The degradation of DFC was further consolidated by the analysis of degradation products with HPLC-TOF-MS (Figure 6.12), which were further used to hypothesise a pathway for

its mineralisation by the p-n heterostructure of Co_3O_4/WO_3. The results showed that before initial degradation, DFC was stable with the only observed peaks due to diclofenac conjugate base picking up a proton in positive mode (m/z = 296.0242) and some unconverted diclofenac sodium with m/z = 318.0063 (Figure 6.12 a). Different intermediates were formed after 60 minutes of degradation and the concentration of diclofenac decreased (Figure 6.12 b). The decrease in DFC concentration intensity was higher as the degradation progressed to 120 minutes under visible light radiation (Figure 6.12 c) and new by-products formed (m/z = 240.2326, 209.0597, 167.0544 and 97.0193) and the intermediates observed at 60 minutes (m/z = 278.0138, 318.0063, 250.0189) had disappeared. After 180 minutes of degradation (Figure 6.12 d), DFC and all intermediates observed after 120 minutes of degradation had decreased while other lower molecular weight intermediates formed (m/z = 160.0971 and 67.0762). The degradation of diclofenac sodium at pH 10.7 occurs first by its conversion to diclofenac by picking up a proton.

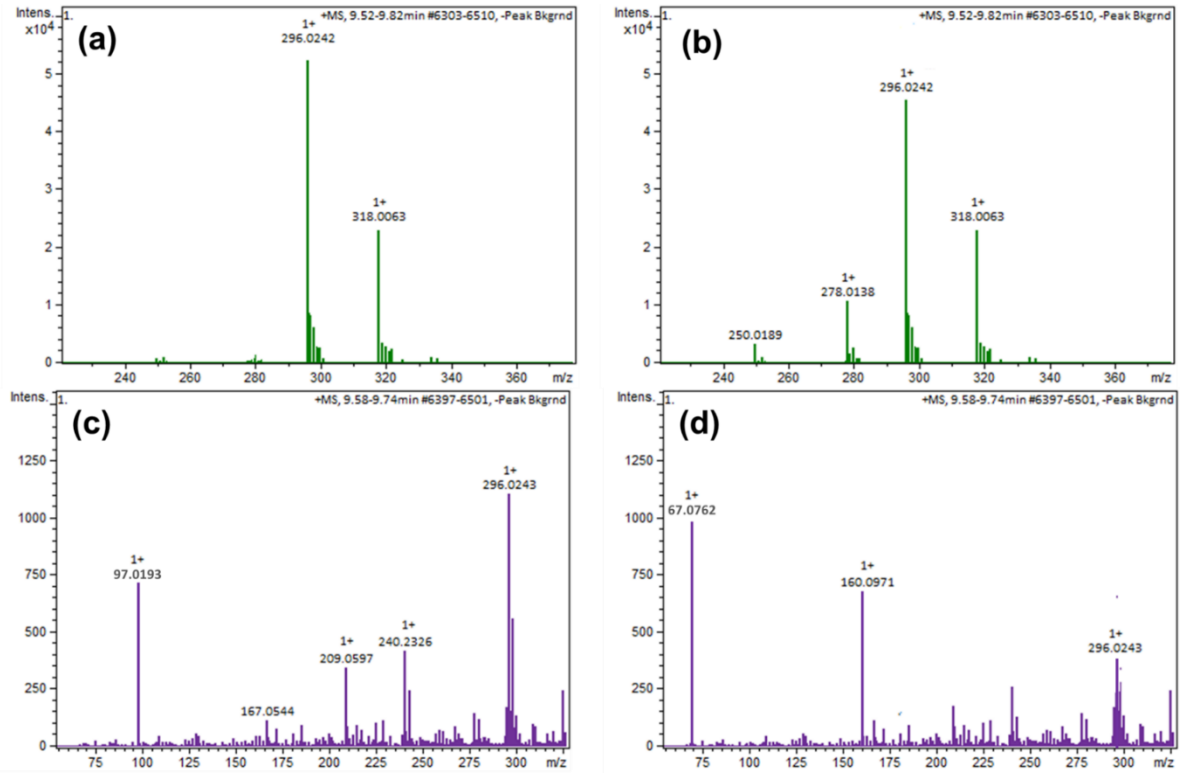

Figure 6.12: Mass spectra of UHPLC-TOF-MS during degradation of DFC at (a) 0 minutes, (b) 60 minutes, (c) 120 minutes and (d) 180 minutes

Generally, the intensity of the detected DFC reduced from around 5.6 X 10^4 to as low as below 550. Therefore, it can be concluded that the p-n heterostructure formed by Co_3O_4/WO_3 effectively degraded DFC and the intermediates products into lower molecular structures and aliphatic compounds. The aliphatic and low molecular compounds were

further transformed into hydrogen nitrate anion ($H_4NO_3^-$), water and carbon dioxide reducing its toxicity due to chloro-organic compounds by release of chloride ions at pH 10.7. The rapid formation of the non-selective hydroxyl radicals can be credited for the observed non-selective oxidation of DFC and its intermediates. Numerous researchers reported different pathways for DFC degradation under different conditions due to presence of different radicals induced by different environmental conditions.[414,416,417] Their theoretical results and the obtained results identified according to molecular weight as analysed by HPLC-TOF-MS were used to propose the degradation of DFC at pH 10.7 in the presence of the synthesised heterostructure (CW2). The degradation of DFC by CW2 is proposed to transpire in two general routes (Figure 6.13).

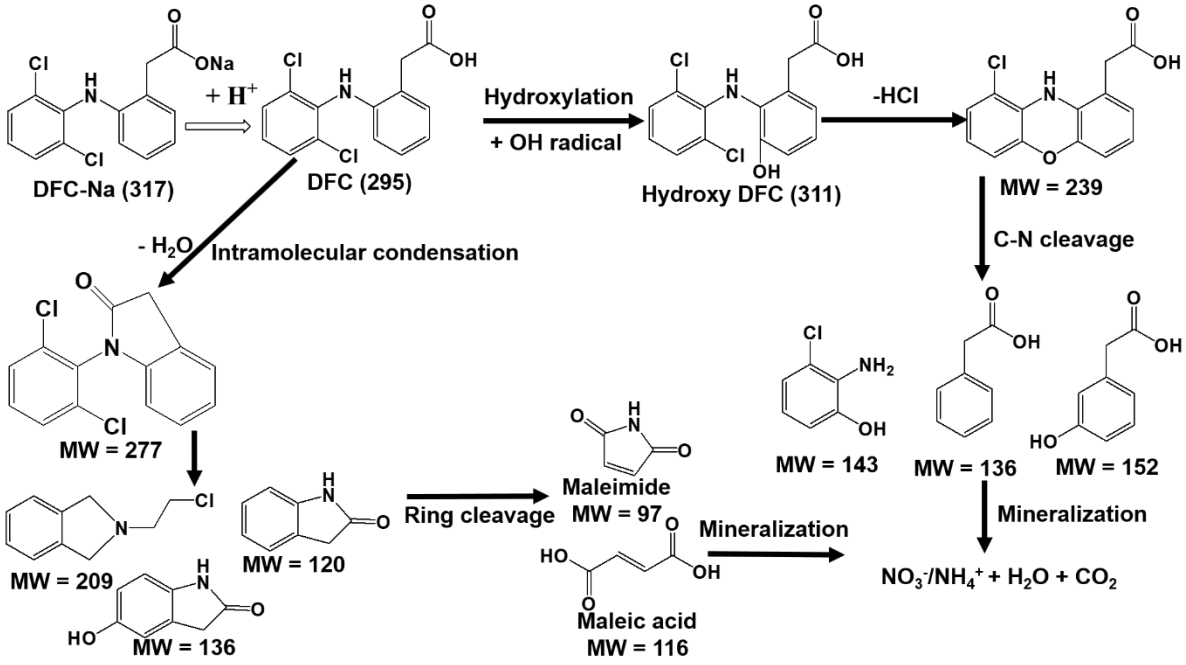

Figure 6.13: Hypothesised pathway for mineralisation of DFC by CW2 at pH 10.7

The main route involved the hydroxylation of the aromatic ring which produced hydroxylated DCF (mw = 311) that was not detected but could be deduced from the detected ($C_{14}H_9O_3N$, m/z = 240). Generally, three different forms of the hydroxylated DCF (MW 311) were reported by Liu et al who further proposed their oxidation by h^+ and hydroxyl radical to the corresponding quinine imine (MW 309).[414] However, some by-products were not determined, likely due to the low response or high conversion to other intermediates under our experimental conditions. The other route involved the intramolecular condensation as reported by Banaschik et al resulting in $C_{14}H_{10}NOCl_2$ product (m/z = 278). Continued hydroxylation and dechlorination of the main intramolecular condensation product leads to cleavage of the C-N and the benzene ring structure and formation of small molecular weight compounds (mw = 209, mw = 136 and

mw = 120). The cleavage of the C-N bond was reported to result in different by-products depending on the spatial orientation of the hydroxyl radical attack.[416] Maleimide (mw = 97) was therefore detected as the main by-product of the ring cleavage which are further mineralised to hydrogen nitrate anion ($H_4NO_3^-$). The $H_4NO_3^-$ is very unstable and can transform to NO_3^- or NH_4^+ by undergoing a series of reactions hypothesised to be catalysed by the CW2 nanocomposite. The removal of protons on the $H_4NO_3^-$ anion will result in formation of H_2O and NO_3^- anions in solution. This abstraction can happen quickly as the resonance delocalised pi electrons around the nucleus of the NO_3^- anion[418,419] are proposed to form weak bonds resulting in the formation of the unstable $H_4NO_3^-$. The NH_4^+ formation is a little bit complex to comprehend if it indeed occurs and more studies needs to be done to authenticate its formation as a by-product of the degradation of nitrogen containing organic pollutants. However, studies were reported where nitrogen fixation was achieved forming ammonia (NH_3) in aqueous or humid environment using a titanium based semiconductor even though its mechanism was not well understood.[420–424] This process was first believed to occur using UV light activation until it was recently proven that visible light nitrogen fixation is also possible.[423] The possibility of nitrogen release from DFC cannot be ignored and the formation of NH_4^+ is conjectured to occur through two routes: first the formation of dinitrogen that forms NH_3 which is transformed into NH_4^+ in solution or the conversion of NO_3^- to NH_3 then NH_4^+ ions. Moreover, other studies have reported that the photoexcited electrons and holes can reduce nitrate to ammonia ($NO_3^- + 9H^+ + 8e^- \rightarrow NH_3 + 3H_2O$)[421] which can easily form NH_4^+ ions in aqueous solution and formed the basis for the second mechanism occurring to result in NH_4^+ cations. Other mineralisation products from the aliphatic organic molecules can be water and carbon dioxide. Similar by-products observed and the degradation pathways are similar for those hypothesised for plasma treatment and Fenton-processes reported by other authors.[425–427] Therefore, the release of chloride was supported by the obtained intermediates products to be the driving mechanism towards the degradation of DFC. The results implied that h^+ and OH radicals played the most important role during the decomposition process.

6.4 Photocatalyst recycling and stability

The photocatalyst reusability and stability are important aspects of photocatalytic metal oxide semiconductors and can be evaluated by re-using the catalyst and analysing the re-used catalyst to determine if there are any changes in either the morphology or crystallinity of the nanocomposite after re-use. Figure 6.14 a shows the photocatalyst re-usability over 4 cycles and the efficiencies were 98.7 %, 98.6 %, 96. 9% and 94.3 % respectively. The reusability studies were performed under optimum conditions and

showed that the catalyst was stable and could be recycled up to four cycles without affecting its degradation efficiency. Moreover, the reused catalyst was evaluated using XRD which proved that it was instead stable and retained all its peaks due to WO_3 and the 311 planes of Co_3O_4 in the nanocomposite (Figure 6.14 b).

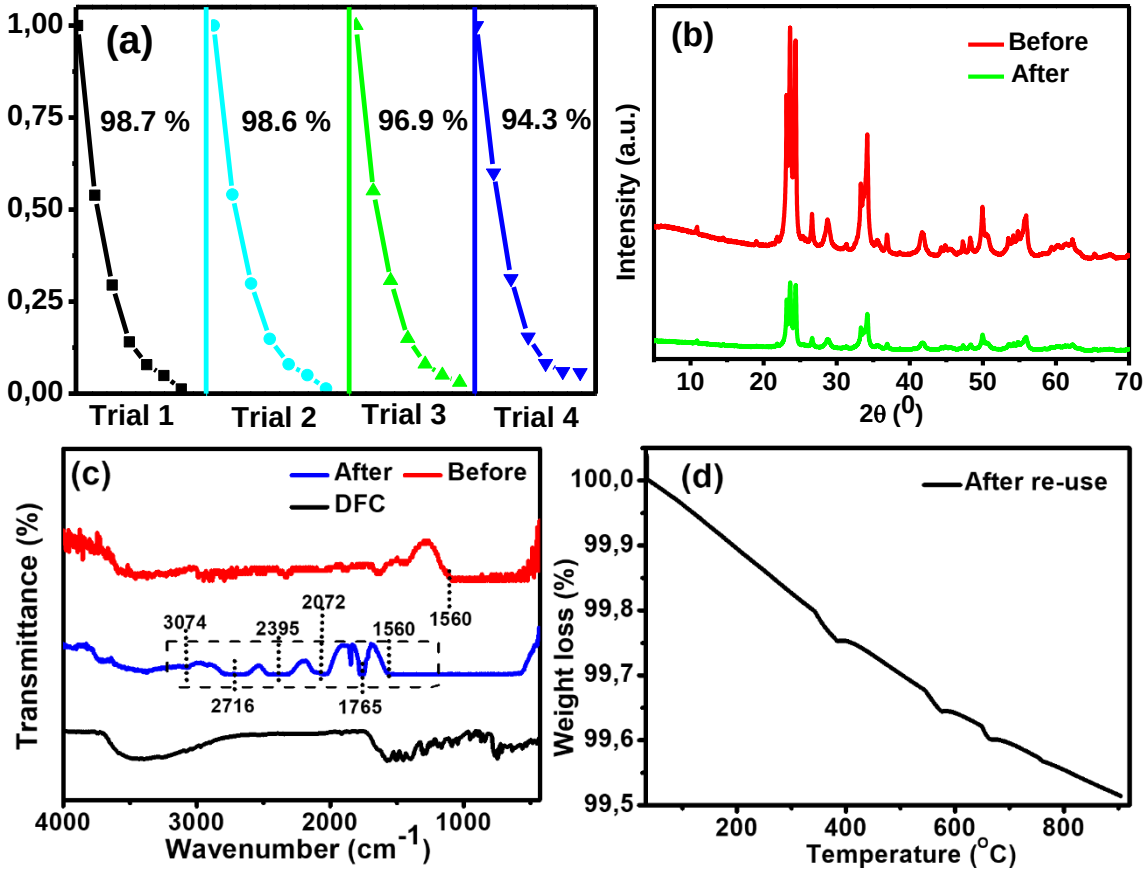

Figure 6.14: Photocatalyst (a) re-usability, (b) stability and (c, d) coking formation evaluation

The high stability can be attributed to the pH used (10.7) as some authors have reported that the leaching of Co_3O_4 is dependent on pH and they have proved that at pH values above 7.9, the Co_3O_4 ions leaching is negligible due to its stability when used in combination with other metal oxides.[428] Therefore, the catalyst was very stable with only the reduction in the intensity of peaks after four cycles of degradation implying that WO_3 was still monoclinic while Co_3O_4 was cubic. No other peaks were observed. Coking is a common phenomenon that occurs during catalytic reactions of organic compounds or CO_2 (especially under elevated temperatures) where it can either form on the surface blocking passage to the active sites or it can form on the active sites within the catalysts.[429–431] The validation of cake layer formation was previously studied by soaking of the catalyst in different solvents such as KOH solution and subsequently characterising the extract with different techniques such as TGA, XRD and FTIR or via coke combustion which is the

more documented and common method and the determination of C/H ratio is used for its authentication.[432,433] In this study, solvent extraction of the re-used catalyst was outside the scope but the recycled catalysed was analysed with FTIR making comparisons with the spectra of the catalyst before use and that of pure DFC (Figure 6.14 c). Evidently, new functional groups were observed between 1560 and 3080 cm^{-1} in the reused catalyst some of which did not exist before the catalyst was used and in pure DFC which suggested catalyst coking. Based on the FTIR results which is a surface technique, the coke layer formation in CW2 photocatalyst can be hypothesised to occur on the surface of the catalyst blocking passage to catalytic active sites. The slow rate of coke deposits formation was observed by sharp little weight losses around 400, 590 and 660 °C on TGA graph (Figure 6.14 d). It was reported elsewhere that the amorphous coke deposits are lost between 400 °C and 480 °C while between 600 °C and 680 °C, the loss of crystalline coke deposits occurs.[431,433] The mechanism of catalyst coking, and the various techniques used to validate it do not form the scope of this work but different reviews have been made on this topic by different authors for further reading.[431,433] However, they reported that coking depends on different parameters such as the kind of feed as some compounds are strong coke layer formation agent precursors than others and coke resistant semiconductors have been developed recently.[432] Moreover, the rate of coke layer formation is not directly proportional to the rate of catalytic deactivation and in some instances, removal of a coke layer deposit did not appreciably augment catalytic activity.[431] Herein, despite the observed catalyst coking during batch photocatalytic processes, little reduction in degradation efficiency of DFC suggested the little effect of coking in deactivation of the CW2 nanocomposite photoactivity. However cobalt ions were determined to leach into solution with a concentration of 0.18 ppm of cobalt detected after four cycles which can be addressed by use of supports to minimize the rate of leaching or suitable membranes to recover them.

6.5 Probing reactive oxygen species

The degradation of organic molecules by semiconductor heterogeneous photocatalysis is initiated by absorption of photons by ground state electrons in the semiconductor which initiate formation of different reactive oxygen species for complete mineralisation of pollutants. Moreover, photogenerated holes have been reported to also initiate the degradation of organic pollutants by different authors.[411,412,428] To this effect, different scavenger studies have been used to determine the different reactive oxygen species involved in the degradation of DFC by different semiconductors. Figure 6.15 shows different scavengers used to study the reactive oxygen species (ROSs) involved in

degradation of DFC by the p-n heterostructure of Co_3O_4/WO_3 under visible light irradiation. Tetra-butanol (t-BuOH), benzoquinone (BQ), EDTA, and nitrobenzene were used as hydroxyl radical, superoxide radical, holes and hydroxyl and chloride radicals respectively. When compared with the efficiency when no additives were present, the addition of 2 mM BQ as superoxide anion radical scavenger proved that the degradation of DFC by CW2 involved no generation of superoxide anion radical as only 4 % reduction was observed in the overall degradation efficiency of DFC at pH 10.7

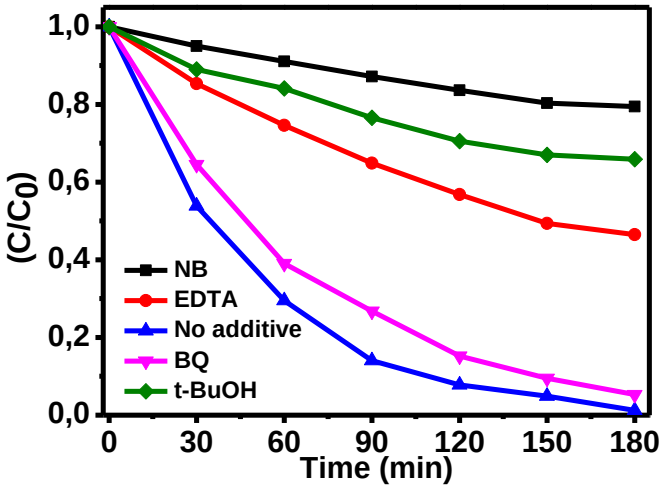

Figure 6.15: Used scavengers to determine ROSs in CW2 degradation of DFC

The addition of 2 mM EDTA proved that the photogenerated holes were involved in the degradation of DFC at pH 10.7 with overall reduction in efficiency of 45.2 % while the use of 2 mM NB achieved 78.2 % reduction in efficiency. The efficiencies were 94.7 %, 53.5 % and 20.5 % for BQ, EDTA and NB respectively. NB has been reported to be a scavenger for both chloride radicals and hydroxyl radicals in degradation of DFC.[414] However, the effect of only chloride radicals can be quantified by using only a scavenger for photogenerated holes which proved that their effect was minimal as the use of 1.5 mM t-BuOH resulted in efficiency reduction of 13.6 %.

6.6 Charge separation and proposed photocatalyst activity

The interaction of semiconductors is important in photocatalysis and was evaluated based on the FE-SEM results which showed that spherical particles of Co_3O_4 are attached and interconnected on the surface and the sides of 3D platelets of WO_3 nanoparticles. Figure 6.16 (a) shows the interaction between the metal oxide semiconductors which was important to minimize leaching of the Co_3O_4 nanoparticles in the solution and improve the photocatalytic activity of the CW2 nanocomposite.

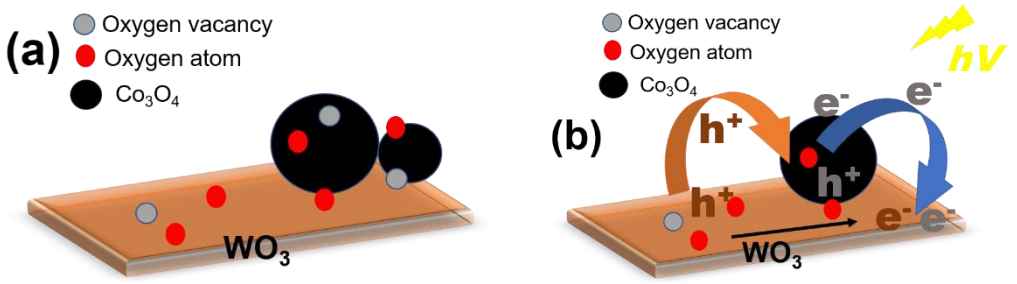

Figure 6.16: (a) Interaction and (b) charge transfer mechanism in CW2 composite

Based on the interaction between the nanoparticles, the presence of the oxygen vacancies and the results of scavenger reactions, the charge transfer in the nanocomposite was proposed and is shown in Figure 6.16 (b). To further understand the charge transfer and describe the ROSs involved in the degradation of the nanocomposite, conduction and valence band edge potentials were calculated for both WO_3 and Co_3O_4. Figure 6.17 shows the proposed charge transfer and the respective p-n heterojunction formed to minimize photoexcited electrons and holes recombination in CW2 nanocomposite. The potential of electrons required to convert ambient oxygen into the superoxide anion radical versus (Vs.) normal hydrogen electrode (NHE) is known to be -0.33 eV. If the electrons on the conduction band of the semiconductor are more positive, they cannot convert ambient oxygen to superoxide anion radical but can undergo a series of other reactions with water to form hydrogen peroxide that can dissociate into the hydroxyl radical. To calculate the conduction band edge potential (E_{CB}) and the valence band edge potential (E_{VB}) of a semiconductor, Equations 6.8 and 6.9 can be used, respectively.

$$E_{VB} = X - E^e + 0.5E_g \quad (6.8)$$

$$E_{CB} = E_{VB} - E_g \quad (6.9)$$

where E_g is the bandgap of the semiconductor, E^e is the energy of free electrons vs. normal hydrogen electrode (4.5 eV) and X is the electronegativity of the semiconductor. The electronegativity of the semiconductor can be calculated from the individual atoms' electronegativity using Equation 6.10.

$$\boldsymbol{X} = [(\boldsymbol{A})^{\boldsymbol{a}}\, \boldsymbol{X}\, (\boldsymbol{B})^{\boldsymbol{b}}]^{\mathbf{1}/(\boldsymbol{a}+\boldsymbol{b})} \quad (6.10)$$

where a and b are the number of atoms A and B in the compound. The values of E_g and *X* for WO_3 are 2.74 and 6.3 eV and 1.96 and 5.9 eV for Co_3O_4, respectively. Therefore, the E_{CB} and E_{VB} of WO_3 were calculated to be +0.43 and +3.17 eV while the E_{CB} and E_{VB} are

calculated to be +0.42 and +2.38 eV for Co_3O_4 VS NHE. According to the conduction band potential of WO_3 and Co_3O_4, the electrons on any of their levels cannot directly reduce oxygen to the superoxide anion radical ($O_2/^{\bullet}O_2^-$ = -0.33 VS NHE) but can convert it to H_2O_2 (O_2/H_2O_2 = +0.693). However, the valence band edge potential of WO_3 is more positive (+3.17) than the energy required to oxidise hydroxyl anion into the hydroxyl radical ($OH^-/OH^{\bullet}$ = +2.7 eV VS NHE). Therefore, there is generation of more hydroxyl radicals in the formed p-n heterojunction between Co_3O_4 and WO_3 which is involved in the degradation of DFC to its intermediates and further to the final products (aliphatic compounds, H_2O and CO_2).

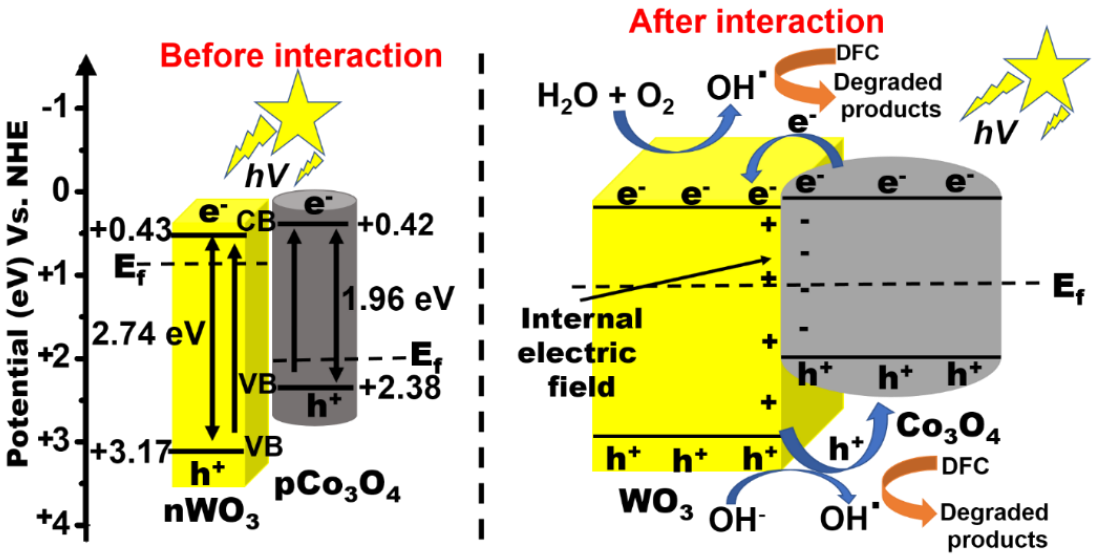

Figure 6.17: Proposed degradation mechanism in Co_3O_4/WO_3 p-n heterojunction

By considering the bandgap and valence and conduction band levels of the individual semiconductors, the band-alignment diagram of the Co_3O_4/WO_3 p-n heterojunction is shown in Figure 6.17. Under illumination by visible light, electron-hole pairs generate in both Co_3O_4 and WO_3. The fermi level energy (E_f) in p type Co_3O_4 is located near its valence band while the fermi level of n type WO_3 is located near its conduction band before contact.[434] For the heterostructure to be formed between a p type semiconductor and an n type semiconductor, the fermi level energy of each semiconductor is adjusted such that it reaches equilibrium. The Mulliken electronegativity theory (geometrical mean of individual atoms electronegativity) governs band edge positions[435] and it has been proved that for a p-n heterojunction formation; as the energy of the fermi levels shift to reach equilibrium the band edge energies shift.[435,436] In a standard type II heterostructure, the energy band potential of Co_3O_4 rises resulting in virtual staggered band alignment.[437] However, this band

shift was not greater than -0.33 eV that is the required conduction band energy level for formation of superoxide anion radicals from photoexcited electrons[438] as per the obtained scavenger experiments and the determined bioproducts that are a result of $h^+/OH^\bullet$ attack. The ROSs trapping experiments proved little involvement of the superoxide anion radical in the overall degradation efficiency of DFC and proved this point. The Fermi-level energies of the semiconductors reach an equilibrium and when this happen, the photogenerated electrons move from the conduction band (CB) of Co_3O_4 to the less negative CB of WO_3 forming a more negative electric charge in the p-type semiconductor and more positive induced electric charge in the n-type WO_3 semiconductor to enhance the separation of the photoexcited electron and holes in a bidirectional manner. This means holes will migrate from the more positive induced electric field to the VB of Co_3O_4 with subsequent oxidation of OH^- to $OH^\bullet$. The significant CW2 performance enhancement is therefore attributed to the effective charge separation and the strong interaction from spheroids Co_3O_4 and 3D platelets of WO_3 in agreement with the SEM and PL results. In summary, the photoexcited electrons and holes and the formation of ROSs can be presented by Equations 6.11 - 6.15.

$$\mathbf{Co_3O_4/WO_3 + hv \rightarrow Co_3O_4\,(e^-) + WO_3\,(h^+)} \quad \mathbf{(6.11)}$$

$$\mathbf{O_2 + H_2O + e^- \rightarrow H_2O_2 + OH^-} \quad \mathbf{(6.12)}$$

$$\mathbf{H_2O_2 + hv \rightarrow 2OH^\bullet} \quad \mathbf{(6.13)}$$

$$\mathbf{OH\text{-} + h+ \rightarrow OH^\bullet} \quad \mathbf{(6.14)}$$

$$\mathbf{DFC + {}^\bullet OH \rightarrow Intermediates \rightarrow H_2O + CO_2} \quad \mathbf{(6.15)}$$

Therefore, the degradation of DFC is initiated by reaction of hydroxyl radicals except the photogenerated h^+ which also help to improve the interaction between the negatively charged DFC after dissociation and the nanocomposite.

CHAPTER 7

DIRECT Z-SCHEME Co_3O_4/BIOI FOR IBUPROFEN AND TRIMETHOPRIM DEGRADATION

7.1 Introduction

Organic pollutants existence as mixtures in the environmental wastewaters and the performance of techniques that can remove them is certainly significant. Their intermediates often interact with each other during degradation processes resulting in difficulties in complete mineralisation and formation of unknown by-products that may be more toxic than the parent compounds. Ibuprofen is a widely used and detected pharmaceutical while trimethoprim in the most common antibiotic used since its discovery. The possibility of bioaccumulation and different reports on lethal acute and chronic exposure to these pollutants warrants their investigation.[439]

The past decade has revealed enormous upsurge in novel synthesis and applications of visible light semiconductors such as bismuth oxyhalides, metal sulphites, chalcogenides etc.[440] Z- scheme heterostructures that mimic the natural photosynthesis arose as scientists deliberated on development of heterojunctions for escalation of the technical acumen established on coupling two or more semiconductors.[83,441] Indirect Z-scheme systems employ electron mediators like the plasmonic metals (Ag, Pt, Bi etc) or carbon materials (like exfoliated graphite, EG) to enhance recombination of electrons and holes from the conduction band of one semiconductor to the valence band of another[442] while in direct Z-scheme, intersystem recombination occurs due to different factors such as band alignment without the use of any mediators.[443] The discussion of the interaction of powder semiconductors on formation of Z-scheme heterostructures in heterogeneous photocatalysis needs further evaluation to increase the literacy and knowledge in this field. Moreover, the use of Co_3O_4 and BiOI has never been reported anywhere according to literature investigations.

This work established the fabrication of visible light active semiconductors using Co_3O_4 and BiOI through a self-assembly method that is discussed in detail in **Section 3.2.9** with improved synergy for a Z-scheme heterojunction formation with strong visible light absorption for degradation of a mixture of IBU and TMP. This constructure has benefits such as rapid pollutants mineralization and enhanced facile charge separation.

7.2 Results and discussion

The photocatalytic performance of the Z-scheme heterojunction was systematically inspected for degradation of IBU and a mixture of both IBU and TMP. Different techniques were employed to get insights into physical, chemical, structural and optical properties of the synthesised materials. Moreover, the Z-scheme photocatalytic charge transfer mechanism of Co_3O_4/BiOI was hypothesised to occur and discussed in detail after investigations with different techniques such as photoluminescence, FE-SEM and some control experiments using charge carrier scavengers. The stability of the semiconductor was also evaluated while UV-Vs and TOC were used to evaluate the degradation process.

7.2.1 SEM/EDX

The morphology of the as synthesised photocatalysts was evaluated by field emission scanning electron microscopy (FE-SEM) to understand the growth mechanism that resulted in synergy by combining Co_3O_4 and BiOI. Figure 7.1 a shows that Co_3O_4 developed into worm like spheroids that were aggregated and stacked on top of each other while the synthesised BiOI appeared as flowerlike spheres with distinctive curvatures (Figure 7.1 b).

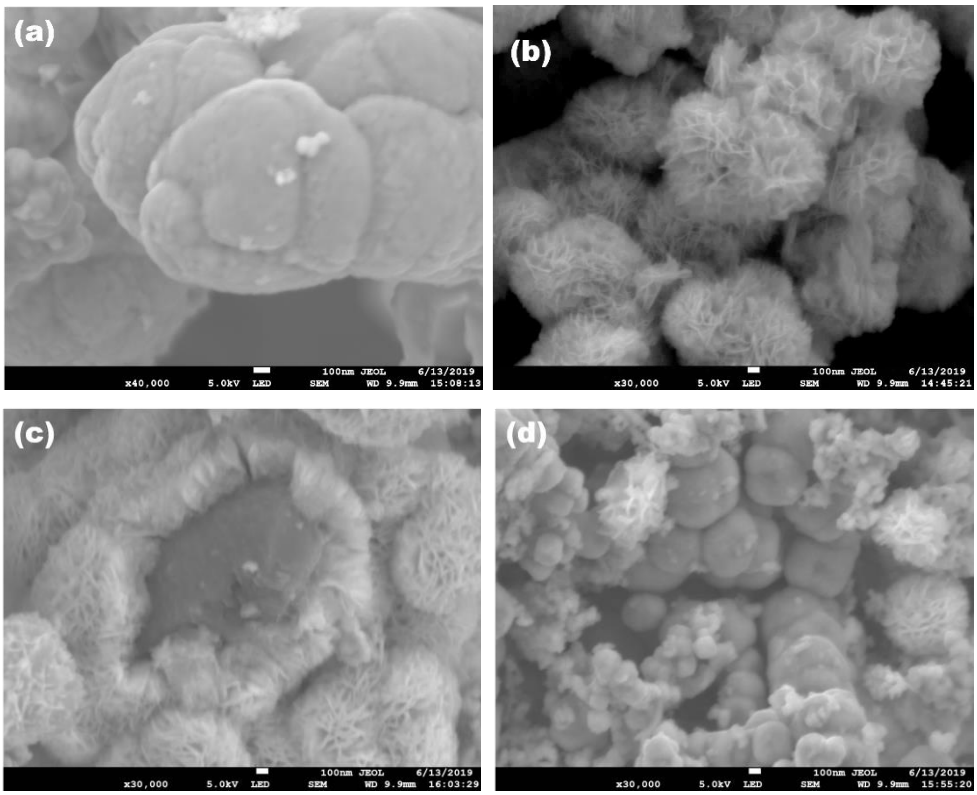

Figure 7.1: SEM images of (a) Co_3O_4, (b) BiOI, (c) CoBi2 and (d) CoBi3

The CoBi2 nanocomposite displayed worm like 3D spherical plates of Co_3O_4 engulfed by aggregates of BiOI microspheres with only the top surface of an epitaxial layer of Co_3O_4

disc appearing (Figure 7.1 C). Further increase in Co_3O_4 completely changed the morphology of the composite with BiOI microspheres deposited on adjacent 3D spherical particles of Co_3O_4 (Figure 7.1 d). Moreover, the BiOI microspheres were unevenly distributed on the surface of Co_3O_4 in CoBi3 nanocomposite.

Elemental composition of the nanocomposite was confirmed by EDX analysis to confirm the different elements present in the nanocomposites (Figure 7.2). In all the analysed semiconductor photocatalysts, carbon was present from the carbon coating and stabs. Figure 7.2 a confirmed the synthesised Co_3O_4 with peaks due to Co, O and C observed with atomic compositions of 38.9 %, 35.0 % and 26.1 % respectively. The EDX spectrum of BiOI also showed peaks due to C, O, I and Bi with atomic weights of 71.6 %, 14.0 %, 6.0 % and 8.4 % respectively (Figure 7.2 b). All the peaks due to individual atoms observed in the pristine materials were also observed in the composite confirming that indeed BiOI and Co_3O_4 coexisted (Figure 7.2 c). The atomic compositions in the composite were 33.7 %, 14.6 %, 43.7 %, 3.7 % and 4.2 % for C, O, Co, I and Bi respectively. The elemental composition of the nanocomposite agreed with the precursor ratios used during the synthesis.

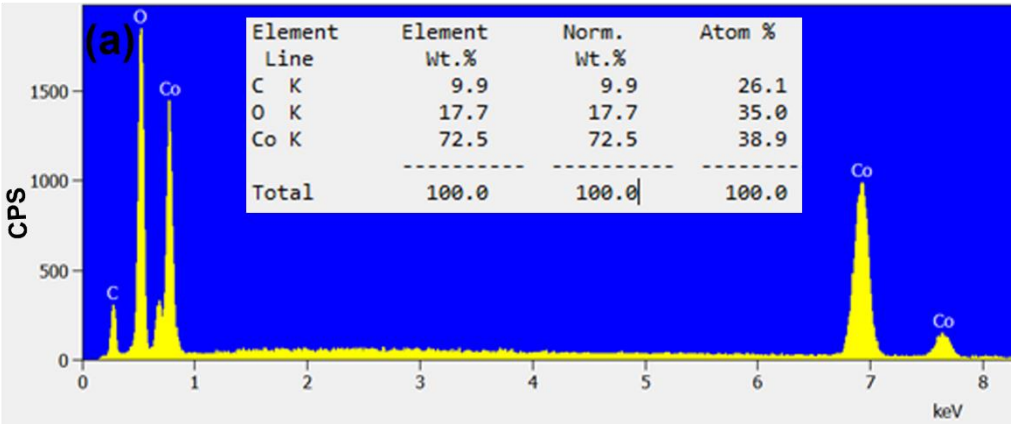
(a)
O
Co
C
Co
Co
CPS
1500
1000
500
0
0
1
2
3
4
5
6
7
8
keV
Element Line | Element Wt.% | Norm. Wt.% | Atom %
C K | 9.9 | 9.9 | 26.1
O K | 17.7 | 17.7 | 35.0
Co K | 72.5 | 72.5 | 38.9
Total | 100.0 | 100.0 | 100.0

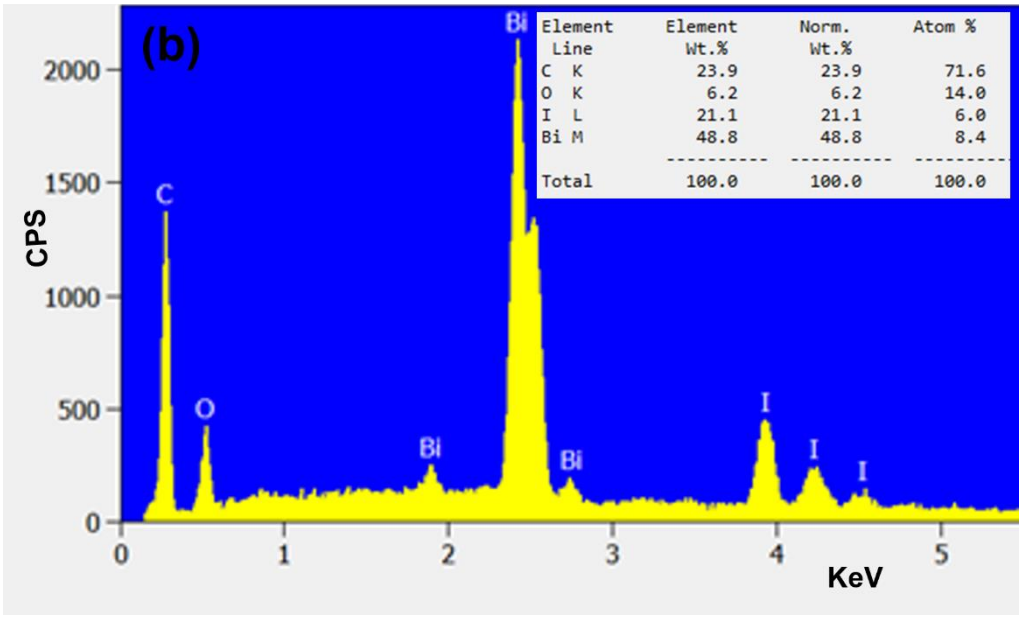
(b)
Bi
C
O
Bi
Bi
I
I
I
CPS
2000
1500
1000
500
0
0
1
2
3
4
5
KeV
Element Line | Element Wt.% | Norm. Wt.% | Atom %
C K | 23.9 | 23.9 | 71.6
O K | 6.2 | 6.2 | 14.0
I L | 21.1 | 21.1 | 6.0
Bi M | 48.8 | 48.8 | 8.4
Total | 100.0 | 100.0 | 100.0

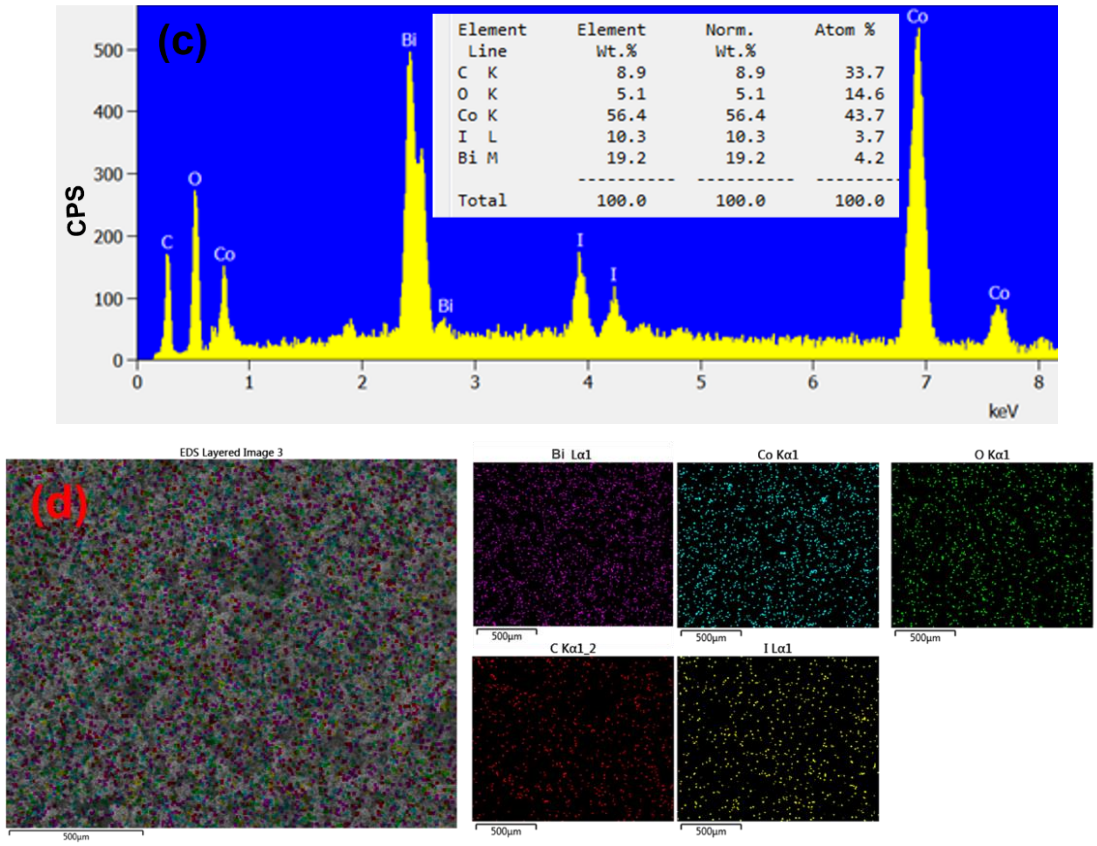

Figure 7.2: EDX spectra of (a) Co_3O_4, (b) BiOI, (c) CoBi2 and EDS mapping of CoBi2

The oxygen vacancies in the nanocomposite are important in enhancing the photocatalytic degradation activity as reported in our previous work.[120] Moreover, the oxygen vacancies also existed in the pristine materials with nonstoichiometric ratios of the oxygen atom evident from the elemental weight percentages. The mapping of the CoBi2 nanocomposite proved that all elements existed (Bi, Co, O, I and C from carbon conducting tape (Figure 7.2 d)) as expected. Therefore, it can be inferred that despite the Co_3O_4 being engulfed by BiOI cauliflower spheres, the distribution was even throughout the composite.

7.2.2 TEM/HR-TEM/SAED

The crystal structure and morphologies of the synthesised nanomaterials were investigated by TEM analysis (Figure 7.3). The morphology of Co_3O_4 showed discs that are interlocked and grew in two directions resulting in wormy epitaxy of spheroids (Figure 7.3 a). The different directions were confirmed by HR-TEM with d spacings of 0.118 and 0.158 nm that are due to the 111 and 511 planes respectively (Figure 7.3 b). The stacking of spheroidal Co_3O_4 occurred such that the exposed facets were the 111 planes. The SAED images confirmed the presence of the 111, 220, 311, 222, 400, 422, 511 and 440 planes and the synthesised Co_3O_4 was highly crystalline (Figure 7.3 c). TEM images of

BiOI showed cauliflower morphologies with stems that distinctively differentiated the curvatures of the sheets on the BiOI (Figure 7.3 d). The HR-TEM image (Figure 7.3 e) of BiOI displayed d spacings of 102 and 110 planes. The stems or rod like BiOI grow along the 102 planes while the direction of the flower - like BiOI grew along the 110 planes. The planes of 102, 110, 200 and 212 (Figure 7.3 f) were present on BiOI SAED spectra. Moreover, the cauliflower morphology like BiOI was highly crystalline. The nanocomposite TEM images (Figure 7.3 g) distinctively showed the Co_3O_4 spheroids engulfed inside the BiOI micro flowers and the exposed facet of Co_3O_4 in the nanocomposite was 511 planes[236] growing along the 110 planes of BiOI[263] as shown by HR-TEM images (Figure 7.3 h) and concordant with the XRD results with d spacing of 0.159 nm and 0.3021 nm respectively. Figure 7.3 i confirmed that the nanocomposite semiconductors maintained their crystallinity with the outer planes being due to BiOI which is expected to reduce the leachability of Co_3O_4 into the solution.

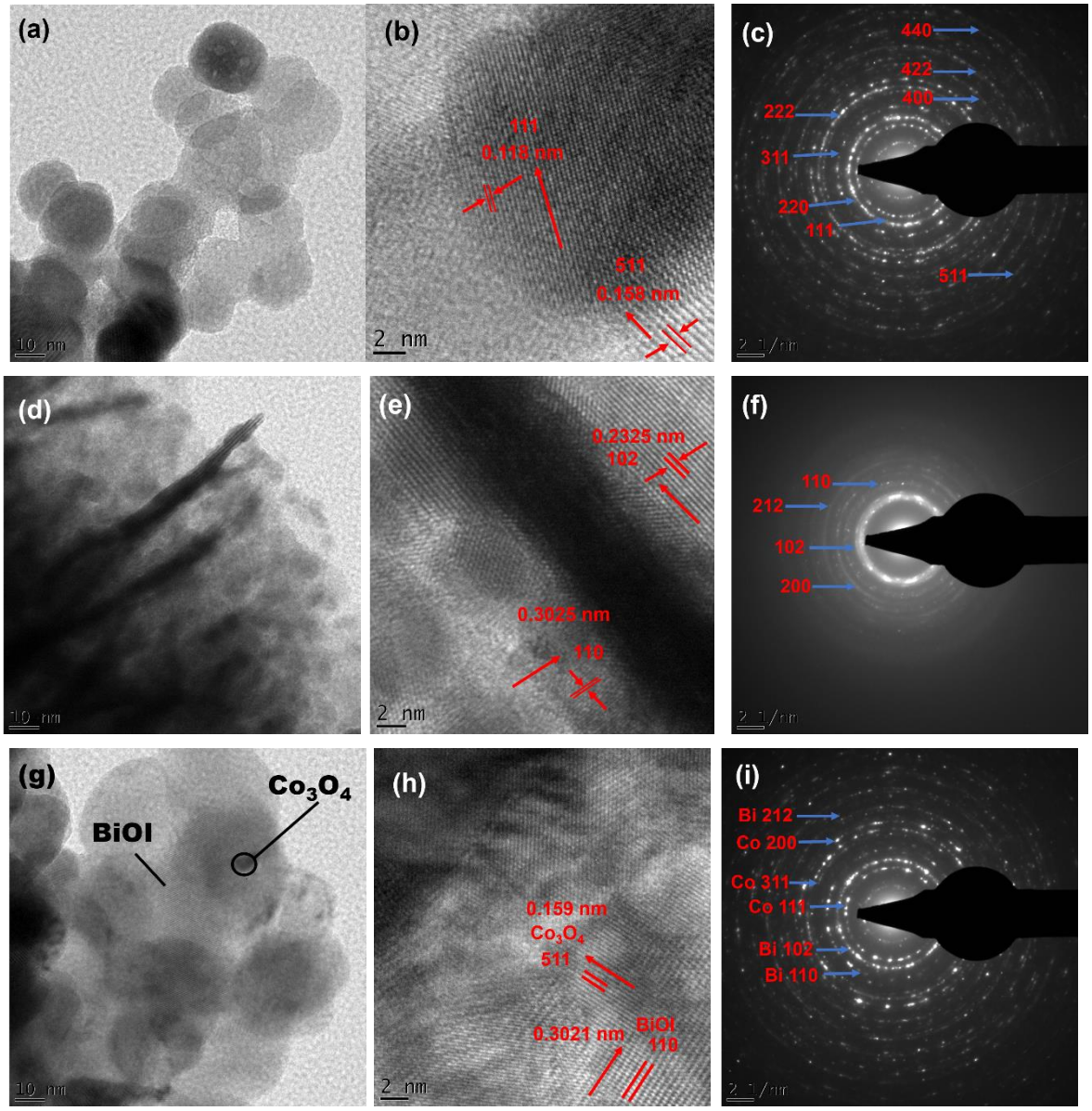

Figure 7.3: TEM, HR-TEM and SAED images of (a, b, c) Co_3O_4, (d, e, f) BiOI and (g, h, i) CoBi2

In the nanojunctions, Co_3O_4 and BiOI particles closely attached to each other on a nano-level. Such junctions could help keep Co_3O_4 nanoparticles from falling off from the BiOI support while ultrasonication and agitation occur during the catalytic reaction. The method of nano-assembly is important in enhancing the interaction between the pristine materials and minimizing leaching of cobalt ions.

7.2.3 XRD and FTIR

The phase and crystallographic structure of the materials were determined by XRD. Figure 7.4 a shows the XRD patterns of different as-synthesised nanomaterials. All diffraction peaks from Co_3O_4 catalyst were indexed to the space group 227 ($Fd\bar{3}m$) (PDF

01- 074-1657) of the cubic structure[444] with the peaks at 2θ = 19.04°, 31.46°, 38.87°, 38.70°, 44.97°, 55.79°, 59.60° and 65.38° corresponding to 111, 220, 311, 222, 400, 422, 511 and 440 planes respectively. The XRD pattern of pure BiOI correspond to the tetragonal structure and the peaks matched very well with the standard diffraction pattern (JCPDS No. 10-0445).[104] The peaks at 2θ = 28.87°, 31.82°, 45.59° and 55.06° were indexed to 102, 110, 200 and 212 planes of BiOI microspheres. All peaks due to BiOI and the 311 lattice plane due to Co_3O_4 can be observed in the XRD spectra of the nanocomposites. Moreover, the intensity of the 311 lattice plane increased with increasing amount of Co_3O_4 in the composites from CoBi1 to CoBi3. The mean grain size (d) was assessed using the Debye–Scherrer equation that gives the relationship between the Bragg angle (θ) in radians, the corrected full-width at half maximum (FWHM, β) in radians and the X-ray wavelength (λ = 1.5406 A˚) by ($d = 0.9\lambda/\beta\sin\theta$) while (D = $0.9\lambda/\beta\cos\theta$) was used to determine the crystallite size of the materials (D). The mean d values were 0. 2325, 0.1180, 0.2016, 0.2017 and 0.2017 nm while the D values were 12.95, 18.11, 24.40, 19.50 and 9.01 nm for BiOI, Co_3O_4, CoBi1, CoBi2 and CoBi3 respectively. Interestingly, an increase in the crystallite sizes of the CoBi1 and CoBi2 were observed compared to pristine semiconductors with the increase more in CoBi2 than CoBi1. Therefore, incorporation of Co_3O_4 in BiOI improved the crystallinity hence the photocatalytic activity is expected to be higher. However, further increase in the Co_3O_4 content in the nanocomposite to form CoBi3 ration reduced the crystalline size and is expected to exhibit low photocatalytic activity.[445] These results coherently support the SEM analysis results as CoBi2 had Co_3O_4 nanoparticles engulfed in flowerlike BiOI with improved interaction while CoBi3 only conveyed that BiOI microspheres self-assembled on Co_3O_4 resulting in weak interaction that results in reduced crystallite size (Figure 7.2 c and d). The average diffusion time (Ƭ) of charge carriers from bulk to surface of a photocatalyst is expressed by Equation 7.1.[446]

$$Ƭ = r^2\pi^2D \qquad (7.1)$$

In this equation, r is the grain radius and D is the diffusion coefficient of the charges and the calculation assumes only a defect-assisted recombination type of process called steady-state Shockley–Read–Hall recombination. According to this equation, the large particle size of a photocatalyst will lead to the long diffusion time. Hence, opportunity for recombination of electron-hole pairs will be greatly increased, leading to decreased photocatalytic activity. Therefore, the decrease in the d values of CoBi1, CoBi2 and CoBi3 compared to BiOI confirms that the photocatalytic activity of the composites will be greatly

enhanced compared to BiOI as their mean grain sizes decreased. The micro-strain values were derived from the relationship ($\varepsilon = \beta/4\tan\theta$) and were determined to be 0.000796, 0.00147, 0.000501, 0.000626 and 0.00136 for BiOI, Co_3O_4, CoBi1, CoBi2 and CoBi3 respectively. The micro-strain values of CoBi1 and CoBi2 decreased when compared to that of BiOI. This implies that there was an increase in the crystallinity of these composites that is expected to result in increased photoactivity. Further increase of the Co_3O_4 content in CoBi3 resulted in decreased crystallinity suggesting synergy caused by interaction of BiOI and Co_3O_4 depends on the amount with the effect higher at low amounts of Co_3O_4. Therefore, it can be inferred that the formation of a direct z-scheme occurred as there are obvious differences in the micro-strain values of the pristine semiconductors and the nanocomposites which can be attributed to strong interactions that lead to synergistic effects towards photocatalytic degradation of the selected pollutants.

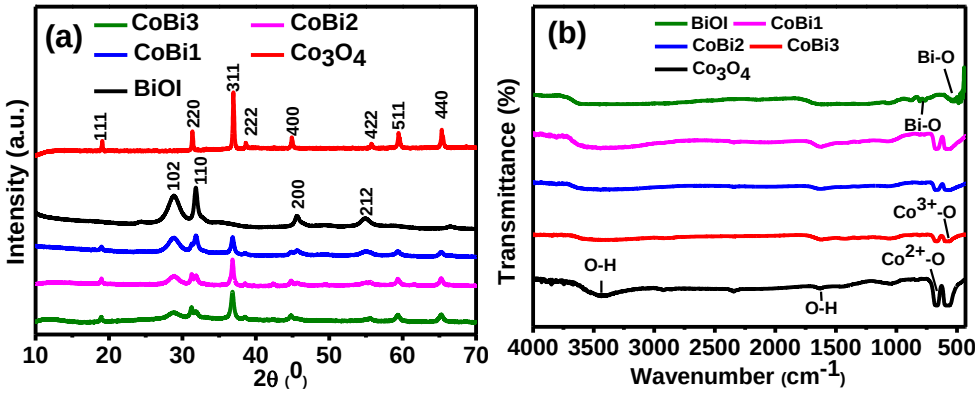

Figure 7.4: (a) XRD and (b) FTIR spectra of as synthesised nanocomposites

Figure 7.4 b gives the Fourier transform infrared (FT-IR) spectra of Co_3O_4, BiOI and Co_3O_4/BiOI composites. In the spectrum of pure BiOI, the peak corresponding to v(Bi–O) was observed at 491 cm^{-1} and belongs to symmetrical A2u-type vibration of the Bi-O bond.[135,447] The absorption at 764 cm^{-1} originated from asymmetrical stretching vibration of the Bi-O bond. The characteristic peaks of BiOI at 764, 1068, 1311 and 1604 cm^{-1} were obviously present in BiOI and the nanocomposites. For Co_3O_4, the strong band at 579 cm^{-1} was due to Co-O of octahedrally coordinated Co^{3+} and the one at 670 cm^{-1}can be assigned to the stretching vibration mode of Co-O in which Co is Co^{2+} and is tetrahedrally coordinated. The bands at 3433 and 1633 cm^{-1} were assigned to the stretching and bending vibrations of absorbed water molecule on Co_3O_4, BiOI and the synthesised composites.

7.2.4 BET

Figure 7.5 describes typical N_2 adsorption−desorption isotherms and the corresponding pore size distributions of BiOI, Co_3O_4, and CoBi2 nanoparticles. The BiOI hierarchical

microspheres, Co_3O_4 and CoBi2 showed a type II adsorption−desorption isotherm, in which the weak adsorption−desorption hysteresis indicated monolayer absorption (Figure 7.5 a). Moreover, the shapes of hysteresis loops resembled type H3, which is associated with slit-shaped pores between analogous sheets believed to be between the 3D spherical micro-discs for Co_3O_4, flowery curvatures for BiOI and a combination of both in CoBi2.[120]

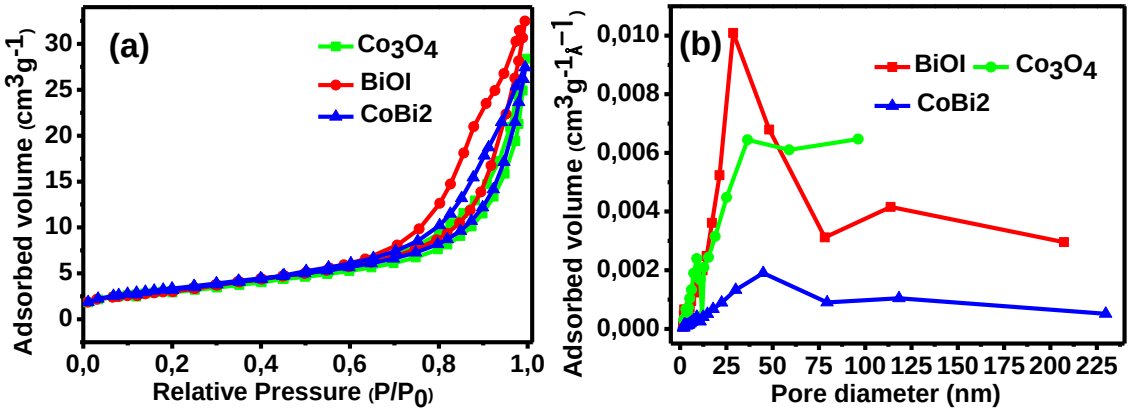

Figure 7.5: (a) N_2 adsorption desorption isotherms and (b) Pore diameter distribution of Co_3O_4, BiOI and CoBi2

The pore size distribution curves were calculated through the Barrett−Joyner−Halenda (BJH) method by the BET software. As shown in Figure 7.5 b, pore size distribution curves of all materials showed some materials that had no micropores (below 2 nm), mesoporous (2 nm – 50 nm) and macroporous (above 50 nm). The smaller mesopores reflect pores within nanosheets, whereas larger ones can be correlated to the pores formed between stacked nanosheets. The synthesised BiOI, Co_3O_4, and CoBi2 showed BET surface areas of 17.4721, 13.4082, and 3.6774 m^2g^{-1} respectively. There is an astonishing decrease in the surface area of the CoBi2 nanocomposite compared to the pristine materials which suggested that when BiOI microspheres and Co_3O_4 spheroids discs are self-assembled, they block the accessible surfaces resulting in a decrease in the pore volume capacity. The corresponding pore volumes were 0.050403, 0.043775 and 0.010582 cm^3/g for BiOI, Co_3O_4 and CoBi2 respectively. Therefore, adsorption was not prominent towards removal of the pollutants and they were influenced by other factors such as rate of formation of EHPs, reduction in EHPs recombination and improved electrostatic interaction between pollutants and the catalyst that can be caused by surface charges (negative on pollutant and positive on catalyst).

7.2.5 TGA

The thermal stability of the materials was evaluated by thermogravimetric analysis (Figure 7.6 a). Co_3O_4 showed high thermal stability over the entire temperature range while BiOI exhibited two major weight losses and became stable after 800 °C. The first weight loss

(22.5 %) was observed from 300 °C – 550 °C while the second weight loss of 7.5 % occurred between 650 °C and 750 °C. Moreover, the thermogram of the composite (CoBi2) confirmed the presence of the pristine materials with matching decompositions as expected.

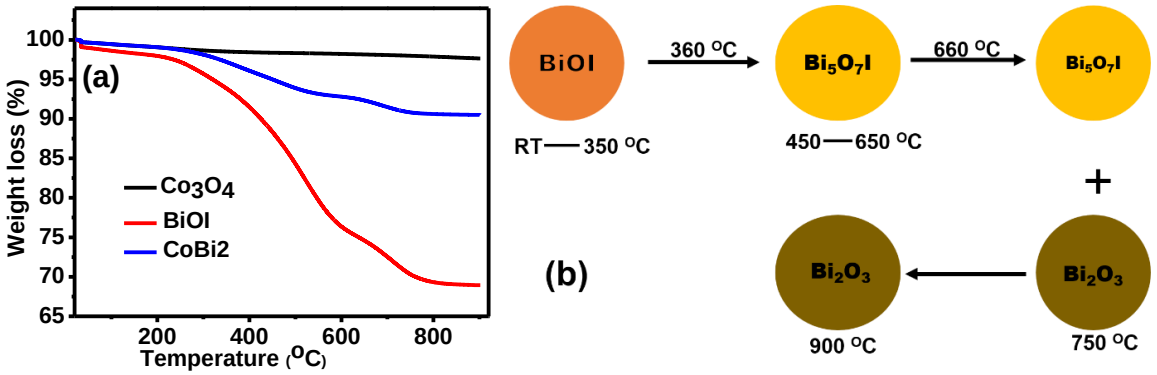

Figure 7.6: (a) TGA of Co_3O_4, BiOI and CoBi2 and (b) corresponding phase transformation in BiOI

The weight losses observed in BiOI were probed with multiple analysis results to study the different phase changes (Figure 7.6 b). The first weight loss corresponds to the transformation of BiOI to Bi_5O_7I that can be expressed as ($5BiOI + O_2 \rightarrow Bi_5O_7I + 2I_2$) while the second weight loss is due to formation of the stable Bi_2O_3 that corresponded to ($2Bi_5O_7I + 1/2O_2 \dashrightarrow 5Bi_2O_3 + I_2$). These results were in agreement with a similar study reported by Yu et al. based on TGA analysis of BiOI powders.[448]

7.2.6 Optical property analysis

To explore the optical properties of the synthesised nanomaterials, diffuse reflectance measurements were performed on the composites (Figure 7.7 a). All materials absorbed visible light with BiOI showing strong absorption in the UV region with an absorption edge around 600 nm which is typical of BiOI.[449] Co_3O_4 absorbed in the entire UV-Vis range (200 nm – 800 nm) due to transitions from the highest occupied molecular p orbitals of oxygen to the empty d orbitals of Co^{2+} or Co^{3+} in the spinel structure which is mostly common in its cubic crystalline form. Moreover, it also showed strong coefficient of absorption in the visible region of the spectrum which implies it may be activated by low energy light for formation of photoexcited electrons and holes pairs. This property makes them attractive materials for industrial photocatalytic applications under solar irradiation.

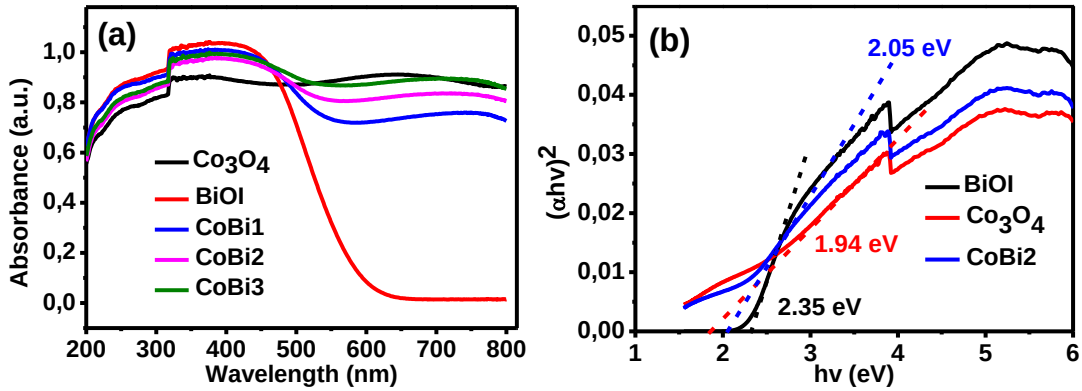

Figure 7: (a) UV-Vis spectra of different composites and (b) Tauc plots of CO_3O_4, BiOI and CoBi2

The formation of nanocomposites between BiOI and Co_3O_4 resulted in strong visible light absorption in the entire UV-Vis region confirming synergistic effect of both BiOI and Co_3O_4 for enhanced visible light absorption. The optical bandgap energy (E_g) of semiconductors is calculated based on the absorption edge of the samples by ($E_g = 1240/\lambda_{Absorp:Edge}$) and Equation 7.2.[245]

$$\alpha h\nu = A(h\nu - E_g)^{n/2} \qquad (7.2)$$

where α, v, E_g, and A are absorption coefficient, light frequency, bandgap, and a constant based on the properties of the semiconductor respectively. The absorption coefficient α, is a measure of the quantum energy that a catalyst can absorb while the inverse of the absorption coefficient, α^{-1} estimate the photon distance before it is absorbed for engineering of static fixed bed reactors. The estimated value of α^{-1} for CoBi2 is 0.7375 nm/M^2 signalling the short distance travelled by a photon before being absorbed by the nanocomposite to generate photoexcited electron hole pairs in a square meter area of CoBi2 nano-catalyst. Therefore, the thickness of 2 nm will be enough for the nanocomposite to exhibit the synergistic effect in the nanocomposite for pilot scale applications depending on the required surface area. Moreover, n depends on the characteristics of the transition in a semiconductor, i.e., direct transition (n = 1) or indirect transition (n = 4). The n value for Co_3O_4, BiOI and the composites was fitted for both direct and indirect transitions. The bandgap energy (E_g value) of the resulting samples can be estimated from a plot of $(\alpha h\nu)^2$ versus photon energy (hv) where the intercept of the tangent to the X axis gives a good approximation of the bandgap energy of the samples which were determined to be 1.94, 2.35, 2.07, 2.05 and 2.01 eV for Co_3O_4, BiOI, CoBi1, CoBi2 and CoBi3 (Figure 7.7 b). The decrease in the bandgap energies of the nanocomposites with increasing Co_3O_4 confirmed that Co_3O_4 reduced the energy required

to pioneer formation of photoexcited electrons and holes pairs in the nanocomposite resulting in improved optical synergy.

Figure 7.8 shows photoluminescence spectra of BiOI, CoBi2 and CoBi3 after excitation at 320 nm. Pristine BiOI exhibited a sharp peak at around 450 nm that decreased in CoBi3.

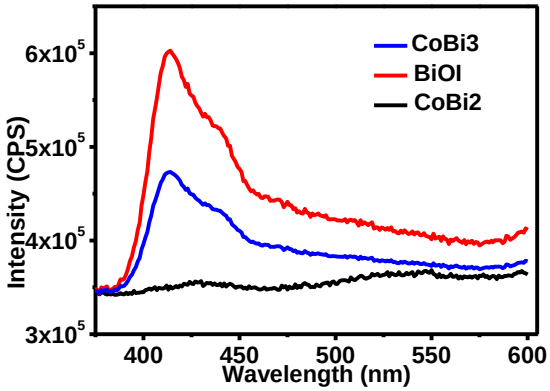

Figure 7.8: Photoluminescence spectra of BiOI, COBi2 and CoBi3

CoBi2 showed the lowest peak intensity confirming the reduction in photoexcited charge carrier's recombination in the composites. This is attributed to the strong interaction resulting from the observed morphology of the nanocomposite as shown by FE-SEM results.

7.3 Degradation of ibuprofen

The UV-Vis spectra for the degradation of IBU and a mixture of IBU and TMP are presented in Figure 7.9. There was a decrease in the absorbance of 30 ppm IBU with time at 255 nm confirming the destruction of the chromophore responsible for the absorbance. Up to 76.1% of IBU was degraded at pH 7.4 (Figure 7.9 a).

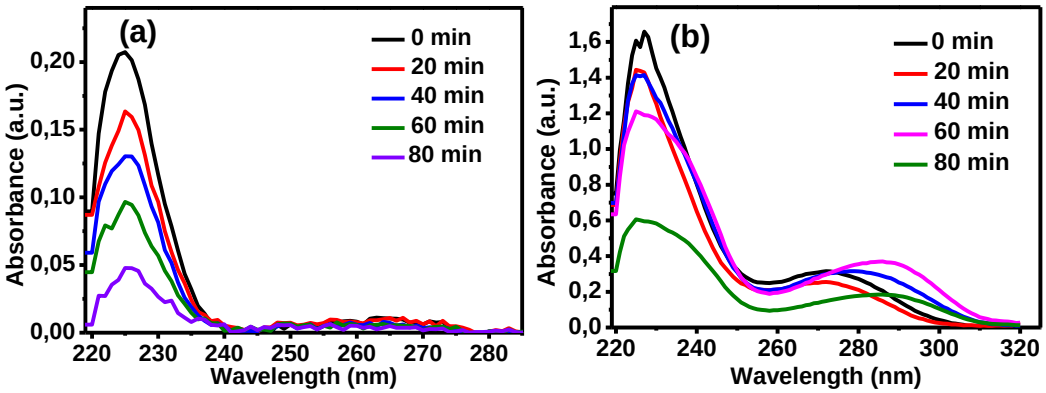

Figure 7.9: UV-Vis spectra for degradation of (a) IBU and (b) IBU and TMP

The degradation of a mixture of 10 ppm IBU and 20 ppm TMP was monitored by the decrease in the peak at 228 nm. 62.89 % of the TMP was degraded in 100 minutes (Figure 7.9 b) at pH 7.4. There was a slight red shift in the peak position for TMP and IBU

mixture which could be attributed to transformation of TMP to other higher wavelengths species or by-products or the interaction of the intermediates between TMP and IBU. The reduction in the new peak positions also suggested that the intermediates were completely degraded and alleviated the possibility of toxic by-products formation.

The different parameters were evaluated for their influence of the degradation of IBU and the results are summarized in Figure 7.10. Figure 7.10 a shows the results when different amounts of photocatalyst were used to degrade 10 ppm IBU with efficiencies of 80.31, 90.82, 93.87 and 57.84 % for 15, 30, 40 and 50 mg catalyst respectively. The efficiency increases gradually with increase in amount of catalyst which can be attributed to increased generation of reactive oxygen species (ROSs) and presence of catalysts active sites. However, at 50 mg of catalyst there was a decrease in photo-efficiency due to light obstruction and scattering by the nanoparticles in the slurry.

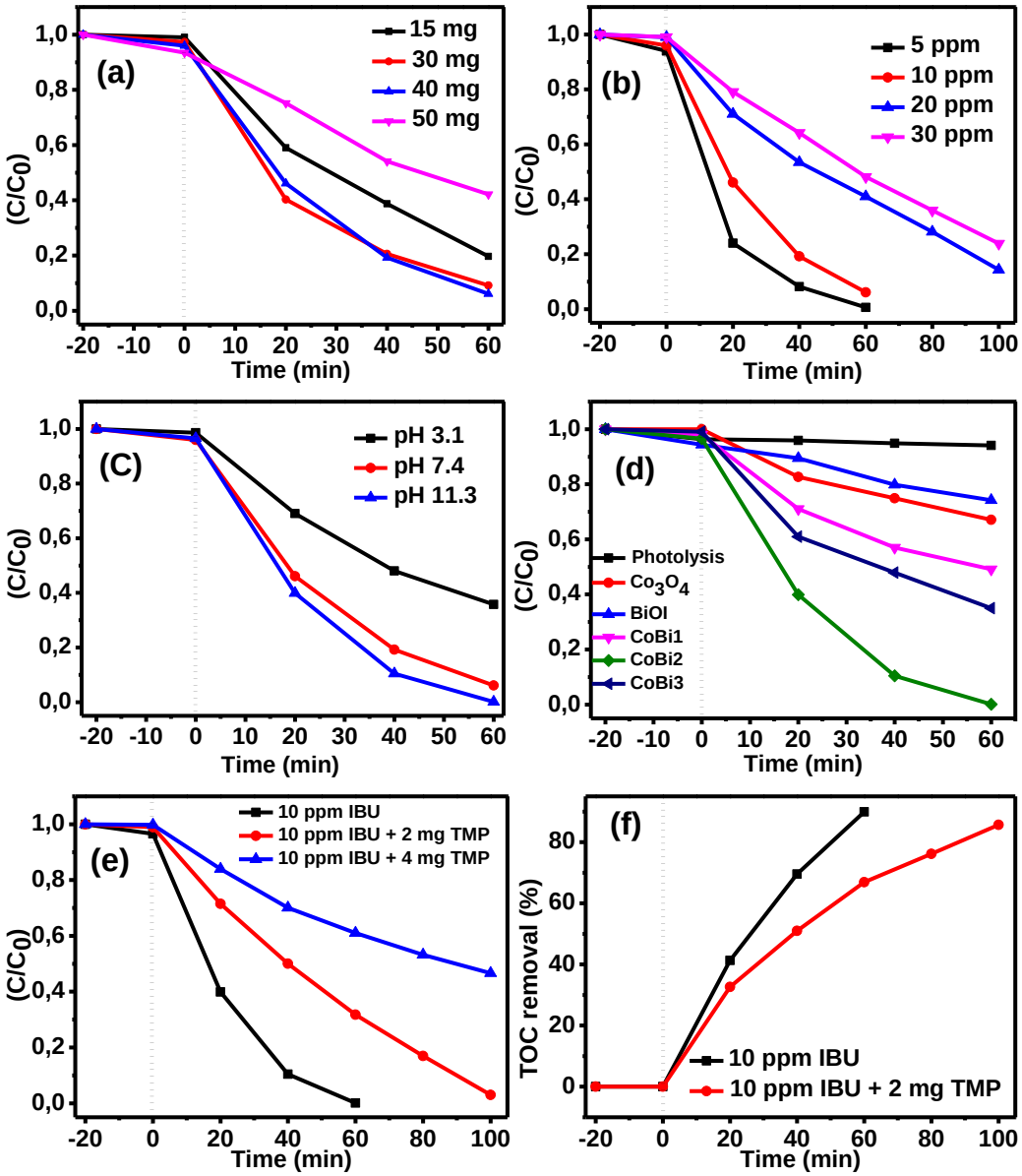

Figure 7.10: Optimisation of (a) Catalyst amount, (b) IBU concentration, (c) pH of solution and (d) Catalyst composition (e) effect of TMP and (f) TOC results

Low IBU concentrations resulted in increased degradation efficiency with efficiencies of 51.81, 58.99, 93.87 and 99.38 % for 30, 20, 10 and 5 ppm IBU respectively (Figure 7.10 b). Further increase of irradiation time to 100 minutes resulted in continued improved efficiency of 85.67 and 76.1 5 for 20 and 30 ppm IBU respectively. This increase suggested that more irradiation time may be required to completely degrade IBU at higher concentrations. Evaluation of the effect of pH on degradation showed that IBU degradation was higher at pH 7.4 and 11.3 which are above the pKa value for the IBU of around 4.91. IBU molecules exists mainly as negatively charged species when pH ≥ pKa which promotes strong interaction with the photocatalyst for efficient degradation. Neutral IBU (pH ≤ pKa) exists and interact poorly with the nanocomposite resulting in low

efficiencies irrespective of the surface charge of the catalyst. The efficiencies were 64.25, 93.87 and 99.98 % at pH 3.1, 7.4 and 11.3 respectively (Figure 7.10 c). The transformation of fully protonated IBU and the pKa required to form a negative charge due to a loss of a proton is presented by Figure 7.11.

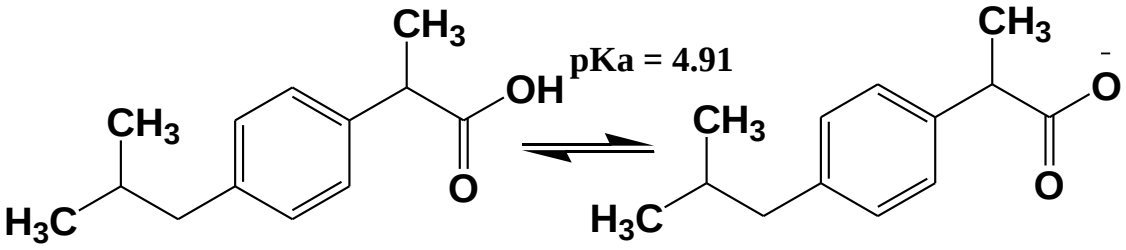

Figure 7.11: Changes to Lewis base of IBU and corresponding pKa

The formation of the conjugate base of IBU increased its degradation at pH values greater than the pKa value and further increase in hydroxide anion concentration during pH adjustment resulted in a synergistic effect as the excess hydroxide anion enhances formation of $OH^{\bullet}$, and not antagonist effect caused by competition for active sites between pollutant and negatively charged hydroxide anions. Figure 7.10 d showed efficiencies of 5.92, 32.91, 25.77, 50.89, 99.98 and 65.02 % for photolysis, Co_3O_4, BiOI, CoBi1, CoBi2 and CoBi3 respectively. The high efficiency of all composites can be attributed to the synergistic effects[362] that can be evaluated by synergy (S) from the rate of the composite ($K_{combined}$) and the sum of rate constants of individual semiconductors (ΣK_i).

$$\mathbf{S = Kcombined - \Sigma K_i / Kcombined} \qquad \mathbf{(7.2)}$$

The synergistic effect of Z-scheme fabrication of BiOI and Co_3O_4 was evident from the obtained positive value of 0.9133 for degradation of IBU at pH 11.3. Moreover, adsorption behaviour was investigated and the adsorption of IBU and a mixture of IBU and TMP reached equilibrium at around 15 minutes and TMP decreased the overall adsorption capacity of IBU (Figure 7.12 a). Therefore, adsorption only played a minimal role on the total removal efficiencies reported which supported the BET results as there was an observed decrease in BET surface area in the composite compared to BiOI. The experimental data were tested with pseudo-first-order ($\ln (Q_e-Q_t = \ln Q_e - K_1 t$) and pseudo-second-order ($t/Q_t = 1/K_2Q_e + t/Q_e$) kinetic models respectively [450], where Q_t and Q_e signify the quantity of adsorbed pollutants at a specific time and at equilibrium (mg/g) with corresponding rate constants K_1 (min^{-1}) for pseudo first order and K_2 (min^{-1}) for pseudo second order.

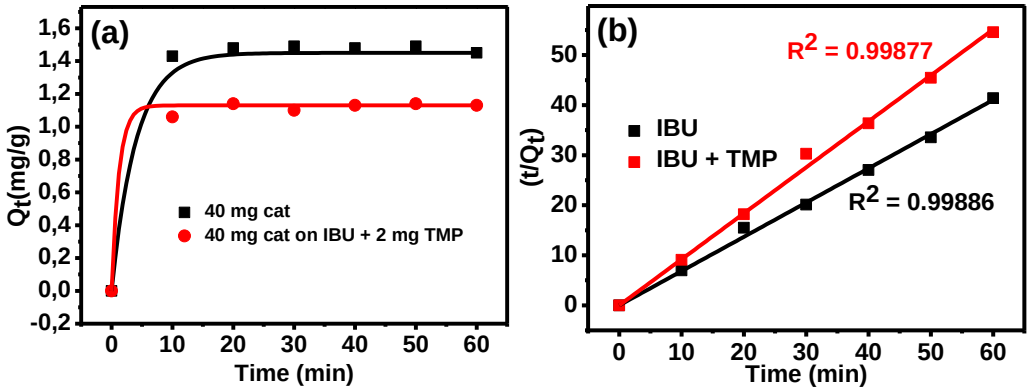

Figure 7.12: (a) Adsorption isotherms and (b) Pseudo second order rate constants for IBU and IBU + 2 mg TMP

The correlation coefficient of first order and second order reactions respectively were (R^2 = 0.45852 and R^2 = 0.39066) and (R^2 = 0.99886 and R^2 = 0.99877) suggesting that the adsorption of IBU and IBU + TMP mixture followed pseudo second order kinetics model in agreement with experimental (Figure 7.12 b) and some literature results on organic pollutants adsorption.[450,451]

The effect of addition of different amounts of TMP was investigated on the degradation efficiency and the highest efficiency of 97.02 % was achieved in 100 min when 2 mg of TMP was added to 10 ppm IBU which was degraded in just 60 minutes to 99.98 % at pH 11.3 (Figure 7.10 e). Further increase of TMP to 4 mg reduced the efficiency to 53.37 % in 100 minutes. The ratio of adsorption capacities (R_q) is defined by $R_q = Q_e/Q_0$) where Q_e is the adsorption capacity of pollutant in the binary or multi-component solution and Q_0 is the adsorption capacity of the pollutant with the same initial concentration in a mono-component solution. It was observed that (a) if $R_q > 1$, the adsorption of pollutant is promoted by the presence of other pollutants, (b) if $R_q = 1$, there is no effect on adsorption capacity of pollutant, and (c) if $R_q < 1$, the presence of other pollutants suppresses the adsorption of the pollutant.[452] For IBU, Rq < 1 hence the presence of TMP does not only supress the degradation efficiency but also the adsorption of IBU by CoBi2 nanocomposite. TOC removals of 89.95 % and 85.68 % were observed for IBU and a mixture of 10 ppm IBU and 2 mg TMP respectively (Figure 7.10 f). Therefore, it can be inferred that degradation of IBU and a mixture of IBU and TMP resulted in residual amounts of the carbon containing compounds.

The kinetics of IBU degradation was also investigated by Langmuir Hinshelwood model and fitted to the pseudo first-order equation (Equation 7.3).

$$\mathbf{Kt} = \boldsymbol{ln}\left(\frac{C0}{Ct}\right) \qquad \textbf{(7.3)}$$

where k signifies the pseudo first-order rate constant (min^{-1}), C_t and C_0 are final and initial concentrations of IBU respectively.

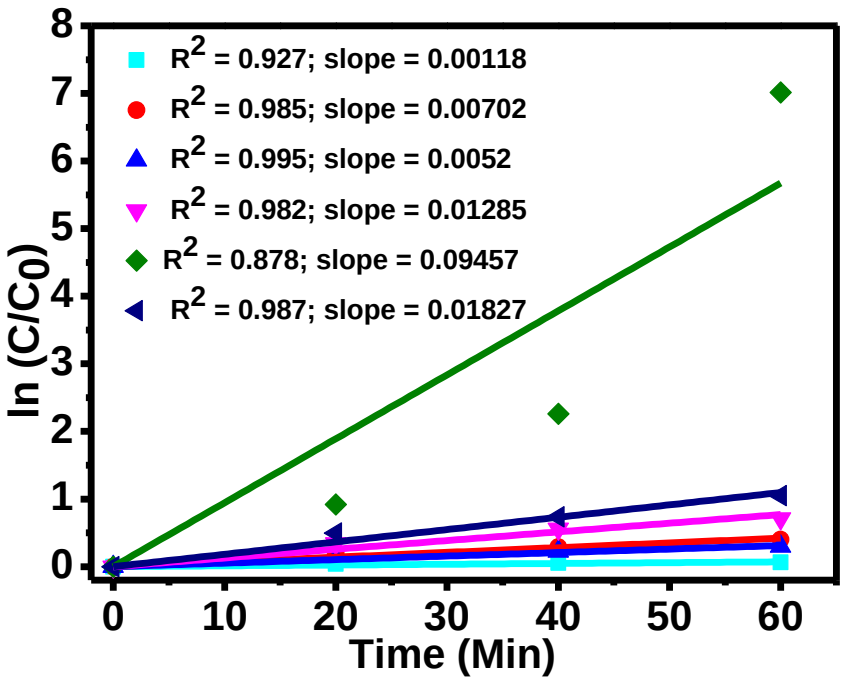

Figure 7.13: Rate constants and linear regression constants for (a) Photolysis, (b) BiOI, (c) Co_3O_4, (d) CoBi1, (e) CoBi3 and (f) CoBi2

The rate constants, k, (Figure 7.13) were 0.00118, 0.00702, 0.0052, 0.01285, 0.09457 and 0.01827 min^{-1} for photolysis, Co_3O_4, BiOI, CoBi1, CoBi2 and CoBi3 respectively. CoBi2 exhibited the highest rate constant k, which is more than nine-fold that of BIOI microspheres. Therefore, it can be concluded that the formation of a Z-scheme through Co_3O_4 getting engulfed in BiOI microspheres resulted in enhanced photocatalytic activity.

7.4 Catalyst stability, recycling and scavenging

The photocatalyst stability was evaluated using XRD following recyclability tests and the results are presented in Figure 7.14. The material was re-used for up to three cycles with efficiencies of 99.98 %, 98. 72 % and 95.03 % (Figure 7.14 a). The pollutant adsorption followed a similar pattern in the recycled material compared to fresh or initial degradation.

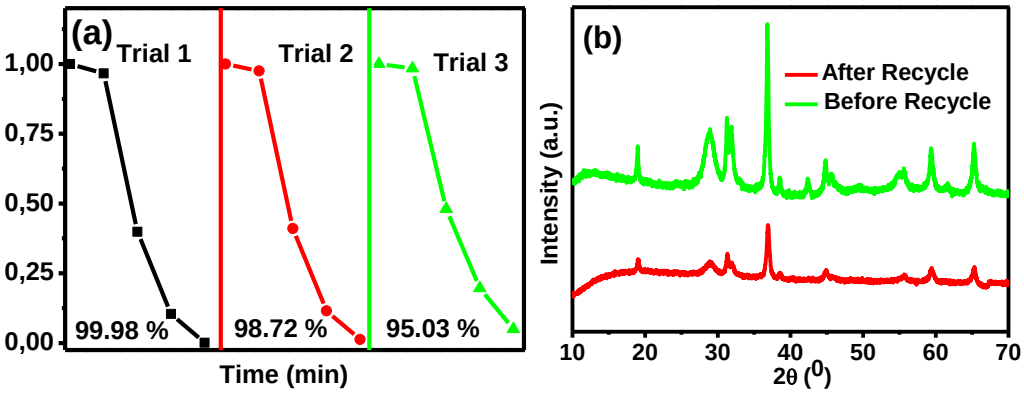

Figure 7.14: (a) Catalyst reusability and (b) Stability at pH 11.3

The stability of the recycled nanocomposite as evaluated by XRD (Figure 7.14 b) proved that the catalyst is very stable with only minor reduction in the peak intensities. The crystalline structure was maintained confirming that the degraded by-products were desorbed from the nanocomposite surface. Furthermore, there were no observed structural changes in XRD patterns obtained before and after degradation signalling that the composite was very stable.

Leaching of heavy metals is another important aspect of photocatalysis using semiconductors and it was investigated for cobalt ions that have been reported to endanger human lives when available in concentrations above 2 ppb. The concentration of the cobalt ions after using the composite at pH 7.4 were determined to be 1.69 ppm while the recycled composite after three cycles gave 0.23 ppm at pH 11.3. This proved that at alkaline pH values, there is low leachability of cobalt ions in solution however, the values were still high and can be reduced by use of supports such as exfoliated graphite or dendrimers to minimise leaching. The use of supports enhance photocatalytic degradation, prevent leaching and enhance separation of the catalyst after reuse.[453–455]

To further determine the main active species responsible for the degradation processes, investigations through elemental trapping experiments were performed using radical scavengers (Figure 7.15).

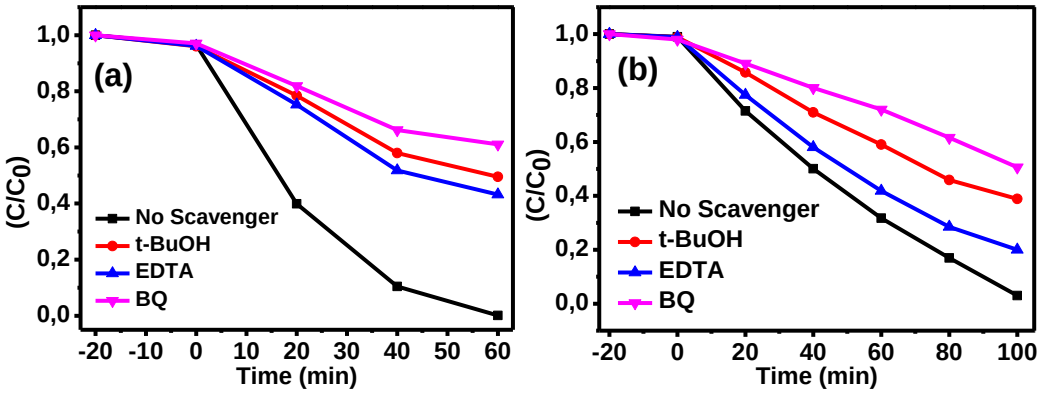

Figure 7.15: Scavenger results for (a) IBU and (b) IBU and TMP degradation

Ethylenediamine tetra-acetic acid (EDTA), Benzoquinone (BQ) and tert-butanol (t-BuOH) were used as the hole, superoxide and hydroxyl radicals' scavengers. From the radical trapping experiments for pure IBU (Figure 7.15 a) the degradation process was suppressed by addition of BQ, t-BuOH and EDTA which reduced the degradation efficiency of the nanocomposite. The superoxide radical, holes and hydroxyl radical scavengers reduced the efficiency by 61.07, 43.17 and 49.54 % respectively. The addition of BQ showed the highest reduction in efficiency hence the superoxide radical was the main active species for degradation of IBU. This was further confirmed by trapping experiments for a mixture of IBU and TMP with reduction in efficiencies of 47.63, 16.99 and 35.92 % for BQ, EDTA and t-BuOH respectively (Figure 7.15 b). Interestingly, the fact that even a mixture of IBU and TMP showed a similar trend means the nanocomposite was not selective on the pollutant target and there was consistent generation of ROSs under visible light excitation.

7.5 Charge transfer and proposed mechanism

In order to get insight into the electronic properties, and the charge transfer processes during the degradation, a mechanism for the synergist interaction of Co_3O_4 and BiOI, based on first principles density functional theory and previously reported results was proposed.[456–458] The irradiation of CoBi2 nanocomposite with visible light results in the generation of photoexcited electrons and holes in both Co_3O_4 and BiOI since they are visible light active. The internal electric field in BiOI along the 110 plane induces positive electric charge on Co_3O_4 and prohibits the transfer of electrons from the conduction band of Co_3O_4 to the conduction band of BiOI. However, the electrons from the conduction band of BiOI recombine with the holes in the valence band of Co_3O_4 resulting in intersystem recombination that enhance the separation of the nanocomposite photogenerated charge carriers for improved generation of hydroxyl radicals ($OH^{\bullet}$) and superoxide anion radicals ($^{\bullet}O_2^-$). The enhanced formation of the ROS is paramount in

photodegradation of pollutants and can be proposed by evaluating the work functions of BiOI (110) and Co_3O_4 (311) facets according to Equation 6.4.[456]

$$\phi = E_{vac} - E_f \quad (6.4)$$

where E_{vac} and E_f are electrostatic potentials of the vacuum energy and Fermi energy, respectively. Since the semiconductors are both p-type, their fermi levels are close to their respective valence band with the one for Co_3O_4 higher than that for BiOI due to their respective valence band edge potentials that are determined by ($E_{VB} = X - E^e + 0.5E_g$) while the conduction band edge was determined by ($E_{CB} = E_{VB} - E_g$). E_g is the bandgap of the semiconductor, E^e is the energy of free electrons vs. normal hydrogen electrode (4.5 eV) and is the electronegativity of the semiconductor and can be derived from Equation 6.5.[237]

$$\boldsymbol{X} = [(\boldsymbol{A})^{\boldsymbol{a}}\, \boldsymbol{X}\, (\boldsymbol{B})^{\boldsymbol{b}}]^{\mathbf{1}/(\boldsymbol{a}+\boldsymbol{b})} \quad (6.5)$$

where a and b are the number of atoms A and B in the compound. The generalised charge transfer in the z-scheme CoBi2 nanocomposite is presented by Figure 7.16. The reactions that are involved in formation of the generated ROSs due to photoexcited charge carries is summarized in (Equation 6.6 – Equation 6.9).

$$Co_3O_4/BiOI + hv \rightarrow Co_3O_4/BiOI\ (h^+ + e^-) \quad (6.6)$$

$$OH^- + h^+ \rightarrow OH^\bullet \quad (6.7)$$

$$^\bullet O_2^- + e^- \rightarrow {}^\bullet O_2^- \quad (6.8)$$

$$^\bullet O_2^-/h^+/OH^\bullet + IBU/TMP \rightarrow CO_2 + H_2O \quad (6.9)$$

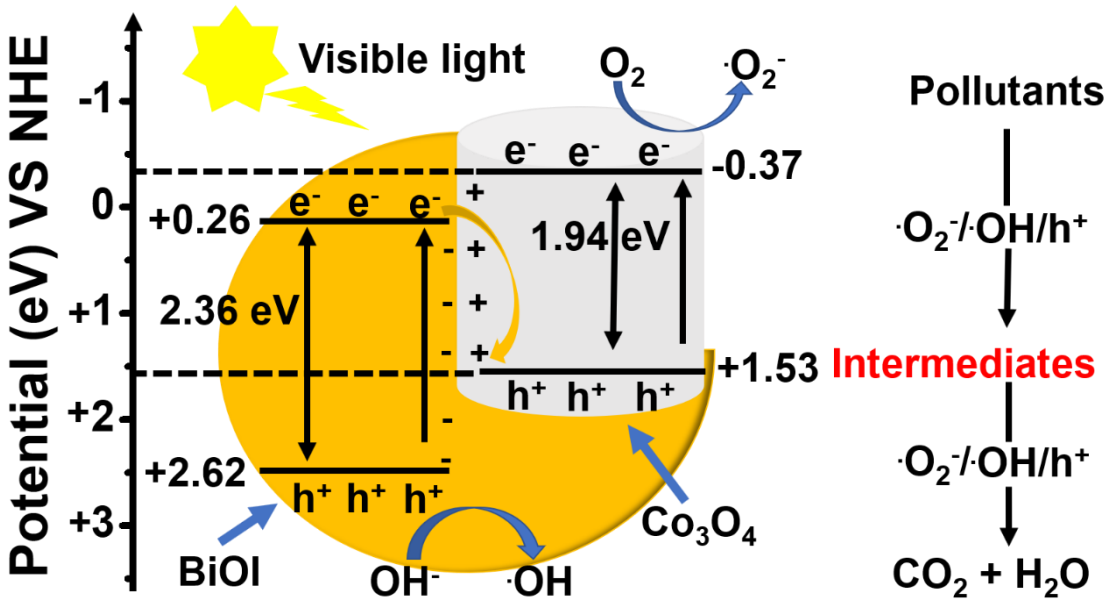

Scheme 7.16: Charge transfer and proposed degradation mechanism

The electrons on the conduction band of Co_3O_4 with more negative potential ($O_2/^{\bullet}O_2^-$ = -0.33 VS NHE), will directly reduce adsorbed oxygen to $^{\bullet}O_2^-$. Since the generation of photoexcited electrons requires less energy, more electrons will be generated resulting in $^{\bullet}O_2^-$ being the major ROS formed for degradation of the pollutants first into intermediates and then water and carbon dioxide. Moreover, the E_{VB} of the BiOI is more positive than the redox potential of $OH^-/OH^{\bullet}$ (1.99 eV vs NHE), resulting in the formation of hydroxyl radical.[417] However contradicting reports of the above narrative state that the redox potential of $OH^-/OH^{\bullet}$ is 2.71 eV vs NHE.[120,459] ROSs trapping experiments vividly confirmed the involvement of $OH^{\bullet}$. Moreover, some literature suggested that $^{\bullet}O_2^-$ has the water splitting capability to convert H_2O into first hydrogen peroxide and then the hydroxyl anion (OH^-) (Equation 7.10).[83,442] The OH^- can easily be further oxidised to $OH^{\bullet}$ and the involvement of this ROS species cannot be ignored in the degradation of the selected polutants by the z-scheme photocatalyst with improved synergistic effect. In addition, electrons that are on the conduction band of BiOI can form H_2O_2 that can further dissociate into $OH^{\bullet}$ (H_2O_2 + hv → $2OH^{\bullet}$) upon absorption of photons before they recombine with holes on the valence band of Co_3O_4.[120] Indexing the source of the involved $OH^{\bullet}$ will require spiking tests that can be performed with in-situ electron spin resonance spectroscopy. The improved crystallinity in BiOI in the CoBi2 nanocomposite and their ability to absorb lower energy photons to form photoexcited electrons and holes results in enhanced photodegradation of IBU and TMP as charge carrier recombination will be reduced through Z-scheme intersystem recombination of electrons from the conduction band of BiOI and holes on the valance band of Co_3O_4. Moreover, BiOI has an induced

internal electric field that enhances the intersystem recombination and efficiently combats recombination of electrons and holes in the individual Co_3O_4 or BiOI semiconductors. This intersystem recombination is a necessity towards driving the formation of the proposed Z-scheme mechanism. Moreover, several authors have confirmed that BiOI 110 facet has the empathy to trap and convert oxygen to the superoxide anion radical thereby increasing the generation of this ROS to initiate the degradation pathway of organic pollutants into water and carbon dioxide.[460] Therefore, when Co_3O_4 is engulfed by BiOI, improved morphology and interaction for successful formation of the nanocomposite with direct Z-scheme capability towards efficient charge separation and degradation efficiency due to quick generation of radicals is realised.

CHAPTER 8
CONCLUSIONS AND RECOMMENDATIONS

8.1 Conclusions

This study efficaciously accomplished the set objectives and the following general and specific conclusions can be drawn from the investigations that stemmed from various materials characterization and applications in this work:

- The low calcination temperatures (350 – 400 °C) and composition (presence of TPP, EG, RGO or Co_3O_4) favours the formation of the monoclinic crystalline phase of WO_3 and has resulted in high photocatalytic activity.
- The use of TPP, EG and RGO changed the crystal phase (the monoclinic phase formed when 0.5 % TPP was used) and particle shape of WO_3, reduced agglomeration of the nanoparticles.
- Use of EG and RGO increased the specific surface area in the nanocomposites by more than 50 % which is important for pollutant adsorption.
- Degradation of AB25 was rapid in acidic pH value of 5 while the degradation of IBU, TMP and DFC was optimum in basic medium of pH 10 - 11 by virtue of improved interaction between the pollutants and the photocatalysts.
- The composites of TPP/WO_3/RGO, TPP/WO_3/EG, Co_3O_4/WO_3 and Co_3O_4/BiOI gave the highest degradation efficiencies of 85.1 %, 99.2 % (both for degradation of AB25), 98.7 % (degradation of DFC) and 99.98 % (degradation of IBU and TMP) respectively.
- The nanocomposites had reduced rate of the recombination of photoexcited electrons and holes compared to pristine semiconductors and the bandgap of WO_3 was reduced from 3.2 eV by RGO and TPP to 2.4 while TPP and EG resulted in reduction of WO3 band gap from eV to eV.
- Co_3O_4 minimized the recombination of photoexcited electron-holes and reduced the band gap of BiOI and WO_3 from 2.35 eV and 2.74 eV to 2.05 eV and 2.61 eV respectively.
- In-situ method resulted in rectangular prisms of WO_3 (around 190 nm) with exposed 020 plane of monoclinic WO_3 surrounded by 111 planes of Co_3O_4 particles of around 65 nm strongly attached to it.
- Exfoliated graphite (EG) and reduced graphene oxide can be used as suitable and cheap support materials in the development of buoyant heterogeneous

photocatalyst semiconductors that are easy to separate, have improved performance and can enhance separation of photoexcited charge carriers.

- Visible light absorbing semiconductors WO_3, BiOI and Co_3O_4 were synthesized and their photocatalytic activity can be greatly enhanced by formation of heterojunctions, phase engineering and presence of lattice defects such as oxygen vacancies.
- The as synthesized composites showed good stability towards the degradation of AB25, DFC, IBU and TMP and could be re-used five times, four times and three times respectively without affecting their crystal structure as proved by XRD.
- The mineralization of DFC into aliphatic compounds, nitrates, water and carbon dioxide was achieved and detoxification was achieved via the dechlorination and complete mineralization of DFC and its intermediates via oxidation with non-selective hydroxyl radicals using the CW2 composite.
- A composite of Co_3O_4 and WO_3 was resistant to coking with high thermal stability.

8.2 Recommendations

This project was successfully executed but the following recommendations were made from the attained results:

- The nanocomposites had high degradation efficiencies and can be explored for large scale applications
- The synthesised composites of TPP/WO_3/EG, TPPWO_3/RGO, Co_3O_4/WO_3 and Co_3O_4/BiOI demonstrated good photocatalytic activity and their performance can be evaluated on real wastewater samples from WWTPs effluents or different industries.
- The systematic analysis of how the synthesised photocatalysts can perform under solar irradiation could be explored.
- Future studies can focus on the use of Co_3O_4 and the selected semiconductors (WO_3 and BiOI) or other semiconductors inside support materials such as EG, RGO, Dendrimers, carbon nanotubes, etc. to minimize leaching of cobalt in aqueous solutions.

REFERENCES

1 WFFP, *Living Planet Report 2016 Risk and Resilience in a New Era*, 2016.

2 H. Bigas, in *The Global Water Crysis: Addressing an Urgent Security Issue*, Papers for the InterAction Council 2011-2012, UNU-INWEH, Hamilton Canada., 2012, pp. 1–176.

3 W. A. Jury and H. J. Vaux, *Adv. Agron.*, 2007, **95**, 1–77.

4 United Nations, *E-GOVERNMENT SURVEY 2018*, 2018.

5 N. Mancosu, R. L. Snyder, G. Kyriakakis and D. Spano, *Water*, 2015, **7**, 975–992.

6 United Nations, Goal 6: Ensure access to water and sanitation for all, https://www.un.org/sustainabledevelopment/water-and-sanitation/, (accessed 23 June 2019).

7 C. Wang, J. Li, G. Mele, G. Yang, F. Zhang, L. Palmisano and G. Vasapollo, *Catal. B Environ.*, 2007, **76**, 218–226.

8 U. Sarkar, K. C. Ravindra, E. Large, C. L. Young, D. Rivera-burgos, J. Yu, M. Cirit, D. J. Hughes, J. S. Wishnok, D. A. Lauffenburger, L. G. Griffith and S. R. Tannenbaum, *Drug Metab. Dispos.*, 2017, **45**, 855–866.

9 M. Jothibas, C. Manoharan, S. J. Jeyakumar, P. Praveen, I. K. Punithavathy and J. P. Richard, *Sol. Energy*, 2018, **159**, 434–443.

10 R. S. Andre, J. C. Pereira, L. A. Mercante, D. Locilento, L. H. C. Mattoso and D. S. Correa, *J. Alloys Compd.*, 2018, **767**, 1022–1029.

11 R. Afroz, M. M. Masud, R. Akhtar and J. B. Duasa, *Environ. Urban. ASIA*, 2014, **5**, 63–81.

12 A. J. Ebele, M. A. Abdallah and S. Harrad, *Emerg. Contam.*, 2017, **3**, 1–16.

13 M. H. Wu, J. Shi and H. P. Deng, *Arab. J. Chem.*, 2018, **11**, 924–934.

14 S. A. Zikalala, A. T. Kuvarega, B. B. Mamba, S. D. Mhlanga and E. N. Nxumalo, *Mater. Today Chem.*, 2018, **10**, 1–18.

15 C. Chacón, M. Rodríguez-Pérez, G. Oskam and G. Rodríguez-Gattorno, *J. Mater. Sci. Mater. Electron.*, 2015, **26**, 5526–5531.

16 J. Fu, L. Chen, Y. Dai, F. Liu, S. Huang and C. Chen, *Mol. Catal.*, 2018, **455**, 214–223.

17 Z. Xiang, Y. Wang, D. Zhang and P. Ju, *J. Ind. Eng. Chem.*, 2016, **40**, 83–92.

18 Z. C. Sun, Y. Bin She, Y. Zhou, X. F. Song and K. Li, *Molecules*, 2011, **16**, 2960–

2970.

19 A. Priya, P. Arunachalam, A. Selvi, J. Madhavan, A. M. Al-mayouf and M. A. Ghanem, *Opt. Mater. (Amst).*, 2018, **81**, 84–92.

20 M. M. Ghangrekar and P. Chatterjee, *Water Pollutants Classification and Its Effects on Environment*, India, 2018.

21 Q. Xiao, S. Yu, L. Li, Y. Zhang and P. Yi, *Water Res.*, 2019, **150**, 310–320.

22 X. He, M. Pelaez, J. A. Westrick, K. E. O. Shea, A. Hiskia, T. Triantis, T. Kaloudis, M. I. Stefan, A. A. De and D. D. Dionysiou, *Water Res.*, 2011, **46**, 1501–1510.

23 M. M. Ghangrekar and I. I. T. Kharagpur, *Wastewater Manag.*, 1–5.

24 S. Benkhaya, S. El Harfi and A. El Harfi, *Appl. J. Environ. Eng. Sci.*, 2017, **3**, 311–320.

25 M. Hou, G. L. Baughman and T. A. Perenich, *Dye. Pigment.*, 1991, **16**, 291–297.

26 U. S. EPA/SEMARNAP, *Pollut. Prev. Work Gr.*, 1996, 1–167.

27 S. Tavazzi, B. Paracchini, G. Suurkuusk, G. Mariani, R. Loos, M. Ricci and B. M. Gawlik, *Water Framework Directive. Watch List Method: Analysis of diclofenac in water*, Luxembourg, 2014.

28 M. A. Hassaan and A. EL Nemr, *Am. J. Environ. Sci. Eng.*, 2017, **1**, 64–67.

29 WRC and WHO, *Water Treatment*, Europe, 1989.

30 F. M. D. Chequer, G. A. Rodrigues de Oliveira, E. R. A. Ferraz, J. C. Cardoso, M. V. B. Zanoni and D. Palma de Oliveira, in *Textile dyes*, INTECH, New York, co-Friendl., 2013, pp. 151–176.

31 A. Ghorani-Azam, B. Riahi-Zanjani and M. Balali-Mood, *J. Res. Med. Sci.*, 2016, **21**, 65–76.

32 M. Dinari, M. M. Momeni and M. Ahangarpour, *Appl. Phys. A Mater. Sci. Process.*, 2016, **122**, 876–884.

33 R. Giovannetti, E. Rommozzi, M. Zannotti and C. A. D'Amato, *Catalysts*, 2017, **7**, 305.

34 M. B. Tahir, G. Nabi, M. Rafique and N. R. Khalid, *Int. J. Environ. Sci. Technol.*, 2017, **14**, 2519–2542.

35 R. Manikandan, A. V. Anand and G. D. Muthamani, *Int. J. Curr. Microbiol. Appl. Sci.*, 2013, **2**, 15–19.

36 A. E. Ghaly, R. Ananthashankar, M. Alhattab and V. V Ramakrishan, *J. Chem. Eng. Process Technol.*, 2013, **05**, 1–18.

37 Wikipedia the free encyclopedia, Acid Blue 25, https://en.wikipedia.org/wiki/Acid_Blue_25, (accessed 01 October 2019).

38 E. Önder, *IARC Monogr.*, 1977, **99**, 55–67.

39 S. Sen Gupta and D. Chakrabortty, *Indian J. Chem. A*, 2017, **56**, 1293–1301.

40 H. Ghodbane and O. Hamdaoui, *Chem. Eng. J.*, 2010, **160**, 226–231.

41 W. Schmidt and C. H. Redshaw, *Ecotoxicol. Environ. Saf.*, 2015, **112**, 212–222.

42 P. G. Conaghan, *Rheumatol. Int.*, 2012, **32**, 1491–1502.

43 L. Mzukisi, N. Tawanda and L. Chimuka, *J. Pharm. Biomed. Anal.*, 2018, **147**, 624–633.

44 P. Paíga, M. Correia, M. João, A. Silva, M. Carvalho, J. Vieira, S. Jorge, J. Gabriel, C. Freire and C. Delerue-matos, *Sci. Total Environ.*, 2019, **648**, 582–600.

45 G. McEneff, W. Schmidt and B. Quinn, *Pharmaceuticals in the Aquatic Environment: A Short Summary of Current Knowledge and the Potential Impacts on Aquatic Biota and Humans*, Wexford, 2015, vol. Report No.

46 P. Bottoni, S. Caroli and A. B. Caracciolo, *Toxicol. Environ. Chem.*, 2010, **92**, 549–565.

47 C. Daughton, *Drug Usage and Disposal: Overview of Environmental Stewardship and Pollution Prevention (with an emphasis on some activities in the Federal Government)*, North Carolina, 2008.

48 A. B. A. Boxall, V. D. J. Keller, J. O. Straub, S. C. Monteiro, R. Fussell and R. J. Williams, *Environ. Int.*, 2014, **73**, 176–185.

49 N. Zhang, G. Liu, H. Liu, Y. Wang, Z. He and G. Wang, *J. Hazard. Mater.*, 2011, **192**, 411–418.

50 K. A. K. Musa and L. A. Eriksson, *Phys. Chem. Chem. Phys.*, 2009, **11**, 4601–4610.

51 P. Iovino, S. Chianese, S. Canzano, M. Prisciandaro and D. Musmarra, *Desalin. Water Treat.*, 2017, **61**, 293–297.

52 J. L. Oaks, M. Gilbert, M. Z. Virani, R. T. Watson, C. U. Meteyer, B. A. Rideout, H. L. Shivaprasad, S. Ahmed, M. Jamshed, I. Chaudhry, M. Arshad, S. Mahmood, A. Ali and A. A. Khan, *Lett. to Nat.*, 2004, **427**, 2002–2005.

53 R. Naidoo, L. C. Weaver, G. Stuart-Hill and J. Tagg, *J. Appl. Ecol.*, 2011, **48**, 310–316.

54 A. Margalida, G. Bogliani, C. G. R. Bowden, J. A. Donazar, F. Genero, M. Gilbert, W. B. Karesh, R. Kock, J. Lubroth, X. Manteca, V. Naidoo, A. Neimanis, J. A.

Sanchez-Zapata, M. A. Taggart, J. Vaarten, L. Yon, T. Kuiken and R. E. Green, *Sci. Regul.*, 2014, **346**, 1296–1298.

55 C. A. Harris, P. B. Hamilton, T. J. Runnalls, V. Vinciotti, A. Henshaw, D. Hodgson, T. S. Coe, S. Jobling, C. R. Tyler and J. P. Sumpter, *Environ. Health Perspect.*, 2011, **119**, 306–311.

56 T. Haap, R. Triebskorn and H.-R. Kohler, *Chemosphere*, 2008, **73**, 353–359.

57 S. Kim and D. S. Aga, *J. Toxicol. Environ. Heal. - Part B Crit. Rev.*, 2007, **10**, 559–573.

58 Y. Rao, M. Chen and M. Zhou, *J. Adv. Oxid. Technol.*, 2014, **17**, 145–151.

59 E. O. Adawaren, L. Mukandiwa, E. M. Njoya, L. Bekker, N. Duncan and V. Naidoo, *Environ. Toxicol. Pharmacol.*, 2018, **62**, 147–155.

60 B. P. Gumbi, B. Moodley, G. Birungi and P. G. Ndungu, *Chemosphere*, 2017, **168**, 1042–1050.

61 L. M. Madikizela and L. Chimuka, *Water SA*, 2017, **43**, 264–274.

62 F. O. Agunbiade and B. Moodley, *Environ. Monit. Assess.*, 2014, **186**, 7273–7291.

63 H. B. Quesada, A. Takaoka, A. Baptista, L. F. Cusioli, D. Seibert, C. D. O. Bezerra and R. Bergamsco, *Chemosphere*, 2019, **222**, 766–780.

64 F. Mendez-Arriaga, S. Esplugas and J. Gimenez, *Water Res.*, 2010, **44**, 589–595.

65 R. S. Y. Wong, *Adv. Pharmacol. Sci.*, 2019, **2019**, 3418975–3418984.

66 K. D. Rainsford, *Inflammopharmacology*, 2009, **17**, 275–342.

67 A. P. Ferreira, *J. Adv. Biol.*, 2014, **4**, 305–313.

68 A. Zarghi and S. Arfaei, *Iran. J. Pharm. Res.*, 2011, **10**, 655–683.

69 A. Pena, C. Delerue-matos and M. Montenegro, *J. Hazard. Mater.*, 2018, **175**, 45–95.

70 R. M. Botting, *J. Physiol. Pharmacol.*, 2006, **57**, 113–124.

71 J. Villanueva, I. J. Allan, M. Reid, N. Peyraube and P. Le Coustumer, *Int. J. Environ. Sci.*, 2017, **2**, 248–257.

72 T. Qureshi, N. Memon, S. Q. Memon and H. Shaikh, *Am. J. Mod. Chromatogr.*, 2014, **1**, 45–54.

73 S. J. Williams, J. Gabe and P. Davis, *Sociol. Health Illn.*, 2008, **30**, 813–824.

74 P. Paíga, L. H. M. L. M. Santos, C. G. Amorim, A. N. Araújo, M. C. B. S. M. M. Montenegro, A. Pena and C. Delerue-matos, *Environ. Sci. Pollut. Res*, 2013, **20**, 2410–2420.

75 R. Manikandan, N. Ezhili, N. Muthulakshmiandal, P. J. C. Favas and P. Venkatachalam, *J. Mater. Environ. Sci.*, 2016, **7**, 2259–2266.

76 H. Besada and K. Werner, *Int. J. Water Resour. Dev.*, 2015, **31**, 120–133.

77 A. B. Prevot, C. Baiocchi, M. C. Brussino, G. Marc and L. Palmisano, *Environ. Sci. Technol.*, 2001, **35**, 971–976.

78 B. Aruna, L. R. Silviya, E. S. Kumar, P. R. Rani, D. V. R. Prasad and D. Vijayalakshmi, *Int. J. Currrent Microiology Appl. Sci.*, 2015, **4**, 1015–1024.

79 A. Fujishima, T. N. Rao and D. A. Tryk, *J. Photochem. Photobiol. C Photochem. Rev.*, 2000, **1**, 1–21.

80 M. N. Chong, B. Jin, C. W. K. Chow and C. Saint, *Water Res.*, 2010, **44**, 2997–3027.

81 M. C. Collivignarelli, R. Pedrazzani, S. Sorlini, A. Abbà and G. Bertanza, *Sustain.*, 2017, **9**, 1–14.

82 Y. Wang, H. Suzuki, J. Xie, O. Tomita, D. J. Martin, M. Higashi, D. Kong, R. Abe and J. Tang, *Chem. Rev.*, 2018, **118**, 5201–5241.

83 M. E. Malefane, B. Ntsendwana, P. J. Mafa, N. Mabuba, U. Feleni and A. T. Kuvarega, *ChemistrySelect*, 2019, **4**, 8379–8389.

84 E. Grabowska, *Appl. Catal. B Environ.*, 2016, **186**, 97–126.

85 J. Herrmann, *Catal. Today*, 1999, **53**, 115–129.

86 D. G. Wang, P. Tan, H. Wang, M. Song, J. Pan and G. C. Kuang, *J. Solid State Chem.*, 2018, **267**, 22–27.

87 M. A. Lazar, S. Varghese and S. S. Nair, *Catalysts*, 2012, **2**, 572–601.

88 A. Fujishima, X. Zhang and D. A. Tryk, *Surf. Sci. Rep.*, 2008, **63**, 515–582.

89 V. D. Santo, *Catalysts*, 2018, **8**, 591–594.

90 A. T. Kuvarega, R. W. M. Krause and B. B. Mamba, *Appl. Surf. Sci.*, 2015, **329**, 127–136.

91 U. Sidwaba, N. Ntshongontshi, U. Feleni, L. Wilson, T. Waryo and E. I. Iwuoha, *Electrocatalysis*, 2019, **10**, 323–331.

92 J. A. Torres-Luna, N. R. Sanabria and J. G. Carriazo, *Powder Technol.*, 2016, **302**, 254–260.

93 S. M. Reda, M. Khairy and M. A. Mousa, *Arab. J. Chem.*, 2020, **13**, 86–95.

94 X. Lan, L. Wang, B. Zhang, B. Tian and J. Zhang, *Catal. Today*, 2014, **224**, 163–170.

95 Z. V. Baldissarelli, T. De Souza, L. Andrade, L. F. Cappa de Oliveira, H. J. Jose and R. de F. P. M. Moreira, *Appl. Surf. Sci.*, 2015, **359**, 868–874.

96 Q. Zhang, Y. Q. He, X. G. Chen, D. H. Hu, L. J. Li, T. Yin and L. L. Ji, *Chinese Sci. Bull.*, 2011, **56**, 331–339.

97 X. Zhao, Y. Wang, W. Feng, H. Lei and J. Li, *RSC Adv.*, 2017, **7**, 52738–52746.

98 M. Duan, J. Li, G. Mele, C. Wang, X. Lu, G. Vasapollo and F. Zhang, *J. Phys. Chem. C*, 2010, **114**, 7857–7862.

99 T. Al-fahdi, F. Al Marzouqi, A. T. Kuvarega, B. B. Mamba, S. M. Z. Al Kindy, Y. Kim and R. Selvaraj, *J. Photochem. Photobiol. A Chem.*, 2019, **374**, 75–83.

100 S. Y. Chai, Y. J. Kim and W. I. Lee, *J. Electroceramics*, 2006, **17**, 909–912.

101 Q. A. Drmosh, A. Hezam, A. H. Y. Hendi, M. Qamar, Z. H. Yamani and K. Byrappa, *Appl. Surf. Sci.*, 2020, **499**, 143938–143947.

102 M. Khairy and W. Zakaria, *Egypt. J. Pet.*, 2014, **23**, 419–426.

103 H. Xue, F. Wang, Q. Bai, H. Sun, J. Qu, P. Liu and K. Wang, *Mater. Lett.*, 2018, **219**, 148–151.

104 A. Malathi, P. Arunachalam, A. Nirmala, J. Madhavan and A. M. Al-mayouf, *Appl. Surf. Sci.*, 2017, **412**, 85–95.

105 D. Fukushi, A. Sasaki, H. Hirabayashi and M. Kitano, *Microelectron. Reliab.*, 2017, **79**, 1–4.

106 X. Hu, P. Xu, H. Gong and G. Yin, *Materials (Basel).*, 2018, **11**, 147–155.

107 L. Zhang, W. Wang, S. Sun and D. Jiang, *Appl. Catal. B Environ.*, 2015, **168**–**169**, 9–13.

108 J. Gou, X. Li, H. Zhang, R. Guo, X. Deng, X. Cheng, M. Xie and Q. Cheng, *J. Ind. Eng. Chem.*, 2018, **59**, 99–107.

109 Q. Zhao, J. Wang, Z. Li, Y. Qiao, C. Jin and Y. Guo, *Ceram. Int.*, 2016, **42**, 13273–13277.

110 K. Ramanathan, D. Avnir, A. Modestov and O. Lev, *Chem. Mater.*, 1997, **9**, 2533–2540.

111 R. Rahimi, S. Zargari, A. Ghaffarinejad and A. Morsali, *Environ. Prog. Sustain. Energy*, 2016, **35**, 642–652.

112 N. Serpone, *Catalysts*, 2018, **8**, 553–651.

113 Y. Bai, X. Shi, P. Wang, L. Wang, H. Xie, Z. Li, L. Qu and L. Ye, *J. Taiwan Inst. Chem. Eng.*, 2018, **91**, 358–368.

114 F. Kovanda, J. Balaba, K. Jira, D. Kolous and L. Obalova, *React. Kinet. Mech. Catal.*, 2017, **121**, 121–139.

115 C. Li, H. Wang, D. Lu, W. Wu, J. Ding, X. Zhao, R. Xiong, M. Yang, P. Wu, F. Chen and P. Fang, *J. Alloys Compd.*, 2017, **699**, 183–192.

116 B. Ntsendwana, M. G. Peleyeju and O. A. Arotiba, *J. Environ. Sci. Heal. Part A*, 2016, **51**, 571–578.

117 P. Ramesh and S. Sampath, *Anal. Chem.*, 2003, **75**, 6949–6957.

118 H. M. A. Asghar, S. N. Hussain, H. Sattar, N. W. Brown and E. P. L. Roberts, *J. Ind. Eng. Chem.*, 2014, **20**, 1936–1941.

119 M. S. Dresselhaus and G. Dresselhaus, *Adv. Phys.*, 2002, **51**, 1–186.

120 M. E. Malefane, U. Feleni and A. T. Kuvarega, *New J. Chem.*, 2019, **43**, 11348–11362.

121 X. Luo and D. D. L. Chung, *Carbon N. Y.*, 2001, **39**, 985–990.

122 D. Chung, *Applied Materials Science*, Chapman & Hall/CRC CRC Press LLC, Washington, DC, 2001.

123 E. H. Umukoro, M. G. Peleyeju, J. C. Ngila and O. A. Arotiba, *Chem. Eng. J.*, 2017, **317**, 290–301.

124 D. D. L. Chung, *J. Mater. Sci.*, 2016, **51**, 554–568.

125 Z. Wang, Q. Dai, S. Guo, R. Wang, M. Ye and K. Y. Yap, *Constr. Build. Mater.*, 2017, **134**, 412–423.

126 P. Cataldi, A. Athanassiou and I. Bayer, *Appl. Sci.*, 2018, **8**, 1438.

127 B. H. Nguyen, V. H. Nguyen and D. L. Vu, *Adv. Nat. Sci. Nanosci. Nanotechnol.*, 2015, **6**, 033001.

128 T. Ndlovu, A. T. Kuvarega, O. A. Arotiba, S. Sampath, R. W. Krause and B. B. Mamba, *Appl. Surf. Sci.*, 2014, **300**, 159–164.

129 A. P. Yaroshenko, M. V Savos'kin, V. N. Mochalin and N. I. Lazareva, *Russ. J. Appl. Chem.*, 2007, **80**, 754–756.

130 O. N. Shornikova, E. V. Kogan, D. V. Petrov, N. V Maksimova and N. E. Sorokina, *Pore Structrue of Exfoliated Graphite*, Moscow, 2015.

131 J. Li, J. Gao, Z. Jia and L. Feng, *Catal. Letters*, 2009, **129**, 247–249.

132 E. H. Umukoro, S. S. Madyibi, M. G. Peleyeju, L. Tshwenya, E. H. Viljoen, J. C. Ngila and O. A. Arotiba, *Solid State Sci.*, 2017, **74**, 118–124.

133 R. Muzyka, S. Drewniak, T. Pustelny, M. Chrubasik and G. Gryglewicz, *Materials*

(Basel)., 2018, **11**, 1050–1064.

134 M. A. S. Badri, M. M. Salleh, N. F. M. Noor, M. Y. A. Rahman and A. A. Umar, *Mater. Chem. Phys.*, 2017, **193**, 212–219.

135 P. J. Mafa, A. T. Kuvarega, B. B. Mamba and B. Ntsendwana, *Appl. Surf. Sci.*, 2019, **483**, 506–520.

136 X. Yang, J. Chen, Y. Chen, P. Feng, H. Lai, J. Li and X. Luo, *Nano-Micro Lett.*, 2018, **10**, 15–25.

137 M. Faraldos and A. Bahamonde, *Catal. Today*, 2017, **285**, 13–28.

138 D. R. Dreyer, S. Park, C. W. Bielawski and R. S. Ruoff, *Chem. Soc. Rev.*, 2010, **39**, 228–240.

139 C. N. R. Rao, U. Maitra and H. S. S. R. Matte, *Graphene: Synthesis, Properties, and Phenomena.*, Wiley-VCH Verlag GmbH & Co. KGaA, London, UK, First Edit., 2013.

140 A. O. Idris, N. Mabuba, D. Nkosi and O. A. Arotiba, *Int. J. Environ. Anal. Chem.*, 2017, **97**, 534–547.

141 S. Gadipelli and Z. X. Guo, *Prog. Mater. Sci.*, 2015, **69**, 1–60.

142 T. K. Das and S. Prusty, *Polym. Plast. Technol. Eng.*, 2013, **52**, 319–331.

143 G. Wang, X. Shen, J. Yao and J. Park, *Carbon N. Y.*, 2009, **47**, 2049–2053.

144 M. S. L. Hudson, *RSC Adv.*, 2018, **8**, 20440–20449.

145 M. Lv, T. Mei, C. Zhang and X. Wang, *RSC Adv.*, 2014, **4**, 9261–9270.

146 R. Giovannetti, E. Rommozzi, M. Zannotti, C. A. D. Amato, S. Ferraro, M. Cespi, G. Bunacucina, M. Minicucci and A. Di Cicco, *RSC Adv.*, 2016, **6**, 93048–93055.

147 B. Wei, L. Wang, Y. Wang, Y. Yuan, Q. Miao, Z. Yang and W. Fei, *J. Power Sources*, 2016, **307**, 129–137.

148 R. Balasubramanian and S. Chowdhury, *J. Mater. Chem. A Mater. energy Sustain.*, 2015, 1–22.

149 Y. Wang, S. Chou, H. Liu and S. Dou, *Carbon N. Y.*, 2013, **57**, 202–208.

150 R. S. Das, S. K. Warkhade, A. Kumar and A. V Wankhade, *Res. Chem. Intermed.*, 2019, 1–18.

151 N. R. Khalid, A. Majid, M. B. Tahir, N. A. Niaz and S. Khalid, *Ceram. Int.*, 2017, **43**, 14552–14571.

152 F. Lu, X. Wang, Y. Zhao, G. Yang, J. Zhang, B. Zhang and Y. Feng, *J. Power Sources*, 2016, **333**, 1–9.

153 L. Zhang, J. Zhang, H. Jiu, C. Ni, X. Zhang and M. Xu, *J. Phys. Chem. Solids*, 2015, **86**, 82–89.

154 D. C. Nguyen, K. Y. Cho and W. Oh, *RSC Adv.*, 2017, **7**, 29284–29294.

155 M. Gouterman, *J. Chem. Phys.*, 1959, **30**, 1139–1161.

156 W. Küster, *Hoppe. Seylers. Z. Physiol. Chem.*, 1912, **82**, 463–483.

157 A. W. Johnson and I. T. Kay, *J. Chem. Soc.*, 1960, **1**, 2418–2423.

158 M. M. Makhlouf, A. El-denglawey, H. M. Zeyada and M. M. El-nahass, *J. Lumin.*, 2014, **147**, 202–208.

159 Y. Chen, Z. H. Huang, M. Yue and F. Kang, *Nanoscale*, 2014, **6**, 978–985.

160 Y. Zhong, J. Wang, R. Zhang, W. Wei, H. Wang, X. Lü, F. Bai, H. Wu, R. Haddad and H. Fan, *Nano Lett.*, 2014, **14**, 7175–7179.

161 T. J. Dougherty, D. G. Boyle, K. R. Weishaupt, B. A. Henderson, W. R. Potter, D. A. Bellnier and K. E. Wityk, *Photodegradation Therapy- Clininal and Drug Advances*, New York, D. Kessel., 1983.

162 M. T. Cox, T. T. Howarth, A. H. Jackson and G. W. Kenner, *J. Chem. Soc. Perkin Trans. 1*, 1974, **24**, 512–516.

163 Y. Chen, A. Li, Z.-H. Huang, L.-N. Wang and F. Kang, *Nanomaterials*, 2016, **6**, 51–72.

164 D. Duc La, A. Rananaware, H. P. Ngunen Thi, L. Jones and S. V Bhosale, *Adv. Nat. Sci. Nanosci. Nanotechnol.*, 2017, **8**, 015009.

165 D. Duc La, RMIT University, 2017.

166 S. Cherian and C. C. Wamser, *J. Phys. Chem. B*, 2000, **104**, 3624–3629.

167 K. Kalyanasundaram, N. Vlachopoulos, V. Krishnan, A. Monnier and M. Graetzel, *J. Phys. Chem.*, 1987, **91**, 2342–2347.

168 N. Vlachopoulos, P. Liska, A. J. McEvoy and M. Grätzel, *Surf. Sci.*, 1987, **189**–**190**, 823–831.

169 R. Dabestani, A. J. Bard, A. Campion, M. A. Fox, T. E. Mallouk, S. E. Webber and J. M. White, *J. Phys. Chem.*, 1988, **92**, 1872–1878.

170 G. K. Boschloo and A. Goossens, *J. Phys. Chem.*, 1996, **100**, 19489–19494.

171 B. Meunier, *Chem. Rev.*, 1992, **92**, 1411–1456.

172 S. Afzal, W. A. Daoud and S. J. Langford, *ACS Appl. Mater. Interfaces*, 2013, **5**, 4753–4759.

173 J. Roales, J. M. Pedrosa, M. Cano, M. G. Guillén, T. Lopes-Costa, P. Castillero, A.

Barranco and A. R. González-Elipe, *RSC Adv.*, 2014, **4**, 1974–1981.

174 X. Zhao, Y. Wang, W. Feng, H. Lei and J. Li, *RSC Adv.*, 2017, **7**, 52738–52746.

175 M. A. Ahmed, Z. M. Abou-Gamra, H. A. A. Medien and M. A. Hamza, *J. Photochem. Photobiol. B Biol.*, 2017, **176**, 25–35.

176 S. Kladsomboon, S. Pratontep and T. Kerdcharoen, in *Electrical Engineering/Electronics Computer Telecommunications and Information Technology (ECTI-CON), 2010 International Conference on*, 2010, pp. 3–6.

177 M. da G. H. Vicente and K. M. Smith, *Curr. Org. Synth.*, 2014, **11**, 3–28.

178 S. D. Gokakakar and A. V. Salker, *Indian J. Chem. Technol.*, 2009, **16**, 492–498.

179 X. T. Zhou, H. B. Ji and X. J. Huang, *Molecules*, 2012, **17**, 1149–1158.

180 S. K. Deb, *Sol. Energy Mater. Sol. Cells*, 2008, **92**, 245–258.

181 M. Alaei, A. R. Mahjoub and A. Rashidi, *Iran. J. Chem. Chem. Eng.*, 2012, **31**, 31–36.

182 D. Hidayat, A. Purwanto, W. N. Wang and K. Okuyama, *Mater. Res. Bull.*, 2010, **45**, 165–173.

183 Y. Wicaksana, S. Liu, J. Scott and R. Amal, *Molecules*, 2014, **19**, 17747–17762.

184 S. Thangavel, M. Elayaperumal and G. Venugopal, *Mater. Express*, 2012, **2**, 327–334.

185 M. C. Rao, *J. od Non-Oxide Glas.*, 2013, **5**, 1–8.

186 S. Adhikari, D. Sarkar and H. S. Maiti, *Mater. Res. Bull.*, 2014, **49**, 325–330.

187 B. H. Nguyen, V. H. Nguyen and D. Lam Vu, *Adv. Nat. Sci. Nanosci. Nanotechnol.*, 2015, **6**, 033001.

188 M. Zhu, Z. Li, B. Xiao, Y. Lu, Y. Du, P. Yang and X. Wang, *ACS Appl. Mater. Interfaces*, 2013, **5**, 1732–1740.

189 S. I. Boyadjiev, T. Nagyne Kovács, I. Lukács and I. M. Szilágyi, in *AIP Conference*, 2016, pp. 140003-1-140003–4.

190 E. Lassner and W.-D. Schubert, *Tungsten Properties, Chemistry, Technology of the Element, Alloys, and Chemical Compounds*, Kluwer Academic / Plenum Publishers, New York USA, 1999.

191 I. M. Szilágyi, B. Fórizs, O. Rosseler, Á. Szegedi, P. Németh, P. Király, G. Tárkányi, B. Vajna, K. Varga-Josepovits, K. László, A. L. Tóth, P. Baranyai and M. Leskelä, *J. Catal.*, 2012, **294**, 119–127.

192 S. I. Boyadjiev, G. dos L. Santos, J. Szűcs and I. M. Szilágyi, in *AIP Conference*,

2016, vol. 140004, pp. 140004-1-140004–4.

193 R. Chatten, A. V. Chadwick, A. Rougier and P. J. D. Lindan, *J. Phys. Chem. B*, 2005, **109**, 3146–3156.

194 Y. Wu, Z. Xi, G. Zhang, J. Yu and D. Guo, *J. Cryst. Growth*, 2006, **292**, 143–148.

195 W. Sun, M. T. Yeung, A. T. Lech, C. W. Lin, C. Lee, T. Li, X. Duan, J. Zhou and R. B. Kaner, *Nano Lett.*, 2015, **15**, 4834–4838.

196 Y. M. Solonin, O. Y. Khyzhun and E. A. Graivoronskaya, *Cryst. Growth Des.*, 2001, **1**, 473–477.

197 Y. P. Xie, G. Liu, L. Yin and H.-M. Cheng, *J. Mater. Chem.*, 2012, **22**, 6746–6751.

198 X. Liu and H. Fan, *R. Soc. Open Sci.*, 2018, **5**, 1711921.

199 D. W. Bullett, *J. Phys. C Solid State Phys.*, 1983, **16**, 2197–2207.

200 J. Zhang, P. Zhang, T. Wang and J. Gong, *Nano Energy*, 2015, **11**, 189–195.

201 E. Salje, *Acta Crystallogr. Sect. B*, 1977, **33**, 574–577.

202 J. Waring, *Publications of the National Bureau of Standards*, National Bereau of Standards Library, Washington DC, Publicatio., 1966.

203 of standards The national Bueau, *Publications of the National Bureau of Standards: 1977 Catalog*, Washington, D. C., 1978.

204 K. R. Locherer, I. P. Swainson and E. K. H. Salje, *J. Phys. Condens. Matter*, 1999, **11**, 4143–4156.

205 C. V. Ramana, S. Utsunomiya, R. C. Ewing, C. M. Julien and U. Becker, *J. Phys. Chem. B*, 2006, **110**, 10430–10435.

206 F. Corà, M. G. Stachiotti, C. R. A. Catlow and C. O. Rodriguez, *J. Phys. Chem. B*, 1997, **101**, 3945–3952.

207 Y. Oaki and H. Imai, *Adv. Mater.*, 2006, **18**, 1807–1811.

208 Z. Gu, H. Li, T. Zhai, W. Yang, Y. Xia, Y. Ma and J. Yao, *J. Solid State Chem.*, 2007, **180**, 98–105.

209 M. I. Szilagyi, J. Madarasz, G. Pokol, P. Kiraly, G. Tarkanyi, S. Saukko, J. Mizsei, A. L. Toth, A. Szabo and K. Varga-Josepovits, 2008, 4116–4125.

210 Q. Xiang, G. F. Meng, H. B. Zhao, Y. Zhang, H. Li, W. J. Ma and J. Q. Xu, *J. Phys. Chem. C*, 2010, **114**, 2049–2055.

211 Z. Meng, A. Fujii, T. Hashishin, N. Wada, T. Sanada, J. Tamaki, K. Kojima, H. Haneoka and T. Suzuki, *J. Mater. Chem. C*, 2015, **3**, 1134–1141.

212 F. Tonus, V. Fuster, G. Urretavizcaya, F. J. Castro and J.-L. Bobet, *Int. J. Hydrogen*

Energy, 2009, **34**, 3404–3409.

213 Y. Yan, S. Sun, Y. Song, X. Yan, W. Guan, X. Liu and W. Shi, *J. Hazard. Mater.*, 2013, **250**–**251**, 106–114.

214 A. B. C. Ekwealor, S. U. Offiah, S. C. Ezugwu and F. I. Ezema, *Indian J. Mater. Sci.*, 2014, **2014**, 367950.

215 M. Mauro, M. Crosera, M. Pelin, C. Florio, F. Bellomo, G. Adami, P. Apostoli, G. De Palma, M. Bovenzi, M. Campanini and F. L. Filon, *Int. J. Environ. Res. Public Health*, 2015, **12**, 8263–8280.

216 R. K. Gupta, A. K. Sinha, B. N. R. Sekhar, A. K. Srivastava, G. Singh and S. K. Deb, *Appl. Phys. A Mater. Sci. Process.*, 2011, **103**, 13–19.

217 J. Chen, X. Wu and A. Selloni, *Phys. Rev. B*, 2011, **83**, 1–24.

218 L. P. Kozeeva, M. Y. Kamaneva, A. I. Smolentsev, V. S. Danilovich and N. V Podberezskaya, *J. Struct. Chem.*, 2008, **49**, 1108–1113.

219 S. Gupta and S. B. Carrizosa, *J. Electron. Mater.*, 2015, **44**, 4492–4509.

220 W. Shi and N. Chopra, *ACS Appl. Mater. Interfaces*, 2012, **4**, 5590–5607.

221 X. Shi, S. Han, R. J. Sanedrin, F. Zhou and M. Selke, *Chem. Mater.*, 2002, **14**, 1897–1902.

222 Q. Yuanchun, Z. Yanbao and W. Zhishen, *Mater. Chem. Phys.*, 2008, **110**, 457–462.

223 K. H. Mahmoud, *Polym. Compos.*, 2016, 1881–1885.

224 K. F. Wadekar, K. R. Nemade and S. A. Waghuley, *Res. J. Chem. Sci.*, 2017, **7**, 53–55.

225 H. Kumar, P. Sangwan and Manisha, *Adv. Appl. Phys. Chem. Sci. Sustain. Approach*, 99–104.

226 S. L. Chou, J. Z. Wang, H. K. Liu and S. X. Dou, *J. Power Sources*, 2008, **182**, 359–364.

227 S. M. Borghei and F. Bakhtiyari, *Acta Phys. Pol. A*, 2017, **131**, 332–335.

228 J. Chen, X. Wu and A. Selloni, *Phys. Rev. B - Condens. Matter Mater. Phys.*, 2011, **83**, 245204–245207.

229 S. . Jagtap, A. S. Tale and S. D. Thakre, *Int. J. Res. Eng. Appl. Sci.*, 2017, **7**, 1–7.

230 M. Pudukudy and Z. Yaakob, *Chem. Pap.*, 2014, **68**, 1087–1096.

231 S. L. Sharifi, H. R. Shakur, A. Mirzaei, A. Salmani and M. H. Hosseini, *Int. J. Nanosci. Nanotechnol.*, 2013, **9**, 51–58.

232 S. Farhadi, M. Javanmard and G. Nadri, *Acta Chim. Slov*, 2016, **63**, 335–343.

233 S. A. Bin Asif, S. B. Khan and A. M. Asiri, *Nanoscale Res. Lett.*, 2014, **9**, 910–908.

234 L. Hu, G. Zhang, M. Liu, Q. Wang, S. Dong and P. Wang, *Sci. Total Environ.*, 2019, **647**, 352–361.

235 L. Hu, G. Zhang, Q. Wang, Y. Sun, M. Liu and P. Wang, *Chem. Eng. J.*, 2017, **326**, 1095–1104.

236 S. Bao, N. Yan, X. Shi, R. Li and Q. Chen, *Appl. Catal. A Gen.*, 2014, **487**, 189–194.

237 C. Tang, E. Liu, J. Wan, X. Hu and J. Fan, *Appl. Catal. B Environ.*, 2016, **181**, 707–715.

238 Y. Li and N. Chopra, *J. Catal.*, 2015, **329**, 514–521.

239 L. N. Nguyen, T. Dieu, D. Truong and I. Honma, *Chem. An asian J.*, 2018, **13**, 1530–1534.

240 M. Wu and S. Huang, *Mol. Clin. Oncol.*, 2017, **7**, 738–746.

241 S. Yu, Y. Zhang, F. Dong, M. Li, T. Zhang and H. Huang, *Appl. Catal. B Environ.*, 2018, **226**, 441–450.

242 P. A. Mangrulkar, M. M. Joshi, S. N. Tijare, V. Polshettiwar, N. K. Labhsetwar and S. S. Rayalu, *Int. J. Hydrogen Energy*, 2012, **37**, 10462–10466.

243 P. Shi, R. Su, S. Zhu, M. Zhu, D. Li and S. Xu, *J. Hazard. Mater.*, 2012, **229**–**230**, 331–339.

244 H. Lee, Y. Park, S. Kim, B. Kim and S. Jung, *J. Ind. Eng. Chem.*, 2015, **32**, 259–263.

245 E. Bardos, G. Kovacs, T. Gyulavari, K. Nemeth, E. Kecsenovity, P. Berki, L. Baia, Z. Pap and K. Hernádi, *Catal. Today*, 2018, **300**, 28–38.

246 J. Han, D. Wang, Y. Du, S. Xi, J. Hong, S. Yin, Z. Chen, T. Zhou and R. Xu, *J. Mater. Chem. A*, 2015, **3**, 20607–20613.

247 J. Vakros, C. Kordulis and A. Lycourghiotis, *Langmuir*, 2002, **18**, 417–422.

248 R. Alanís-oaxaca, R. Alanís-oaxaca and J. Jiménez-becerril, *J. Mex. Chem. Soc.*, 2010, **54**, 164–168.

249 C. Tan, G. Zhu, M. Hojamberdiev, K. Okada, J. Liang, X. Luo, P. Liu and Y. Liu, *"Applied Catal. B, Environ.*, 2014, **152**–**153**, 425–436.

250 Y. Li, H. Yao, J. Wang, N. Wang and Z. Li, *Mater. Res. Bull.*, 2011, **46**, 292–296.

251 A. P. Periasamy, S. Yang and S. Chen, *Talanta*, 2011, **87**, 15–23.

252 X. Su, J. Yang, X. Yu, Y. Zhu and Y. Zhang, *Appl. Surf. Sci.*, 2018, **433**, 502–512.

253 C. Hsu, Y. Li, H. Jian, S. G. Harroun, S. Wei, R. Ravindranath, J. Lai, C. Huang and H. Chang, *Nanoscale*, 2018, **10**, 11808–11819.

254 K. Ye, Z. Chai, J. Gu, X. Yu, C. Zhao, Y. Zhang and W. Mai, *Nano Energy*, 2015, **18**, 222–231.

255 J. Cao, Y. Zhao, H. Lin, B. Xu and S. Chen, *J. Solid State Chem.*, 2013, **206**, 38–44.

256 C. Zhankui, S. Mengmeng, Z. Zhi, M. Liwei, F. Wenjun and J. Huimin, *Catal. Commun.*, 2013, **42**, 121–124.

257 H. Huang, K. Xiao, T. Zhang, F. Dong and Y. Zhang, *Appl. Catal. B Environ.*, 2017, **203**, 879–888.

258 A. C. Mera, Y. Moreno, J.-Y. Pivan, O. Pena and H. D. Mansilla, *J. Photochem. Photobiol. A Chem.*, 2014, **289**, 7–13.

259 L. A. Mabuti, I. K. S. Manding and C. C. Mercado, *RSC Adv.*, 2018, **8**, 42254–42261.

260 A. C. Mera, A. M. Cruz, E. Pérez-tijerina, M. F. Meléndrez and H. Valdés, *Mater. Sci. Semicond. Process.*, 2018, **88**, 20–27.

261 H. Wang, Z. Hu, Y. Chang, Y. Chen, Z. Lei, Z. Zhang and Y. Yang, *Electrochim. Acta*, 2010, **55**, 8974–8980.

262 W.-W. Dai and Z.-Y. Zhao, *Catalysts*, 2016, **6**, 133–147.

263 C. Chen, J. Fu, J. Chang, S. Huang, T. Yeh, J. Hung, P. Huang, F. Liu and L. Chen, *J. Colloid Interface Sci.*, 2018, **532**, 375–386.

264 C. Siao, H. Chen, L. Chen, J. Chang, T. Yeh and C. Chen, *J. Colloid Interface Sci.*, 2018, **526**, 322–336.

265 R. He, J. Zhang, J. Yu and S. Cao, *J. Colloid Interface Sci.*, 2016, **478**, 201–208.

266 F. A. Bannister, *Mineral. Mag. J. Mineral. Soc.*, 1935, **XXIV**, 49–58.

267 S. Bunda and V. Bunda, *Acta Phys. Pol. A*, 2014, **126**, 272–273.

268 A. Han, J. Sun, X. Lin, C. H. Yuan, G. K. Chuah and S. Jaenicke, *RSC Adv.*, 2015, **5**, 88298–88305.

269 M. Pan, H. Zhang, G. Gao, L. Liu and W. Chen, *Environ. Sci. Technol.*, 2015, **49**, 6240–6248.

270 L. Ye, L. Tian, T. Peng and L. Zan, *J. Mater. Chem.*, 2011, **21**, 12479–12484.

271 S. Luo, J. Chen, Z. Huang, C. Liu and M. Fang, *ChemCatChem*, 2016, **8**, 3780–3789.

272 L. Shan, Y. Liu, J. Suriyaprakash, C. Ma and Z. Wu, *J. Mol. Catal. A Chem.*, 2016,

411, 179–187.

273 H. Fu, S. Sun, X. Yang, W. Li, X. An, H. Zhang and Y. Dong, *Powder Technol.*, 2018, **328**, 389–396.

274 A. Lee, Y. Wang and C. Chen, *J. Colloid Interface Sci.*, 2019, **533**, 319–332.

275 M. Ji, R. Chen, J. Di, Y. Liu, K. Li, Z. Chen, J. Xia and H. Li, *J. Colloid Interface Sci.*, 2019, **533**, 612–620.

276 T. He, D. Wu and Y. Tan, *Mater. Lett.*, 2016, **165**, 227–230.

277 Y. Wang, X. Cheng, X. Meng, H. Feng, S. Yang and C. Sun, *J. Alloys Compd.*, 2015, **632**, 445–449.

278 D. Sánchez-Martínez, A. Martínez-De La Cruz and E. López-Cuéllar, *Mater. Res. Bull.*, 2013, **48**, 691–697.

279 S. Supothina, P. Seeharaj, S. Yoriya and M. Sriyudthsak, *Ceram. Int.*, 2007, **33**, 931–936.

280 K. Chakraborty, T. Pal and S. Ghosh, *ACS Appl. Nano Mater.*, 2018, **1**, 3137–3144.

281 M. Salavati-Niasari, N. Mir and F. Davar, *J. Phys. Chem. Solids*, 2009, **70**, 847–852.

282 D. Zhang, F. Wang, S. Cao and X. Duan, *RSC Adv. Open*, 2018, **8**, 5967–5975.

283 J. Theerthagiri, R. A. Senthil, A. Malathi, A. Selvi, J. Madhavan and M. Ashokkumar, *RSC Adv.*, 2015, **5**, 52718–52725.

284 L. Dinescu, M. Dinica, C. Miron and E. S. Barna, *Rom. Reports Phys.*, 2013, **65**, 578–590.

285 F. Ye and A. Ohmori, *Surf. Coatings Technol.*, 2002, **160**, 62–67.

286 V. H.-T. Thi and B.-K. Lee, *Mater. Res. Bull.*, 2017, **96**, 171–182.

287 C. G. Silva, University of Porto, 2008.

288 F. Scattarella, L. De Caro, D. Siliqi and E. Carlino, *Crystals*, 2017, **7**, 186–204.

289 Y. Deng, M. Xing and J. Zhang, *Appl. Catal. B Environ.*, 2017, **211**, 157–166.

290 X. Yan, K. Yuan, N. Lu, H. Xu, S. Zhang, N. Takeuchi, H. Kobayashi and R. Li, *Appl. Catal. B Environ.*, 2017, **218**, 20–31.

291 Oxford Instruments, *Quantitative EDS Analysis using AZtec software platform: Good Practices*,AZtec, United Kingdom, 2011.

292 A. T. Raghavender, N. Hoa, K. Joon, M. Jung, Z. Skoko, M. Vasilevskiy, M. F. Cerqueira and A. P. Samantilleke, *J. Magn. Magn. Mater.*, 2013, **331**, 129–132.

293 S. Schlorholtz, *Standard Operating Procedure for XRD*, London, United Kingdom, 2004.

294 A. Fakhri and S. Behrouz, *Sol. Energy*, 2015, **112**, 163–168.

295 S. Bai, Y. Ma, R. Luo, A. Chen and D. Li, *RSC Adv.*, 2016, **6**, 2687–2694.

296 N. H. Patel, Sardar Patel University, 2015.

297 Y. Chen, C. Zou, M. Mastalerz, S. Hu and C. Gasaway, *Int. J. Mol. Sci.*, 2015, **16**, 30223–30250.

298 C. Berthomieu and Æ. R. Hienerwadel, *Photosynth Res*, 2009, **101**, 157–170.

299 M. N. Dole, P. A. Patel, S. D. Sawant and P. S. Shedpure, *Int. J. Pharm. Sci. Rev. Res.*, 2011, **7**, 159–166.

300 L. B. Mostaço-guidolin and L. Bachmann, *Appl. Spectrosc. Rev.*, 2011, **46**, 388–404.

301 C. Siregar, S. Martono and A. Rohman, *J. Appl. Pharm. Sci.*, 2018, **8**, 151–156.

302 G. E. A. Swann and S. V Patwardhan, *Clim. Past*, 2011, **7**, 65–74.

303 N. Abidi, E. Hequet and L. Cabrales, in *Fourier Transforms - New Analytical Approaches and FTIR Strategies*, ed. P. G. Nikolic, InTech, Rijeka, Croatia, Ed., 2011, pp. 89–114.

304 C. V Raman and K. S. Krishanan, *Nature*, 1928, **121**, 501–502.

305 C. Karuppiah, S. Sakthinathan, S.-M. Chen, K. Manibalan, S.-M. Chen and S.-T. Huang, *Appl. Organomet. Chem.*, 2016, **30**, 40–46.

306 A. Gorski, A. Starukhin, S. Stavrov, S. Gawinkowski and J. Waluk, *Spectrochim. Acta Part A Mol. Biomol. Spectrosc.*, 2017, **173**, 350–355.

307 J. Hodkiewicz and M. Wall, *Nanotech*, 2010, **5**, 318–321.

308 Wikipedia, BET theory, http://en.wikipedia.org/wiki/BET_theory, (accessed 17 November 2017).

309 D. Li, D. Chandra, K. Saito, T. Yui and M. Yagi, *Nanoscale Res. Lett.*, 2014, **9**, 542–549.

310 J. M. Zielinski and L. Kettle, *Physical Characterization : Surface Area and Porosity*, John Willey and Sons Manchester, UK, 2013.

311 P. Wurm, *BET Standard Operating Procedure (SOP) Surface Area & Pore Size Distribution Analyses*, micromeritics, United Kingdom, 2010.

312 E. Okon, H. Shehu, I. Orakwe and E. Gobina, *J. Mater. Sci. Chem. Eng.*, 2017, **5**, 1–16.

313 O. M. Ama, N. Mabuba and O. A. Arotiba, *Electrocatalysis*, 2015, **6**, 390–397.

314 Q. Rong, B. Y. Zi, J. C. Hu, Z. Y. M, Z. Q. Zhu, J. Zhang and Q. J. Liu, *J. Mol. Sci.*,

2018, **2**, 1–5.

315 M. Zhang, H. Wang, Z. Li and B. Cheng, *RSC Adv.*, 2015, **5**, 13840–13849.

316 K. N. Shinde, S. J. Dhoble, H. C. Swart and K. Park, in *Springer Series in Materials Science 174*, Springer, Verlag Berlin Heidelberg, XIV., 2013, pp. 41–60.

317 R. Ye and A. R. Barron, *Photoluminescence Spectroscopy and its Applications*, London, United Kingdom, 2011.

318 PerkinElmer, *An Introduction to Fluorescence Spectroscopy*, Buckinghamshire, United Kingdom, 2000.

319 G. D. Gilliland, *Mater. Sci. Eng.*, 1997, **R18**, 99–400.

320 Y. Chen and K. Liu, *J. Hazard. Mater.*, 2017, **324**, 139–150.

321 N. P. Ferraz, F. C. F. Marcos, A. E. Nogueira, A. S. Martins, M. R. V. Lanza, E. M. Assaf and Y. J. O. Asencios, *Mater. Chem. Phys.*, 2017, **198**, 331–340.

322 E. K. Im, Z. J. Iang and N. O. Kwangsoo, *Jpn. J. Appl. Phys.*, 2000, **39**, 4820–4825.

323 Shimadzu, *TOC Application Handbook*, Europe.

324 Leco Corpration, *Total/Organic Carbon and Nitrogen in Soils*, St. Joseph, 2010.

325 V. Jensen, K. J. Andersen and M. Krysell, *Desk study on total organic carbon (TOC)*, London, United Kingdom, 2003.

326 D. A. Reckhow, *Analysis of Total Organic Carbon*, Amherst, 2012.

327 R. Liu, Q. Jin, G. Tao, L. Shan, J. Huang, Y. Liu, X. Wang, W. Mao and S. Wang, *J. Mass Spectrom.*, 2010, **45**, 553–559.

328 D. Kempińska and A. Kot-Wasik, *Monatshefte fur Chemie*, 2018, **149**, 1595–1604.

329 E. Chekmeneva, G. Dos Santos Correia, M. Gómez-Romero, J. Stamler, Q. Chan, P. Elliott, J. K. Nicholson and E. Holmes, *J. Proteome Res.*, 2018, **17**, 3492–3502.

330 M. Voigt, C. Savelsberg and M. Jaeger, *Toxicol. Environ. Chem.*, 2017, **99**, 624–640.

331 B. Ntsendwana, University of Johannesburg, 2012.

332 P. Chen, Q. Zhang, Y. Su, L. Shen, F. Wang, H. Liu, Y. Liu, Z. Gai, W. Lv and G. Liu, *Chem. Eng. J.*, 2018, **332**, 737–748.

333 Z. Wang, C. Chen, F. Wu, B. Zou, M. Zhao, J. Wang and C. Feng, *J. Hazard. Mater.*, 2009, **164**, 615–620.

334 A. T. Kuvarega, N. Khumalo, D. Dlamini and B. B. Mamba, *Sep. Purif. Technol.*, 2018, **191**, 122–133.

335 T. Wang, C. Wang, M. Drost, F. Tu, Q. Xu, H. Ju, J. Ko, D. Wechsler, M. Franke,

H. Pan, H. Marbach, P. Steinruck, J. Zhu and O. Lytken, *ChemistrySelect*, 2016, **1**, 6103–6105.

336 C. Liu, X. Han, S. Xie, Q. Kuang, X. Wang, M. Jin, Z. Xie and L. Zheng, *Chem. Asian J*, 2013, **8**, 282–289.

337 S. Stankovich, D. A. Dikin, R. D. Piner, K. A. Kohlhaas, A. Kleinhammes, Y. Jia, Y. Wu, S. T. Nguyen and R. S. Ruoff, *Carbon N. Y.*, 2007, **45**, 1558–1565.

338 Saepurahman, M. A. Abdullah and F. K. Chong, *J. Hazard. Mater.*, 2010, **176**, 451–458.

339 A. Enferadi-Kerenkan, A. S. Ello and T.-O. Do, *Ind. Eng. Chem. Res.*, 2017, **56**, 10639–10647.

340 S. Gayathri, P. Jayabal, M. Kottaisamy and V. Ramakrishnan, *AIP Adv.*, 2014, **4**, 027116.

341 H. Asgar, K. M. Deen, U. Riaz, Z. U. Rahman, U. H. Shah and W. Haider, *Mater. Chem. Phys.*, 2018, **206**, 7–11.

342 M. Toyoda, H. Katoh, A. Shimizu and M. Inagaki, *Carbon N. Y.*, 2003, **41**, 731–738.

343 R. Saleh, A. Taufik and S. P. Prakoso, *Appl. Surf. Sci.*, 2019, **480**, 697–708.

344 G. Pavoski, T. Maraschin, F. D. C. Fim, N. M. Balzaretti, G. B. Galland, N. Regina, D. S. Basso, P. Alegre, P. Alegre, C. De Tecnologia, P. Alegre and P. Alegre, *Mater. Res.*, 2017, **20**, 53–61.

345 P. Lian, X. Zhu, S. Liang, Z. Li, W. Yang and H. Wang, *Electrochim. Acta*, 2010, **55**, 3909–3914.

346 S. N. Ahmed and W. Haider, *Nanotechnology*, 2018, **29**, 342001–342028.

347 S. P. Gupta, V. B. Patil, N. L. Tarwal, S. D. Bhame, S. W. Gosavi, I. S. Mulla, D. J. Late, S. S. Suryavanshi and P. S. Walke, *Mater. Chem. Phys.*, 2019, **225**, 192–199.

348 J. Li, X. Du, L. Yao and Y. Zhang, *Mater. Lett.*, 2014, **121**, 44–46.

349 Y. Shen, Q. Xu, J. Shi, M. Li and Y. Zhang, *Desalin. Water Treat.*, 2017, **65**, 313–326.

350 O. Bilsel, J. Rodriguez, S. N. Milam, P. A. Gorlin, G. S. Girolami, K. S. Suslick and D. Holten, *J. Am. Chem. Soc.*, 1992, **114**, 6528–6538.

351 S. Zargari, R. Rahimi, A. Ghaffarinejad and A. Morsali, *J. Colloid Interface Sci.*, 2016, **466**, 310–321.

352 B. Ahmed, A. K. Ojha, A. Singh, F. Hirsch, I. Fischer, D. Patrice and A. Materny, *J.*

Hazard. Mater., 2018, **347**, 266–278.

353 Y. Ren, F. Nan, L. You, Y. Zhou, Y. Wang, J. Wang and X. Su, *small*, 2017, **13**, 1603457–1603463.

354 Y. Gong, C. Yang, H. Ji, C. Chen, W. Ma and J. Zhao, *Chem. Asian J*, 2016, **11**, 3568–3574.

355 Y. Ma, X. Wang, J. Ye, K. Ge, Y. Wang, J. He, Y. Zhang and Y. Yang, *Chem. Asian J.*, 2019, **14**, 1066–1075.

356 S. Mishra, D. Du, E. Jeanneau, F. Dappozze, C. Guillard, J. Zhang and S. Daniele, *Chem. Asian J.*, 2016, **11**, 1658–1663.

357 S. Ibrahim, S. Chakrabarty, S. Ghosh and T. Pal, *ChemistrySelect*, 2017, **2**, 537–545.

358 K. Chakraborty, S. Ghosh and T. Pal, *ChemistrySelect*, 2018, **3**, 8637–8643.

359 S. Xu, D. Fu, K. Song, L. Wang, Z. Yang, W. Yang and H. Hou, *Chem. Eng. J.*, 2018, **349**, 368–375.

360 O. P. Bajpai, S. Mandal, R. Ananthakrishnan, P. Mandal, D. Khastgir and S. Chattopadhyay, *New J. Chem.*, 2018, **42**, 10712–10723.

361 M. B. Tahir, M. Sagir and K. Shahzad, *J. Hazard. Mater.*, 2019, **363**, 205–213.

362 M. B. Tahir, G. Nabi, T. Iqbal, M. Sagir and M. Rafique, *Ceram. Int. J.*, 2018, **44**, 6686–6690.

363 J. Chen, X. Xiao, Y. Wang and Z. Ye, *Appl. Surf. Sci.*, 2019, **467**–**468**, 1000–1010.

364 E. Zhu, X. Yan, S. Wang, M. Xu, C. Wang, H. Liu, J. Huang, W. Xue, J. Cai, H. Heinz, Y. Li and Y. Huang, *Nano Lett.*, 2019, acs.nanolett.9b00867.

365 A. Jia, X. Zhang, F. Li and Y. Wang, *New J. Chem.*, 2019, 34–36.

366 G. Liu, Y. Zhang, L. Xu, B. Xu and F. Li, *New J. Chem.*, 2019, **43**, 3469–3475.

367 R. A. Senthil, A. Priya, J. Theerthagiri, A. Selvi, P. Nithyadharseni and J. Madhavan, *Ionics (Kiel).*, 2018, **24**, 3673–3684.

368 R. K. Mandal, S. Kundu, S. Sain and S. K. Pradhan, *New J. Chem.*, 2019, **43**, 2804–2816.

369 M. Salimi, M. Behbahani, H. R. Sobhi, M. Gholami, A. Jonidi Jafari, R. Rezaei Kalantary, M. Farzadkia and A. Esrafili, *New J. Chem.*, 2019, **43**, 1562–1568.

370 O. M. Ama, *Hum. Journals*, 2018, **8**, 23–38.

371 U. Sah, K. Sharma, N. Chaudhri, M. Sankar and P. Gopinath, *Colloids Surfaces B Biointerfaces*, 2017, **162**, 108–117.

372 O. M. Ama and O. A. Arotiba, *J. Electroanal. Chem.*, 2017, **803**, 157–164.

373 H. Zhou, Z. Wen, J. Liu, J. Ke, X. Duan, S. Wang and P. Ag, *Appl. Catal. B Environ.*, 2019, **242**, 76–84.

374 I. J. Puentes-cárdenas, G. M. Chávez-camarillo, C. M. Flores-ortiz, M. C. Cristiani-urbina, A. R. Netzahuatl-muñoz, J. C. Salcedo-reyes, A. M. Pedroza-rodríguez and E. Cristiani-urbina, *J. Nanomater.*, 2016, **2016**, 3542359–3542373.

375 T. Xiao, Z. Tang, Y. Yang, L. Tang, Y. Zhou and Z. Zou, *Appl. Catal. B Environ.*, 2018, **220**, 417–428.

376 S. M. Tichapondwa, S. Tshemese and W. Mhike, *Chem. Eng. Trans.*, 2018, **70**, 847–852.

377 K. Huang, Q. Pan, F. Yang, S. Ni, X. Wei and D. He, *J. Phys. D. Appl. Phys.*, , DOI:10.1088/0022-3727/41/15/155417.

378 Z. Muñoz, A. S. Cohen, L. M. Nguyen, T. A. McIntosh and P. E. Hoggard, *Photochem. Photobiol. Sci.*, 2008, **7**, 337–343.

379 L. Cheng, S. Qiu, J. Chen, J. Shao and S. Cao, *Mater. Chem. Phys.*, 2017, **190**, 53–61.

380 M. Zhang, Y. Chen, B. Chen, Y. Zhang, L. Lin, X. Han, P. Zou, G. Wang, J. Zeng and M. Zhao, *New J. Chem.*, 2019, **43**, 5088–5098.

381 X. Hu, P. Xu, H. Gong and G. Yin, *Materials (Basel).*, 2018, **11**, 147–162.

382 T. Kamachi, S. M. A. H. Siddiki, Y. Morita, M. N. Rashed, K. Kon, T. Toyao, K. Shimizu and K. Yoshizawa, *Catal. Today*, 2018, **303**, 256–262.

383 Ratna and B. S. Padhi, *Int. J. Environ. Sci.*, 2012, **3**, 940–955.

384 E. Safaei and S. Mohebbi, *J. Mater. Chem. A*, 2016, **4**, 3933–3946.

385 Y. Ruan, R. Wu, J. C. W. Lam, K. Zhang and P. K. S. Lam, *Water Res.*, 2019, **149**, 607–616.

386 J. Wang, Y. Li, Y. Qiao, G. Yu, J. Wu, X. Wu, W. Qin and L. Xu, *New J. Chem.*, 2018, **42**, 18001–18009.

387 Z. Han, Y. Yu, W. Zheng and Y. Cao, *New J. Chem.*, 2017, **41**, 9724–9730.

388 J. Zhang, L. Zhang, X. Li, S.-Z. Kang and J. Mu, *J. Dispers. Sci. Technol.*, 2011, **32**, 943–947.

389 M. Mousavi, A. Habibi-yangjeh and M. Abitorabi, *J. Colloid Interface Sci.*, 2016, **480**, 218–231.

390 X. Zeng, Z. Wang, G. Wang and T. R. Gengenbach, *Appl. Catal. B Environ.*, 2017,

218, 163–173.

391 X. Yan, K. Ye, T. Zhang, C. Xue, D. Zhang, C. Ma, J. Wei and G. Yang, *New J. Chem.*, 2017, **41**, 8482–8489.

392 S. K. Patra, S. Rahut and J. K. Basu, *New J. Chem.*, 2018, **42**, 18598–18607.

393 N. Vieno and M. Sillanpää, *Environ. Int.*, 2014, **69**, 28–39.

394 R. Manigandan, K. Giribabu, R. Suresh, L. Vijayalakshmi, A. Stephen and V. Narayanan, *Chem. Sci. Trans.*, 2013, **2**, 47–50.

395 F. Manteghi, S. H. Kazemi, M. Peyvandipour and A. Asghari, *RSC Adv.*, 2015, **5**, 76458–76463.

396 R. M. Fernández-Domene, R. Sánchez-Tovar, B. Lucas-granados, M. J. Muñoz-Portero and J. García-Antón, *Chem. Eng. J.*, 2018, **350**, 1114–1124.

397 M. B. Tahir, *J. Inorg. Organomet. Polym. Mater.*, 2018, **28**, 2160–2168.

398 H. Cui, H. Liu, J. Shi and C. Wang, *Int. J. Photoenergy*, 2013, **2013**, 1–16.

399 Y. Guo, Y. Dai, W. Zhao, H. Li, B. Xu and C. Sun, *Appl. Catal. B Environ.*, 2018, **237**, 273–287.

400 X. Wang, H. Zhang, L. Liu, W. Li and P. Cao, *Mater. Lett.*, 2014, **130**, 248–251.

401 M. Ahmadi, R. Younesi and M. J.-F. Guinel, *J. Mater. Res.*, 2014, **29**, 1424–1430.

402 M. Chowdhury, O. Oputu, M. Kebede, F. Cummings, O. Cespedes, A. Maelsand and V. Fester, *RSC Adv.*, 2015, **5**, 104991–105002.

403 G. Dong, H. Hu, X. Huang, Y. Zhang and Y. Bi, *J. Mater. Chem. A*, 2018, **6**, 21003–21009.

404 S. Pocoví-martínez, I. Zumeta-dube and D. Diaz, *J. Nanomater.*, 2019, **2019**, 6461493–6461503.

405 M. Karimi-Nazarabad and E. K. Goharshadi, *Sol. Energy Mater. Sol. Cells*, 2017, **160**, 484–493.

406 T. A. Egerton, *Molecules*, 2014, **19**, 18192–18214.

407 R. Vinoth, S. G. Babu, R. Ramachandran and B. Neppolian, *Appl. Surf. Sci.*, 2017, **418**, 163–170.

408 Q. Li, J. Yao, M. Arif, T. Huang, X. Liu and G. Duan, *J. Environ. Chem. Eng.*, 2018, **6**, 1969–1978.

409 K. S. Westphal, S. C. Chapra and W. Sung, *J. Am. Water Resour. Assoc.*, 2004, **1772**, 795–809.

410 T. I. Nkambule, R. W. M. Krause, J. Haarhoff and B. B. Mamba, *Phys. Chem.*

Earth, 2012, **50**–**52**, 132–139.

411 E. T. Saka and S. Yasemin, *Catal. Letters*, 2017, **147**, 1471–1477.

412 J. Yu, D. Xu, H. Nan, C. Wang, L. Kun and D. F. Chi, *Mater. Lett.*, 2016, **166**, 110–112.

413 A. Gordedo-Garcia, G. T. Palomino, L. Hinojosa-Reyes, J. L. Guzman-Mar, L. Maya-Tevino and A. Hernandez,-Ramirez, *Environ. Sci. Pollut. Res.*, 2017, **24**, 4613–4624.

414 D. Liu, J. Wang, J. Zhou, Q. Xi, X. Li, E. Nie, X. Piao and Z. Sun, *Chem. Eng. J.*, 2019, **369**, 968–978.

415 H. Yu, E. Nie, J. Xu, S. Yan, W. J. Cooper and W. Song, *Water Res.*, 2013, **47**, 1909–1918.

416 R. Banaschik, H. Jablonowski, P. J. Bednarski and J. F. Kolb, *J. Hazard. Mater.*, 2018, **342**, 651–660.

417 W. Li, R. Yu, M. Li, N. Guo, H. Yu and Y. Yu, *Chemosphere*, 2019, **218**, 966–973.

418 Y. J. Kim, S. N. Spak, G. R. Carmichael, N. Riemer and C. O. Stanier, *J. Geophys. Res. Atmos.*, 2014, **119**, 420–445.

419 S. Cagnina, P. Rotureau and C. Adamo, *Chem. Eng. Trans.*, 2013, **31**, 22–28.

420 H. Hirakawa, M. Hashimoto, Y. Shiraishi and T. Hirai, *J. Am. Chem. Soc.*, 2017, **139**, 10929–10936.

421 J. M. Walls, J. S. Sagu and K. G. U. Wijayantha, *RSC Adv.*, 2019, **9**, 6387–6394.

422 M. Cheng, *J. Mater. Chem. A*, 2019, **7**, 19616–19633.

423 B. Liu, A. S. Yasin, T. Musho, J. Bright, H. Tang, L. Huang and N. Wu, *J. Electrochem. Soc.*, 2019, **166**, H3091–H3096.

424 R. Shi, Y. Zhao, I. N. Waterhouse, S. Zhang and T. Zhang, *ACS Catal.*, 2019, **9**, 9739–9750.

425 C. Sarangapani, D. Ziuzina, P. Behan, D. Boehm, B. F. Gilmore, P. J. Cullen and P. Bourke, *Sci. Rep.*, 2019, **9**, 3955–3969.

426 R. Banaschik, H. Jablonowski, P. J. Bednarski and J. F. Kolb, *J. Hazard. Mater.*, 2018, **342**, 651–660.

427 K. V. Plakas, A. Mantza, S. D. Sklari, V. T. Zaspalis and A. J. Karabelas, *Chem. Eng. J.*, 2019, **373**, 700–708.

428 M. Chowdhury, S. Kapinga, F. Cummings and V. Fester, *Water Sci. Technol.*, 2019, **79**, 947–957.

429 N. Masiran, D. V. N. Vo, M. A. Salam and B. Abdullah, *Procedia Eng.*, 2016, **148**, 1289–1294.

430 P. Forzatti and L. Lietti, *Catal. Today*, 1999, **52**, 165–181.

431 E. E. Wolf and F. Alfani, *Catal. Rev.*, 1982, **24**, 329–371.

432 Z. Li, Z. Wang and S. Kawi, *ChemCatChem*, 2019, **11**, 202–224.

433 C. H. Bartholomew, *Appl. Catal. A Gen.*, 2001, **212**, 17–60.

434 C. Liu, J. Zhou, J. Su and L. Guo, *Appl. Catal. B Environ.*, 2019, **241**, 506–513.

435 H. Anwer, A. Mahmood, J. Lee, K. H. Kim, J. W. Park and A. C. K. Yip, *Nano Res.*, 2019, **12**, 955–972.

436 G. M. Reda, H. Fan and H. Tian, *Adv. Powder Technol.*, 2017, **28**, 953–963.

437 X. Zhao, Z. Lu, W. Ma, M. Zhang, R. Ji, C. Yi and Y. Yan, *Chem. Phys. Lett.*, 2018, **706**, 440–447.

438 F. Wang, Y. T. Zhang, Y. Xu, X. Wang, S. Li, H. Yang, X. Liu and F. Wei, *J. Environ. Chem. Eng.*, 2016, **4**, 3364–3373.

439 A. Shraim, A. Diab, A. Alsuhaimi, E. Niazy, M. Metwally, M. Amad, S. Sioud and A. Dawoud, *Arab. J. Chem.*, 2017, **10**, S719–S729.

440 C. Yang, G. Gao, Z. Guo, L. Song, J. Chi and S. Gan, *Appl. Surf. Sci.*, 2017, **400**, 365–374.

441 A. Kheradmand, Y. Zhu, W. Zhang, A. Marianov and Y. Jiang, *Int. J. Hydrogen Energy*, 2019, 1–13.

442 S. Xue, C. Wu, S. Pu, Y. Hou, T. Tong, G. Yang, Z. Qin, Z. Wang and J. Bao, *Environ. Pollut.*, 2019, **250**, 338–345.

443 W. Zhao, Y. Feng, H. Huang, P. Zhou, J. Li, L. Zhang, B. Dai, J. Xu, F. Zhu, N. Sheng and D. Y. C. Leung, *Appl. Catal. B Environ.*, 2019, **245**, 448–458.

444 K. Ng, K. Kok and B. Ong, *ACS Appl. nano Mater.*, 2018, **1**, 401–409.

445 A. B. D. Nandiyanto, R. Zaen and R. Oktiani, *Arab. J. Chem.*, , DOI:10.1016/j.arabjc.2017.10.010.

446 M. Shang, W. Wang, S. Sun, L. Zhou and L. Zhang, *J. Phys. Chem. C*, 2008, **112**, 10407–10411.

447 J. Cao, B. Xu, H. Lin, B. Luo and S. Chen, *Dalt. Trans.*, 2012, **41**, 11482–11490.

448 C. Yu, C. Fan, J. C. Yu, W. Zhou and K. Yang, *Mater. Res. Bull.*, 2011, **46**, 140–146.

449 J. Wu, X. Chen, C. Li, Y. Qi, X. Qi, J. Ren, B. Yuan, B. Ni, R. Zhou, J. Zhang and

T. Huang, *Chem. Eng. J.*, 2016, **304**, 533–543.

450 S. Wang, Y. Guan, L. Wang, W. Zhao, H. He and J. Xiao, *Appl. Catal. B Environ.*, 2015, **169**, 448–457.

451 A. Malathi, P. Arunachalam, A. Nirmala and J. Madhavan, *Appl. Surf. Sci.*, 2017, **412**, 85–95.

452 X. Luo, Z. Zhang, P. Zhou, Y. Liu, G. Ma and Z. Lei, *J. Ind. Eng. Chem.*, 2015, **27**, 164–174.

453 A. O. Ibhadon and P. Fitzpatrick, *Catalysts*, 2013, **3**, 189–218.

454 M. J. Lima, L. M. Pastrana-Martínez, M. J. Sampaio, G. Dražić, A. M. T. Silva, J. L. Faria and C. G. Silva, *ChemistrySelect*, 2018, **3**, 8070–8081.

455 N. Garino, A. Sacco, M. Castellino, J. A. Muñoz-Tabares, M. Armandi, A. Chiodoni and C. F. Pirri, *ChemistrySelect*, 2016, **1**, 3640–3646.

456 T. Hu, P. Li, J. Zhang, C. Liang and K. Dai, *Appl. Surf. Sci.*, 2018, **442**, 20–29.

457 Y. Mi, H. Li, Y. Zhang and W. Hou, *J. Colloid Interface Sci.*, 2019, **534**, 301–311.

458 X. Ren, J. Yao, L. Cai, J. Li, X. Cao, Y. Zhang, B. Wang and Y. Wei, *New J. Chem.*, 2019, **43**, 1523–1530.

459 A. Bafaqeer, M. Tahir, A. A. Khan, N. Aishah and S. Amin, *Ind. Eng. Chem. Res.*, 2019, **58**, 8612–8624.

460 S. Hou, J. Li, X. Huang, X. Wang, L. Ma and W. Shen, *Appl. Sci.*, 2017, **7**, 852–862.